Interacting bosons and fermions in one-dimensional lattice potentials

Dissertation

Alexander Mering

Vom Fachbereich Physik der Technischen Universität Kaiserslautern zur Verleihung des akademischen Grades „Doktor der Naturwissenschaften" genehmigte Dissertation

Betreuer: Prof. Dr. Michael Fleischhauer

Zweitgutachter: Prof. Dr. Sebastian Eggert

Datum der wissenschaftlichen Aussprache: 09. Juni 2010

D 386

Für Marena

Contents

Abstract

Ultracold atoms in optical lattices allow for a fascinating insight in the
world of quantum many-body systems. The comparatively easy control of
many parameters of these systems gives the opportunity to study many
models of solid-state theory experimentally without disturbing influences. In
particular, mixtures of several kinds of atoms promise an insight into physi-
cal processes whose observations in solid state systems are close to impossible.

This thesis deals with analytic as well as numeric studies of the ground state
of mixtures of a bosonic and (spin-polarized) fermionic species in periodic
potentials. Experimental realizations of such mixtures in the framework
of quantum optics already showed several new effects. Furthermore mix-
tures are of particular interest since the underlying models have a close
relationship to the research on high-temperature superconductors. To
investigate the phase diagram of such mixtures, a treatment in terms of the
Bose-Fermi-Hubbard model is applied, which is valid for small temperatures.
As a result of the large number of free parameters in this system, a detailed
investigation and comprehensive understanding of the phase diagram will
not cover the full parameter space; restrictions to special cases nevertheless
allow for a rather accurate description of physics of this system.

After introducing the model and the basic physics, the first part of the
thesis which is based on an earlier diploma thesis deals with the influence
of ultraheavy fermions onto the bosonic phase diagram. At this point
it has to be distinguished, whether the ground state is reached for the
full system or the bosonic sector for a given fermion distribution. In the
first case, the fermions either arrange themselves with a maximal distance
between each other or group close to each other. This depends on the
effective coupling between the fermions and is primarily determined by the
boson-fermion interaction. The second case describes a bosonic system with
binary disorder, where the special sort of disorder leads, as in the first case,

to the formation of new incompressible phases at non-integer filling. In both cases, analytic theories are presented, allowing to predict the bosonic phase diagram.

In the second part, the situation of light fermions is considered. The strongly enhanced fermionic mobility leads to an effective long-range interaction between the bosons. A deeper investigation of this interaction shows, that the assumption of completely uncoupled fermions leads to divergences which have to be renormalized by inclusion of the back-action of the bosons onto the fermions. Apart from the derivation of the effective bosonic interaction, the resulting bosonic phase diagram is discussed. Starting from the effective bosonic Hamiltonian it is shown, that the induced interaction leads to the formation of bosonic density waves, accompanied by fermionic ones, representing a further incompressible phase beside the Mott insulators. From the discussion of boundary effects the existence of a thermodynamically instable phase is found, which comprises density waves and Mott insulators simultaneously.

Recent experimental results suggest that the theory of ultracold atoms in optical lattices based on a first-band model does not explain all occurring effects. The third part of this thesis is devoted to an effective theory for the first band, which takes effects of all higher bands into account by means of virtual transitions between the first band and the higher ones. Based on this effective (renormalized) first-band model, the influence of the higher bands, as well as the influence of the fermions on the bosonic superfluid to Mott-insulator transition is studied and the results are compared to experimental results.

Finally, part four of this thesis studies the Jaynes-Cummings-Hubbard model, which describes the coupling of two-level atoms in a lattice to a bosonic field. Although this does not describe a boson-fermion mixture, an approach where the two-level atoms are treated approximately as fermions allows the easy calculation of the phase diagram. This solution is applied to the case of ions in a linear Paul trap which present a realization of the Jaynes-Cummings-Hubbard model. Additionally, the findings are compared to results from a degenerate perturbation theory as well as to numerical data.

Zusammenfassung

Ultrakalte Atome in optischen Gittern erlauben einen faszinierenden und
darüber hinaus kontrollierbaren Einblick in die Welt der quantenmechanischen Vielteilchenphysik. Durch die vergleichsweise einfache Kontrolle vieler
Parameter dieser Systeme lassen sich eine Vielzahl festkörpertheoretischer
Modellsysteme ohne störende Einflüsse experimentell untersuchen. So
versprechen insbesondere Mischungen mehrerer Atomsorten ein detailliertes
Studium physikalischer Prozesse, deren Beobachtung im Festkörper in
diesem Maße nicht möglich ist.

In der hier vorliegenden Arbeit werden sowohl analytische, als auch
numerische Untersuchungen an Mischungen einer bosonischen und einer
(spin-polarisierten) fermionischen Spezies in einem periodischen Potential im
Grundzustand durchgeführt. Experimentelle Realisierungen solcher Mischungen haben im Rahmen der Quantenoptik bereits eine Vielzahl neuer Effekte
hervorgebracht. Sie sind weiterhin von besonderem Interesse, da die zugrunde liegenden Modelle beispielsweise eine direkte Verbindung zur Theorie der
Hochtemperatur-Supraleitung haben. Für die hier gemachten Untersuchungen des Phasendiagramms wird das Bose-Fermi-Hubbard-Modell verwendet,
welches solche Mischungen im Fall niedriger Temperaturen beschreibt.
Durch die Vielzahl freier Parameter in diesem System kann eine detaillierte
Untersuchung und ein genaues Verständnis des Phasendiagramms nur
sehr schlecht den gesamten Parameterraum abdecken; Beschränkungen auf
spezielle Parameterbereiche erlauben hier dennoch einen fundierten Einblick.

Nach einer Einführung in das Modell und die dadurch beschriebene Physik
wird im ersten Teil dieser Arbeit aufbauend auf meiner vorangegangenen
Diplomarbeit der Einfluß sehr schwerer Fermionen auf das bosonische
Phasendiagramm studiert. Hier ist zu unterscheiden, ob das Gesamtsystem
oder nur der bosonische Sektor bei fest vorgegebener Fermionenverteilung
den Grundzustand erreicht. Im ersten Fall ergibt sich ein Bild, in dem

die Fermionen entweder einen maximalen Abstand zueinander bevorzugen oder sich in benachbarten Gitterplätzen ansammeln. Dies hängt von einer effektiven Kopplung der Fermionen untereinander ab und ist primär durch die Boson-Fermion-Wechselwirkung bestimmt. Der zweite Fall beschreibt ein bosonisches System mit einer binären Unordnung, wobei die spezielle Unordnung ebenso wie im ersten Fall zur Ausbildung neuer inkompressibler Phasen mit nicht-ganzzahliger Füllung führt. Für beide Fälle werden analytische Theorien präsentiert, die eine Vorhersage für das bosonische Phasendiagramm erlauben.

Der zweite Teil betrachtet die Situation sehr leichter Fermionen. Hier führt die, im Vergleich zu den Bosonen stark erhöhte Mobilität der Fermionen zu einer durch diese induzierten effektiven Wechselwirkung zwischen den Bosonen. Eine genaue Untersuchung dieser Wechselwirkung zeigt, dass eine Annahme völlig entkoppelter Fermionen Divergenzen liefert, welche jedoch durch eine Berücksichtigung der Rückwirkung der Bosonen auf die Fermionen renormalisiert werden können. Neben der Herleitung der effektiven bosonischen Wechselwirkung steht die Diskussion des bosonischen Phasendiagramms im Vordergrund. Ausgehend vom effektiven bosonischen Hamilton-Operator lässt sich zeigen, dass die induzierte Wechselwirkung durch die Fermionen zur Ausbildung von bosonischen und damit auch fermionischen Dichtewellen führt, welche eine weitere inkompressible Phase neben den bekannten Mott-Isolatoren beschreibt. Eine Diskussion des Einflusses der Randbedingungen zeigt überdies noch die Existenz von thermodynamisch instabilen Phasen in denen Dichtewellen und Mott-Isolatoren koexistieren.

Aktuelle experimentelle Ergebnisse zeigen, dass eine Beschreibung ultrakalter Atome in optischen Gittern im Rahmen eines Einband-Modells nicht alle Effekte beschreiben kann. Dazu wird im dritten Teil eine effektive Theorie des ersten Bandes entwickelt, welche den Einfluss aller höheren Bänder durch virtuelle Übergänge zwischen dem ersten und den höheren Bändern berücksichtigt. Im Rahmen dieses effektiven (renormierten) Einband-Modells wird der Einfluss der höheren Bänder sowie der Fermionen auf den bosonischen Superfluid-zu-Mott-Isolator Übergang untersucht und in Relation zu experimentellen Ergebnissen gesetzt.

Abschließend wird in Teil vier das Jaynes-Cummings-Hubbard-Modell betrachtet. Dieses beschreibt die Kopplung von Zwei-Niveau-Atomen in einem regelmäßigen Gitter an ein bosonisches Feld. Obwohl hier zwar keine Mischung aus Bosonen und Fermionen vorliegt, erlaubt die Näherung die Zwei-

Niveau-Atome als Fermionen zu betrachten (effektives Fermionenmodell) eine einfache Bestimmung des Phasendiagramms dieses Modells. Die so gefundene Lösung wird dann zur Beschreibung von Ionen in einer linearen Paul-Falle angewendet, was eine Realisierung des Jaynes-Cummings-Hubbard-Modells darstellt. Die Ergebnisse dieser Näherung werden schließlich zu einer entarteten Störungstheorie sowie numerischen Resultaten in Beziehung gesetzt.

Introduction and foundations

Introduction

Starting from the development of efficient laser cooling techniques for neutral atoms [1, 2, 3], the field of ultracold atoms developed quickly, reaching the long-term goal of a Bose-Einstein condensate (BEC) [4, 5] in Sodium [6, 7], Rubidium [8, 9] and Lithium [10] in the mid 1990th. More elaborate cooling steps finally led to the achievement of a degenerate Fermi gas [11, 12] and further improvements in the experiments subsequently allowed to impose optical lattices to the BEC (for an overview see [13]), culminating in the first observation of a bosonic superfluid to Mott-insulator transition [14] in Rubidium [15]. For the fermionic analog, very recently the Mott insulating state for stronger lattices was reached [16, 17].

Apart from realizations in ultracold atoms, BECs can also be observed in other physical systems as for instance in magnons in the solid state [18], exciton polaritons in semiconductor microcavities [19] or, with some limitations in liquid Helium as in the early works of [20, 21]. Even Cooper-pairs [22] in superconduction theory [23, 24] can be seen as a BEC. However, only within the framework of quantum optics it is possible to manipulate important system parameters such as the interaction between the constituents or the geometry in a precise way. Because of this and the fact that the nature of the resulting ground and excited states can be studied by a variety of different experimental methods, ultracold atoms provide the state-of-the-art approach to study many-body physics experimentally under maximum external control.

Alkali elements are most suitable for laser cooling and trapping because of their atomic level structure [25], but earth-alkali elements (Calcium [26], Strontium [27]) and other elements as Ytterbium [28], metastable Helium [29, 30] and Hydrogen [31] could also be used for a BEC. Important is the achievement of a BEC of Chromium [32], since Cr has a large dipole moment, thus realizing a dipolar BEC with intrinsic long-range (orientation dependent) interactions.

After the step of a simultaneous trapping of bosonic (e.g. ^{7}Li, ^{41}K or ^{87}Rb) and fermionic isotopes (e.g ^{6}Li or ^{40}K) of the same or different elements [33, 34, 35, 36], the combination of the degenerate mixture with an optical lattice setup [37, 38] opened the route to study a large variety of different physical model systems. The most prominent is the Bose-Fermi-Hubbard model [39], introduced in section 1.3, which is the key model studied in this thesis.

Beyond the issues of preparation of the BEC or degenerate mixtures, a large progress in the manipulation and analysis of the ultracold-atom system was made in the last decade. Starting from simple absorption images of the atomic cloud, modern setups allow for a direct, *in-situ*, imaging of a two-dimensional BEC [40, 41] or the usage of electron microscopy [42] with single-site resolution. Additional to imaging, the physics of the BEC (with our without lattice) was studied by noise interferometry [43] as well as by several spectroscopic methods, including microwave [44], lattice modulation [45, 46], radio-frequency [47] or Bragg spectroscopy [48, 49]. The latter method was recently extended to a momentum-resolved measurement of the excitation spectrum, allowing to study the full band structure as well as interaction effects on it [50, 51]. For further details of the experimental methods refer to the review [13] and references therein. [52] gives a short introduction on the realization of a BEC using atom chips, another promising implementation of ultracold atoms.

As latest points in the long list of achievements in the systems of ultracold atoms, the controlled realization of (cold) chemical reactions [53, 54, 55] and the in-deep study of genuine many-body states such as Efimov-trimers [56, 57, 58] shows the enormous possibilities of ultracold atoms. Nevertheless, many questions are still open. Though providing a fully controllable tool for the simulation of well known Hamiltonians ranging from the Bose-Hubbard model [59], the Hubbard model [16, 17] to effective spin models [60, 61, 62] in various lattice geometries (dimensionality [63, 64], lattice types [65, 66, 67] or including disorder [68, 69, 70, 71]), the nature of the different quantum phase transitions still gives open questions. Considering ultracold atoms as a quantum simulator [72], the implementations of quantum phase gates [73, 74] are a further step towards a (scalable) quantum information technology. As a far goal, the understanding of various important, but yet unclear phenomena such as high-T_C superconductivity [75, 76, 77] or the physics of strongly imbalanced interacting fermions [78, 79] are prominent outstanding problems to be explored. For all of these kinds of models, ul-

tracold atoms provide a controllable environment to study individual effects of the system which could not be discriminated against further effects in other experimental realizations. Finally, the application of the lattice setup opens the route to single-atom trapping which is important to metrology [80].

Focussing on the physics of mixtures of bosons and fermions in the optical lattice, described by the Bose-Fermi-Hubbard model, we study in this thesis the influence of the fermionic admixture on the well understood bosonic phase diagram. This model is of special interest due to its relation for instance to the coupling of fermions to phonons [81], fermionic polarons [82] or composite particles [83]. In a series of experiments [37, 38, 84] a strong influence of the fermions to the bosonic superfluid to Mott-insulator transition was seen. Similar experiments in Bose-Bose mixture reveal that only a small overlap of the different atomic clouds suffices to observe the effect of inter-species interactions [85]. Though some analytics and numerics has been done to understand these effects [86, 87, 88, 89, 90], several aspects are not understood yet. Limiting on different regions of the parameter space, we develop analytic approaches to provide a better understanding of the physics of interacting bosons and fermions, supported by numerical simulations. This allows for the construction of the bosonic phase diagram as well as the prediction of qualitatively new phases.

Outline

Throughout the whole thesis we present different approaches to the physics of interacting bosons and fermions, each of them allowing for the prediction of the phase diagram in different parameter regimes. Starting with the discussion of the general physics of ultracold bosons in optical lattices, the first part of this thesis deals with the physics of the Bose-Fermi-Hubbard model with vanishing fermionic mobility. Extending the results from a prior diploma thesis, we study the influence of the fermions on the bosonic phase diagram. In this limit, the fermions are treated as a source of disorder which is assumed to be either quenched or annealed. In both cases, incompressible phases with non-integer fillings arise together with the prediction of a Bose-glass phase [Mering2008].

In the second part, the opposite limit is considered. Assuming the fermions to be ultrafast, i.e., having almost infinite mobility, an effective bosonic theory yielding induced long-range density-density interactions is derived [Mering2010]. A first treatment of the induced interactions reveals the need for a renormalization scheme, including the back-action of the resulting bosonic charge-density wave phase to the fermions. Within the renormalized effective model, a strong-coupling theory gives analytic estimates for the phase diagram, pointing to the existence of thermodynamically unstable phases of coexistence between a charge-density wave phase and a Mott insulator. Here, boundary issues are crucial for the understanding of the system, leading to phases displaying a spatial separation of a Mott insulator and a charge-density wave, also seen in numerical simulations.

Ultracold atoms in deep optical lattices are usually described by means of a first-band model. Recent experimental results suggest however, that this approach does not hold for a full understanding of certain aspects of these systems. This problem, being discussed in the third part of this thesis, is resolved by the inclusion of the higher bands into the Bose-Fermi-Hubbard

model. Though contributing to the Hamiltonian, an adiabatic elimination of these higher bands condenses their effect to an effective first-band description extended by contributions due to virtual transitions to the higher bands. Starting from this effective Hamiltonian, the effect of the higher bands as well as the effect of the fermions to the bosonic superfluid to Mott-insulator transition is studied and compared to experimental results.

The final part of this thesis studies the Jaynes-Cummings-Hubbard model which describes the physics of two-level atoms coupled to a bosonic lattice field. Approximating the two-level systems as fermions [Mering2009], the Jaynes-Cummings-Hubbard model is easily solved with analytic expressions for the phase diagram. Special application of this solution to the physics of ions in a linear Paul trap displaying long-ranged bosonic hopping gives a first estimate for the phase diagram of this system. Perturbation theory as well as numerical results for the phase diagram finally validate the made approximations.

Foundations

In this chapter we provide the basic theory for the description of ultracold atoms and mixtures in optical lattices and give a short overview over the most important properties of the different phases. Before treating the mixture, we focus on the discussion of the pure bosonic system, introducing the main quantities and defining the notation. All this is done for a one-dimensional system.

1.1 Bosons in optical lattices

Jaksch *et al.* realized in a pioneering work [59], that ultracold bosonic atoms in an optical lattice are well described by the Bose-Hubbard model. Assuming a local interaction $V(z-z') = g_{\mathrm{BB}}\delta(z-z')$ for the bosons with $g_{\mathrm{BB}} = \frac{4\pi\hbar^2}{m_B}\, a_{BB}$ and a_{BB} being the s-wave scattering length, the continuous Hamiltonian reads

$$
\begin{aligned}
\hat{\mathcal{H}} = \int \mathrm{d}z\, \Psi_B^\dagger(z) \left[-\frac{\hbar^2}{2m_B}\Delta + V_{\mathrm{Pot}}^B(z) \right] \Psi_B(z) \\
+ \frac{g_{\mathrm{BB}}}{2} \int \mathrm{d}z\, \Psi_B^\dagger(z)\Psi_B^\dagger(z)\Psi_B(z)\Psi_B(z).
\end{aligned}
\tag{1.1}
$$

A potential $V_{\mathrm{Pot}}^B(z) = \eta_B \sin^2(kz)$ is considered with k being the wave-vector of the optical lattice laser and η_B the amplitude of the potential. No additional harmonic confinement is included. Details about the physical effects of the lattice potential can be found in section 17.1 and in [13, 91]. Here we shortly summarize the main features of this system.

For the field operators it is convenient to switch to a localized basis in terms of Wannier functions (see section 1.2), i.e., decomposing $\Psi_B(z)$ as

$$\Psi_B(z) = \sum_j \hat{a}_j \, w^B(z - ja) \tag{1.2}$$

with a being the lattice spacing. We only incorporated Wannier functions from the first Bloch band, which is a good approximation for deep lattices and low temperatures, i.e., if the temperature is small compared to the band gap[1]. The replacement of the field operators in the continuous Hamiltonian leads to a lattice model, the well known Bose-Hubbard model [14]:

$$\hat{H}_{\mathrm{BHM}} = -J_B \sum_j \left(\hat{a}_j^\dagger \hat{a}_{j+1} + \hat{a}_{j+1}^\dagger \hat{a}_j \right) + \frac{U}{2} \sum_j \hat{n}_j \left(\hat{n}_j - 1 \right) + \Delta_B \sum_j \hat{n}_j. \tag{1.3}$$

$\hat{n}_j = \hat{a}_j^\dagger \hat{a}_j$ is the number operator and $\hat{a}_j^\dagger$ ($\hat{a}_j$) the bosonic creation (annihilation) operator at lattice site j. This model also describes the physics of liquid ^{4}He in pouros media [92] or an array of Josephson junctions [93, 94]. The first term is the kinetic energy, i.e., the hopping of a single particle from one site to its nearest-neighbors with amplitude

$$J_B = -\int \mathrm{d}z \, \bar{w}^B(z-a) \left[-\frac{\hbar^2}{2m_B} \frac{\partial^2}{\partial z^2} + V_{\mathrm{Pot}}^B(z) \right] w^B(z), \tag{1.4}$$

the second term the local nonlinearity with

$$U = g_{\mathrm{BB}} \int \mathrm{d}z \, \bar{w}^B(z) \bar{w}^B(z) w^B(z) w^B(z) \tag{1.5}$$

and the last term is the band energy

$$\Delta_B = \int \mathrm{d}z \, \bar{w}^B(z) \left[-\frac{\hbar^2}{2m_B} \frac{\partial^2}{\partial z^2} + V_{\mathrm{Pot}}^B(z) \right] w^B(z). \tag{1.6}$$

A discussion of the properties of these amplitudes as a function of the lattice depth η_B is found in the next section. Generally, we set the energy scale by $U = 1$. All other amplitudes, though not explicitly written, are referred to this energy. In Hamiltonian (1.3) no other contributions occur beside

---

[1]In part III we show that this assumption is too strong and does not allow a full understanding of experimental results; higher bands are important in the experimental situation but here they unnecessarily complicate the system and are henceforth left out throughout the whole thesis besides part III.

local interactions and nearest-neighbor hopping. This is a common simplification for these kinds of models, since all other amplitudes are much smaller.

For the treatment of the Bose-Hubbard model, the band energy is not important as it gives just an energy shift since the total number of particles $\hat{N} = \sum_j \hat{n}_j$ commutes with the Hamiltonian. This accounts for the description of the system in the canonical ensemble, i.e., fixing the number of particles. For the discussion of the phase boundaries, this description turns out to be more suitable than the grand-canonical ensemble, i.e., including a chemical potential described by

$$\hat{K} = \hat{H} - \mu_B \sum_j \hat{n}_j. \tag{1.7}$$

Nevertheless the different phases are discussed in the (μ_B, J_B)-plane where the chemical potential, which gives the energy cost when changing the number of particles, is defined as

$$\mu_B = \frac{\partial E}{\partial N} = E(N+1) - E(N) \tag{1.8}$$

This also leads to the definition of the compressibility which accounts for the change of the number of particles with the chemical potential:

$$\kappa = \frac{\partial \langle \hat{N} \rangle}{\partial \mu_B}. \tag{1.9}$$

For phases with non-zero compressibility, the system in ungapped (with respect to particle-hole excitations), i.e., it does not cost energy to change the number of particles. For the Bose-Hubbard model (1.3), two different phases exist, distinguished by the compressibility.

a)   Plain Bose-Hubbard model

The model described in (1.3) will be referred to as the *plain Bose-Hubbard model*, which is the basis of our discussions. We will present two important extensions later. First we discuss the phase diagram of the plain model.

In the interaction dominated regime $U \gg J_B$ and for commensurate filling $N = nL$, the ground state is given by the so-called Mott insulator, displaying the same number of particles n on each lattice cite, i.e.,

$$|\Psi\rangle_{\text{Mott}} \sim \sum_j \left(\hat{a}_j^\dagger \right)^n |0\rangle. \tag{1.10}$$

A single particle-hole excitation $\hat{a}_j^\dagger \hat{a}_{l \neq j} \left| \Psi \right\rangle_{\text{Mott}}$ has an extra energy U (for $J_B = 0$) compared to the Mott insulator and therefore the Mott insulating phase is incompressible; it costs energy to add or remove a particle.

In the hopping dominated regime $U \ll J_B$ and for any filling, the ground state is a superfluid with

$$\left| \Psi \right\rangle_{\text{SF}} \sim \left(\sum_j \hat{a}_j^\dagger \right)^N \left| 0 \right\rangle. \tag{1.11}$$

This state does not display a particle-hole gap, it is compressible.

For vanishing hopping $J_B = 0$, the phase diagram is easily constructed for the grand-canonical Bose-Hubbard Hamiltonian (1.7). The Hamiltonian becomes local and the number n of particles per site which minimizes the energy is given by

$$n = \max\{0, [1/2 + \mu_B]\}, \tag{1.12}$$

$[x]$ is the integer closest to x. For non-integer μ_B, the number of bosons is well defined and constant over a wide range of μ_B values whereas for integer μ_B/U the system becomes degenerate with the possible number states $\left| \lfloor 1/2 + \mu_B \rfloor \right\rangle$ and $\left| \lfloor 1/2 + \mu_B \rfloor + 1 \right\rangle$, yielding a quantum critical point. $\lfloor x \rfloor$ is the largest integer smaller than x. For non-vanishing hopping J_B these quantum critical points extend to a compressible region. This phase is referred to as the *superfluid* phase. Together with the increase of the superfluid phase with increasing hopping, the Mott insulator regions get smaller until the upper and the lower boundary come together. At this point, termed the *tip of the Mott lobe*, a quantum phase transition occurs from the superfluid to Mott-insulator phase. For integer filling, this transition at the tip is of the Kosterlitz-Berezinsky-Thouless type [95, 96], i.e., with exponentially diverging correlations at the transition.

The resulting phase diagram for the (plain) Bose-Hubbard model is shown in figure 1.1. The boundaries of the Mott insulator are taken from strong-coupling results [97], showing a good agreement with various numerical calculations not discussed here. Beside the compressibility, the superfluid and Mott insulating phase can be distinguished from the behavior of the first-order correlations $\left\langle \hat{a}_j^\dagger \hat{a}_{j+d} \right\rangle$. In a one-dimensional system, these decay in the superfluid algebraically $\sim m^{-K/2}$ and exponentially $\sim e^{-m/L_c}$ for the Mott insulator. K is the so-called Luttinger parameter, which in principal can be
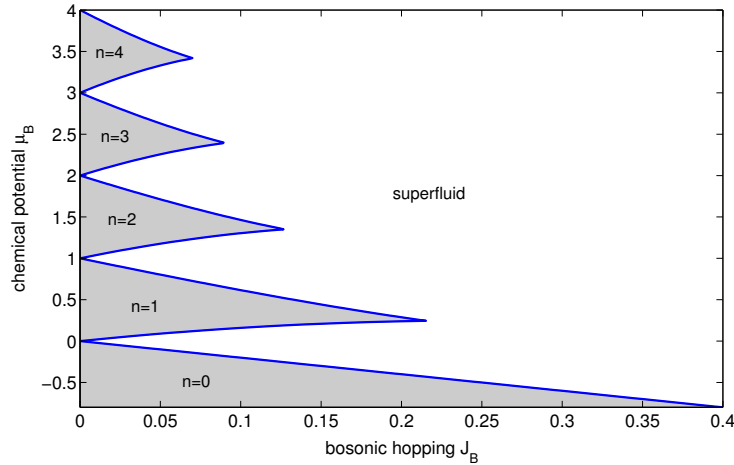
Figure 1.1: Phase diagram of the Bose-Hubbard model. Gray regions are the Mott insulators, outside lies the superfluid region. The phase boundaries were obtained according to [97]. The interaction energy $U = 1$ is set as energy scale. Within the Mott insulators, the first-order correlations decay exponentially, within the superfluid algebraically.

calculated from other approaches as Bethe ansatz [98, 99] and the algebraic decay is seen from a bosonization approach [99, 100, 101, 102, 103].

b) Disordered Bose-Hubbard model

In the plain Bose-Hubbard model, no locally varying potential is present. Including local potentials as

$$\hat{H}_{\text{dBHM}} = \hat{H}_{\text{BHM}} + \sum_j \varepsilon_j \hat{n}_j, \tag{1.13}$$

the resulting Bose-Hubbard Hamiltonian allows for a description of various different situations such as bosons in an external (harmonic) confinement with $\varepsilon_j = \omega \, (j - L/2)^2$, superlattice structures as $\varepsilon_j = V\delta(\sin(\pi j/2))$ or disordered systems with $\varepsilon_j \in [-\Delta/2, \Delta/2]$ chosen randomly.

Here we discuss the situation of a weak $(\Delta < U)$, bound random disorder. For strong or unbound disorder the situation qualitatively stays the same, where the main difference to weak disorder is given by the full vanishing of all Mott insulating lobes. The disorder distribution itself does not play any role for the discussion of the phase diagram with one exception pointed out
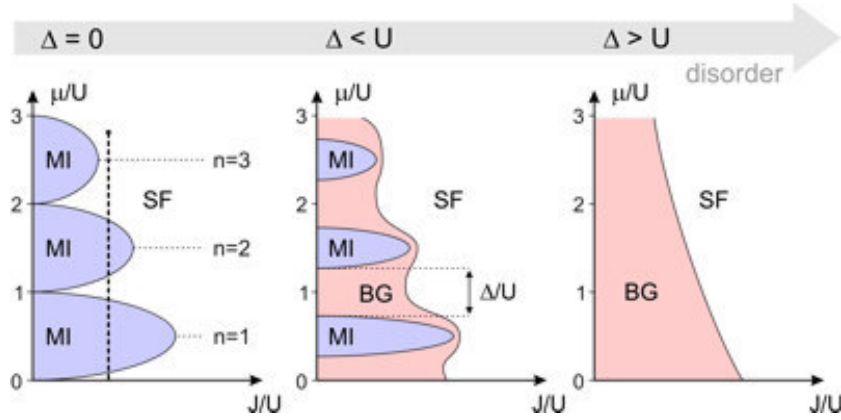
Figure 1.2: Phase diagram of the disordered Bose-Hubbard model in three dimensions for different strengths of the disorder Δ taken from [71]. For vanishing disorder, the typical lobe structure is seen with a decrease of the Mott lobes (MI) for weak ($\Delta < U$) disorder. For large or unbound disorder, all Mott lobes vanish with only a Bose glass (BG) and superfluid phase (SF) remaining.

in section 3.1.

For zero bosonic hopping ($J_B = 0$) and weak disorder, the disorder leads to a shift of the upper and lower boundary of the Mott insulators. Due to the inhomogeneity of the system and the continuous disorder distribution, additional particles can always be added without cost in energy. This holds, until commensurate filling is reached, according to the Mott insulating state. The energy to add another particle is now given by the change in interaction energy nU as well as the smallest local energy $\min(\varepsilon_j) = -\Delta/2$, the chemical potential for the upper boundary of the Mott insulator therefore equals $nU - \Delta/2$. Accordingly, the lower boundary is given by $(n-1)U + \Delta/2$. This indicates a shrinking of the Mott insulating region by Δ with the appearance of a compressible phase in between[2] (see figure 1.2).

The Mott insulating gap closes with increasing hopping as in the plain system. The intermediate compressible phase turns out to be of a different character than the superfluid. This is seen in the correlations of the system, which still decay exponentially hence indicating a localization of the bosons,

---

[2]This explains the distinction between weak and strong disorder. For the strong disorder case, the disorder induced shifts of the upper and lower boundaries are beyond the width of the Mott insulator.

as well as in the vanishing superfluid fraction

$$\varrho_S = \frac{2L^2}{\pi^2 N_B}\left(E^{apbc} - E^{pbc}\right).$$ (1.14)

The superfluid fraction is defined by the energy difference of the ground states of the system with anti-periodic and periodic boundary conditions [104, 105], thus accounting for the response of the system to a phase gradient. This compressible, not superfluid *Bose-glass* phase is a direct consequence of the disorder and up to now a main research object theoretically and experimentally. Again, ultracold atoms allow for the observation of this glass phase in controlled experiments [69, 71, 106] with a clear observation of the predicted properties.

c) Bose-Hubbard model with nearest-neighbor interactions

Including nearest-neighbor density-density interactions

$$\hat{H}_{\text{eBHM}} = \hat{H}_{\text{BHM}} + V\sum_j \hat{n}_j \hat{n}_{j+1},$$ (1.15)

to the plain Bose-Hubbard model, another important phase is present. For repulsive interactions V, the bosons try to avoid states with two adjacent bosons. This gives a stable configuration, where only every second lattice site is occupied. The resulting phase is again incompressible, since the addition of another particle increases the energy by $2V$. This *charge-density wave* (CDW) phase with a periodic modulation of the boson density is thus extended in the (μ_B, J_B)-plane like the Mott insulator. For fillings above one, the CDW phase with filling $\varrho_B = \frac{2n-1}{2}$ is given by a state with n bosons on every second lattice site and $n-1$ bosons in the remaining half of the lattice.

According to numerical results, the CDW phase is characterized by a vanishing of the superfluid fraction ϱ_S and a finite static structure factor [108]

$$S(q) = \frac{1}{N_B^2}\sum_{ij} e^{iq(i-j)}\ \langle \hat{n}_i \hat{n}_j \rangle$$ (1.16)

at momentum $q = \pi$. Possible phases with $S(\pi) > 0$ and $\varrho_S > 0$, so-called *supersolids* are a recent matter of research and will be discussed briefly in part II.
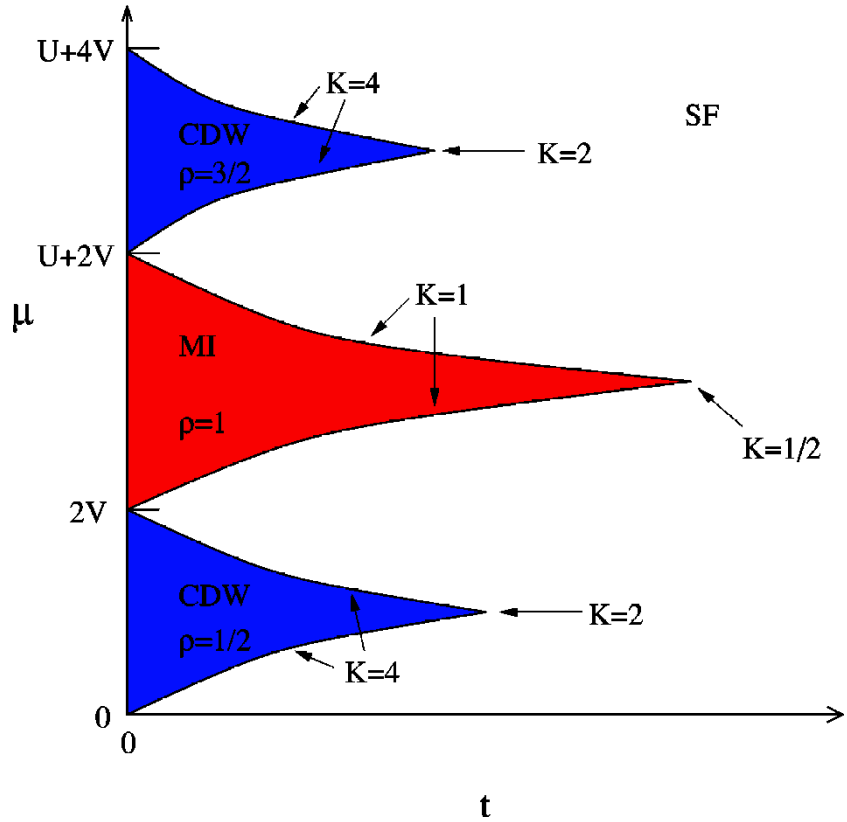
Figure 1.3: Schematic phase diagram of the extended Bose-Hubbard model taken from [107]. Beside the usual Mott insulator (MI), shifted due to the nearest-neighbor interaction by $2V$, charge-density wave phases (CDW) arise for different fillings. The different Luttinger parameters K are the values at the phase transition. Outside the incompressible phases, a superfluid phase (SF) is present.

Figure 1.3 shows the phase diagram of the extended Bose-Hubbard model with repulsive nearest-neighbor interaction. The Mott insulators are shifted by $2V$ with intermediate CDW phases for half-integer filling. The given Luttinger parameters represent values at the phase transition. These, calculated for instance by means of microscopic theories [100, 109], also allow for the determination of the phase transition from a fitting of the first-order correlations to an algebraic decay [107].

1.2 Wannier functions

In the derivation of the Bose-Hubbard Hamiltonian (1.3), the field operators were expanded in the local basis of Wannier functions. Following [110], these are obtained from the solution of the single particle Schrödinger equation

$$\left(-\frac{\partial^2}{\partial z^2} + \eta_B \, \sin^2(z) \right) \Phi(z) = E \, \Phi(z), \tag{1.17}$$

where all energies are given in units of the recoil energy $E_{rec} = \frac{\hbar^2 k^2}{2 m_B}$ and all lengths in units of $1/k$. Since the system is periodic with period π, the Hamiltonian commutes with the (discrete) translation operator and the eigenfunctions are given in terms of Bloch waves [111]

$$\Phi_{n,p}(z) = u_{n,p}(z) e^{ipz}. \tag{1.18}$$

$u_{n,p}(z)$ is periodic with the lattice spacing. The eigenenergies of form certain ranges $E_{n,p}$ with n giving the different Bloch bands. Dealing with the notion of different sites, the delocalized Bloch waves $\Phi_{n,p}(z)$ are replaced by the more suitable Wannier functions [112], being localized within the different potential minima. They are given by

$$w_n(z) = \frac{1}{\sqrt{2}} \int\limits_{-1}^{1} \mathrm{d}p \, \Phi_{n,p}(z), \tag{1.19}$$

but are not uniquely defined due to an arbitrary phase factor. Nevertheless they fall off exponentially [113, 114] and can be chosen to be symmetric in the odd bands and antisymmetric in the even bands [113].

Only in the limit $\eta_B \to \infty$ the Wannier functions have simple analytic expressions. Here the lattice potential is properly approximated by a harmonic potential, giving the oscillator eigenfunctions for the Wannier functions in the *harmonic oscillator approximation*. Numerically, the Wannier functions are calculated from the Schrödinger equation (1.17) together with the Bloch waves (1.18). For the periodic part in (1.18), the differential equation

$$\left(\left(-i\frac{\partial}{\partial z} + p \right)^2 + \eta_B \, \sin^2(z) \right) u_{n,p}(z) = E_{n,p} \, u_{n,p}(z) \tag{1.20}$$

together with a Fourier transform

$$u_{n,p}(z) = \sum_m a_m^{(n,p)} \, e^{2imz} \tag{1.21}$$
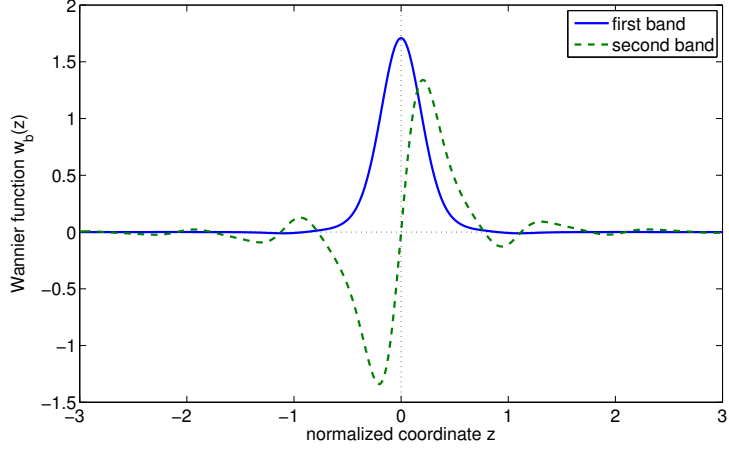
Figure 1.4: Wannier functions for the first and second band for $\eta_B = 10$.

reduces to the linear equation for the Fourier components $a_m^{(n,p)}$

$$\left((2m+p)^2 + \frac{\eta_B}{2}\right) a_m^{(n,p)} - \frac{\eta_B}{4}\left(a_{m-1}^{(n,p)} + a_{m+1}^{(n,p)}\right) = E_{n,p}\ a_m^{(n,p)}. \qquad (1.22)$$

Beside the determination of the Fourier transformed Wannier function via

$$\widetilde{w}_n(k) = \frac{1}{\sqrt{2}}\ a_{[\frac{k}{2}]}^{(n,k-2[\frac{k}{2}])}, \qquad (1.23)$$

this also allows for the calculation of the full band structure $E_{n,p}$. For the first two bands, figure 1.4 displays the resulting Wannier functions. Figure 1.5 shows the band structure for three different values of the lattice depth η_B as a function of the moment p (restricted to the first Brillouin zone) for the first few bands.

With the knowledge of the Wannier functions, the parameters J_B, U, μ_B of the model are calculated as a function of the lattice depth η_B. Whereas for the interaction amplitude U the numerical results of the Wannier functions have to be used, the hopping and chemical potential simplify considerably. Using the fact, that the Bloch waves are eigenfunctions of the single-particle Hamiltonian (1.17), the hopping and chemical potential can be expressed by the band structure via

$$J_B^n = -\frac{1}{2}\int\limits_{-1}^{1}\mathrm{d}p\int\limits_{-1}^{1}\mathrm{d}p'\int\mathrm{d}z\ \Phi_{n,p'}(z)e^{i\pi p'}E_{n,p}\Phi_{n,p}(z) = -\frac{1}{2}\int\limits_{-1}^{1}\mathrm{d}p\ e^{i\pi p}E_{n,p},$$

$$(1.24)$$
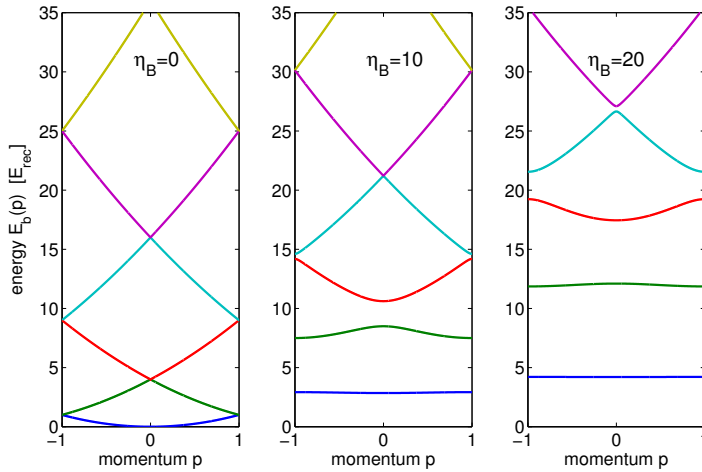
Figure 1.5: Band structure of the optical lattice for three different values η_B. For vanishing lattice η_B the typical quadratic band structure for free particles can be seen. With increasing hopping, the band gaps open and the bands get more and more flat.

$$\mu_B^n = -\frac{1}{2}\int\limits_{-1}^{1}\mathrm{d}p\int\limits_{-1}^{1}\mathrm{d}p'\int\mathrm{d}z\ \Phi_{n,p'}(z)E_{n,p}\Phi_{n,p}(z) = -\frac{1}{2}\int\limits_{-1}^{1}\mathrm{d}pE_{n,p}. \qquad (1.25)$$

The band index defines the amplitude for the different bands, where band-mixing amplitudes vanish per se due to the orthogonality of the Bloch waves for different bands. A different derivation of the hopping amplitudes and other parameters can be found in [115], restricting to the solution of two bosons in an optical lattice. [116] presents another method for the determination of localized states with special applications to disordered lattices and [67] discusses the situation for a superlattice.

Figure 1.6 shows the calculated hopping amplitudes J_B^n and the band energy Δ_B^n as a function of the lattice amplitude η_B. Additionally, the ratio of the next-nearest to the nearest-neighbor hopping amplitude is shown. This proves, that the next-nearest hopping is small compared to the other quantities in the system and consistently left out.
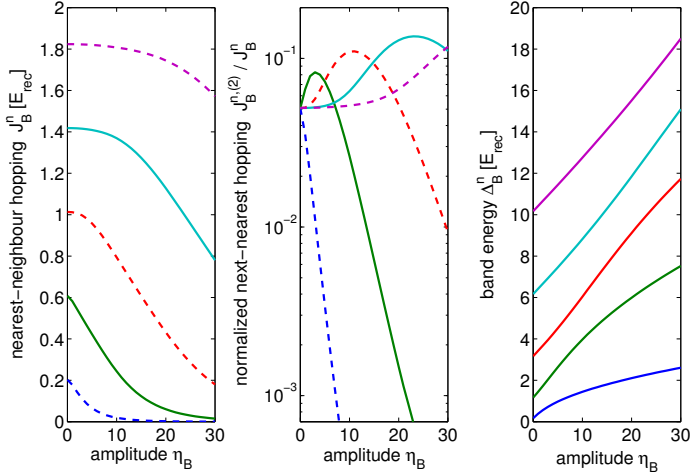
Figure 1.6: Hopping J_B^n and band energy Δ_B^n of the first few bands (from bottom to top) as function of the lattice depth η_B. Left: absolute value of the nearest-neighbor hopping amplitude J_B^n; the dashed lines belong to positive amplitudes, the solid lines belong to negative amplitudes. Middle: absolute value of the ratio of the next-nearest to the nearest-neighbor hopping amplitude. Right: band energy of the different bands.

1.3 Bose-Fermi-Hubbard model

So far, we only discussed the physics of bosons in an optical lattice setup. Adding fermions, the continuous Hamiltonian is given by [39]

$$
\begin{aligned}
\hat{\mathcal{H}} = \int \mathrm{d}z \, \Psi_B^\dagger(z) \left[-\frac{\hbar^2}{2m_B}\Delta + V_{\mathrm{Pot}}^B(z) \right] \Psi_B(z) \\
+ \frac{g_{\mathrm{BB}}}{2} \int \mathrm{d}z \, \Psi_B^\dagger(z)\Psi_B^\dagger(z)\Psi_B(z)\Psi_B(z) \\
+ \int \mathrm{d}z \, \Psi_F^\dagger(z) \left[-\frac{\hbar^2}{2m_F}\Delta + V_{\mathrm{Pot}}^F(z) \right] \Psi_F(z) \\
+ \frac{g_{\mathrm{BF}}}{2} \int \mathrm{d}z \, \Psi_B^\dagger(z)\Psi_F^\dagger(z)\Psi_F(z)\Psi_B(z).
\end{aligned}
\tag{1.26}
$$

with the bosonic and fermionic kinetic energy and the corresponding interaction contributions. For the boson-fermion interaction again s-wave scattering with $V(z - z') = g_{\mathrm{BF}}\delta(z - z')$ is taken into account with $g_{\mathrm{BF}} = \frac{4\pi\hbar^2}{m_R} a_{BF}$. $m_R = \frac{m_B m_F}{m_B + m_F}$ is the reduced mass and a_{BF} the s-wave scattering length. Due to Pauli's principle, no s-wave scattering for the fermions occurs. Introducing

Wannier functions for both, bosons $[w^B(z)]$ and fermions $[w^F(z)]$, we arrive at the Bose-Fermi-Hubbard model

$$
\begin{aligned}
\hat{H} = &-J_B \sum_j \left(\hat{a}_j^\dagger \hat{a}_{j+1} + \hat{a}_{j+1}^\dagger \hat{a}_j \right) + \frac{U}{2} \sum_j \hat{n}_j \left(\hat{n}_j - 1 \right) - \mu_B \sum_j \hat{n}_j \\
&- J_F \sum_j \left(\hat{c}_j^\dagger \hat{c}_{j+1} + \hat{c}_{j+1}^\dagger \hat{c}_j \right) + V \sum_j \hat{n}_j \hat{m}_j.
\end{aligned}
\tag{1.27}
$$

$\hat{m}_j = \hat{c}_j^\dagger \hat{c}_j$ is the fermionic number operator and $\hat{c}_j^\dagger$ $(\hat{c}_j)$ the fermionic creation (annihilation) operator. We included the chemical potential for the bosons for completeness, whereas we always fix the number of fermions, i.e., being in a semi-canonical description. The additional amplitudes in the Hamiltonian describe the fermionic kinetic energy

$$
J_F = -\int \mathrm{d}z \, \bar{w}^F(z - a) \left[-\frac{\hbar^2}{2m_F} \frac{\partial^2}{\partial z^2} + V_{\mathrm{Pot}}^F(z) \right] w^F(z),
\tag{1.28}
$$

and the local boson-fermion interaction

$$
V = \frac{g_{\mathrm{BB}}}{2} \int \mathrm{d}z \, \bar{w}^B(z) \bar{w}^F(z) w^F(z) w^B(z).
\tag{1.29}
$$

Here, we still restrict ourselves to nearest-neighbor hopping and local interactions. Again the bosonic interaction energy defines the energy scale by $U = 1$.

In general, we are not interested in the dependence of the different amplitudes on the lattice depth η_B, but discuss the influence of the different amplitudes on the system directly. Due to the four-dimensional[3] parameter space of the Bose-Fermi-Hubbard model, an easy understanding of the model is not possible. For several limiting cases, the prediction of various different phases exist, partly verified by numerical means. Most prominent phases beside the bosonic Mott insulators are paired or composite phases, polaritons and supersolids [82, 83, 89, 117, 118, 119, 120] as well as studies on the influence of disorder or superlattices on the Bose-Fermi-Hubbard model [121, 122, 123, 124]. A more detailed discussion of the existing literature can be found in the introductions to the different aspects of the Bose-Fermi-Hubbard model.

---

[3]Hoppings J_B, J_F, Bose-Fermi interaction V and bosonic chemical potential μ_B.

Part I

The Bose-Fermi-Hubbard model in the limit of ultraheavy fermions

CHAPTER 2

Introduction

Disorder in experimentally studied systems always affects the measurements, usually in a negative way. Nevertheless, disorder sometimes even enhances physical effects such as the conductance in graphene p-n junctions [125], the Curie temperature in the Anderson-Hubbard model [126, 127, 128], the synchronization of an array of Josephson junctions [129] or the phase coherence [130]. Most prominent feature of the effect of disorder is the localization of non-interacting particles in a weak disordered potential predicted by Anderson [131]. Although being observed in a variety of different systems [132], ultracold atoms allowed for the first observation of the exponential localization [133, 134]. In addition to it, the full control of ultracold atom systems opens the route to an understanding of the effects of localization for interacting particles beyond Anderson localization [135, 136, 137].

In the (strongly) interacting regime, the so-called Bose glass is of importance [14, 109]. Partly possessing properties of the Mott insulator (no long-range phase coherence) and the superfluid (being compressible), the experimental search for the Bose glass in ultracold atoms reached the line with its observation in the excitation spectrum of cold atoms [71]. Further experiments studied the influence of the disorder on the condensate fraction [106] or transport [138]. Theoretically, the Bose-glass phase is also found in systems without random on-site disorder but with disorder in the interaction [139, 140] or the hopping amplitude [140, 141, 142].

Whereas in solid-state systems and other interesting models the nature and origin of disorder cannot be controlled (beside doping), several implemen-

tations of the disorder are available in ultracold atoms. Superimposing the optical lattice with a speckle pattern from a diffusive plate [69] and the interference of two, non-commensurate optical lattices [71, 143, 144, 145, 146] are the easiest realizations of on-site disorder. Holographic methods used in [41] might also become interesting. The most intriguing source of disorder is the usage of a second, immobile species. First studied in [147], this source of disorder quickly gained wide interest [148, 149, 150, Mering2008] with applications to fermionic or bosonic impurities.

In this part of the thesis, we focus on the case of the Bose-Fermi-Hubbard model in the limit of immobile fermions, i.e., we consider the limit $J_F = 0$. Here the effect of the fermions reduces to a binary random potential at site j for the bosons, depending on whether a fermion is at a given site j or not. This means that the local bosonic chemical potential is altered by

$$\delta\mu_j = \begin{cases} V, & \text{if a fermion is present at site } j, \\ 0, & \text{otherwise.} \end{cases} \tag{2.1}$$

The disorder distribution is thus given by $\Delta(x) = (1 - \varrho_F)\delta(x) + \varrho_F\delta(x - V)$ with $\delta(x)$ being Dirac's δ-function and V the boson-fermion interaction. The resulting model is closely related to the Falicov-Kimball model [151], describing the mixture of a mobile and an immobile fermionic species or the Hubbard model with binary-alloy disorder [127, 152].

We systematically investigate to what extent this limit of the Bose-Fermi-Hubbard model can be described as a specific instance of a *disordered Bose-Hubbard* model with binary disorder and study the phase diagram which to our knowledge is not yet done[1]. This simple model shows important features of the full Bose-Fermi-Hubbard model but displays important qualitative differences to the phase diagram of the disordered Bose-Hubbard model with continuously distributed on-site disorder, as studied for instance in [14, 105, 153, 154, 155]. Depending on the physical situation of interest, we consider two cases of disorder: If the fermionic tunneling is small but sufficiently large such that on the time scales of interest relaxation to the state of total minimum energy is possible, the fermion induced disorder is referred to as being *annealed*. In this case the ground state is determined by minimization over all possible fermion distributions. If the fermion tunneling is too slow or the temperature too high the disorder is an actually random distribution which is then called *quenched*.

---

[1]Earlier studies mainly concentrated on the density-of-states and other quantities.

Incompressible phases

3.1 Ultradeep lattices

We first discuss the phase diagram of the incompressible phases for the simple case of an ultradeep lattice for the bosons, such that their hopping can be neglected. In this situation, where $J_F = J_B = 0$, the Hamiltonian becomes diagonal in the occupation number basis, denoted as $\{|n_1, m_1\rangle \cdots |n_L, m_L\rangle\}$, where $m_j = 0, 1$ is the number of fermions at site j and $n_j = 0, 1, ...$ the corresponding number of bosons. L labels the total number of lattice sites in the one-dimensional system. The problem of finding the ground state reduces to identifying product states with the lowest energy. By fixing the total number of fermions $N_F = L\varrho_F$, where ϱ_F denotes the fermionic filling factor, this amounts to minimize

$$E = \frac{1}{2} \sum_j n_j(n_j - 1) - (\mu_B - V) \sum_{j \in \mathcal{F}} n_j - \mu_B \sum_{j \in \mathcal{N}} n_j. \qquad (3.1)$$

$\mathcal{F}$ denotes the set of $\varrho_F L = N_F$ sites with a fermion and $\mathcal{N}$ the set of $(1 - \varrho_F)L = L - N_F$ sites without a fermion. The energy is degenerate for all fermion distributions and the ground state is given by an equal mixture of all states with state vectors

$$|\psi\rangle = \bigotimes_{i \in \mathcal{F}} |n_1, 1\rangle \bigotimes_{j \in \mathcal{N}} |n_0, 0\rangle. \qquad (3.2)$$

Here,

$$n_1 = \max\left\{0, [1/2 + (\mu_B - V)]\right\}, \qquad n_0 = \max\left\{0, [1/2 + \mu_B]\right\}, \qquad (3.3)$$

is the local boson number for sites with ($\mathcal{F}$) or without ($\mathcal{N}$) a fermion and [.] denotes the closest integer bracket. In other words, the degenerate states with lowest energy will have $\varrho_F L$ sites with n_1 bosons and one fermion and $L(1 - \varrho_F)$ sites with n_0 bosons and no fermion. For the case of unity (zero) fermion filling, $\varrho_F = 1$ ($\varrho_F = 0$), the situation becomes particularly simple as we encounter the pure Bose-Hubbard model with an effective chemical potential $\mu_B^{\text{eff}} = \mu_B - V$ (μ_B).

Since n_1 and n_0 are integers there are adjacent intervals of μ where the occupation numbers do not change as it is the case in the plain Bose-Hubbard model. In these intervals the system is incompressible, i.e., the compressibility vanishes. Following [83] we label the difference $n_0 - n_1$ in the bosonic number mediated through the presence of a fermion by s. The local ground state can either consist of n_0 bosons and no fermion or $n_1 = n_0 - s$ bosons and one fermion. These state vectors will be denoted as $|n_0, 0\rangle = |0\rangle$ and $|n_0 - s, 1\rangle = |1\rangle$. The value of s depends on μ and V and can be a positive or negative integer. Both vectors are eigenvectors of the number operator

$$\hat{Q}_j = \hat{n}_j + s\hat{m}_j \tag{3.4}$$

with the same integer eigenvalue n_0 and $\langle \Delta \hat{Q}_j^2 \rangle = 0$. Thus incompressible phases have a commensurate number $\hat{Q}$ and can be characterized by the two integers n_0 and s.

This behavior, illustrated in figure 3.1, is very similar to that of the Bose-Hubbard model except that here the bosons can be incompressible even for non-integer filling ϱ_B since $\varrho_B = n_0 + \varrho_F (n_1 - n_0)$ [83, 156, Mering2008]. Since n_0 and n_1 are integers and increase monotonically with μ, there is a jump in the total number of bosons when moving from one incompressible phase to the adjacent one. All systems with boson numbers between these values are critical and have the same chemical potential since $J_B = 0$. The average boson number per site in the incompressible phases does not have to be an integer, however. The existence of Mott phases with non-commensurate boson number is a direct consequence of the interaction of the bosons with the fermions. At (random) sites with a fermion, the bosons experience an effective local potential which resembles the physics of a disordered system. Due to the nature of this disorder, i.e., the occurrence of only two possible values, the immobile fermions act as a binary disorder to the bosons. A similar behavior, i.e., the existence of non-integer incompressible lobes has been shown for superlattices, which can be considered as binary disorder in the special case of anti-clustering [157, Muth2008].
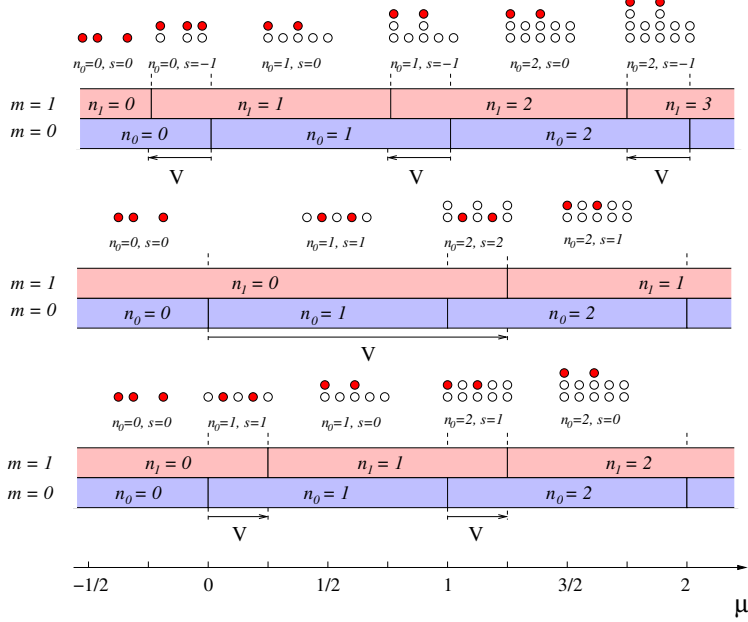
Figure 3.1: Phases of Bose-Fermi-Hubbard model for $J_B = J_F = 0$ for different inter-species couplings $0 < V < 1$ (lowest diagram), $1 < V < 2$ (middle diagram), $-1 < V < 0$ (upper diagram), and $U = 1$. n indicates the number of bosons (empty circles) at the site, m the number of fermions (red filled circles). The horizontal red bars illustrate the boson number n_1 for sites with a fermion ($m = 1$) as function of the chemical potential, the horizontal blue bars correspondingly the boson number n_0 for sites without a fermion ($m = 0$), which is identical to the Bose-Hubbard model. The values of μ where a transition between different boson numbers n_0 occurs are quantum critical points.

In general Mott-insulating phases with incommensurate boson numbers exist for any disorder distribution that is non-continuous, i.e., containing a gap within the distribution. This stems from the fact, that the different disorder values account to a shift of the $J_B = 0$ phase diagram of the Bose-Hubbard model. For a gapped disorder distribution, these shifts leave regions with the same number of bosons open, as seen in figure 3.1 for the binary disorder distribution. In this sense, also the behavior of the non-integer Mott lobes for arbitrary superlattices can be understood.

3.2 Minimum energy distribution of fermions for small bosonic hopping

In order to understand the physics of disorder due to the presence of fermions we need to discuss the influence of the distribution of fermions to the ground-state energy. The energetic degeneracy of different fermion distributions in the incompressible phases is lifted if a small bosonic hopping J_B is taken into account. Near the quantum critical points the boson hopping leads to the formation of possibly critical phases with growing extent. We first restrict ourselves to regions where incompressibility is maintained, i.e., sufficiently far away from the critical points.

In order to obtain a qualitative understanding of the effects of a finite bosonic hopping we performed a numerical perturbation calculation on a small lattice. Figure 3.2 shows different distributions of 4 fermions over a lattice of 8 sites ordered according to their energy for different parameters in 6th order perturbation.

One notices that the lowest energy states are either given by fermion distributions with maximum mutual distance (anti-clustered configuration) or minimum mutual distance (clustered configuration) modified by boundary effects. This behavior can in part be explained by a composite fermion picture introduced in [83]. The composite fermions are defined for the phase (n_0, s) by the annihilation operators

$$\hat{f}_i = \sqrt{\frac{(n_0 - s)!}{n_0!}} \left(\hat{b}_i^\dagger\right)^s \hat{c}_i, \qquad \text{for } s \geq 0 \tag{3.5}$$

$$\hat{f}_i = \sqrt{\frac{n_0!}{(n_0 - s)!}} \left(\hat{b}_i\right)^{-s} \hat{c}_i, \qquad \text{for } s < 0, \tag{3.6}$$

and describe the fermions surrounded by a bosonic (bosonic hole) cloud on top of a boson see. For details, refer to [83].

For each (n_0, s), the full Bose-Fermi-Hubbard Hamiltonian (1.27), with $J_F = 0$ gives, in second order in J_B, rise to an effective Hamiltonian [83, 121, 158, 159, 160]

$$\hat{H}_{\text{eff}} = K_{\text{eff}} \sum_{\langle i,j \rangle} (\hat{f}_i^\dagger \hat{f}_i)(\hat{f}_j^\dagger \hat{f}_j). \tag{3.7}$$
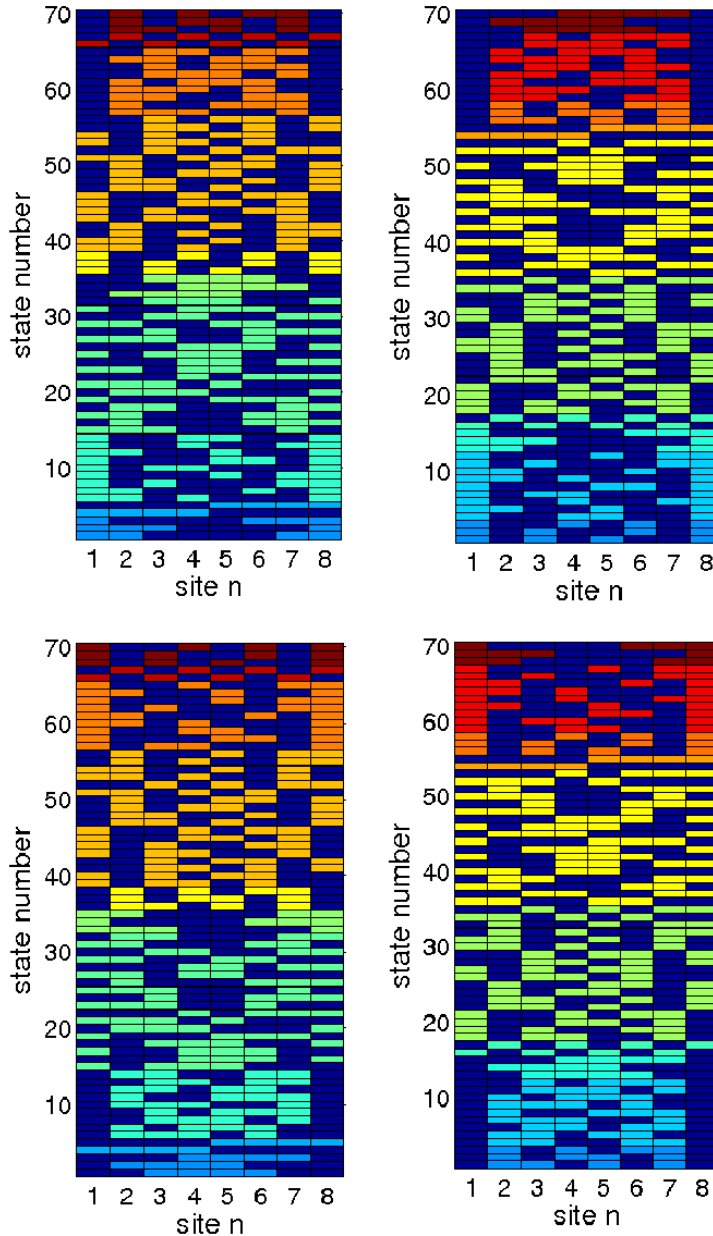
Figure 3.2: Fermion distributions ordered increasingly by ground-state energy for $J_F = 0$, $J_B = 0.02$, $U = 1$. The energy ranges from small (blue) to larger (red) values. Top: attractive boundary, left: $(V, n_0, s) = (1, 1)$, i.e., $K_{\text{eff}} = -0.002$, and right: $(1.5, 2, 1)$, i.e., $K_{\text{eff}} = 0.001$. Bottom: repulsive boundary, left: $(-1.5, 0, -1)$, i.e., $K_{\text{eff}} = -0.002$, right: $(-1.5, 1, -1)$, i.e., $K_{\text{eff}} = 0.001$. For the definition of K_{eff} refer to equation (3.8).

The effective coupling (note that $U = 1$ and $J_F = 0$ in contrast to [83]) reads

$$K_{\text{eff}} = 4J_B^2 \left[\frac{n_0(n_0 + 1 - s)}{1 - s + V} + \frac{(n_0 - s)(n_0 + 1)}{1 + s - V} \right.$$
$$\left. - n_0(n_0 + 1) - (n_0 - s)(n_0 + 1 - s) \right]. \quad (3.8)$$

Composite fermions cannot occupy the same lattice site, but there is a nearest-neighbor attraction ($K_{\text{eff}} < 0$) or repulsion ($K_{\text{eff}} > 0$), depending on (n_0, s) and V. Associating a site with a composite fermion with a spin-up state and a site without a fermion with spin down, equation (3.8) corresponds to the classical Ising model with fixed magnetization and anti-ferromagnetic ($K_{\text{eff}} > 0$) or ferromagnetic coupling ($K_{\text{eff}} < 0$). At this point it should be mentioned, that introduction of the composites does not explain important properties of the system. As pointed out in our previous work [161, Mering2008], the fluctuations of the composite number operator are non-zero which cannot be seen from the effective Hamiltonian (3.8). Nevertheless it gives an effective understanding of the behavior of the fermions in the system.

As a consequence, if $K_{\text{eff}} < 0$, the energy is smallest for composite (and therefore fermion) distributions that minimize the surface area of sites with and without a fermion (referred to as *clustering*). In this setting, the fermion distribution forms a block of occupied sites. For this block, the open boundary condition either yields attractive or repulsive interaction with the boundary which explains the behavior of the energy of the different distributions in figure 3.2. If $s > 0$, the boundaries are attractive, otherwise repulsive as seen in the figure.

The other regime is the one for $K_{\text{eff}} > 0$. Then, the fermions repel each other and form a pattern with maximum number of boundaries for small J_B, referred to as *anti-clustering*. The fact that the fermions attain a distribution with maximum distance cannot be explained by the effective model due to its perturbative nature. In all of our numerical simulations using DMRG we found however that a positive K_{eff} always leads to anti-clustering with maximum distance. This behavior of clustering and anti-clustering is also reported in [83, 162] for slightly different parameters J_F.

From figure 3.2, another important feature can be seen. As the color code shows, the energies for the different distributions differ only by a small amount on the order of J_B^2/U or even higher orders n. This means, that for temperatures which are still small enough to treat the
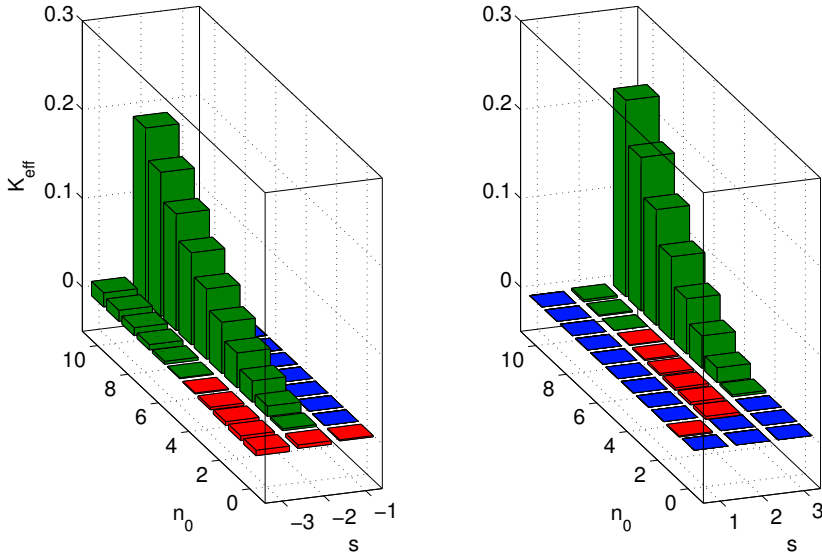
Figure 3.3: Effective couplings K_{eff} for $V = -2.7$ (left) and $V = 2.2$ (right) for different combinations (n_0, s). Green bars depict positive K_{eff} and red ones are negative. The combinations (n_0, s) which do not occur in the phase diagram are plotted blue.

bosonic system with given disorder as an effective $T = 0$ problem, but larger than the energy gap between different fermion distributions, i.e., for $J_B(J_B/U)^n \ll k_B T \ll J_B$, the various fermion distributions are equally populated. Thus the (fermionic) system never reaches the minimal energy distribution. This leads to the conclusion, that the treatment of a real disordered system with random disorder is more natural than the discussion of the annealed case. This has important consequences for the phase diagram.

Figure 3.3 shows the value of K_{eff} for two choices of the interspecies interaction V. Going from the lowest lobe to higher ones, both signs may occur for a fixed interaction V. This means, that one part of the incompressible lobes display the clustering, the other part the anti-clustering behavior. For the numerical calculation of the phase diagram using the DMRG method this has some major consequences. Observing the expectation value of the local number operator for the fermions in this parameter regime shows that the fermions are bunching together, but in several, equally spaced small blocks rather than in one full block. We believe this to be an artefact

of the build-up mechanism (for details see [163]) in the DMRG code[1], which nevertheless does not limit the applicability of our results. More recent implementations of the DMRG method without finite size build-up [167, 168, 169] could perhaps overcome this problem.

3.3   Incompressible phases for finite J_B

For finite bosonic hopping J_B we extend the strong-coupling expansion applied in [97] to the Bose-Hubbard model and complement the results with numerical DMRG simulations. This formulation of the strong-coupling expansion provides a rather accurate description of the Bose-Hubbard model even on a quantitative level, with further improvements from the employment of a field theoretic approach [170, 171, 172, 173].

In the zero hopping limit $J_B = 0$, all fermion distributions give the same energy. Considering the phase with (n_0, s) and $N_F = \varrho_F L$ fermions, the ground-state vector is found to be

$$\left|\psi\right\rangle = \bigotimes_{j \in \mathcal{F}} \frac{\hat{c}_j^\dagger \big(\hat{a}_j^\dagger\big)^{(n_0 - s)}}{\sqrt{(n_0 - s)!}} \bigotimes_{k \in \mathcal{N}} \frac{\big(\hat{a}_k^\dagger\big)^{n_0}}{\sqrt{n_0!}} \left|0\right\rangle, \tag{3.9}$$

where $\left|0\right\rangle = \left|0, \ldots, 0\right\rangle_B \otimes \left|0, \ldots, 0\right\rangle_F$ is the total vacuum of both bosons and fermions at all sites. The energy density is given by

$$\varepsilon_0 = \frac{U}{2}\Big[(1 - \varrho_F)n_0(n_0 - 1) + \varrho_F(n_0 - s)(n_0 - s - 1)\Big] + V\varrho_F(n_0 - s).$$

For a state with a single additional boson (bosonic hole), we have to distinguish two cases compared to the usual Bose-Hubbard model. First the boson (bosonic hole) can be added to a site with a fermion, or second, without a fermion. Up to normalization, we have

---

[1]The DMRG code used was provided by Prof. Dr. U. Schollwöck. Unfortunately, the code does not allow to change the intrinsic routines to get rid of unwanted effects. This prevented us to study further interesting quantities in the system. Nevertheless, all important physical quantities calculated using the DMRG code are sufficient for the study and prediction of the new phases described throughout the whole work. The usage of open-source program packages as the ALPS [164, 165] or PwP [166] projects is not possible since these are not yet implemented for Bose-Fermi mixtures.

$$\left|\psi_{\mathcal{F}}^{\pm}\right\rangle^j = \hat{a}_j^\dagger\left|\psi_0\right\rangle, \qquad \left|\psi_{\mathcal{F}}^-\right\rangle^j = \hat{a}_j\left|\psi_0\right\rangle, \qquad \text{for } j \in \mathcal{F}, \qquad (3.10)$$

for sites with a fermion and

$$\left|\psi_{\mathcal{N}}^+\right\rangle^j = \hat{a}_j^\dagger\left|\psi_0\right\rangle, \qquad \left|\psi_{\mathcal{N}}^-\right\rangle^j = \hat{a}_j\left|\psi_0\right\rangle, \qquad \text{for } j \in \mathcal{N}, \qquad (3.11)$$

for sites without a fermion. All of these vectors are eigenvectors of the Bose-Fermi-Hubbard Hamiltonian for $J_B = 0$ with respective energies

$$E_{\mathcal{F}}^+ = E_0 + V + U(n_0 - s), \qquad\qquad E_{\mathcal{N}}^+ = E_0 + Un_0, \qquad (3.12)$$
$$E_{\mathcal{F}}^- = E_0 - V + U(n_0 - s - 1), \qquad E_{\mathcal{N}}^- = E_0 + U(n_0 - 1), \quad (3.13)$$

where $E_0 = L\varepsilon_0$. The corresponding chemical potentials read

$$\bar{\mu}_{\mathcal{F}}^+ = E_{\mathcal{F}}^+ - E_0 = V + U(n_0 - s), \qquad (3.14)$$
$$\bar{\mu}_{\mathcal{F}}^- = E_0 - E_{\mathcal{F}}^- = \bar{\mu}_{\mathcal{F}}^+ - U,$$

and

$$\bar{\mu}_{\mathcal{N}}^+ = E_{\mathcal{N}}^+ - E_0 = Un_0, \qquad (3.15)$$
$$\bar{\mu}_{\mathcal{N}}^- = E_0 - E_{\mathcal{N}}^- = \bar{\mu}_{\mathcal{N}}^+ - U.$$

Except from the special case $V = Us$, the energies $E_{\mathcal{F}}^\pm$ and $E_{\mathcal{N}}^\pm$ all differ from each other. Thus we can determine the phase boundaries for $J_B \neq 0$ by degenerate perturbation theory within the subspaces with the additional boson (bosonic hole) in sites $j \in \mathcal{F}$ or $j \in \mathcal{N}$ separately.

There will be a second order contribution in J_B for sites j that have at least one neighboring site of the same type. For isolated sites degenerate perturbation theory will lead only to higher order terms in J_B. Since the boundaries of the incompressible phases are determined by the overall lowest-energy particle-hole excitations, we can construct the expected phase diagram in the case of extended connected regions of fermion sites coexisting with extended connected regions of non-fermion sites. In this case we can directly apply the results of [97] to sites with and without fermions yielding

$$\mu_{\mathcal{F}/\mathcal{N}}^\pm = \bar{\mu}_{\mathcal{F}/\mathcal{N}}^\pm + \delta\mu^\pm(n_0, J_B) \qquad (3.16)$$

where

$$\delta\mu^+(n_0, J_B) = -2J_B(n_0 + 1) + J_B^2 n_0^2 + J_B^3 n_0(n_0 + 1)(n_0 + 2),$$
$$\delta\mu^-(n_0, J_B) = 2J_B n_0 - J_B^2(n_0 + 1)^2 - J_B^3 n_0(n_0^2 - 1). \qquad (3.17)$$
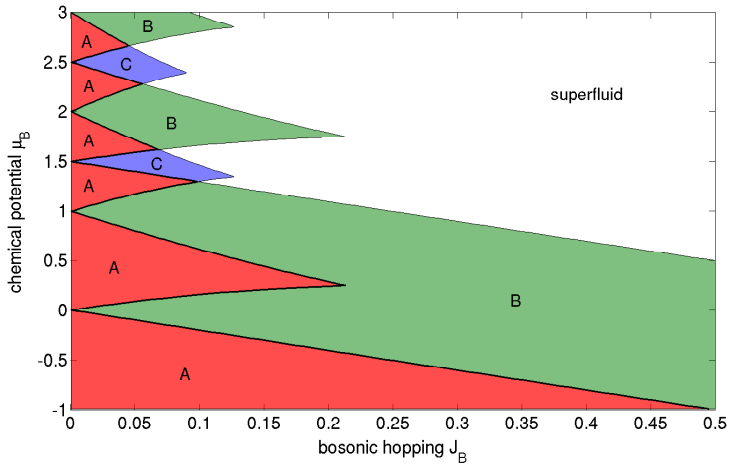
Figure 3.4:   Phase diagram from strong-coupling expansion with $U = 1, V = 1.5$. Red areas (A) indicate truly incompressible Mott regions with gapped particle-hole excitations everywhere. Green (B) and blue (C) areas are partially compressible quasi-Mott regions with gapped particle-hole excitation for sites with (B) or without (C) a fermion but ungapped excitation in the complementary region. Outside the three regions, the system is completely compressible.

This gives rise to two overlapping sequences of the usual Mott-insulating lobes, one for the sites with and one for the sites without fermions. According to (3.14), the shift is given by the boson-fermion interaction V and the effect on the phase diagram is shown in figure 3.4. In [149], similar results including higher dimensions can be found.

As seen in the figure, the system is truly incompressible only in the overlap region (A) of the quasi-Mott lobes for sites with and without fermions. Points which are within one of the two sequences of quasi-Mott lobes but not in both (cases B or C) are not compressible in the whole system but only in a region. Thus the energy for a particle-hole excitation is gapped within this sublattice and ungapped in the other part upon addition of a boson (bosonic hole). Outside the three described regions, the system is fully compressible. It should be mentioned that a similar procedure allows to describe the phases in the (general) disordered Bose-Hubbard model, which can have many shifted Bose-Hubbard phase diagrams overlapping, also explaining the emergence of non-integer incompressible phases for weak, gapped disorder.

The analytic result (3.17) for the different phases allows for a direct comparison to numerical results from DMRG. Therefore we employ DMRG with open boundary conditions and two different fermionic distributions, the clustered and the anti-clustered one. Throughout the whole thesis, the local dimension of the Hilbert space in the DMRG as well as the dimension of the blocks are chosen in such a way, that no significant change in the numerical results upon increasing the two quantities could be observed. Figure 3.5 shows the corresponding numerical results together with the analytic prediction from (3.17). For the phase diagrams throughout this part, a finite size extrapolation (see section 3.4 and [107]) is performed.

One recognizes nearly perfect agreement between numerics and strong-coupling prediction in the case of clustering. This is expected since in the clustered case the majority of sites has neighbors of the same type. In the case of anti-clustering, however, the incompressible lobes extend much further into the region of large boson hopping with a critical J_B of about 1 for a fermion filling of $\varrho_F = 0.25$ at $V = -1.5$. This behavior is expected since in this case hopping to nearest-neighbors is suppressed if the neighboring sites are of a different type ($\mathcal{F}$ or $\mathcal{N}$). For this situation, the curves of the critical chemical potential $\mu_{\mathrm{crit}}(J_B)$ that correspond to a bosonic particle-hole excitation at a fermion site (here $\mu_{\mathrm{crit}}(0) = -1.5, -0.5, 0.5, 1.5$ etc.) start with a power J_B^{γ} determined by the minimum number of hops required to reach the next fermion site, i.e., $\gamma = 1/\rho_F$, if $\varrho_F \leq 1/2$. If the fermion filling is larger than $1/2$ the behavior changes and the non-fermion sites (hole sites) cause $\mu_{\mathrm{crit}}(J_B) \sim J_B^{\gamma}$ with $\gamma = 1/(1 - \varrho_F)$. In principle it is possible to extend the strong-coupling perturbation expansion to any fermion distribution (compare the method presented in section C.1), which is however involved. In [175, 176] a numerically assisted strong-coupling theory termed *cell-strong-coupling expansion* is developed. Since the anti-clustered situation is equivalent to the Bose-Hubbard model with a superlattice, the semi-analytic results from this method can be applied directly. Figure 3.6 shows a comparison of the numerical results using DMRG from figure 3.5 for $V = -1.5$ to the results from the cell-strong-coupling approach[2] showing a very good agreement as expected[3].

---

[2]Thanks to P. Buonsante for the cell-strong-coupling results of the phase boundaries.

[3]It should be noted that the loop-hole insulator phases [174, 177, 178, Muth2008] predicted for a super-lattice are for the present parameters too small to be visible in the DMRG simulation and are nevertheless expected to disappear after averaging over disorder distributions.
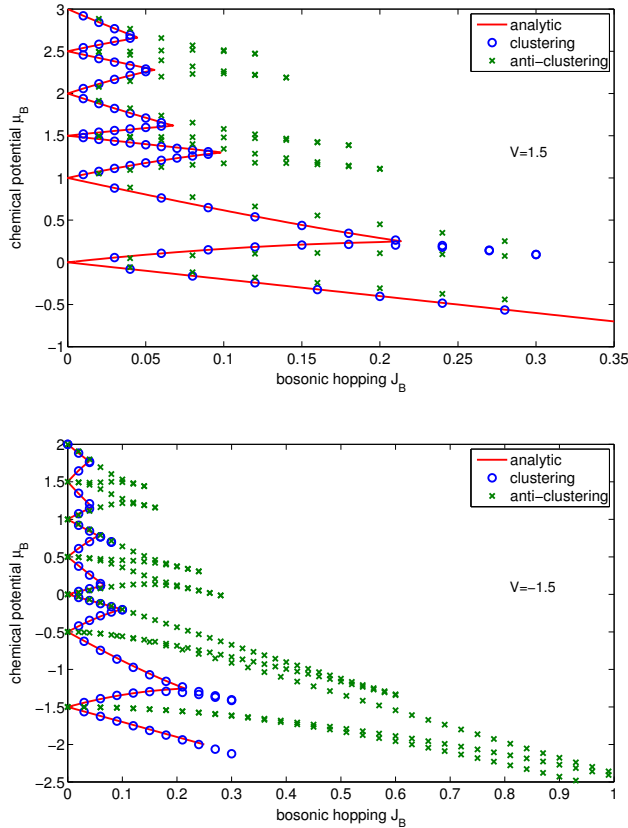
Figure 3.5: Comparison of the incompressible phases predicted from the strong-coupling approximation (solid line) to DMRG results (circles,crosses) for two fixed distributions of fermions. Circles: clustering, Crosses: anti-clustering with maximal distance. $V = 1.5$ (top figure) and $V = -1.5$ (bottom figure). $\varrho_F = 0.25$, and $U = 1$.

So far we did not discuss the issue of fermionic distributions which are unequal the two cases. For the situation of random disorder, i.e., a fixed fermionic distribution, the so-called *rare events* [97, 155] are of major importance to the phase diagram. In the thermodynamic limit, all possible disorder configurations appear within the system; in particular also the *optimal* situation of a large clustered region. Here, optimal is used in the sense that the superfluid to Mott-insulator transition occurs in this configuration first. Thus our strong-coupling results describe the phase diagram properly for binary disorder in the thermodynamic limit because the clustered distribution is always the optimal one.
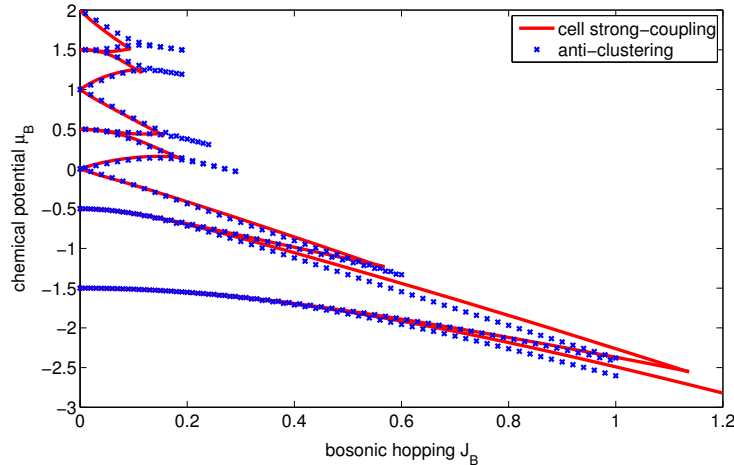
Figure 3.6: Comparison of cell-strong-coupling approximation (solid line) from [174] and DMRG for boundaries of incompressible phases for fixed distribution of fermions corresponding to anti-clustering with maximum distance (crosses). $V = -1.5$, $\varrho_F = 0.25$, and $U = 1$.

Unlike for random fermions, in the case of an *annealed* system, the strong-coupling expansion gives only less accurate results, at least in the regions where $K_{eff} > 0$, i.e., where the ground state of the whole system is obtained by the anti-clustered configuration. This can be seen from figure 3.7, where we compare the predictions of the strong-coupling approximation with those from a DMRG simulation for annealed fermionic disorder and a mean-field ansatz. Within the mean-field approach [158, 179], hopping is included to the system as a perturbation to the ground state

$$|g\rangle = \sqrt{1 - \varrho_F}\,|n_0, 0\rangle + \sqrt{\varrho_F}\,|n_0 - s, 1\rangle \qquad (3.18)$$

 in second order. Using this ground state and introducing a global bosonic order parameter ψ, the phase boundaries can be found using the usual Landau argumentation [179, 180, 181]. When comparing the different data sets in figure 3.7 one recognizes that the mean-field predictions are qualitatively correct but, as expected, quantitatively only moderately precise. The numerical data were obtained by letting the DMRG code freely evolve in the manifold of fermionic distributions. The initial fermion distribution is not fixed but determined by the build-up process inherent to the initial infinite-size DMRG algorithm which is then followed by finite-size sweeps. The final distribution of fermions converges quite well to the expected anti-clustering, where deviations come from the truncations of the method
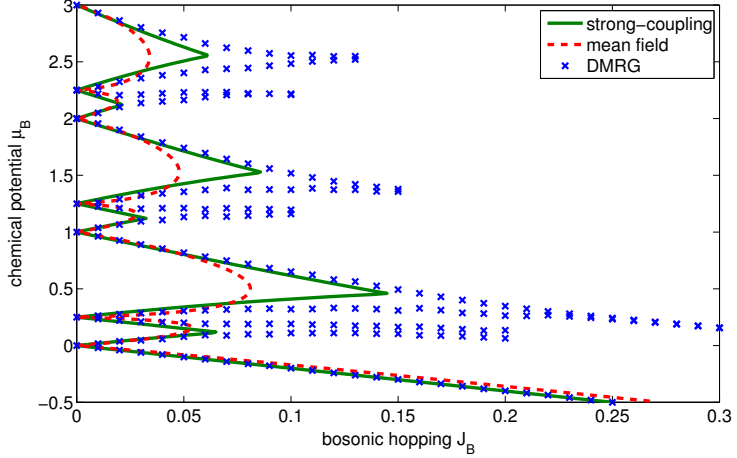
Figure 3.7: Incompressible phases for annealed fermions and $U = 1$, $V = 0.25$, $\varrho_F = 0.25$. Within the incompressible phases, the final fermion distributions correspond to the totally anti-clustered state, in agreement with the analytic predictions of section 3.2. Shown are the strong-coupling results (solid line), the mean-field results from [179] (dashed line) and results from a DMRG calculation with $J_F = 0$ (crosses) for annealed fermions.

and the complex energy manifold with many metastable low-energy states. Since the DMRG method is prone to get stuck in local minima we checked the consistency of our results by implementing different sweep algorithms after the initial infinite size algorithm. In these sweep algorithms, the fermionic hopping was not taken to be zero but was given a finite initial value which was decreased during the DMRG sweeps to the final value zero. To ensure proper convergence we compared the data for a few representative points ($J_B = 0.07$ boundaries of $(n_0, s) = (1, 1)$ lobe; $J_B = 0.15$ boundaries of $(1, 0)$ lobe; $J_B = 0.03$ boundaries of $(2, 0)$ lobe) to the data obtained from two different sweep strategies[4]. The difference in the chemical potential is of the order of 3% independent of the sweep strategy an therefore negligible on the scale of the plot. It should be noted, that the build-up procedure

---

[4] The sweep strategy was implemented by first applying an infinite size algorithm up to the system length, then applying 5 finite size sweeps, all at $J_F = J_B/2$. Subsequently the hopping was reduced after a complete sweep and again 3 sweeps were carried out to ensure convergence again with the new hopping amplitude. Repeatedly, the hopping was slightly reduced until after 30 sweeps the fermionic hopping is set to be 0 with another 3 sweeps. In the first method the hopping was reduced according to an exponential decay followed by a linear decay to zero. In the second method the hopping was reduced according to a cosine followed by a linear decay to zero.
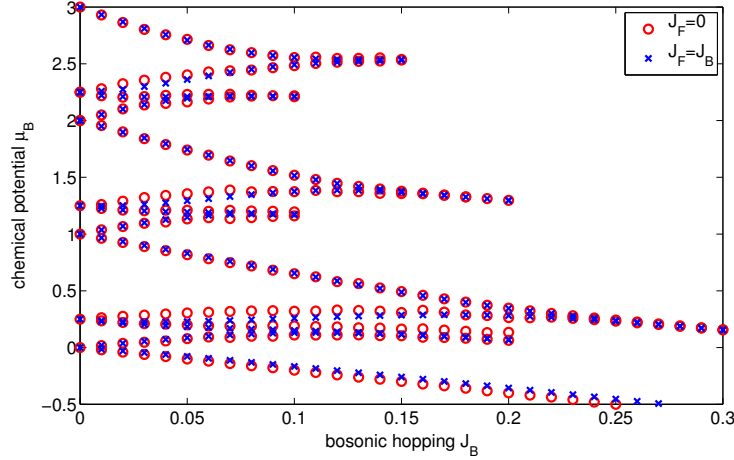
Figure 3.8: Incompressible regions for $U = 1$, $V = 0.25$, $\varrho_F = 0.25$. Shown are the results from a DMRG calculation with $J_F = 0$ and annealed fermionic disorder (circles) (see figure 3.7) and $J_F = J_B$ (crosses). The agreement is quite good, which indicates that the established interpretation for $J_F = 0$ also holds at least partially for $J_F > 0$.

during the infinite-size part of the DMRG algorithm inherently behaves bad for annealed fermions in the case of a clustered ground state, i.e., $K_{\text{eff}} < 0$ and $J_F = 0$ as already pointed out.

3.4 Fermions with finite mobility and infinite size scaling

A priori it is not clear what happens to the phase diagram for non-frozen fermions, i.e., $J_F \neq 0$. From the discussion above it is clear, that the general arguments do not change. Obviously, the situation for $J_F \neq 0$ should be compared to the case $J_F = 0$ for annealed fermionic disorder. This is done in figure 3.8 which shows a comparison of DMRG data for $J_F = 0$ from figure 3.7 and $J_F = J_B$. One recognizes that the influence of a small fermionic hopping is rather small and does not considerably change the structure of the incompressible lobes. This allows for the conclusion that even for fermionic hopping as large as the bosonic hopping amplitude the picture of fermion-induced disorder is an adequate description of the bosonic subsystem. Our findings support the picture of an insulating ground state
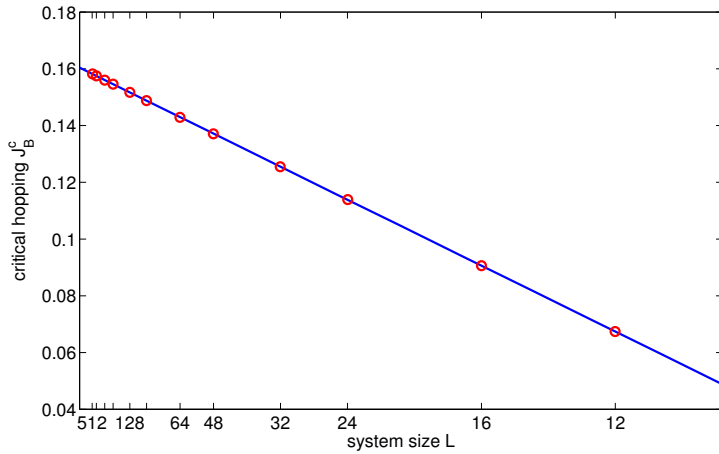
Figure 3.9: Thermodynamic limit extrapolation for the critical point of the $n_0 = 1, s = 1$ lobe ($\varrho_F = 0.25, \varrho_B = 0.75$) in figure 3.8. The critical point is found at $J_B^c = 0.16038$

developed in [182]

As final property of the incompressible phases we study the behavior of the critical hopping amplitude of one lobe as a function of the system size. In finite size numerical situations, boundary effects are always present when using open boundary conditions. As example, in the finite system the spectrum is always gapped, even within the superfluid phase. Considering free bosons, described by the Hamiltonian

$$\hat{H} = -J_B \sum_j \left(\hat{a}_j^\dagger \hat{a}_{j+1} + \hat{a}_{j+1}^\dagger \hat{a}_j \right), \tag{3.19}$$

the energy cost per particle is proportional to $1/L$, with L being the system size. For the calculation of the tip of the Mott insulators, a finite size scaling in $1/L$ turns out to be suitable to obtain the infinite size limit [183]. Exemplarily we study the finite size scaling of the lowest lobe $(n_0, s) = (1, 1)$ in figure 3.8 for $J_F = J_B$. Figure 3.9 shows the critical point calculated from DMRG for various system sizes as function of $1/L$. From a fit of J_B^c to $\log(L)$ we find the critical point in the thermodynamic limit $J_c = 0.16038$. The data for different system lengths show the expected $1/L$ behavior for the Bose-Hubbard model [183].

CHAPTER 4

Compressible and partially compressible phases

So far, our discussion was restricted to the fully incompressible phases. As shown in figure 3.4, beside the usual incompressible and superfluid phases, our strong-coupling treatment suggests the existence of a second kind of phases. These phases are characterized by the fact, that the bosonic particle-hole excitations are gapless if they occur on a fermion (non-fermion) site but have a finite gap on a complementary, i.e., a non-fermion (fermion) site. These phases are termed *partial compressible* in the following, where a distinction of partial compressibility for sites with or without fermions is not necessary.

A precise definition of the partially compressible phases can be done via the compressibility (1.9). As shown in figure 4.1, where the expectation value of different total number operators is shown as a function of the chemical potential μ_B for $J_F = 0$, a distinction of the different phases is seen numerically by these expectation values. Whereas in the fully incompressible phases the total number of particles $\left\langle \sum_j \hat{n}_j \right\rangle$ is constant, the different partial incompressible phases manifest themselves in constant particle numbers only for a subset of the system. Defining the partial compressibilities

$$\kappa_{\mathcal{F}} = \frac{\partial \left\langle \sum_{i \in \mathcal{F}} \hat{n}_i \right\rangle}{\partial \mu}, \qquad\qquad \kappa_{\mathcal{N}} = \frac{\partial \left\langle \sum_{i \in \mathcal{N}} \hat{n}_i \right\rangle}{\partial \mu}, \qquad (4.1)$$
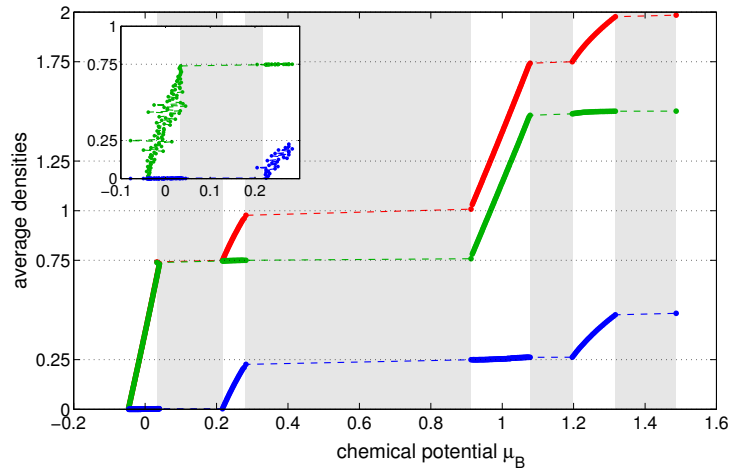
Figure 4.1: Density cut along the μ_B-axis in figure 3.8 for $J_F = 0$ (annealed) and $J_B = 0.02$, $U = 1$, $V = 0.25$, $\varrho_F = 0.25$. From top to bottom: overall average density $\left\langle \sum_j \hat{n}_j \right\rangle$, average density for sites without a fermion $\left\langle \sum_{j \in \mathcal{N}} \hat{n}_j \right\rangle$ and average density for sites with a fermion $\left\langle \sum_{j \in \mathcal{F}} \hat{n}_j \right\rangle$, all after averaging as described in the main text. Inset: Dependence of the particle number as function of chemical potential without averaging. The system size is chosen to be $L = 128$ sites. Gray background indicates the regions of the full incompressible phases, i.e., the quasi-Mott insulators.

the two different phases from figure 3.4 are

$$
\begin{array}{llll}
\text{B:} & \qquad \kappa_{\mathcal{F}} = 0 & \qquad \kappa_{\mathcal{N}} \neq 0 \\
\text{C:} & \qquad \kappa_{\mathcal{F}} \neq 0 & \qquad \kappa_{\mathcal{N}} = 0.
\end{array}
\tag{4.2}
$$

Within each of the partial compressible phases, all additional particles enter the sublattices denoted $\mathcal{F}$ or $\mathcal{N}$, depending on the chemical potential.

For vanishing fermionic hopping, the results for the different number of particles in the subset of the lattice are displayed in figure 4.1. Here the average boson number per site obtained from a DMRG simulation with annealed disorder is shown as a function of the chemical potential for $J_B = 0.02$. Also shown are the corresponding values only for fermion sites and non-fermion sites respectively. In the partially compressible phases the average boson number increases only for one type of sites while it stays constant for the other. As seen in the inset of the figure, the chemical potential is not a monotonous function of the filling as it should be. This

artefact of the numerical method in this highly demanding parameter regime is overcome by an averaging of the chemical potential of a small number of different fillings. These averaged results are shown in the main part of the figure. As mentioned earlier, the problem stems from the complex energy surface in the parameter space and the trapping of the numerical algorithm in metastable states close to the ground state.

We now discuss the properties of the single-particle density matrix $\langle \hat{a}_i^\dagger \hat{a}_{i+m} \rangle$ in the partially incompressible phases. In general, for very large values of J_B the system is expected to have a Luttinger-liquid behavior [184, 185, 186] in one dimension with $\langle \hat{a}_i^\dagger \hat{a}_{i+m} \rangle \sim m^{-K/2}$ and to possess long-range off-diagonal order in higher dimensions. K is the so-called Luttinger parameter which is essential for the understanding of the existing phases. In one dimension, we expect the Luttinger-liquid behavior to disappear in the partially incompressible phases and correlations to decay exponentially as $\langle \hat{a}_i^\dagger \hat{a}_{i+m} \rangle \sim e^{-m/L_c}$. This is because in this case a single (static) impurity is sufficient to prevent the build-up of long-range correlations. This accounts for a percolation problem, where for higher dimensions there will be a critical fermion (or hole) filling above which off-diagonal order is suppressed. This critical filling is determined by percolation thresholds and for annealed fermionic disorder depends on the actual fermion distribution in the ground state (e.g. clustered or anti-clustered). For a (quenched) random fermion distribution in two dimensions, the threshold is $\varrho_F^{\mathrm{crit}} = 0.5927$ (or $1 - \varrho_F^{\mathrm{crit}} = 0.5927$ if non-fermion sites are incompressible) and $\varrho_F^{crit} = 0.3116$ for three dimensions [187]. See [188] for the percolation threshold of a variety of two-dimensional lattices.

Figure 4.2 shows the first-order correlations $\langle \hat{a}_i^\dagger \hat{a}_{i+m} \rangle$ as function of the distance m for an annealed fermion distribution obtained from DMRG simulations for a rather large lattice of 512 sites with incommensurate boson filling ($N_B = 448$) and $\varrho_F = 0.25$. i and $i + m$ are chosen symmetrically around the center. For $J_B = 0.07$, strong exponential decay with correlation length $L_c = 1.3$ is found corresponding to a glass-type behavior (due to the finite compressibility), while for $J_B = 0.2$ correlations decay algebraically with $\langle \hat{a}_i^\dagger \hat{a}_{i+m} \rangle \sim m^{-0.32}$, which corresponds to a Luttinger liquid. The Luttinger parameter $K = 0.64$ is slightly smaller than the known value for the critical point of the superfluid to Bose-glass transition $K = 2/3$ [109] with box-disorder thus being close to the transition. It should be mentioned that so far it is not clear whether the result for the superfluid to Bose-glass transition for boxed disorder, i.e., a disorder distribution with $\Delta(x) = \frac{1}{\Delta}\Theta(\Delta - x)\Theta(x)$ is applicable also for the binary disorder with
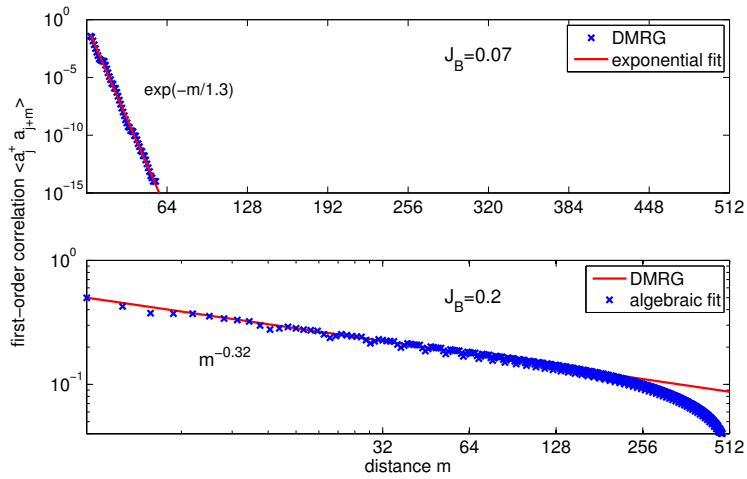
Figure 4.2: DMRG simulations (crosses) of first-order correlations $\langle \hat{a}_i^\dagger \hat{a}_{i+m} \rangle$ for $V = 0.25$, $\varrho_F = 0.25$ and $U = 1$ for a lattice of $L = 512$ sites and $N_B = 448$ bosons in the case of annealed disorder. Top: Within the partial compressible phase ($J_B = 0.07$), the line corresponds to the exponential fit $\sim \exp\{-m/L_c\}$ with $L_c = 1.3$. The exponential decay is apparent. Bottom: Superfluid region ($J_B = 0.2$), the line corresponds to the algebraic fit $\sim m^{-K/2}$ with the exponent $K = 0.64$.

$\Delta(x) = (1 - \varrho_F)\delta(x) + \varrho_F \delta(x - V)$ case. Nevertheless it serves as a rough estimate. Another evidence for the existence of a glass-like phase in this system is seen in [189], where the superfluid fraction is calculated from a Gutzwiller approach. This study shows the existence of a region outside the Mott insulators with zero compressibility, indicating the partial compressible phases.

The phases in figure 3.4 display another uncommon feature. Since the early work of Fisher *et al.* [14] and an (incomplete) DMRG study by Pai *et al.* [190], the question of the nature of the phase transition at the tip of the lobe for boxed disorder stayed open. Different scenarios were discussed, distinguishing between a direct superfluid to Mott-insulator transition even for $\Delta > 0$ or the existence of an intermediate Bose-glass phase. Though numerical [105] and analytic results [97] favored the existence of an intermediate Bose-glass phase, the strict proof was only found recently by Pollet *et al.* for the case of generic, bounded disorder [191, 192]. For our situation of a binary disorder distribution, the strong-coupling results suggest the existence of a direct superfluid to Mott-insulator transition. A final, decisive answer to this question related to the nature of our disorder
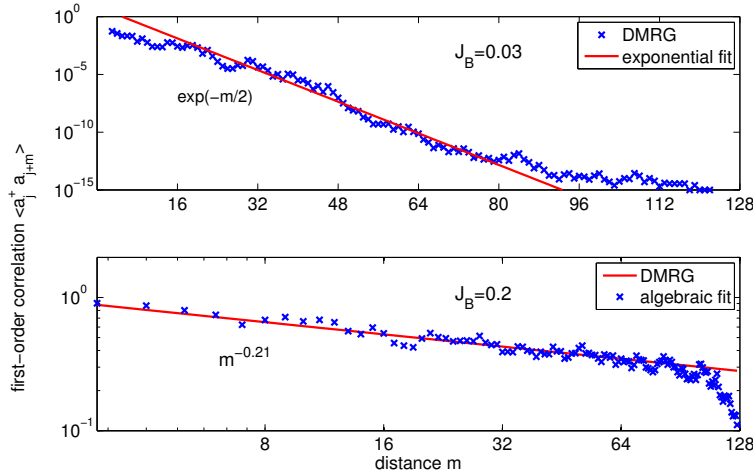
Figure 4.3: DMRG simulations (crosses) of first-order correlations $\langle \hat{a}_i^\dagger \hat{a}_{i+m} \rangle$ for $V = 1.5$, $\varrho_F = 0.375$ and $U = 1$ for a lattice of $L = 128$ sites and $N_B = 184$ bosons, averaged over 100 fermion distributions. Top: $J_B = 0.03$, the line corresponds to the exponential fit $\sim \exp\{-m/L_c\}$ with $L_c = 2$. The exponential decay is apparent. Bottom: $J_B = 0.2$, the line corresponds to the algebraic fit $\sim m^{-K/2}$ with the exponent $K = 0.42$. To avoid finite size effects at short and long ranges, the fitting is done only for intermediate distances.

distribution can however not be given at this point.

Figure 4.3 shows the first-order correlations for random, quenched fermion distribution averaged over 100 realizations with non-commensurate boson number ($\varrho_B = N_B/N = 184/128$). Despite the sampling noise one recognizes the transition between exponential decay with correlation length $L_c = 2$ for $J_B = 0.03$, and a power-law decay with $m^{-0.21}$ for $J_B = 0.2$ corresponding to a Luttinger liquid with $K = 0.42$. $J_B = 0.03$ is within a partially incompressible phase, $J_B = 0.2$ outside, proving that our picture of partially compressible phases holds in both cases, annealed and quenched disorder.

Numerical results for the situation of non-vanishing but small fermionic hopping reveal that (strict) partial incompressibility is lost. But still the increase of the boson number with increasing chemical potential at one type of sites is substantially less that that on the complementary type of sites:

$$\kappa_{\mathcal{F}} \ll \kappa_{\mathcal{N}} \qquad \text{or} \qquad \kappa_{\mathcal{N}} \ll \kappa_{\mathcal{F}}. \tag{4.3}$$
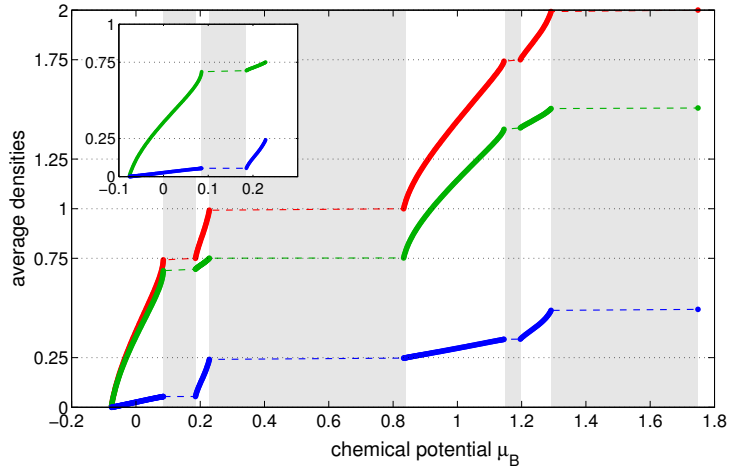
Figure 4.4: Density cut for the same parameter as figure 4.1 but for $J_B = J_F = 0.02$ (see figure 3.8). The gray region depicts the incompressible phases.

Figure 4.4 shows the corresponding density cut obtained from DMRG simulations for the same parameters as in figure 4.1 but for $J_B = J_F = 0.02$, i.e., a cut along the chemical potential in figure 3.8. It should be noted that in contrast to figure 4.1 averaging over the chemical potential is not needed due to the finite mobility of the fermions which improves the convergence of the numerical method. The simulations show that the glass-type character of the phases survives. This is also seen in the exponential decay of the correlations shown in figure 4.5.
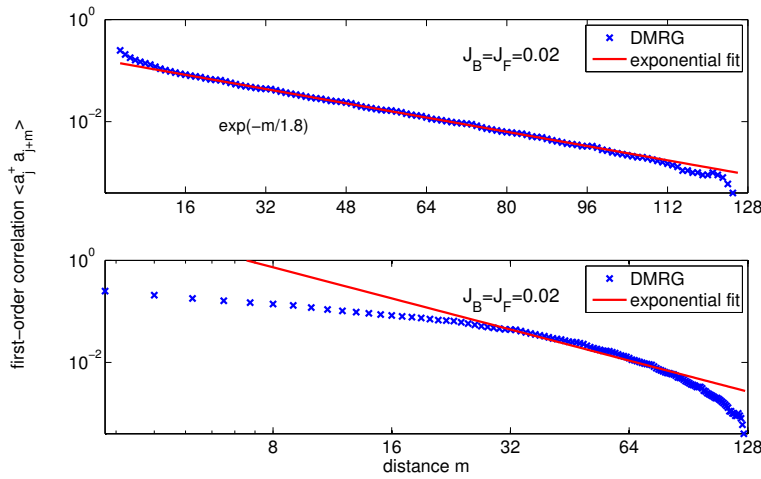
Figure 4.5: First-order correlations $\langle \hat{a}_i^{\dagger} \hat{a}_{i+m} \rangle$ for $V = 0.25$, $\varrho_F = 0.25$ and $U = 1$ for a lattice of 128 sites and $N_B = 204$ bosons in the case of equal hopping amplitudes $J_F = J_B = 0.02$. Top: Logarithmic plot showing the exponential decay with $L_c = 1.8$. Bottom: Double-logarithmic plot for the same data. A proper fitting is not feasible as may be seen by the solid line.

CHAPTER 5

Conclusion and outlook

Studying the phase diagram of the Bose-Fermi-Hubbard model in the limit of immobile fermions, we were able to point out the connection of the system to the disordered Bose-Hubbard model. Because of the unique disorder distribution, new incompressible phases with non-integer filling arise, as is the case for any gapped disorder distribution. Employing a generalization of the strong-coupling method, we analytically derived the phase diagram for the case of quenched binary disorder, being in perfect agreement with numerical results. From this approach, the existence of partially compressible phases is predicted, being identified with a Bose glass phase. For annealed fermions, the resulting fermion distribution is understood in terms of an effective model, where the situation of anti-clustering fermions is similar to that of the Bose-Hubbard model in a superlattice potential.

From the strong-coupling theory, a direct Mott-insulator to superfluid transition is predicted for the case of binary disorder, which is not common in the disordered Bose-Hubbard model. A deeper investigation of this transition by analytic and numerical means should give a further understanding of the processes taking place at the tip of the lobe. Furthermore, a better insight into the nature of the special glass phases could be obtained from studies of the superfluid density or the Edwards-Anderson order parameter [121, 193, 194] not considered so far. Additionally, the lack of knowledge about the Luttinger parameter at the Bose-glass to superfluid transition for this special disorder realization is another important starting point for further studies.

Part II

Induced interactions in the Bose-Fermi-Hubbard model from ultrafast fermions

CHAPTER **6**

Introduction

Recent experiments on very cold ^{4}He [195] found a supersolid behavior predicted nearly forty years ago [196, 197, 198]. In a supersolid, superfluidity coexists with a solid structure, where the superfluidity is believed to be related to vacancies in the solid ^{4}He with possible issues from remaining ^{3}He in the sample as well as disorder (see overview [199]). As shown by several authors, supersolids also exist in bosonic systems with long-range interactions [108, 200, 201, 202, 203] or in multi-species systems with a purely local interaction [117, 120, 204, 205, 206, 207, 208, 209, 210]. Beside the prediction of a supersolid phase, a multitude of other phases in mixed systems such as phase separation between the species [118, 119, 200, 201, 204, 205, 211], CDW phases [118, 205, 211, 212, Mering2010] and coexistence regions of different phases [206, 208, Mering2010] are reported and are a vital field of research.

As believed in the case of Helium, the supersolid exists because of a particle or hole doping, where the latter one is similar to the mentioned vacancies. For mixtures of bosons and fermions, Hébert *et al.* showed by numerical means, that a supersolid of the bosons is only present, if and only if the fermions are at half filling and the bosons are doped away from half filling [120]. Special interest gained the situation of double-half filling, where beside the mentioned phases also situations with Luttinger liquid behavior or density wave character [89] as well as fermionic CDW in addition to a bosonic CDW of full amplitude [205] exist.

In the present part, we provide a conclusive analytic theory to understand the physics of the bosonic subsystem in the Bose-Fermi-Hubbard model

for ultrafast fermions. This limit is of natural interest, since in most experimental realizations the fermionic atoms are lighter than the bosonic ones [37, 38], leading to an increased mobility of the fermions compared to the bosons. Alongside the idea of an effective bosonic theory [117] we derive the bosonic Hamiltonian for $J_F \to \infty$, adiabatically eliminating the fermions similar to the approach in [87]. After explaining the nature of the induced long-range couplings between the bosons, a discussion of the bosonic phase diagram is given together with a study of the influence of boundary effects. All results are accompanied by numerical studies using DMRG for the full Bose-Fermi-Hubbard model.

So far, no direct connection between the long-range interacting and the mixture case is pointed out to our knowledge, where this similarity can be seen within an effective approach. As shown in [87, 117, 213, 214, 215, 216], the inclusion of the second species allows for an effective description of the first species in terms of an effective Hamiltonian. Within linear response theory, the induced interactions for the first species are attractive for mixtures of bosons and fermions[1], where so far no effects of the long-range density-density interactions are studied in the framework of ultracold atoms, yet. Nevertheless, quantum monte carlo results in two dimensions [208] suggest the appearance of long-range, sign-alternating interactions at least for double half filling.

---

[1]In [217] the opposite behavior is reported in contrast to the induced attractive interaction reported in [87, 117, 216, Mering2010].

Friedel oscillations: fermion induced superpotential

In this chapter, we present a simple ansatz which provides an intuitive understanding of the physics in the regime of ultrafast fermions. The ansatz assumes a full decoupling of the fermions from the bosons, which, after the solution of the fermionic problem, gives the phase diagram of the bosons in the limit $J_F \to \infty$.

Since the fermions are ultrafast, we expect them to be uninfluenced by the bosons, resulting in a homogeneous spacial distribution of the fermions. This homogeneous distribution described by

$$\langle \hat{m}_j \rangle = \varrho_F \tag{7.1}$$

results in an effective chemical potential for the bosons, since the interaction part

$$V \sum_j \hat{n}_j \hat{m}_j \to V \varrho_F \sum_j \hat{n}_j \tag{7.2}$$

directly enters the chemical potential for the bosons as $\mu_B \mapsto \mu_B - V\varrho_F$. This first, intuitive ansatz holds for periodic boundary conditions. For open boundary conditions as used in DMRG simulations, the ground state of the fermions is changed in a very important way. The fermionic density in the system with open boundaries displays so-called Friedel oscillations [218, 219, 220, 221], which are given by [219]

$$\langle \hat{m}(x) \rangle = \frac{N + \frac{1}{2}}{L+1} - \frac{1}{2(L+1)} \frac{\sin\left(2\pi x \frac{N+\frac{1}{2}}{L+1}\right)}{\sin\left(\frac{\pi x}{L+1}\right)}. \tag{7.3}$$
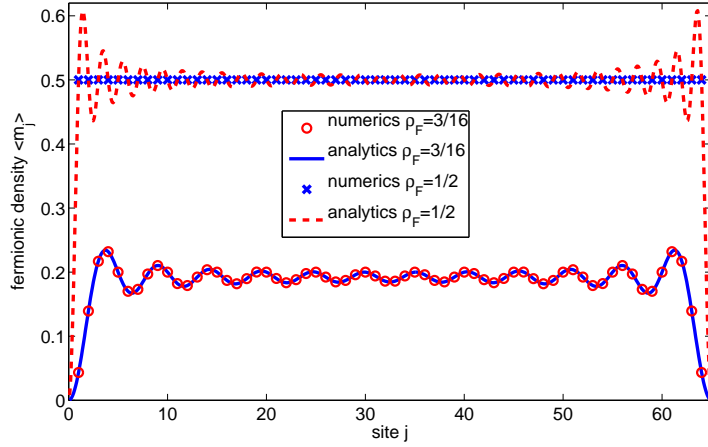
Figure 7.1: Friedel oscillations of the fermionic species for large fermion hopping $J_F = 10$. The DMRG calculation is done with the full Bose-Fermi-Hubbard model for integer filling of the bosons. The density distribution perfectly agrees with the theoretic prediction from equation (7.3). The system parameters are $L = 64$ sites, $J_B = 0$, $V = 1.25$ and $N_B = L$.

In the following we replace, the continuous position x by the lattice site position j. So instead of a resulting homogeneous chemical potential for the bosons, which still holds for an infinite system or periodic boundary conditions, the system may be considered as having a site dependent potential $\sum_j \mu_j \hat{n}_j$ where the chemical potential is given by $\mu_j = \mu_B - V \langle \hat{m}_j \rangle$. This site dependent chemical potential introduces a qualitatively new feature to the system which is equivalent to the disordered Bose-Hubbard model as presented in chapter 1.1. For the Mott-insulating states, it is well justified to neglect any possible influence of the bosons onto the fermions even for finite but large values of J_F. At other densities it will turn out that this does not hold. For this reason, we only discuss the Mott lobes at this point.

In figure 7.1 the numerical results for the density of the fermions from the full Bose-Fermi-Hubbard model are shown for $J_F = 10$, $J_B = 0$ and unity filling of the bosons. The agreement between equation (7.3) and the numerical results is very good. This shows that for integer filling of the bosons the fermions are quite well described by the ground state of free fermions. For the later discussion it should be noted that for the case $\varrho_F = \frac{1}{2}$ the fermionic density does not display any oscillation because the Friedel oscillations are in phase with the lattice.
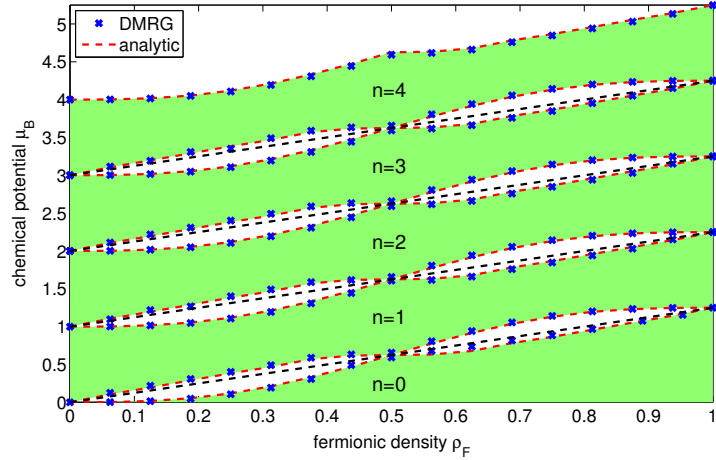
Figure 7.2: Phase diagram of the Bose-Fermi-Hubbard model for zero bosonic hopping $J_B = 0$ as a function of the fermionic filling ϱ_F at large hopping $J_F = 10$. The shaded regions each represent the different Mott lobes, where the shrinking of the Mott lobes is a typical feature of the underlying effective potential as described in the main text. The numerical data are obtained for $L = 64$ with $V = 1.25$ and the agreement with the analytic prediction from the Friedel oscillations is very good. The mean-field shift $V\varrho_F$ is indicated by the straight dashed lines.

On ground of this complemented Bose-Hubbard model we are now able to discuss the phase diagram for $J_B = 0$ in a straightforward way. Considering particle-hole excitations, we find the chemical potentials for the upper and lower lobe of the $n-$th Mott insulator

$$\mu_n^+ = Vn\varrho_F + V \min_j \langle \hat{m}_j \rangle \tag{7.4}$$

$$\mu_n^- = Vn\varrho_F + V \max_j \langle \hat{m}_j \rangle . \tag{7.5}$$

This result is shown in figure 7.2, where numerical results as well as the corresponding analytic curves are presented. In the figure it may be recognized, that with increasing fermion density, the Mott insulators are first shrinking, opening a gap between two adjacent Mott insulators. This gap is maximal around quarter filling with a reclosing for half filling. Beyond half filling, the same structure arises due to particle hole symmetry of the fermions. This property is superimposed onto a mean-field shift $V\varrho_F$ which comes from the first term in equation (7.3).

Although the explanation for the phase diagram is quite intuitive, it lacks an important feature. As can be seen from figure 7.1, the Friedel oscillations for half fermionic filling $\varrho_F = \frac{1}{2}$ are constant over the lattice, resulting in a closing of the gap between the different Mott lobes. Having a closer look at the phase diagram for $\varrho_F = \frac{1}{2}$ for large but not infinite values of J_F reveals a completely different behavior which is shown in figure 7.3. Starting with the local densities of bosons and fermions shown for double half filling, i.e., $\varrho_F = \varrho_B = \frac{1}{2}$, it can be seen that the fermions, in contrast to the Friedel oscillation prediction, as well as the bosons displays a strict oscillating behavior. This is typical for a so-called charge density wave phase which emerges in this case [1]. This CDW is a first evidence that the aforementioned back-action of the bosons to the fermionic ground state is crucial to understand the physics in this regime even for larger values of J_F. This is even better seen in the numerically obtained phase diagram in figure 7.3. There it can be seen, that on the one hand, the Mott lobes do not touch each other and on the other hand, the CDW phase is incompressible. The extent of the CDW phase, or, more strictly speaking, the metastability region of the CDW phase even penetrates that of the Mott insulator, resulting in a thermodynamic instable phase with coexistence of Mott insulator and CDW. With these two indications, pointing to the necessity of a deeper analysis of the system we develop a full effective theory of the bosons in the following chapters, explaining the main features of the phase diagram.

---

[1] It may be seen from figure 7.3 that at the center of the system there exists some kind of *domain wall*. This domain wall is an artefact of the DMRG calculation and only present for zero bosonic hopping $J_B = 0$. The Lanczos diagonalization used in DMRG is sometimes problematic, for instance if the initial state is chosen wrong as happening for the final step of each sweep. This seems to happen in this case, resulting in some numerical problems which are however unimportant in our case since they can be overcome if necessary by methods shortly discussed later. Here I would like to thank the group of Prof. Eggert for useful discussions.
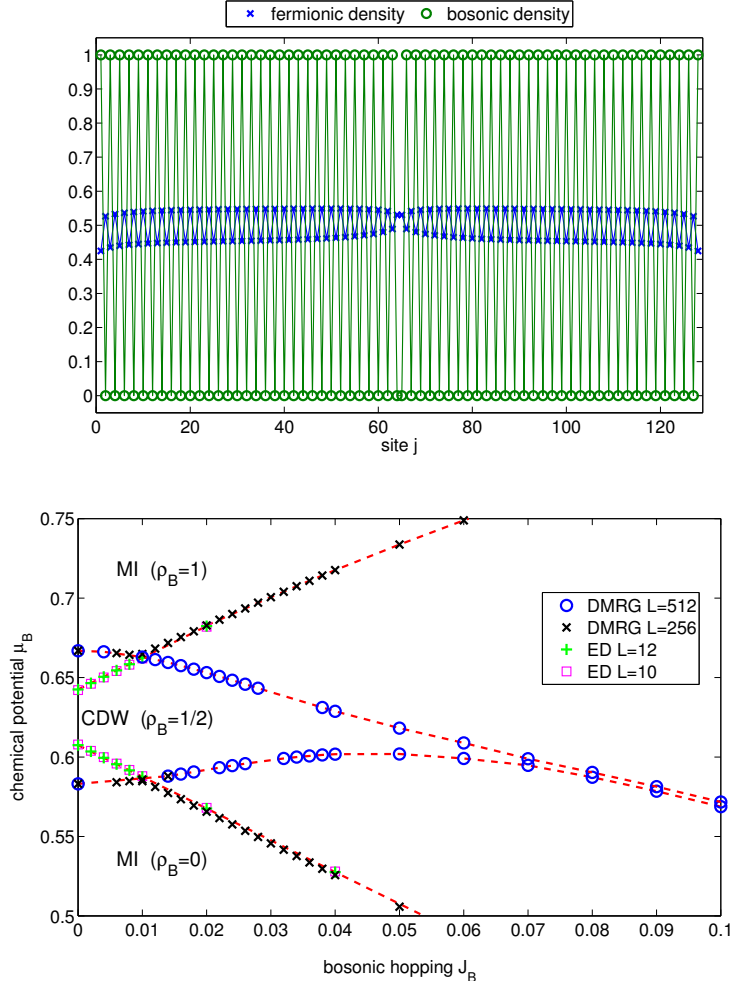
Figure 7.3: Above: Density profile of bosons and fermions[1] for double half filling showing a CDW of both bosons and fermions in contrast to the Friedel oscillations giving $\varrho_F = \frac{1}{2} = const$. The parameters are the same as in the plot below but for $J_B = 0$. Below: Full phase diagram for $\varrho_F = \frac{1}{2}$. It can be seen that the Mott insulators do not touch each other. Furthermore the CDW phase extents over a wide region overlapping with the Mott insulators. For both plots, the numerical data where obtained for $V = 1.25$ and $J_F = 10$, using DMRG and exact diagonalization (ED) for small lattices.

Adiabatic elimination of the fermions

Before we consider the nature of the mentioned back-action, we derive an effective bosonic model explaining the resulting phase diagram. For general fermion filling, this is done by first rewriting the Bose-Fermi-Hubbard Hamiltonian (1.27) such that the notation in the following becomes much simpler. We introduce a bosonic part $\hat{H}_{\mathrm{B}}$, a fermionic part $\hat{H}_{\mathrm{F}}$ and an interaction part $\hat{H}_{\mathrm{I}}$, i.e.,

$$\hat{H}_{\mathrm{BFHM}} = \hat{H}_{\mathrm{B}} + \hat{H}_{\mathrm{F}} + \hat{H}_{\mathrm{I}} \tag{8.1}$$

with

$$\hat{H}_{\mathrm{B}} = -J_B \sum_j \left(\hat{a}_j^\dagger \hat{a}_{j+1} + \hat{a}_{j+1}^\dagger \hat{a}_j \right) + \frac{U}{2} \sum_j \hat{n}_j \left(\hat{n}_j - 1 \right) \tag{8.2}$$

$$\hat{H}_{\mathrm{F}} = -J_F \sum_j \left(\hat{c}_j^\dagger \hat{c}_{j+1} + \hat{c}_{j+1}^\dagger \hat{c}_j \right) + V \sum_j \widetilde{n}_j \hat{m}_j \tag{8.3}$$

$$\hat{H}_{\mathrm{I}} = V \sum_j (\hat{n}_j - \widetilde{n}_j)\hat{m}_j. \tag{8.4}$$

At this step, we already introduced a bosonic mean-field potential $\widetilde{n}_j$ in $\hat{H}_{\mathrm{I}}$ and compensate it by subtracting the term in $\hat{H}_{\mathrm{F}}$. This term serves later as the source for the inclusion of the previously mentioned back-action. For the moment, this term is kept for simplicity, without a deeper meaning. The effective bosonic Hamiltonian is found from an adiabatic elimination, which is performed in the framework of the scattering matrix

$$\hat{\mathcal{S}} = \mathcal{T} \exp \left\{ -\frac{i}{\hbar} \int_{-\infty}^{\infty} \mathrm{d}\tau \hat{H}_{\mathrm{I}}(\tau) \right\} \tag{8.5}$$

of the full system in the interaction picture, i.e., $\hat{H}_{\mathrm{I}}(\tau) = e^{-\frac{i}{\hbar}(\hat{H}_{\mathrm{B}}+\hat{H}_{\mathrm{F}})\tau}\,\hat{H}_{\mathrm{I}}\,e^{\frac{i}{\hbar}(\hat{H}_{\mathrm{B}}+\hat{H}_{\mathrm{F}})\tau}$ and $\mathcal{T}$ being the time ordering operator. Tracing over the fermionic degrees of freedom yields the bosonic scattering matrix

$$\hat{\mathcal{S}}_{\mathrm{eff}}^{\mathrm{B}} = \mathrm{Tr}_{\mathrm{F}}\,\hat{\mathcal{S}}$$

$$= \left\langle \mathcal{T}\exp\left\{ -\frac{i}{\hbar}\,V\sum_j \int\limits_{-\infty}^{\infty} \mathrm{d}\tau\,\left(\hat{n}_j(\tau) - \widetilde{n}_j\right)\hat{m}_j(\tau)\right\}\right\rangle_{\mathrm{F}}. \qquad (8.6)$$

At this point, we make use of the so-called *cumulant expansion* [222, 223, 224], which relates the average of an exponential $\langle\exp\{sX\}\rangle_{\mathrm{X}}$ (with respect to a stochastic variable X) to the exponential of the averages, i.e., the higher order cumulants of the stochastic variable

$$\langle\exp\{sX\}\rangle_{\mathrm{X}} = \exp\left\{\sum_{m=1}^{\infty} \frac{s^m}{m!}\langle\langle X^m\rangle\rangle\right\}. \qquad (8.7)$$

Since the cumulants for the fermionic system vanish for orders higher than two due to the nature of the fermionic state, the final expression for the bosonic S-matrix is given by

$$\hat{\mathcal{S}}_{\mathrm{eff}}^{\mathrm{B}} = \mathcal{T}\exp\left\{ -\frac{i}{\hbar}\,V\sum_j \int\limits_{-\infty}^{\infty} \mathrm{d}\tau\,\left(\hat{n}_j(\tau) - \widetilde{n}_j\right)\langle\langle\hat{m}_j(\tau)\rangle\rangle_{\mathrm{F}} \right. \qquad (8.8)$$

$$\left. -\frac{V^2}{2\hbar^2}\sum_{j,l} \int\limits_{-\infty}^{\infty} \mathrm{d}\tau \int\limits_{-\infty}^{\infty} \mathrm{d}\sigma\,\left(\hat{n}_j(\tau) - \widetilde{n}_j\right)\left(\hat{n}_l(\sigma) - \widetilde{n}_l\right)\langle\langle\mathcal{T}\,\hat{m}_j(\tau)\hat{m}_l(\sigma)\rangle\rangle_{\mathrm{F}}\right\}.$$

At this point, the time ordering in the fermionic cumulants is important as discussed in [225, 226]. So far, no approximations are used, thus the effective bosonic S-matrix is exact. To derive an effective Hamiltonian for the bosonic system, an approximation has to be incorporated. As can be seen in equation (8.5), the relation between the Hamiltonian and the scattering matrix incorporates a single integral. This form can be reached be applying a Markov approximation [227, 228], replacing the two-time bosonic density-density operators by equal time operators, i.e.,

$$\int\limits_{-\infty}^{\infty} \mathrm{d}\tau \int\limits_{-\infty}^{\infty} \mathrm{d}\sigma\,\left(\hat{n}_j(\tau) - \widetilde{n}_j\right)\left(\hat{n}_l(\sigma) - \widetilde{n}_l\right)\langle\langle\mathcal{T}\,\hat{m}_j(\tau)\hat{m}_l(\sigma)\rangle\rangle_{\mathrm{F}}$$

$$\mapsto \int\limits_{-\infty}^{\infty} \mathrm{d}\tau\,\left(\hat{n}_j(\tau) - \widetilde{n}_j\right)\left(\hat{n}_l(\tau) - \widetilde{n}_l\right)\int\limits_{-\infty}^{\infty} \mathrm{d}\sigma\,\langle\langle\mathcal{T}\,\hat{m}_j(\tau)\hat{m}_l(\sigma)\rangle\rangle_{\mathrm{F}}. \qquad (8.9)$$

This approximation is valid since the timescale of the fermionic system is $1/J_F$ and therefore much shorter than any other timescale in the system. This is equivalent to the Born-Oppenheimer approximation in molecular physics, where the heavier (atomic) system is presumed to be static regarding the solution of the lighter (electronic) system. Using the Markov approximation, we rewrite the bosonic S-matrix as

$$
\hat{\mathcal{S}}_{\text{eff}}^{B} = \mathcal{T} \exp \left\{ -\frac{i}{\hbar} \int_{-\infty}^{\infty} \mathrm{d}\tau H_{I}^{\text{eff}}(\tau) \right\}, \tag{8.10}
$$

which defines the effective bosonic interaction Hamiltonian in the interaction picture

$$
\hat{H}_{\text{I}}^{\text{eff}}(\tau) = V \sum_{j} \left(\hat{n}_{j}(\tau) - \widetilde{n}_{j} \right) \langle\langle \hat{m}_{j}(\tau) \rangle\rangle_{\text{F}}
$$
$$
- i \frac{V^2}{2\hbar} \sum_{jl} \left(\hat{n}_{j}(\tau) - \widetilde{n}_{j} \right) \left(\hat{n}_{l}(\tau) - \widetilde{n}_{l} \right) \int_{-\infty}^{\infty} \mathrm{d}\sigma \, \langle\langle \mathcal{T} \, \hat{m}_{j}(\tau) \hat{m}_{l}(\sigma) \rangle\rangle_{\text{F}}. \tag{8.11}
$$

Since the first order cumulant $\langle\langle \hat{m}_{j}(\tau) \rangle\rangle_{\text{F}}$ is equal to the expectation value and the second order cumulant[1] does only depend on the difference T of the times τ and σ and the distance d between the sites j and l as will turn out in the next chapter, the final form of the effective interaction Hamiltonian in the Schrödinger picture can be written as

$$
\hat{H}_{\text{I}}^{\text{eff}} = V \sum_{j} \left(\hat{n}_{j} - \widetilde{n}_{j} \right) \langle \hat{m}_{j} \rangle_{\text{F}} + \sum_{j} \sum_{d=-\infty}^{\infty} g_{d}(\varrho_{F}) \left(\hat{n}_{j} - \widetilde{n}_{j} \right) \left(\hat{n}_{j+d} - \widetilde{n}_{j+d} \right), \tag{8.12}
$$

where the coupling constants $g_{d}(\varrho_{F})$ for the induced long range density-density interactions are given by

$$
g_{d}(\varrho_{F}) = -i \frac{V^2}{2\hbar} \int_{-\infty}^{\infty} \mathrm{d}T \, \langle\langle \mathcal{T} \, \hat{m}_{j}(T) \hat{m}_{j+d}(0) \rangle\rangle_{\text{F}}. \tag{8.13}
$$

With this result, the whole effect of the fermions on the bosonic subsystem is governed by two terms: (i) the mean-field interaction (1st order) and (ii) the induced density-density interactions (2nd order). In a simple pictorial way, the induced interaction means the scattering of a boson with a fermion

---

[1]The definition of the second order cumulant is given by $\langle\langle \hat{m}_{j}(\tau) \hat{m}_{l}(\sigma) \rangle\rangle = \langle \hat{m}_{j}(\tau) \hat{m}_{l}(\sigma) \rangle - \langle \hat{m}_{j}(\tau) \rangle \langle \hat{m}_{l}(\sigma) \rangle$.
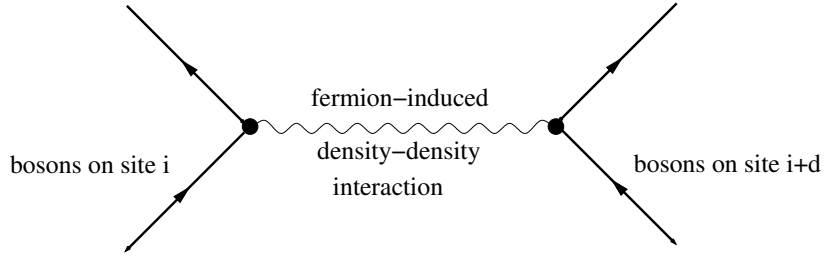
Figure 8.1: Feynman graph representing the fermion induced density-density interaction.

on site j with a subsequent second scattering process between the same fermion and another boson at site $j + d$. A corresponding Feynman diagram for this process can be found in figure 8.1, illustrating the effective interaction.

Finally, the whole effective Hamiltonian for the bosonic subsystem is given by equation (8.2) together with equation (8.12):

$$\hat{H}_{\mathrm{B}}^{\mathrm{eff}} = -J_B \sum_j \left(\hat{a}_j^\dagger \hat{a}_{j+1} + \hat{a}_{j+1}^\dagger \hat{a}_j \right) + \frac{U}{2} \sum_j \hat{n}_j \left(\hat{n}_j - 1 \right) \tag{8.14}$$

$$+ V \sum_j \left(\hat{n}_j - \widetilde{n}_j \right) \langle \hat{m}_j \rangle_{\mathrm{F}} + \sum_j \sum_{d=-\infty}^{\infty} g_d(\varrho_F) \left(\hat{n}_j - \widetilde{n}_j \right) \left(\hat{n}_{j+d} - \widetilde{n}_{j+d} \right).$$

As can be seen from equation (8.13), the remaining task in the calculation of the effective Hamiltonian is to calculate the fermionic density-density correlator $\langle\langle \mathcal{T} \ \hat{m}_j(T)\hat{m}_{j+d}(0) \rangle\rangle_{\mathrm{F}}$ using the fermionic Hamiltonian in (8.3). This will be done in the next chapter for the case of free fermions, i.e., $\widetilde{n}_j \equiv 0$ for all sites j. This case neglects all possible back-actions of the bosons to the fermions which will be incorporated later by a proper choice of the $\widetilde{n}_j$. The knowledge of the coupling constants at the end allows for a construction of the bosonic phase diagram.

Couplings $g_d(\varrho_F)$ for free fermions $\widetilde{n}_j \equiv 0$

9.1 Calculation of the couplings

a) Determination of the cumulant

Here we calculate the coupling constants from equation (8.13) for the case of free fermions. This is, as mentioned the natural choice, since the fermionic hopping amplitude J_F is much larger than any other parameter in the system and hence it can be suspected that the state of the fermions is not affected by the bosons. Therefore the ground state of the fermions is given by the ground state of the fermionic Hamiltonian

$$\hat{H}_{\mathrm{F}} = -J_F \sum_j \left(\hat{c}_j^\dagger \hat{c}_{j+1} + \hat{c}_{j+1}^\dagger \hat{c}_j \right). \tag{9.1}$$

In momentum space, the solution is straightforward. Applying a Fourier transform

$$\hat{c}_j = \frac{1}{\sqrt{L}} \sum_{k=-\frac{L}{2}}^{\frac{L}{2}-1} e^{-2\pi i \frac{kj}{L}} \hat{f}_k, \tag{9.2}$$

the fermionic Hamiltonian transforms into

$$\hat{H}_{\mathrm{F}} = -2J_F \sum_k \cos(2\pi \frac{k}{L}) \, \hat{f}_k^\dagger \hat{f}_k. \tag{9.3}$$

The ground state is the Fermi sphere $\mathcal{K}_F$, which means that all momentum modes k smaller than the Fermi momentum $k_F = N_F/2$ are occupied,

$\mathcal{K}_F = \{k|\ |k| \le k_F\}$. Here N_F is the number of fermions in the system and L is the number of sites. Using the Fourier transform, the real-space density operator in the Heisenberg picture is given by

$$\hat{m}_j(\tau) = \frac{1}{L} \sum_{k_1,k_2} e^{-\frac{i}{\hbar}\tau 2J_F\left[\cos(2\pi\frac{k_1}{L})-\cos(2\pi\frac{k_2}{L})\right]} e^{-2\pi i \frac{(k_1-k_2)j}{L}} \hat{f}^\dagger_{k_1}\hat{f}_{k_2}. \tag{9.4}$$

Together with the ground state

$$|\Psi_F\rangle = \prod_{k\in\mathcal{K}_F} \hat{f}^\dagger_k |0\rangle \tag{9.5}$$

and the four-point function

$$\langle \hat{f}^\dagger_{k_1}\hat{f}_{k_2}\hat{f}^\dagger_{k'_1}\hat{f}_{k'_2}\rangle = \delta_{k_1,k_2}\delta_{k'_1,k'_2}\Theta(k_F - |k_1|)\Theta(k_F - |k'_1|) \tag{9.6}$$
$$+ \delta_{k_1,k'_2}\delta_{k'_1,k_2}\Theta(k_F - |k_1|)\Theta(|k'_1| - k_F),$$

the density-density cumulant reads

$$\langle\langle \hat{m}_j(T)\hat{m}_{j+d}(0)\rangle\rangle_\text{F} = \frac{1}{L^2} \sum_{k_1\in\mathcal{K}_F} \sum_{k'_1\notin\mathcal{K}_F} \tag{9.7}$$
$$\times\ e^{-\frac{i}{\hbar}2J_FT\cos(2\pi\frac{k_1}{L})} e^{\frac{i}{\hbar}2J_FT\cos(2\pi\frac{k_2}{L})} e^{-2\pi i \frac{dk_1}{L}} e^{2\pi i \frac{dk'_1}{L}}.$$

for $T > 0$, where time ordering is irrelevant. To simplify the calculation of the momentum sums it is more convenient to switch to the thermodynamic limit $L \to \infty$. This is reached by defining $\xi = \frac{k}{L}$ and changing $\frac{1}{L}\sum_k$ to $\int \mathrm{d}\xi$. With this, and a further substitution $2\pi\xi \mapsto \xi$, the cumulant simplifies to

$$\langle\langle \hat{m}_j(T)\hat{m}_{j+d}(0)\rangle\rangle_\text{F} = \frac{1}{4\pi^2} \int_{2\pi\ \mathcal{K}_F} \mathrm{d}\xi \int_{2\pi\ \mathcal{K}_F^\text{C}} \mathrm{d}\xi'\ e^{-\frac{i}{\hbar}2J_FT[\cos(\xi)-\cos(\xi')]} e^{-id\xi} e^{id\xi'}. \tag{9.8}$$

Here $\mathcal{K}_F^\text{C}$ is the complement of the Fermi sphere. Using Euler's formula and restricting the integration to the positive momentum part we finally find

$$\langle\langle \hat{m}_j(T)\hat{m}_{j+d}(0)\rangle\rangle_\text{F} = \frac{1}{\pi^2} \int_0^{\varrho_F\pi} \mathrm{d}\xi \int_{\varrho_F\pi}^\pi \mathrm{d}\xi'\ \cos(d\xi)\cos(d\xi')\ e^{-\frac{i}{\hbar}2J_FT[\cos(\xi)-\cos(\xi')]}. \tag{9.9}$$

Figure 9.1 displays the real, imaginary and absolute values of the cumulant for $\varrho_F = 1/2$ and $J_F = 10$. The sharp localization around $T = 0$ furthermore shows the validity of the used Markov approximation (8.9) since the bosonic timescales are much larger. Next we aim at $g_d(\varrho_F)$ by performing the integration over time in (8.13).
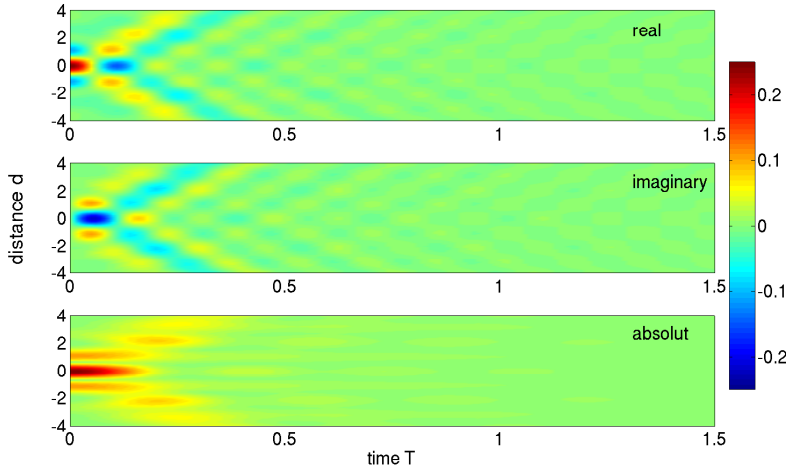
Figure 9.1: Density-density cumulant (9.9) for free fermions splitted in real and imaginary parts as well as the absolute value. $\varrho_F = 1/2$ and $J_F = 10$. The sharp peak around $T = 0$ shows the validity of the used Markov approximation.

b)   Calculation of the time integral

The easiest way to perform the time integral over (9.9) is to make use of the Riemann-Lebesgue lemma, which states, that for any $\mathcal{L}^1$ function $f : \mathbb{R} \to \mathbb{C}$, the Fourier transform of $f(t)$ tends to zero as the frequency tends to infinity [229]

$$\lim_{\omega \to \pm\infty} \int_a^b f(t)\, e^{i\omega t}\, \mathrm{d}t = 0. \tag{9.10}$$

When calculating the time integral over equation (9.9), it turns out to be simpler to rewrite the integration together with the time ordering operator as

$$\int_{-\infty}^{\infty} \mathrm{d}T \, \langle\langle \mathcal{T} \, \hat{m}_j(T)\hat{m}_{j+d}(0)\rangle\rangle_{\mathrm{F}} = 2 \lim_{A \to \infty} \int_0^A \mathrm{d}T \, \langle\langle \hat{m}_j(T)\hat{m}_{j+d}(0)\rangle\rangle_{\mathrm{F}}. \tag{9.11}$$

$$= \lim_{A \to \infty} \frac{2}{\pi^2} \int_0^{\varrho_F \pi} \mathrm{d}\xi \int_{\varrho_F \pi}^{\pi} \mathrm{d}\xi' \, \cos(d\xi) \cos(d\xi') \left[\frac{i\hbar}{2J_F} \frac{e^{-\frac{i}{\hbar} 2J_F T [\cos(\xi) - \cos(\xi')]}}{\cos(\xi) - \cos(\xi')} \right]_0^A.$$

From the Riemann-Lebesgue lemma, we note that the upper integration limit vanishes for $A \to \infty$. The final result for the coupling constants (8.13) for

the case of free fermions, i.e. without any back-action of the bosonic system onto the fermions is thus given by

$$g_d(\varrho_F) = -\frac{V^2}{2\pi^2 J_F} \int\limits_0^{\varrho_F \pi} d\xi \int\limits_{\varrho_F \pi}^{\pi} d\xi' \frac{\cos(d\xi)\cos(d\xi')}{\cos(\xi) - \cos(\xi')}. \tag{9.12}$$

This expression for the couplings will be the starting point for our discussion of the phase diagram shown in figure 7.3. As will be seen later, $g_d(\varrho_F)$ has a singular behavior at $\varrho_F = 0, 1$. For this reason on has to be careful with all steps of the calculation here, and we ask the question whether the Riemann-Lebesgue lemma is applicable for this function. The $\mathcal{L}^1$-norm of the kernel has an upper bound given by the $\mathcal{L}^1$-norm of the kernel of $g_0(\varrho_F)$. Additionally, the denominator is always positive and therefore

$$\int\limits_0^{\varrho_F \pi} d\xi \int\limits_{\varrho_F \pi}^{\pi} d\xi' \left| \frac{\cos(d\xi)\cos(d\xi')}{\cos(\xi) - \cos(\xi')} \right| \leq \int\limits_0^{\varrho_F \pi} d\xi \int\limits_{\varrho_F \pi}^{\pi} d\xi' \frac{1}{\cos(\xi) - \cos(\xi')} = \frac{\pi^2}{4}. \tag{9.13}$$

The last step is proven in the next section. Before we proceed we note that (9.12) shows a particle-hole symmetry $g_d(\varrho_F) = g_d(1 - \varrho_F)$. This can be shown by substituting $\xi \to \pi - \xi$ and $\xi' \to \pi - \xi'$ and interchanging $\xi \leftrightarrow \xi'$ afterwards.

9.2   Couplings in real space

From (9.12), the couplings $g_d(\varrho_F)$ can be calculated numerically. We use the prefactor $\frac{V^2}{2\pi^2 J_F}$ as the energy scale. Only the integral in (9.12) is important and inherits all vital features. Unfortunately, there does not seem to be a general analytic result for it but for $d = 0$, the integrals can be calculated analytically. We find

$$g_0(\varrho_F)\Big|_{\varrho_F \neq 0,1} \sim -\int\limits_0^{\varrho_F \pi} d\xi \int\limits_{\varrho_F \pi}^{\pi} d\xi' \frac{1}{\cos(\xi) - \cos(\xi')} \tag{9.14}$$

$$= -2 \int\limits_{\varrho_F \pi}^{\pi} d\xi' \left[\frac{\mathrm{atanh}\left(\cot\left(\frac{\xi'}{2}\right) \tan\left(\frac{\xi}{2}\right) \right)}{\sin(\xi)} \right]_0^{\varrho_F \pi} \tag{9.15}$$

$$= -\frac{\pi^2}{4} \tag{9.16}$$
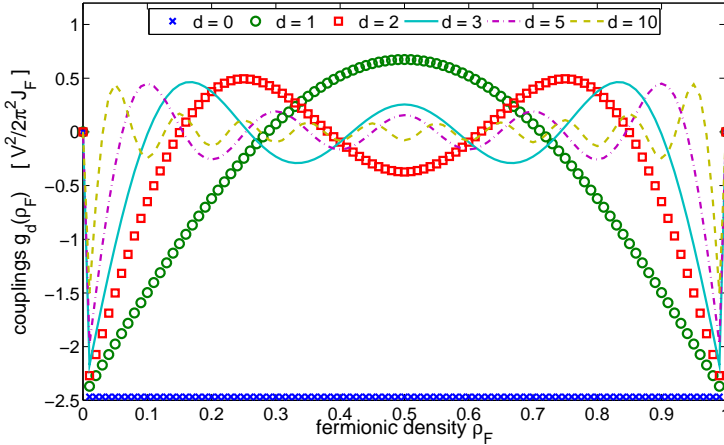
Figure 9.2: Dependence of the coupling strength for various distances d on the fermionic filling ϱ_F. One can obviously see the particle-hole symmetry, reflecting $g_d(\varrho_F) = g_d(1 - \varrho_F)$ as well as the singular behavior for integer filling.

for non-integer fermion filling and naturally $g_0(0) = g_0(1) \equiv 0$, which shows that the couplings for zero distance are independent of the density of the fermions. $g_0 = -\frac{V^2}{8J_F}$ is thus a shift in the bosonic on-site interaction U. This negative shift is in full agreement with the results from [87, 90, 117], predicting the enhancement of the superfluid phase because of a reduction of the on-site interaction U of the bosons. With our approach, we are able to go beyond this renormalization of the local U and incorporate further interaction effects.

Figure 9.2 shows the numerical results for the coupling constants as a function of the fermionic filling ϱ_F. As stated above, the particle-hole symmetry manifests itself in the couplings as $g_d(\varrho_F) = g_d(1 - \varrho_F)$. For the case of zero or unity fermionic filling it should be mentioned, that the coupling constants are zero in these two cases, whereas the limit $\lim_{\varrho_F \to 0,1} g_d(\varrho_F) = g_0(\varrho_F)$ is unequal to zero. This effect can be understood when looking at figure 9.3.

Figure 9.3 shows the dependence of the couplings on the distance d for selected densities ϱ_F. One can see a periodic modulation of the couplings, with the wavelength of the modulation given by $1/\varrho_F$ (for $\varrho_F < \frac{1}{2}$, otherwise the wavelength is given by $1/(1 - \varrho_F)$). Therefore, for $\varrho_F \to 0$ (or 1) the wavelength diverges and all couplings approach the $g_0(\varrho_F)$ value. The
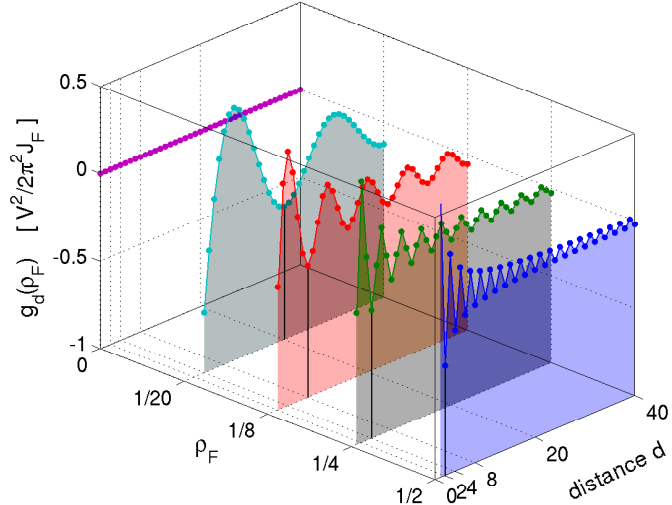
Figure 9.3: Dependence of the coupling strength for selected densities $\varrho_F = 0, 1/20, 1/8, 1/4, 1/2$ on the distance d. The periods of the oscillations are $1/\varrho_F = \infty, 20, 8, 4, 2$. For all cases, the signs in the minima are negative and the maxima positive with a strict alternation from site to site for the case of half filling.

behavior of the couplings is typical for induced couplings of the RKKY-type (Rudermann-Kittel-Kasuya-Yosida) [230, 231, 232]. The most interesting case can be found for $\varrho_F = 1/2$. In this case, the wavelength of 2 leads to a strict alternation in the sign of the couplings from site to site. As a result, the effective Hamiltonian (8.14) displays repulsive nearest-neighbor, attractive next-nearest-neighbor, repulsive next-next-nearest-neighbor interaction and so on. See [208] for a similar, numerical study in this case for two dimensions.

From figure 9.4, the reason why a deeper consideration is inevitable in terms of a back-action can be seen. There, the dependence of the coupling constants is plotted for a larger region of distances for selected ϱ_F. More precisely, the absolute value of the minima, i.e. $-g_{m/\varrho_F}(\varrho_F)$ for $m \in \mathbb{N}$ is shown on a double logarithmic plot. From the figure it can be seen, that the long-range decay of the coupling constants is given by

$$g_d(\varrho_F) \sim \frac{1}{d}. \tag{9.17}$$

Concerning the fitting procedure of the couplings to the numerical data it should be mentioned, that the first few distances were left out and
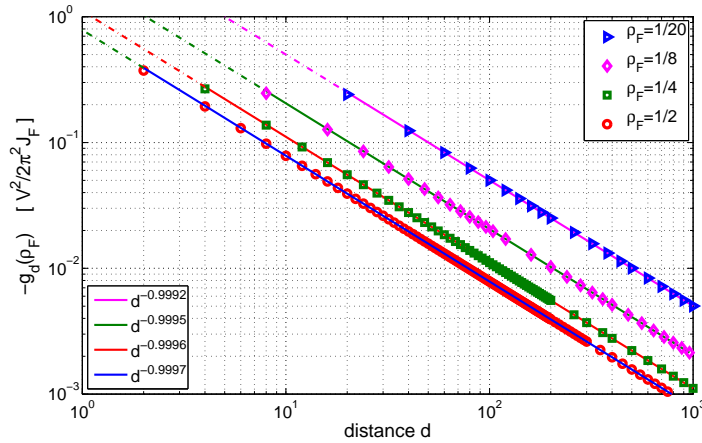
Figure 9.4: Absolute value of the couplings $g_{\frac{m}{\varrho_F}}(\varrho_F)$ as a function of distance d for selected densities ϱ_F. Points are the numerical integration of the double integral and the solid lines are a linear fit in the double logarithmic plot. As indicated, the fitting yields a decay of the couplings inverse to the distance for all densities ϱ_F. The slight deviation of the exponent from one can be attributed to the limited set of fitting points.

that the exponent is slightly less than one because of the finite number of fitting points[1]. This slow decay of the couplings demands to introduce a renormalization procedure, which can be seen from the following argument:

From the numerical data in figure 7.3, we conclude the existence of a CDW phase at double half filling $\varrho_F = \varrho_B = \frac{1}{2}$ as also reported in [89, 205] for slightly different choice of the system parameters. This CDW phase is the result from the induced interactions. A simple explanation at vanishing bosonic hopping J_B can be found by subsequently adding bosons to the system starting from zero filling up to the CDW filling $\varrho_B = \frac{1}{2}$: The first boson will occupy any site, for instance site 0. When the second boson is added to the system, the energy will be minimized in site 2 (or -2), since here the density-density interaction is negative, and the overall energy is reduced. All additional particles will continue occupying all even sites, ending up in the CDW phase at half filling $\varrho_B = 1/2$. But in this configuration, the decay of the couplings with $\frac{1}{d}$ leads to a divergence of the total energy in the thermodynamic limit. Since this argument still holds for $J_B > 0$, this would result in a CDW of full amplitude $\eta_B = 1$ for any

_____

[1]When increasing the number of fitted data points, the exponents saturate at one.
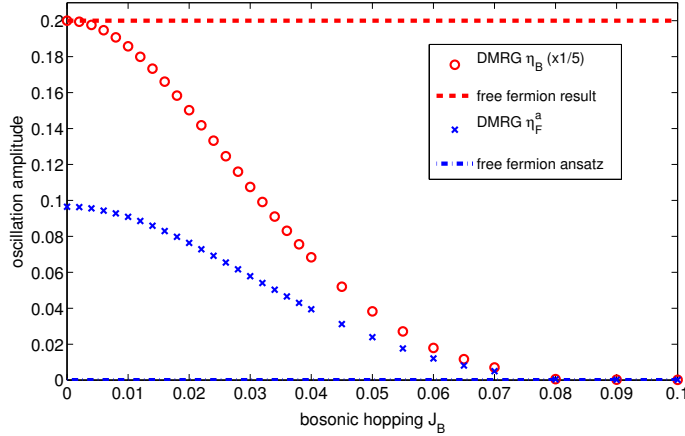
Figure 9.5: Amplitude of the bosonic CDW as a function of the bosonic hopping J_B for $V = 1.25$ and $J_F = 10$. Since the effective theory predicts a CDW for any hopping J_B (dashed lines), the necessity of a renormalization scheme is evident. Additionally the non-zero amplitude of the fermionic CDW is in strong contrast to the underlying ansatz and another indication of a more involved physics. The numerical data are obtained from DMRG for lattice of 512 sites and $N_F = N_B = 256$.

hopping[2]. As can be seen in figure 9.5, where the amplitude of the CDW obtained from DMRG simulations is plotted as a function of the bosonic hopping, the amplitude of the CDW drops for growing J_B, which is in contrast to the results from the coupling constants for free fermions. We attribute this error to the back-action of the bosons on the fermions which is disregarded in the effective Hamiltonian by now. Evidence for the existence of this back-action can also be found from the fermionic CDW amplitude plotted in figure 9.5. Despite the fact, that the effective theory relies on a homogeneous fermion distribution (for $\varrho_F = 1/2$) with a proper prediction of a bosonic CDW, the numerics show that the fermions are also found in a CDW phase, with some small, but non-vanishing amplitude η_F. This means, that the inclusion of a possible back-action is essential in the understanding of the phase diagram of the BFHM in the limit of fast fermions. These arguments also hold in the case of a fermionic density $\varrho_F \neq \frac{1}{2}$, with a ground state which has a boson at every $\frac{1}{\varrho_F}$-th site[3].

---

[2]This means an alternation of filled and empty sites.

[3]If the period of the oscillations is commensurable with the lattice. Otherwise, the situation gets much more complicate.

But before we move onto a scheme including this back-action for $\varrho_F = \frac{1}{2}$ we consider the properties of the coupling constants in momentum space. This will provide a valuable tool to judge the performance of the upcoming renormalization.

9.3 Couplings in momentum space

A different aspect of the nature of the couplings $g_d(\varrho_F)$ can be seen from the Fourier transform of the couplings:

$$\widetilde{g}_{\varrho_F}(k) = \sum_d g_d(\varrho_F) e^{ikd}. \tag{9.18}$$

The analytic form of the couplings (in this case for the free fermion case) shows that the only dependence on the distance d occurs in the numerator of (9.12). The Fourier transform of the numerator is given by

$$\sum_{d=-\infty}^{\infty} \cos d\xi \cos d\xi' e^{ikd} = \frac{\pi}{2} \sum_{l=-\infty}^{\infty} \sum_{C_1,C_2=\pm 1} \delta(2\pi l - C_1\xi - C_2\xi' - k). \tag{9.19}$$

as proven in section A.1 in the appendix. The calculation of (9.18) can be simplified by expanding the integration limits to infinity and introducing Θ functions, since then the evaluation of the δ function is straightforward:

$$\widetilde{g}_{\varrho_F}(k) \sim - \int_0^{\varrho_F \pi} \mathrm{d}\xi \int_{\varrho_F \pi}^{\pi} \mathrm{d}\xi' \frac{\sum_d \cos(d\xi) \cos(d\xi') e^{ikd}}{\cos(\xi) - \cos(\xi')} \tag{9.20}$$

$$= -\frac{\pi}{2} \int_0^{\varrho_F \pi} \mathrm{d}\xi \int_{-\infty}^{\infty} \mathrm{d}\xi' \sum_{l,C_1,C_2} \frac{\Theta(\pi - \xi')\Theta(\xi' - \pi\varrho_F)\delta(2\pi l - C_1\xi - C_2\xi' - k)}{\cos(\xi) - \cos(\xi')}$$

Performing the integral over ξ' finally gives

$$\widetilde{g}_{\varrho_F}(k) = -\frac{V^2}{4\pi J_F} \sum_{l,C_1,C_2} \int_0^{\varrho_F \pi} \mathrm{d}\xi \times \tag{9.21}$$

$$\frac{\Theta(\pi - 2\pi l C_2 + C_1 C_2 \xi + C_2 k)\Theta(2\pi l C_2 - C_1 C_2 \xi - C_2 k - \pi\varrho_F)}{\cos(\xi) - \cos(C_1\xi + k)}$$

as the result for the Fourier transformation of the coupling constants. This form already shows the 2π periodicity of $\widetilde{g}_{\varrho_F}(k)$ due to the sum over l
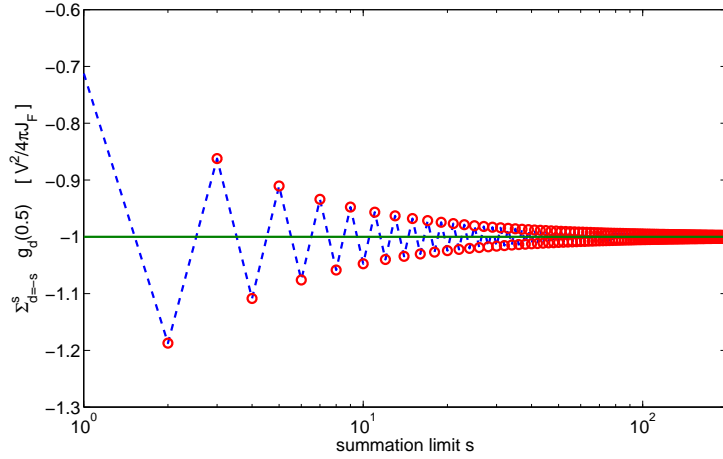
Figure 9.6: Direct summation of the couplings from figure 9.4 for $k = 0$. On can see the convergence for $s \to \infty$ to -1; this agrees with the limit $\lim_{k\to 0} \widetilde{g}_{\frac{1}{2}}(k)$.

(times 2π) and the cosine in the denominator. Therefore it is sufficient to restrict the range of k to $k \in [-\pi, \pi]$. With this restriction, the range of possible l values giving non-zero kernels for the integrals (due to the Θ functions) is strongly limited. For $k = 0$ it turns out that the integral kernel in (9.21) is not well defined. $\widetilde{g}_{\frac{1}{2}}(0)$ therefore has to be evaluated by a direct summation of the numerically integrated real space couplings taken from figure 9.4 for $\varrho_F = \frac{1}{2}$. This is shown in figure 9.6, where the Fourier transform is approximated by a finite sum with increasing limits, yielding $\widetilde{g}_{\frac{1}{2}}(0) = \lim_{k\to 0} \widetilde{g}_{\frac{1}{2}}(k) = -\frac{V^2}{4\pi J_F}$.

Figure 9.7 shows the couplings in momentum space as a function of the momentum k and the density ϱ_F. From the figure a divergence for $k = \pm 2\pi\varrho_F$ may be seen[4]. This divergence (van Hove-singularity [233]), also reported for instance in [117, 213] is directly connected to the earlier discussed divergence of the energy. For arbitrary fermionic density ϱ_F, filling the system with bosons up to a density $\varrho_B = \varrho_F$ results in a distribution of the bosons where the distance between the bosons is given by the wavelength of the coupling constant as presented in figure 9.3. The total energy of this configuration is related to the Fourier transform of the corresponding wavelength, thus being divergent, leading to the peculiarities discussed earlier. With these

---

[4]This strictly holds for $\varrho_F < \frac{1}{2}$.   For $\varrho_F > \frac{1}{2}$, the divergence is situated at $k = \pm 2\pi(1 - \varrho_F)$ due to the particle-hole symmetry.
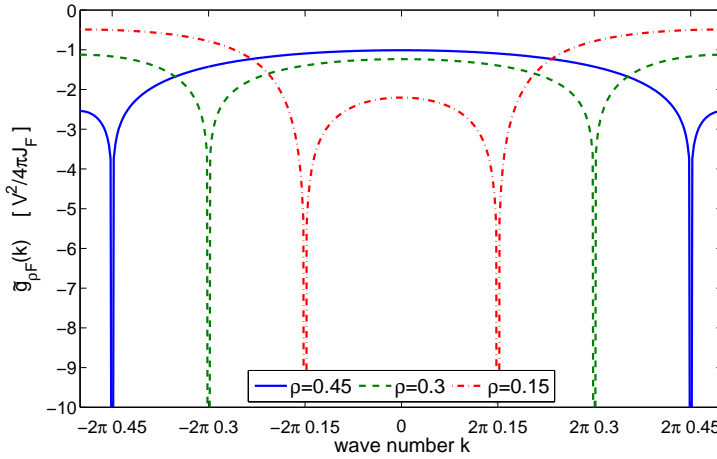
Figure 9.7: Numerical results for the Fourier transform of the couplings from equation (9.21). Shown are the couplings for selected values of ϱ_F. The divergence at $\pm 2\pi\varrho_F$ indicating the need for a renormalization of the fermions is very sharp.

indications for the necessity of including the back-action of bosons to the fermions, our next step in the understanding of the bosonic phase diagram is the renormalization of the fermionic system, resolving issues coming from the divergence of the coupling constants.

Renormalization of the fermionic system and the effective Hamiltonian

In the present chapter we introduce a renormalization scheme for the calculation of the fermionic cumulant in (8.13). The back-action of bosons on fermions is incorporated by the introduction of the bosonic mean-field amplitude $\widetilde{n}_j$ in equation (8.3). A natural choice of these amplitudes is apparent from the discussion in the previous chapter. As discussed, the ansatz of free fermions drives the bosonic system in a CDW phase with a divergent energy in the thermodynamic limit. This bosonic CDW in turn has an influence onto the fermionic system. Our approach incorporates this influence by a mean-field amplitude $\widetilde{n}_j$, following the CDW oscillations of the bosonic subsystem. The bosonic CDW will act as a background potential for the fermions. A drawback of our method is the slightly limited range of applicability. Due to the complexity of the method, only the case of $\varrho_F = 1/2$ is easily tangibly. Although we can generalize the method to other commensurate fermionic fillings $\varrho_F = 1/m$ with $m \in \mathbb{N}$ (as done formally in appendix A.4), we restrict ourselves to half fermionic filling. Finally, the renormalized cumulants are used to calculate and analyze the effective coupling constants together with a short discussion of the arising effective bosonic Hamiltonian.

For the case of a bosonic CDW the mean-field amplitude ansatz[1] is given by

$$\widetilde{n}_j = \varrho_B \left[1 + \eta_B (-1)^j \right] = \varrho_B (1 - \eta_B) + 2\varrho_B \eta_B \; \delta(\sin(\pi \frac{j}{2})), \qquad (10.1)$$

[1]A similar ansatz is used in [81] to study the influence of the wavelength of the bosonic CDW on the fermionic system.

where the latter form serves as a simplification in the following calculation. Here we introduced the amplitude of the bosonic CDW η_B as a free parameter. Figure 9.5 shows, that this amplitude drops to zero for increasing hopping J_B.

The main task in this chapter is to calculate the fermionic cumulants used in the effective bosonic Hamiltonian (8.14), i.e., free fermions in an alternating potential, given by

$$\hat{H}_{\mathrm{F}} = -J_F \sum_j \left(\hat{c}_j^\dagger \hat{c}_{j+1} + \hat{c}_{j+1}^\dagger \hat{c}_j \right) + V 2\varrho_B \eta_B \sum_j \delta(\sin \pi \frac{j}{2}) \hat{m}_j. \qquad (10.2)$$

In this Hamiltonian, a global energy shift $V \varrho_B (1 - \eta_B) \varrho_F$ from the potential is left out and a solution can be found straightforwardly, since the Hamiltonian is only quadratic in the creation and annihilation operators. Although the solution is easy by means of a canonical transformation as presented in appendix A.4 and in [178, 234], the resulting expressions are rather involved and the quantities needed are hard to express. Here we employ a Green's function approach, extracting all needed quantities for the full calculation of the bosonic Hamiltonian for double half filling.

10.1 General framework and initial definitions

Before going into details, we introduce the framework of the calculation. In order to calculate the second order cumulant $\langle\langle \hat{m}_j(T)\hat{m}_{j+d}(0)\rangle\rangle_{\mathrm{F}}$ with respect to the ground state of the fermionic Hamiltonian (10.2) we make use of the Green's function technique [220]. The second order cumulant factorizes by use of Wick's theorem [220, 235, 236] into a product of the advanced and retarded Green's functions

$$\langle\langle \hat{m}_j(T)\hat{m}_{j+d}(0)\rangle\rangle_{\mathrm{F}} = \left\langle \hat{c}_j^\dagger(t+T)\hat{c}_{j+d}(t) \right\rangle \left\langle \hat{c}_j(t+T)\hat{c}_{j+d}^\dagger(t) \right\rangle$$
$$= \mathcal{G}_{j,j+d}^{(+)}(t+T,t)\, \mathcal{G}_{j,j+d}^{(-)}(t+T,t). \qquad (10.3)$$

Here we used $T > 0$ and the definition of the Green's functions

$$\begin{aligned}
\mathcal{G}_{j,j+d}^{(+)}(t+T,t) &= < \mathcal{T}\ \hat{c}_j^\dagger(t+T)\ \hat{c}_{j+d}(t) > \\
\mathcal{G}_{j,j+d}^{(-)}(t+T,t) &= < \mathcal{T}\ \hat{c}_j(t+T)\ \hat{c}_{j+d}^\dagger(t) > .
\end{aligned} \qquad (10.4)$$

To find a solution of the problem it is more convenient to switch to momentum space. The Hamiltonian (10.2) can be transformed to momentum space by

the Fourier transformation (9.2), which gives

$$\hat{H}_{\mathrm{F}} = -2J_F \sum_{k=-L/2}^{L/2-1} \cos(2\pi\frac{k}{L})\,\hat{f}_k^\dagger \hat{f}_k + V\eta_B \varrho_B \sum_{k=-L/2}^{L/2-1}\sum_{\alpha=\pm 1} \hat{f}_{k+\frac{L}{2}\alpha}^\dagger \hat{f}_k \qquad (10.5)$$

apart from a constant energy shift $V\eta_B\varrho_B\varrho_F$ which is neglected. Here it should be mentioned that the summation over α only includes those terms which fulfill $|k| < \frac{L}{2}$. To denote Green's functions in momentum space change indices as $j \to k$ and $j + d \to k'$.

Due to the perturbation of the ground state from the potential V, we first calculate the Green's functions (10.4) for the unperturbed system, i.e., the ground state of Hamiltonian (10.2) for $\eta_B = 0$. This state is the aforementioned Fermi-sphere (9.5). A straightforward calculation gives for the Green's functions

$$\begin{aligned}
\mathcal{G}_{k,k'}^{(0+)}(t,t') &= \Theta(t-t')\Theta(\varepsilon_F - \varepsilon_k)e^{i\varepsilon_k(t-t')}\delta_{k,k'} \\
&\quad - \Theta(t'-t)\Theta(\varepsilon_k - \varepsilon_F)e^{i\varepsilon_k(t-t')}\delta_{k,k'} \\
\mathcal{G}_{k,k'}^{(0-)}(t,t') &= \Theta(t-t')\Theta(\varepsilon_k - \varepsilon_F)e^{i\varepsilon_k(t'-t)}\delta_{k,k'} \\
&\quad - \Theta(t'-t)\Theta(\varepsilon_F - \varepsilon_k)e^{i\varepsilon_k(t'-t)}\delta_{k,k'}
\end{aligned} \qquad (10.6)$$

in the time domain and

$$\mathcal{G}_{k,k'}^{(0\pm)}(\omega) = \pm\delta_{k,k'}\frac{i}{\sqrt{2\pi}}\frac{1}{\varepsilon_k \mp \omega \oplus i\delta} \qquad (10.7)$$

in the frequency domain. Here, the frequency domain is defined by the (time) Fourier transformation

$$\mathcal{G}_{k,k'}^{(0\pm)}(\omega) = \frac{1}{\sqrt{2\pi}}\int_{-\infty}^{\infty} \mathrm{d}T\, \mathcal{G}_{k,k'}^{(0\pm)}(t+T,t)\, e^{-i\omega T}\, e^{\pm\delta T}. \qquad (10.8)$$

The last term in the integral kernel is introduced to assure convergence and will be properly removed later on. In equation (10.6) we introduced the dispersion relation

$$\varepsilon_k = -2J_F \cos(2\pi\frac{k}{L}) \qquad (10.9)$$

of the free particle and

$$\oplus = \begin{cases} + & k \in \mathcal{K}_F \\ - & k \notin \mathcal{K}_F \end{cases} \qquad (10.10)$$

distinguishes between momentum modes within the Fermi sphere and those outside.

Following the technical details presented in [220], we immediately arrive at a Dyson equation for the Green's function since the induced potential is only quadratic in the fermionic operators. In the frequency domain this gives

$$\mathcal{G}_{k,k'}^{(+)}(\omega) = \mathcal{G}_{k,k'}^{(0+)}(\omega) + \frac{i}{\hbar}\sqrt{2\pi}V\eta_B\varrho_B\,\mathcal{G}_{k,k}^{(0+)}(\omega)\sum_{\alpha=\pm1}\mathcal{G}_{k+\frac{L}{2}\alpha,k'}^{(+)}(\omega) \qquad (10.11)$$

for the advanced Green's function and the retarded Green's function is given by

$$\mathcal{G}_{k,k'}^{(-)}(\omega) = \mathcal{G}_{k,k'}^{(0-)}(\omega) + \frac{i}{\hbar}\sqrt{2\pi}V\eta_B\varrho_B\,\mathcal{G}_{k',k'}^{(0-)}(\omega)\sum_{\alpha=\pm1}\mathcal{G}_{k,k'+\frac{L}{2}\alpha}^{(-)}(\omega). \qquad (10.12)$$

These equations allow for an algebraic solution.

10.2   Solution of the Dyson equations

For the solution we only discuss the case of the advanced Green's function, the situation for the retarded one is exactly the same.

The solution of equation (10.11) can be found by considering

$$\mathcal{G}_{k\pm\frac{L}{2},k'}^{(+)}(\omega) = \mathcal{G}_{k\pm\frac{L}{2},k'}^{(0+)}(\omega) + \frac{i}{\hbar}\sqrt{2\pi}V\eta_B\varrho_B\,\mathcal{G}_{k\pm\frac{L}{2},k\pm\frac{L}{2}}^{(0+)}(\omega)\mathcal{G}_{k,k'}^{(+)}(\omega), \qquad (10.13)$$

which are the contributions in the latter part of equation (10.11). Here it should be mentioned that the contribution from $\mathcal{G}_{k\pm L,k'}^{(+)}(\omega)$ vanishes since the momentum modes are limited to the first Brillouin zone $k \in [-\frac{L}{2}, \frac{L}{2}]$ with $k \pm L \notin [-\frac{L}{2}, \frac{L}{2}]$. Plugging these two Green's functions into (10.11) and solving for $\mathcal{G}_{k,k'}^{(+)}(\omega)$ finally gives the solution of the Green's functions in terms of the unperturbed ones:

$$\mathcal{G}_{k,k'}^{(+)}(\omega) = \frac{\mathcal{G}_{k,k'}^{(0+)}(\omega) + \frac{i}{\hbar}\sqrt{2\pi}V\eta_B\varrho_B\,\mathcal{G}_{k,k}^{(0+)}(\omega)\left[\mathcal{G}_{k+\frac{L}{2},k'}^{(0+)}(\omega) + \mathcal{G}_{k-\frac{L}{2},k'}^{(0+)}(\omega)\right]}{1 + \frac{2\pi V^2\eta_B^2\varrho_B^2}{\hbar^2}\mathcal{G}_{k,k}^{(0+)}(\omega)\left[\mathcal{G}_{k+\frac{L}{2},k+\frac{L}{2}}^{(0+)}(\omega) + \mathcal{G}_{k-\frac{L}{2},k-\frac{L}{2}}^{(0+)}(\omega)\right]}.$$

$$(10.14)$$

From (10.7) we note that $\mathcal{G}^{(0\pm)}_{k,k'}(\omega) \sim \delta_{kk'}$ and therefore only the terms $\mathcal{G}^{(+)}_{k,k}(\omega)$, $\mathcal{G}^{(+)}_{k,k\pm\frac{L}{2}}(\omega)$ and $\mathcal{G}^{(+)}_{k\pm\frac{L}{2},k}(\omega)$ of the full Green's functions are non-zero. Applying the same procedure to $\mathcal{G}^{(-)}_{k,k'}(\omega)$ gives a similar expression. The final form for the Green's functions in momentum space and time domain is found by using the precise form of $\mathcal{G}^{(0\pm)}_{k,k'}$ from (10.7) and simplifying the resulting expressions giving

$$\mathcal{G}^{(\pm)}_{k,k}(\omega) = \pm\frac{i}{\sqrt{2\pi}}\frac{\varepsilon_k \pm \omega \oplus i\delta}{(\varepsilon_k \mp \omega \oplus i\delta)(\varepsilon_k \pm \omega \oplus i\delta) + \frac{V^2\eta_B^2\varrho_B^2}{\hbar^2}} \tag{10.15}$$

and

$$\mathcal{G}^{(\pm)}_{k,k\pm\frac{L}{2}}(\omega) = \frac{i\frac{V\eta_B\varrho_B}{\sqrt{2\pi}\hbar}}{(\varepsilon_k \mp \omega \oplus i\delta)(\varepsilon_k \pm \omega \oplus i\delta) + \frac{V^2\eta_B^2\varrho_B^2}{\hbar^2}} = \mathcal{G}^{(\pm)}_{k\pm\frac{L}{2},k}(\omega). \tag{10.16}$$

Here, again $\oplus$ distinguishes between momentum modes k within or outside the Fermi sphere $\mathcal{K}_F$.

This is the main result of this section. It has to be completed by transforming back to the time domain which can be found in appendix A.2. After the Fourier transformation, introducing the renormalized dispersion relation

$$\bar{\varepsilon}_k = \sqrt{\varepsilon_k^2 + \frac{V^2\eta_B^2\varrho_B^2}{\hbar^2}}, \tag{10.17}$$

the Green's functions in momentum space and time domain are found to read

$$\mathcal{G}^{(\pm)}_{k,k}(t+T,t) = \frac{1}{2}e^{-i\bar{\varepsilon}_kT}\left(1 \mp \frac{\varepsilon_k}{\bar{\varepsilon}_k}\right) \tag{10.18}$$

$$\mathcal{G}^{(\pm)}_{k\pm\frac{L}{2},k}(t+T,t) = -\frac{V\eta_B\varrho_B}{2\hbar}\frac{1}{\bar{\varepsilon}_k}e^{-i\bar{\varepsilon}_kT}. \tag{10.19}$$

These expressions allow to calculate the density-density correlations for the fermionic Hamiltonian.

10.3 Green's function in real space

The missing final step, the Fourier transformation from momentum space to real space will be performed together with the transition to the thermodynamic limit. As above, we restrict ourselves on the calculation of $\mathcal{G}^{(+)}_{j,j+d}(t+T,t)$, since the calculation for $\mathcal{G}^{(-)}_{j,j+d}(t+T,t)$ is similar.

Using the definition

$$\mathcal{G}^{(+)}_{j,j+d}(t+T,t) = \left\langle \mathcal{T}\, \hat{c}^{\dagger}_{j}(t+T)\, \hat{c}_{j+d}(t) \right\rangle \tag{10.20}$$

of the Green's functions and the Fourier transformation to momentum space (9.2), the real space Green's functions are connected to the momentum space Green's functions by

$$\mathcal{G}^{(+)}_{j,j+d}(t+T,t) = \frac{1}{L} \sum_{k_1,k_2=-L/2}^{L/2-1} e^{-2\pi i \frac{(k_1-k_2)}{L}j} e^{-2\pi i \frac{k_1}{L}d} \mathcal{G}^{(+)}_{k_2,k_1}(t+T,t). \tag{10.21}$$

From the previous discussions we know, that only certain Green's functions in momentum space are non-zero. This is incorporated by including

$$\delta_{k_1 k_2} + \delta_{k_1+\frac{L}{2} k_2} + \delta_{k_1-\frac{L}{2} k_2} \tag{10.22}$$

to the summation, picking out the non-zero elements. After performing the summation over k_2, a slight restructuring of the exponentials and an application of the symmetry of the Green's functions (10.16), the final result is found to be[2]

$$\mathcal{G}^{(+)}_{j,j+d}(t+T,t) = \frac{1}{2L} \sum_{k} e^{-2\pi i \frac{k}{L}d} \left[\left(1 - \frac{\varepsilon_k}{\bar{\varepsilon}_k}\right) - (-1)^j \frac{V\eta_B \varrho_B}{\hbar} \frac{1}{\bar{\varepsilon}_k} \right] e^{-i\bar{\varepsilon}_k T}. \tag{10.23}$$

For a detailed analysis of the Green's functions, it is more convenient to switch to the thermodynamic limit. As stated earlier, this is achieved by substituting $\xi = \frac{k}{L}$ and changing $\frac{1}{L}\sum_k$ to $\int d\xi$. Furthermore including the definition of the free fermion dispersion (10.9) as well as the renormalized dispersion (10.17) and introducing an amplitude factor

$$a = \frac{V\eta_B \varrho_B}{2\hbar J_F} \tag{10.24}$$

the real space Green's functions in time domain can be written as

$$\mathcal{G}^{(\pm)}_{jj+d}(t+T,t) = \frac{1}{2\pi} \int_0^{\pi} d\xi\, \cos(d\xi)\, e^{-iT2J_F\sqrt{\cos^2(\xi)+a^2}} \left(1 \pm \frac{\cos(\xi)}{\sqrt{\cos^2(\xi)+a^2}}\right)$$

$$- (-1)^j \frac{a}{2\pi} \int_0^{\pi} d\xi\, \cos(d\xi)\, \frac{e^{-iT2J_F\sqrt{\cos^2(\xi)+a^2}}}{\sqrt{\cos^2(\xi)+a^2}}. \tag{10.25}$$

_____

[2]The retarded form $\mathcal{G}^{(-)}_{j,j+d}(t+T,t)$ is found from a similar analysis.

This result is the starting point for the calculation of the density-density correlator. Note that the integration in (10.25) cannot be carried out explicitly for general arbitrary d.

10.4 Expectation values and the density-density correlator

The calculation of the Green's functions does not only allow to calculate of the density-density correlator in equation (8.13) but also gives a prediction of the behavior of the fermionic system, as long as the bosonic CDW amplitude η_B is known. Here we first look at the solution of the fermionic problem itself, i.e., all numerical data shown are calculated for the Hamiltonian (10.2), i.e., only the fermionic problem with an external potential is simulated; not the full Bose-Fermi-Hubbard Hamiltonian.

a)   Local density

The first quantity to study is the fermionic density predicted by the renormalization procedure. With the result for the Green's function in equation (10.25) an analytic form for the fermionic density can be found. Using

$$\langle \hat{m}_j \rangle_{\mathrm{F}} = \mathcal{G}^{(+)}_{j,j+0}(t+0,t) \tag{10.26}$$

the fermionic density evaluates as

$$\langle \hat{m}_j \rangle_{\mathrm{F}} = \frac{1}{2\pi} \int_0^\pi \mathrm{d}\xi \left(1 + \frac{\cos(\xi)}{\sqrt{\cos^2(\xi)+a^2}} \right) - (-1)^j \frac{a}{2\pi} \int_0^\pi \mathrm{d}\xi \frac{1}{\sqrt{\cos^2(\xi)+a^2}}$$

$$= \frac{1}{2} - (-1)^j \frac{a}{\pi\sqrt{1+a^2}} K\left[\frac{1}{1+a^2} \right]. \tag{10.27}$$

The first important result from the renormalization procedure therefore is

$$\langle \hat{m}_j \rangle_{\mathrm{F}} = \frac{1}{2} \left[1 - \eta_F^a (-1)^j \right], \tag{10.28}$$

where $\eta_F^a = \frac{2a}{\pi\sqrt{1+a^2}} K\left[\frac{1}{1+a^2}\right]$ and $K[x]$ is the complete elliptic integral of the first kind [237]. This means, the renormalization procedure results in the prediction of a fermionic CDW with some amplitude η_F^a which is in agreement with the numerical results from figure 9.5. Figure 10.1
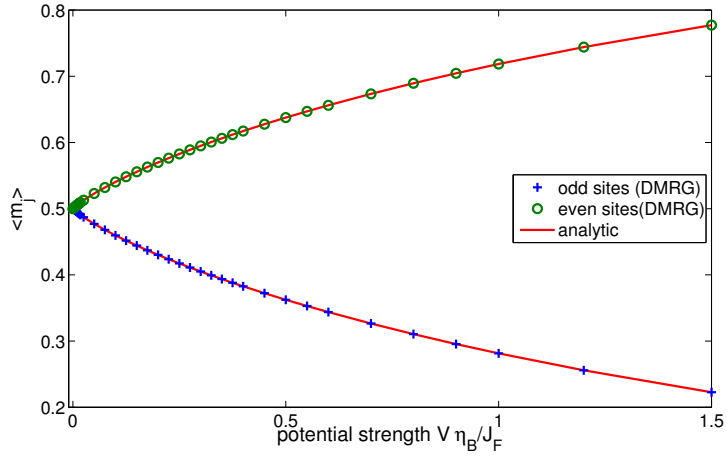
Figure 10.1: Expectation value of the fermionic density operator for even and odd sites for the ground state of the effective renormalized fermionic Hamiltonian (10.2). Points are the numerical results from DMRG calculations with 300 sites and $J_F = 10$. Solid lines are the analytic results from equation (10.28). Shown are the numerical results for $\langle \hat{m}_{150} \rangle_F$ and $\langle \hat{m}_{151} \rangle_F$.

shows numerical calculation of the amplitude of the fermionic CDW from DMRG calculations for the Hamiltonian (10.2) as a function of the potential strength $V\eta_B$ along with the analytic results.

Another feature of (10.28) which will be important for the later discussion of the full Bose-Fermi-Hubbard model is the minus sign in front of the site dependent part. This is a direct consequence of the alternating boson potential ansatz. Since the interaction V is chosen positive, i.e., repulsion between bosons and fermions, it is expected that the phase of the bosonic and fermionic density wave is shifted by π compared to each other. For the case of attractive interaction, both density waves are in phase. This is in full agreement with the numerical results presented in the discussion of the results for the full Bose-Fermi-Hubbard model in chapter 12. In the limit $a \to 0$, corresponding to the free fermion case the result for the density reduces to the result for free fermions at half filling, i.e., $\langle \hat{m}_j \rangle_F = \frac{1}{2}$.

Figure 10.2 shows the numerical results for the amplitudes η_F^a as a function of η_B from figure 9.5 as well as the analytic prediction according to equation (10.28). The numerical data comes from the full Bose-Fermi-Hubbard model.
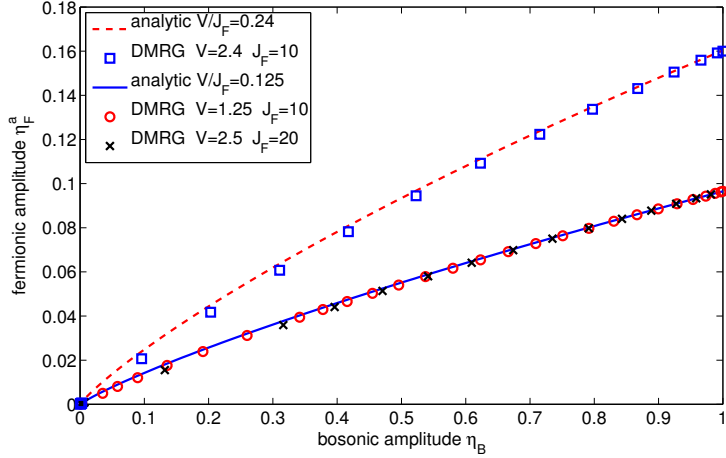
Figure 10.2: Amplitude η_F^a of the fermionic CDW versus the bosonic amplitude η_B for different numerical data. Shown are the numerical results (data points) presented in figure 9.5 and for $V = 2.4$ and $J_F = 10$. The solid lines are the analytic results for η_F^a.

b) First-order correlations

Beside the calculation of the the local density, the Green's function (10.25) allows to calculate the first-order correlations

$$\left\langle \hat{c}_j^\dagger \; \hat{c}_{j+d} \right\rangle = \mathcal{G}_{j,j+d}^{(+)}(t+0,t). \tag{10.29}$$

Unfortunately, the integral expression for the Green's function cannot be evaluated analytically for arbitrary distance d, making a numerical integration necessary. This is done in figure 10.3, where the first-order correlations for the numerical data shown in figure 10.1 are presented. The perfect agreement prooves the validity of the obtained expression for the Green's function.

c) Density-density correlations

Finally we calculate the density-density correlations used in the expression for the coupling constants (8.13) with the renormalized fermionic model. Having a closer look at the result for the Green's function (10.25) it can be seen that both Green's functions are of the general form

$$\mathcal{G}_{j,j+d}^{(\pm)}(t+T,t) = A_\pm - aB. \tag{10.30}$$
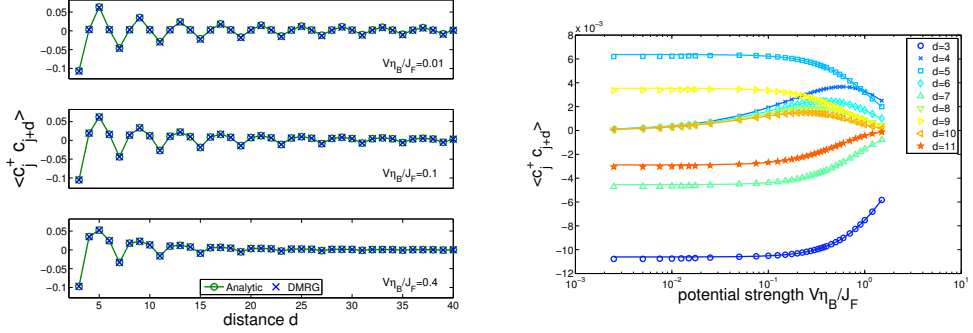
Figure 10.3: First-order correlations $< \hat{c}_j^\dagger \, \hat{c}_{j+d} >$ calculated from the fermion model (10.2). Solid lines are the theoretical results from a numerical integration of (10.25). The points are the numerical results from the data used in figure 10.1. Left: Distance dependence of the correlations for three different interactions $V\eta_B$. Right: Dependence of the correlations for a wide range of interactions $V\eta_B$ for selected distances d.

The definitions of $A_\pm$ and B are obvious from equation (10.25). In equation (10.3) we already noted that the density-density cumulant splits up into the product of advanced and retarded Green's function, which may be written as

$$\langle\langle \hat{m}_j(T)\hat{m}_{j+d}(0)\rangle\rangle_{\mathrm{F}} = A_+ A_- - a(A_+ + A_-) + a^2 B^2. \qquad (10.31)$$

From the definition of the coupling constants (8.13) we can see, that they are proportional to V^2, since they are a second order correction in the effective Hamiltonian (8.14). This means, that in order V^2, only the first term in (10.31) is relevant.

Following this argument, the renormalized form of the density-density cumulant reads

$$\langle\langle \hat{m}_j(t+T)\hat{m}_{j+d}(t)\rangle\rangle = \frac{1}{4\pi^2} \int\limits_0^\pi \int\limits_0^\pi \mathrm{d}\xi \mathrm{d}\xi' \, \cos(d\xi) \, \cos(d\xi')$$
$$\times e^{-iT2J_F\left(\sqrt{\cos^2(\xi)+a^2}+\sqrt{\cos^2(\xi')+a^2}\right)} \qquad (10.32)$$
$$\times \left(1 + \frac{\cos(\xi)}{\sqrt{\cos^2(\xi) + a^2}}\right) \left(1 - \frac{\cos(\xi')}{\sqrt{\cos^2(\xi') + a^2}}\right).$$

This is the main result from the renormalization procedure. Comparing the renormalized result to that of free fermions (at $\varrho_F = \frac{1}{2}$) in equation (9.9)

one can see, that the corresponding limit $a \to 0$ gives the same result as equation (9.9). Note, that the last line in (10.32) serves as a cutoff function which constrains the integration limits to the free fermion values in the limit $a \to 0$. In this limit, the free fermion solution is recovered.

10.5 Discussion of the renormalized couplings

As already done in chapter 9, the second order cumulant needs to be integrated over time according to equation (8.13) in order to obtain the effective coupling constants of the bosonic model. Following the same arguments as in section 9.1b), the time integration may be performed using the Riemann-Lebesgue lemma. The condition, that the integral kernel is a $\mathcal{L}^1$ function is fulfilled since the absolute value of the kernel is less than $\frac{1}{a}(1 - a^{-2})$ (modulo some prefactors). This gives an upper bound which reduces in the limit $a \to 0$ to the free fermion which has already been proven to be $\mathcal{L}^1$. Thus the Riemann-Lebesgue lemma is applicable, giving for the coupling constants the closed form

$$
g_d(a) = -\frac{V^2}{8\pi^2 J_F} \int\limits_0^\pi \int\limits_0^\pi \mathrm{d}\xi \mathrm{d}\xi' \frac{\cos(d\xi)\cos(d\xi')}{\sqrt{\cos^2(\xi) + a^2} + \sqrt{\cos^2(\xi') + a^2}}
$$
$$
\times \left(1 + \frac{\cos(\xi)}{\sqrt{\cos^2(\xi) + a^2}}\right)\left(1 - \frac{\cos(\xi')}{\sqrt{\cos^2(\xi') + a^2}}\right)
$$
(10.33)

for the density-density interaction couplings strengths in the effective bosonic Hamiltonian. Since we restrict ourselves to the case of half filling for the fermions, the additional index ϱ_F is dropped here but the dependence of the renormalized couplings on the amplitude factor a is explicitly written. The result is in accordance to the free fermion case since in the limit $a \to 0$ the second line of equation (10.33) gives a factor of 4 together with a limitation of the integration limits to $\xi \in [0, \frac{\pi}{2}]$ and $\xi' \in [\frac{\pi}{2}, \pi]$ as in (9.12).

Let us discuss the properties of the renormalized coupling constants. Figure 10.4 shows the absolute values for the couplings as a function of the distance d for fixed $a = 0.1$ compared to the free fermion case $a = 0$. Whereas the couplings in the latter case decay as $1/d$ as discussed in chapter 9, the renormalized couplings decay much faster. This leads to the important conclusion, that the divergence for $k = \pm\pi$ as shown in figure 9.7 is lifted.
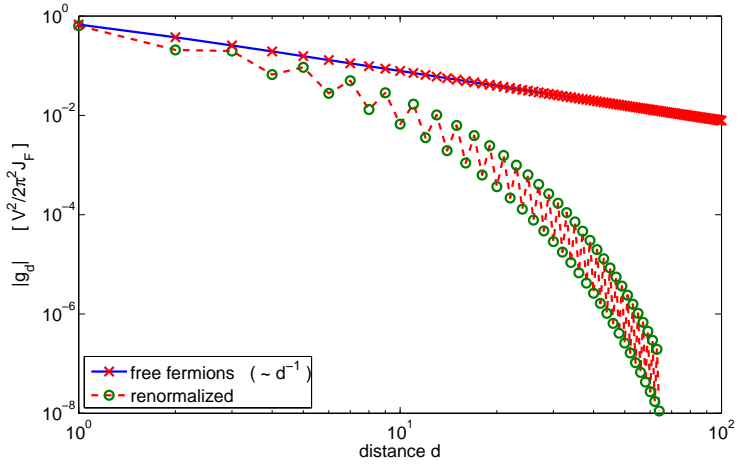
Figure 10.4: Comparison of the couplings for the free fermion case $(a = 0)$ and the renormalized couplings for $a = 0.1$. The free fermion couplings decay as $\frac{1}{d}$, whereas the renormalized couplings decay much faster, preventing the divergence of the energy for the ground state.

Considering the Fourier transform of equation (10.33), the lifting of the divergence can be understood more easy. Using the method introduced in the derivation of equation (9.21) for the free fermions, the Fourier transform of the renormalized couplings is given by

$$\widetilde{g}_a(k) = -\frac{V^2}{16\pi J_F} \sum_{l,C_1,C_2} \int_0^\pi \mathrm{d}\xi \times \tag{10.34}$$

$$\frac{\Theta(\pi - 2\pi l C_2 + C_1 C_2 \xi + C_2 k)\Theta(2\pi l C_2 - C_1 C_2 \xi - C_2 k)}{\sqrt{\cos^2(\xi) + a^2} + \sqrt{\cos^2(C_1\xi + k) + a^2}}$$

$$\times \left(1 + \frac{\cos(\xi)}{\sqrt{\cos^2(\xi) + a^2}}\right)\left(1 - \frac{\cos(C_1\xi + k)}{\sqrt{\cos^2(C_1\xi + k) + a^2}}\right).$$

Again, a detailed discussion of the arising Θ-functions is necessary to understand the contributions from the triple sum. Additionally, the 2π periodicity of $\widetilde{g}_a(k)$ can easily be seen from the equation.

In chapter 9 we already realized, that the divergence of the total energy of the system in the thermodynamic limit is connected to the Fourier transform at the CDW wave vector $k = \pm 2\varrho_F\pi = \pm\pi$. Luckily, the Fourier transform given in equation (10.34) may be evaluated analytically at $k = \pm\pi$
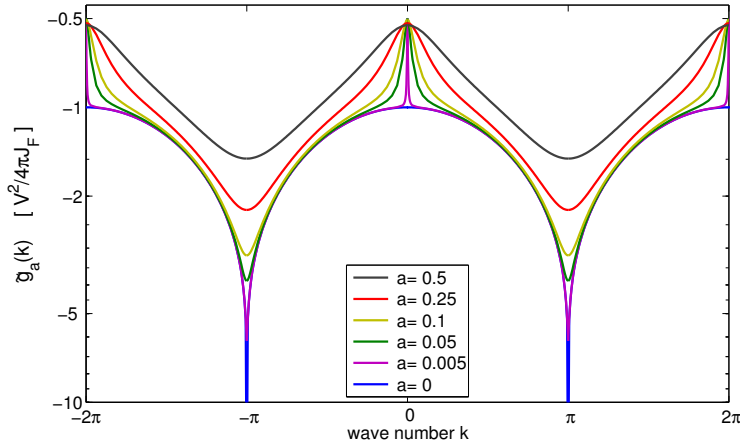
Figure 10.5: Fourier transform of the renormalized couplings $\widetilde{g}_a(k)$ for different amplitude factors a. At $k = \pm\pi$, the divergence for $a \to 0$ is clearly observable. For $k = 0$ the situation is more complicated and a short discussion can be found in the main text.

and $k = 0$. For $k = \pm\pi$, an analysis of the triple sum in (10.34) shows that the only contributions to the integral come from the combinations $(l, C_1, C_2) = (\pm 1, \pm 1, \pm 1)$ and $(0, \mp 1, \mp 1)$, $(0, -1, 1)$ as well as $(0, 1, -1)$ for $k = 0$. In both situations, the integration can be done exactly. This gives

$$\widetilde{g}_a(\pm\pi) = -\frac{V^2}{8\pi J_F}\frac{1}{\sqrt{1+a^2}}\left(2K[\frac{1}{1+a^2}] - E[\frac{1}{1+a^2}]\right) \qquad (10.35)$$

$$\widetilde{g}_a(0) = -\frac{V^2}{8\pi J_F}\frac{1}{\sqrt{1+a^2}}E[\frac{1}{1+a^2}], \qquad (10.36)$$

with $E[x]$ being the complete elliptic integral of second kind [237].

At this point some remarks about the continuity of the coupling constants in Fourier space are necessary. Studies with numerical integration of equation (10.34) show, that the limits $\lim_{a \to 0}$ and $\lim_{k \to 0}$ are not interchangeable. This discontinuity can be seen in figure 10.5, where the Fourier transform of the coupling constants is plotted for different amplitude factors a. Fixing the momentum $k = 0$ and then performing the limit $\lim_{a \to 0}$ gives

$$\lim_{a \to 0}\widetilde{g}_a(0) = -\frac{V^2}{8\pi J_F}, \qquad (10.37)$$

where on the other hand the limit $k \to 0$ with $a = 0$ gives

$$\lim_{k \to 0} \widetilde{g}_0(k) = -\frac{V^2}{4\pi J_F}. \tag{10.38}$$

For $k \to 0$ at given $a = 0$, the kernel in equation (10.34) roughly behaves like a step function of height $1/k$ and a support of width k. This resembles the properties of Dirac's δ-function, leading to the discontinuity. In our later studies, we will nevertheless use the result for the limit $a \to 0$ at fixed $k = 0$ since this turns out to be the proper choice.

10.6   The renormalized Hamiltonian

After the initial discussions we are now able to write down the effective bosonic Hamiltonian for a fixed fermion filling $\varrho_F = 1/2$. It reads

$$\hat{H}_{\mathrm{B}}^{\mathrm{eff}} = -J_B \sum_j \left(\hat{a}_j^\dagger \hat{a}_{j+1} + \hat{a}_{j+1}^\dagger \hat{a}_j \right) + \frac{U}{2} \sum_j \hat{n}_j \left(\hat{n}_j - 1 \right)$$
$$- \bar{\mu} \sum_j \hat{n}_j - \Delta \sum_j \hat{n}_j (-1)^j + \sum_j \sum_d g_d(a) \, \hat{n}_j \hat{n}_{j+d}. \tag{10.39}$$

together with the induced chemical

$$\bar{\mu} = 2\varrho_B \widetilde{g}_a(0) - V/2 \tag{10.40}$$

and an induced alternating potential

$$\Delta = 2\varrho_B \eta_B \widetilde{g}_a(\pi) + V \eta_F^a/2, \tag{10.41}$$

which are a direct consequence of the fermionic density wave

$$\langle \hat{m}_j \rangle_{\mathrm{F}} = \frac{1}{2} \left[1 - \eta_F^a (-1)^j \right] \tag{10.42}$$

with amplitude $\eta_F^a/2$. The coupling constants of the induced density-density interaction are given by (10.33) with the amplitude factor $a = \frac{V \eta_B \varrho_B}{2\hbar J_F}$. For the Fourier transform, the identities

$$\sum_d g_d(a) = \widetilde{g}_a(0) \qquad \text{and} \qquad \sum_d (-1)^d \, g_d(a) = \widetilde{g}_a(\pi), \tag{10.43}$$

hold.

This Hamiltonian (10.39) is the major result in this part. It opens the route for an understanding of the bosonic phase diagram and allows for a straightforward perturbative approach. As stated earlier, this Hamiltonian still has a free parameter $a \sim \eta_B$ which has to be chosen self-consistently. This parameter describes the bosonic density wave

$$\widetilde{n}_j = \varrho_B \left[1 + \eta_B(-1)^j \right] \tag{10.44}$$

with averaged density ϱ_B.

The influence of the correction terms in (10.39) to the plain Bose-Hubbard Hamiltonian are discussed in chapter 12, whereas in the next chapter we first discuss the self-consistent determination of the bosonic amplitude η_B from the renormalization scheme.

CHAPTER 11

Self-consistent determination of η_B

In the previous chapter we introduced a bosonic CDW amplitude η_B as a free parameter. Here we present two approaches for a self-consistent calculation of this amplitude. The general idea is to use a suitable ansatz for the ground state of the system which fulfills the initial condition (10.44) for the bosonic CDW. With this ansatz, the expectation value for the energy in the system is calculated and a minimization of the energy gives the amplitude η_B.

11.1 Coherent state

A first, simple choice for the ground state of the system are local coherent states $|\alpha\rangle$ [238]. With these, the calculation of the expectation value of the Hamiltonian (10.39) for the effective system is straightforward. We use the ansatz

$$|\Psi\rangle^{\mathrm{coh}} = \prod_{j=-\infty}^{\infty} |\alpha_+\rangle_{2j} |\alpha_-\rangle_{2j+1} \tag{11.1}$$

and require

$$^{\mathrm{coh}}\langle\Psi| \hat{n}_j |\Psi\rangle^{\mathrm{coh}} = \frac{1}{2}\left[1 + \eta_B(-1)^j\right]. \tag{11.2}$$

This is equivalent to

$$|\alpha_\pm|^2 = \frac{1}{2} \pm \frac{1}{2}\eta_B. \tag{11.3}$$

Assuming real coherent amplitudes $\alpha_\pm = \sqrt{\frac{1}{2} \pm \frac{1}{2}\eta_B}$, the expectation value for the energy of the effective Hamiltonian is given by

$$^{\text{coh}} \langle \Psi | \hat{H}_{\text{B}}^{\text{eff}} | \Psi \rangle^{\text{coh}} = \sum_j \left[-J_B \sqrt{1 - \eta_B^2} + \frac{U}{8}(1 + \eta_B^2) \right. \tag{11.4}$$

$$\left. - \frac{1}{2}\Delta \eta_B - \frac{1}{2}\bar{\mu} + \sum_d \frac{1}{4}g_d(a) \left[1 + (-1)^d \eta_B \right] + \frac{1}{2}g_0(a) \right].$$

Unfortunately, the coherent state energy functional has a drawback. Since the coherent states inherit contributions from all number states, the interaction part in (11.4) proportional to U dominates. As we are interested in the double half filling case with approximately no occupation of higher number states $n > 1$, we may neglect these contributions. Using the results for the strength Δ of the induced alternating potential (10.41) and the induced chemical potential $\bar{\mu}$ (10.40) the energy functional can be written

$$E\left[\eta_B\right] = -J_B \sqrt{1 - \eta_B^2} + \frac{1}{2}g_0(a) - \frac{1}{4}V\eta_F^a \eta_B - \frac{1}{4}\widetilde{g}_a(\pi)\eta_B^2 - \frac{1}{4}\widetilde{g}_a(0). \tag{11.5}$$

We stress that the amplitude factor $a = \frac{V\eta_B}{4\hbar J_F}$ as well as the fermionic amplitude η_F^a also depend on η_B. The last step is to minimize the energy with respect to η_B as a function of the parameters of the Bose-Fermi-Hubbard model. This needs to be done numerically, since the analytic form of the Fourier transformed couplings are too involved. A further simplification should be mentioned. Since the numerical evaluation of $g_0(a)$ is time consuming, we use an approximative formula for the region $a \in [0, 1]$ which gives a very good agreement to the exact integrals. This is given by

$$g_0(a) \approx -\frac{V^2}{8J_F\pi^2} \left(\pi^2 - 9.92786 \, a + 5.41095 \, a^2 - 1.26419 \, a^3 \right) \tag{11.6}$$

and the relative error to the numerical integration is less than 10^{-5} which is sufficient for our purpose.

Figure 11.1 compares the self-consistent prediction of the bosonic CDW amplitude as a function of the bosonic hopping J_B to the numerical data from figure 9.5 and to data for $V = 2.4$ and $J_F = 10$. One can see that the coherent approach gives a qualitatively good agreement for small J_B, but the quantitative agreement is rather poor in particular for larger J_B because of the strongly simplified ansatz used here.
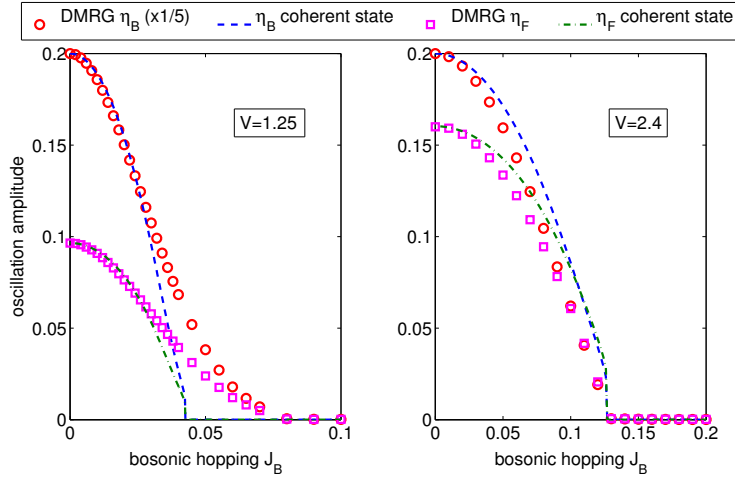
Figure 11.1: Self-consistent determination of the amplitude of the bosonic CDW from the minimization of the energy for the effective Hamiltonian with respect to a coherent state ansatz. Shown are the same numerical results as in figure 9.5 (left plot, $L = 512$) as well as results for $V = 2.4$ and $J_F = 10$ (right, $L = 256$). One can see the rather poor quantitative agreement with a general qualitative agreement.

11.2 Matrix product state

Better results for the CDW amplitude may be found from a matrix product like ansatz. Using a different description of the two-site blocks by the ansatz

$$|\Psi\rangle^{\mathrm{MPS}} = \prod_{j=-\infty}^{\infty} \sum_{i_1,i_2=0}^{1} A_{i_1 i_2} \, |i_1\rangle_{2j} |i_2\rangle_{2j+1} \,, \tag{11.7}$$

the problems arising from the higher number states are ruled out by definition. With the introduction of the prefactors $A_{i_1 i_2}$ which are chosen to be real[1], we introduce four free parameters which have to be minimized in general. This set of parameters can be reduced by further constraints:

- the norm of the two-site block states needs to be unity

$$A_{00}^2 + A_{10}^2 + A_{01}^2 + A_{11}^2 = 1 \tag{11.8}$$

- the density expectation value for even sites must fulfill equation (10.44)

$$^{\mathrm{MPS}}\langle\Psi|\, \hat{n}_j\, |\Psi\rangle^{\mathrm{MPS}} = A_{10}^2 + A_{11}^2 = \frac{1}{2}\left[1 + \eta_B\right], \tag{11.9}$$

---

[1]A detailed analysis shows that this assumption is justified.

- the density expectation value for odd sites must fulfill equation (10.44), too

$$^{\text{MPS}} \langle \Psi | \, \hat{n}_j \, | \Psi \rangle^{\text{MPS}} = A_{01}^2 + A_{11}^2 = \frac{1}{2} \left[1 - \eta_B \right]. \tag{11.10}$$

This set of equations allows to reduce the complexity. Introducing three sign functions $\alpha, \beta, \gamma = \pm 1$ which are still to be determined, the coefficients have the form

$$A_{01} = \alpha A_- \qquad A_{10} = \beta A_+ \qquad A_{11} = \gamma A_{00} \tag{11.11}$$

with

$$A_\pm = \sqrt{\frac{1}{2}(1 \pm \eta_B) - A_{00}^2}, \tag{11.12}$$

which gives a set of parameters which is more easy to handle. The evaluation of the expectation value of the energy as a function of the remaining free parameters is, with exception of the splitting in even and odd sites, straightforward. The result

$$E[\eta_B, A_{00}, \alpha, \beta, \gamma] = \frac{1}{2}(1 - \eta_B^2) \left[g_0(a) - g_1(a) \right] - \frac{V}{2} \eta_F^a \eta_B - \frac{1}{2} \widetilde{g}_a(\pi) \eta_B^2 - \frac{1}{2} \widetilde{g}_a(0)$$

$$+ 2 g_1(a) A_{00}^2 - 2 \gamma J_B \left[\frac{\alpha \beta}{\gamma} A_+ A_- \left(1 + 2 A_{00}^2 \right) + A_{00}^2 \left(1 - 2 A_{00}^2 \right) \right] \tag{11.13}$$

shows, that the choice $(\alpha, \beta, \gamma) = (1, 1, 1)$ directly minimizes the energy. The remaining free parameters are η_B and A_{00}. For these, a numerical minimization has to be performed. Beforehand, a further look at the second line reveals, that only there A_{00} shows up. Analyzing the dependence of the hopping contribution on A_{00} shows, that it is minimal for $A_{00} = 0$, which means that the state minimizing the energy might have been chosen to be

$$|\Psi\rangle^{\text{MPS}} = \prod_{j=-\infty}^{\infty} \left(A_{10} \, |1\rangle_{2j} \, |0\rangle_{2j+1} + A_{01} \, |0\rangle_{2j} \, |1\rangle_{2j+1} \right) \tag{11.14}$$

from the beginning. This simplification brings the energy functional to its final form, which allows for an easy numerical determination of the minimum:

$$E[\eta_B] = -J_B \sqrt{1 - \eta_B^2} - \frac{V}{2} \eta_F^a \eta_B - \frac{1}{2} \widetilde{g}_a(\pi) \eta_B^2 - \frac{1}{2} \widetilde{g}_a(0).$$
$$+ (1 - \eta_B^2) \left[\frac{1}{2} g_0(a) - \frac{1}{2} g_1(a) \right]. \tag{11.15}$$

For the couplings $g_1(a)$ again a series expansion in a is used:

$$g_1(a) \approx \frac{V^2}{2 J_F \pi^2} \left(0.67492 - 0.11149 \, a - 3.395 \, a^2 + 7.4324 \, a^3 - 5.8053 \, a^4 \right) \tag{11.16}$$
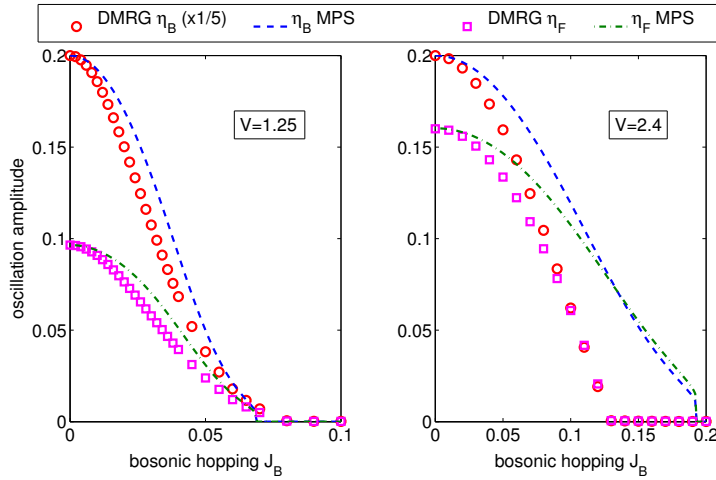
Figure 11.2: Self-consistent determination of the amplitude of the bosonic CDW from the minimization of the energy for the effective Hamiltonian with respect to a matrix product state ansatz. Shown are the same numerical results as for figure 9.5 (left plot, $L = 512$) and results for $V = 2.4$ and $J_F = 10$ (right, $L = 256$). One can see the better quantitative agreement compared to the result for the coherent state in figure 11.1 for small amplitude factor a, i.e., for small interaction V.

The corresponding numerical results for the minimization can be found in figure 11.2. The quantitative agreement is slightly better compared to the coherent state approach for smaller interaction V but still the strong simplification of the ansatz pays its tribute. For larger V, the made matrix product ansatz seems to fail. We believe this to be connected to the increasing induced alternating potential which forsters higher number states. Nevertheless, the two presented self-consistent determinations of the amplitude η_B show that this free parameter in principle may be calculated with more sophisticated ansatzes involving higher number states. As will be seen in the next chapter, an exact calculation of η_B as a function of the bosonic hopping is not of importance however.

Phase diagram of the effective bosonic model

We now use the effective bosonic Hamiltonian

$$\hat{H}_{\mathrm{B}}^{\mathrm{eff}} = -J_B \sum_j \left(\hat{a}_j^\dagger \hat{a}_{j+1} + \hat{a}_{j+1}^\dagger \hat{a}_j \right) + \frac{U}{2} \sum_j \hat{n}_j \left(\hat{n}_j - 1 \right)$$
$$- \bar{\mu} \sum_j \hat{n}_j - \Delta \sum_j \hat{n}_j (-1)^j + \sum_j \sum_d g_d(a)\, \hat{n}_j \hat{n}_{j+d} \quad (12.1)$$

from equation (10.39) to calculate the full phase diagram and compare it to the numerical results from figure 7.3. As a reminder, the potentials $\bar{\mu}$ and Δ are given by

$$\bar{\mu} = 2\varrho_B \widetilde{g}_a(0) - V/2 \qquad\qquad \Delta = 2\varrho_B \eta_B \widetilde{g}_a(\pi) + V\eta_F^a/2. \qquad (12.2)$$

The calculation itself is done in the same way as in part I for the Bose-Fermi-Hubbard model with immobile fermions. The calculation of the incompressible phases is accomplished by calculating the energy of the relevant ground state within the incompressible phase as well as with one particle added or removed. From these energies, the chemical potentials are deduced. In the first section we will restrict ourselves to the zero-hopping limit $J_B = 0$ whereas in the second section we will employ a full degenerate perturbation theory in order to calculate the small J_B behavior of the phases. Concerning the bosonic amplitude η_B it should be mentioned, that both, in the zero hopping limit[1] as well as in the small hopping region, $\eta_B = 1$. In the latter situation this is the case because the perturbation theory starts at $J_B = 0$ and all energies and quantities are to be calculated for this case.

---

[1]Here the amplitude naturally equals one.

12.1 Zero-hopping phase diagram

The calculation of the chemical potentials for $J_B = 0$ is straightforward. Here we only summarize the results; the calculation of some exemplary energies can be found in appendix A.3. We however make some remarks on the nature of the ground state and the notation used.

In the following we deal with states containing a fixed number of particles, or, to be more precise, having a fixed density. For the classification of these states we use a short graphical notation. For instance the ground state of the CDW (with full amplitude) is written as

$$\left| \Psi_{N=L/2} \right\rangle \stackrel{\triangle}{=} \bullet \circ \bullet \circ \| \bullet \| \circ \bullet \circ \bullet, \tag{12.3}$$

where an open circle "$\circ$" means no boson and a filled circle "$\bullet$" means the presence of a boson. This corresponds to the ansatz (10.44) made for the bosonic CDW. With the ansatz (10.44), we explicitly break the symmetry of the system, demanding the bosons to be situated at even sites. This is marked by the introduction of the vertical lines and the boson at site $j = 0$.

For the calculation of the energies we make a suitable ansatz for the sought states and replace the number operators in the Hamiltonian (12.1) by real numbers according to the particular state. This is done for the three incompressible phases presented in figure 7.3 which are at $\varrho_B = 0, \frac{1}{2}, 1$. For each, an exemplary calculation can be found in the appendix A.3. The ansatz in (10.44) together with the bosonic density allows not only for the description of the CDW at half filling with amplitude one ($\varrho_B = \frac{1}{2}, \eta_B = 1$), but also for a possible CDW at unity filling with amplitude two ($\varrho_B = 1, \eta_B = 1$) and a pure Mott insulator ($\varrho_B = 1, \eta_B = 0$).

a) CDW phase $\varrho_B = \frac{1}{2}$

The relevant states for the calculation of the chemical potentials for the upper and the lower boundary of the incompressible CDW region are given for particle numbers $N = L/2 - 1, L/2$ and $L/2 + 1$. For the first two, the ground state can be found easily. Only the case $N = L/2 + 1$ is a bit more complicated.

The energy of the ground state at double half filling, given by the boson distribution shown in (12.3) can be calculated by plugging the density

$n_j = \widetilde{n}_j = \frac{1}{2}\left[1 + (-1)^j\right]$ into the expectation value of the Hamiltonian. This gives

$$E(L/2) = E[\bullet \circ \bullet \circ \,\|\, \bullet \,\|\, \circ \bullet \circ \bullet] = -\frac{1}{2}\bar{\mu}L - \frac{1}{2}\Delta L + \frac{1}{4}L\left[\widetilde{g}_a(0) + \widetilde{g}_a(\pi)\right] \quad (12.4)$$

which naturally depends on the length of the system. But since we are only interested in the chemical potentials

$$\mu_{\frac{1}{2}}^{\pm} = \pm\big(E(L/2 \pm 1) - E(L/2)\big), \quad (12.5)$$

this dependence drops out.

For the calculation of the lower boundary we consider the case of a missing particle. The position, at which the particle is removed, is unimportant, since the system is translationally invariant with a period two. Therefore the energy for this situation is given by

$$\begin{aligned} E(L/2 - 1) &= E[\bullet \circ \bullet \circ \,\|\, \circ \,\|\, \circ \bullet \circ \bullet] && (12.6)\\ &= E[\bullet \circ \bullet \circ \,\|\, \bullet \,\|\, \circ \bullet \circ \bullet] + \bar{\mu} + \Delta - \widetilde{g}_a(0) - \widetilde{g}_a(\pi) + g_0(a) \end{aligned}$$

and the chemical potential for the lower bound results in

$$\mu_{\frac{1}{2}}^{-} = \frac{V}{2} - \frac{V}{2}\eta_F^a - g_0(a). \quad (12.7)$$

As mentioned earlier, we have to choose the amplitude factor $a = \frac{V\eta_B\varrho_B}{2\hbar J_F} = \frac{V\eta_B}{4\hbar J_F}$ for $\eta_B = 1$ and $\varrho_B = \frac{1}{2}$.

The calculation for the upper lobe is a bit more involved, because the suitable ground state is not obvious. Here, two possible situations occur:

$$\bullet \circ \bullet \circ \,\|\, \bullet \,\|\, \bullet \bullet \circ \bullet \qquad \Rightarrow \qquad n_j = \widetilde{n}_j + \delta_{j,1}, \quad (12.8)$$

$$\bullet \circ \bullet \circ \,\|\, \overset{\bullet}{\bullet} \,\|\, \circ \bullet \circ \bullet \qquad \Rightarrow \qquad n_j = \widetilde{n}_j + \delta_{j,0}. \quad (12.9)$$

As shown in appendix A.3, the energies for these two configurations are given by

$$\begin{aligned} E[\bullet \circ \bullet \circ \,\|\, \bullet \,\|\, \bullet \bullet \circ \bullet] &= E[\bullet \circ \bullet \circ \,\|\, \bullet \,\|\, \circ \bullet \circ \bullet] && (12.10)\\ & \quad - \bar{\mu} + \Delta + \widetilde{g}_a(0) - \widetilde{g}_a(\pi) + g_0(a) \end{aligned}$$

and

$$E[\bullet \circ \bullet \circ \| \overset{\bullet}{\bullet} \| \circ \bullet \circ \bullet] = E[\bullet \circ \bullet \circ \| \bullet \| \circ \bullet \circ \bullet] \tag{12.11}$$
$$+ U - \bar{\mu} - \Delta + \widetilde{g}_a(0) + \widetilde{g}_{\bar{a}}(\pi) + g_0(a).$$

From the energy difference

$$E[\bullet \circ \bullet \circ \| \overset{\bullet}{\bullet} \| \circ \bullet \circ \bullet] - E[\bullet \circ \bullet \circ \| \bullet \| \bullet \bullet \circ \bullet] = U - V\eta_F^a, \tag{12.12}$$

a detailed study reveals that for fast fermions ($\frac{V}{J_F} \ll 1$) the ground state is always such that the additional particle goes to an odd site instead to the double occupation. Thus, for the energy equation (12.10) holds and the chemical potential is given by

$$\mu_{\frac{1}{2}}^+ = \frac{V}{2} + \frac{V}{2}\eta_F^a + g_0(a). \tag{12.13}$$

b) Unity filling $\varrho_B = 1$

To calculate the ground state of the Mott insulator with unity filling, there are again two possible states. The easiest choice for the ground state is

$$\bullet \bullet \bullet \bullet \| \bullet \| \bullet \bullet \bullet \bullet \qquad \Rightarrow \qquad n_j = 1, \tag{12.14}$$

which is the typical Mott-insulating ground state ($\eta_B = 0$). However

$$\overset{\bullet}{\bullet} \circ \overset{\bullet}{\bullet} \circ \| \overset{\bullet}{\bullet} \| \circ \overset{\bullet}{\bullet} \circ \overset{\bullet}{\bullet} \qquad \Rightarrow \qquad n_j = 1 + (-1)^j \tag{12.15}$$

($\eta_B = 1$) competes with the Mott state. With the effective Hamiltonian (12.1) for the bosonic density $\varrho_B = 1$, the calculation of the corresponding energies is straightforward. Defining $\bar{a} = \frac{V\eta_B\varrho_B}{2\hbar J_F} = \frac{V\eta_B}{2\hbar J_F} = 2a$, the energies are given by

$$E[\bullet \bullet \bullet \bullet \| \bullet \| \bullet \bullet \bullet \bullet] = L\left[-\bar{\mu} + \widetilde{g}_0(0)\right] \tag{12.16}$$

for the Mott state ($\bar{a} = 0$) and

$$E[\overset{\bullet}{\bullet} \circ \overset{\bullet}{\bullet} \circ \| \overset{\bullet}{\bullet} \| \circ \overset{\bullet}{\bullet} \circ \overset{\bullet}{\bullet}] = L\left[\frac{U}{2} - \bar{\mu} - \Delta + \widetilde{g}_{\bar{a}}(0) + \widetilde{g}_{\bar{a}}(\pi)\right] \tag{12.17}$$

for the CDW of amplitude two ($\eta_B = 1$, $\bar{a} = \frac{V}{2\hbar J_F}$). The decision for the ground state is again made by determining the energy difference

$$E[\overset{\bullet}{\bullet} \circ \overset{\bullet}{\bullet} \circ \| \overset{\bullet}{\bullet} \| \circ \overset{\bullet}{\bullet} \circ \overset{\bullet}{\bullet}] - E[\bullet \bullet \bullet \bullet \| \bullet \| \bullet \bullet \bullet \bullet] = \tag{12.18}$$
$$\frac{U}{2} - \frac{V}{2}\eta_F^{\bar{a}} - \widetilde{g}_{\bar{a}}(0) - \widetilde{g}_{\bar{a}}(\pi) - \widetilde{g}_0(0)$$

which is always positive. This means, that the MI state always has lower energy compared to the double occupied CDW and thus serves as the ground state. Using this result we are able to calculate the energy for the addition or removal of a particle. The actual calculation is again done in the Appendix A.3 with the result

$$E(L \pm 1) = E(L) + \frac{U}{2}(1 \pm 1) \mp \bar{\mu} \mp \Delta \pm 2\widetilde{g}_0(0) + g_0(0). \qquad (12.19)$$

Note that $\eta_B = 0$ and therefore $\Delta = 0$. The chemical potentials

$$\mu_1^\pm = \pm\big(E(L \pm 1) - E(L)\big) \qquad (12.20)$$

are hence given by

$$\mu_1^\pm = \frac{U}{2}(1 \pm 1) + \frac{V}{2} \pm g_0(0), \qquad (12.21)$$

which completes the calculation for unity filling.

c)   Zero filling $\varrho_B = 0$

The discussion for this case is the simplest. For the empty system, the energy is naturally zero, whereas the energy for a single particle described by $n_j = \delta_{j0}$ evaluates straightforwardly as

$$E(1) = \frac{V}{2} + g_0(0). \qquad (12.22)$$

Again the amplitude factor a has to be chosen to be zero since there is no bosonic CDW renormalizing the fermionic system. With this, the chemical potential is given by

$$\mu_0^+ = \frac{V}{2} + g_0(0). \qquad (12.23)$$

d)   Discussion of the phase diagram

Above we derived the chemical potentials for the different incompressible lobes for the effective Hamiltonian given in equation (12.1). These are given by

$$\mu_1^- = \frac{V}{2} - g_0(0), \qquad (12.24)$$

$$\mu_{\frac{1}{2}}^\pm = \frac{V}{2} \pm \frac{V}{2}\eta_F^a \pm g_0(a), \qquad (12.25)$$

$$\mu_0^+ = \frac{V}{2} + g_0(0), \qquad (12.26)$$
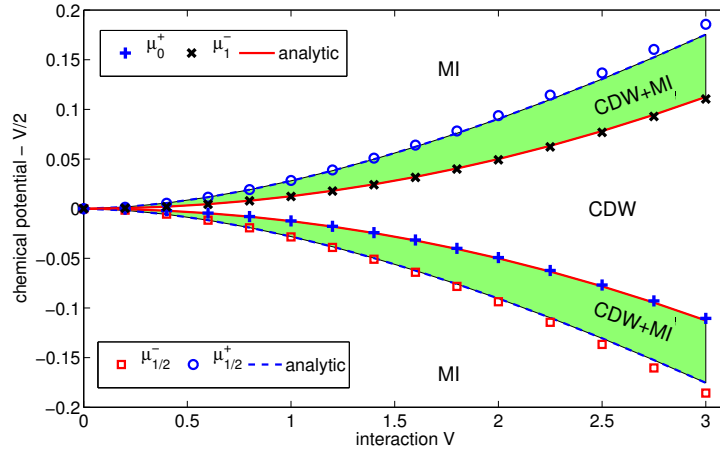
Figure 12.1: Phase diagram of the effective bosonic Hamiltonian for vanishing bosonic hopping $J_B = 0$. Data points are the numerical and the solid lines are the analytic results. The shaded region depicts the region where the extent of the CDW phase overlaps with the Mott insulators giving a phase of coexistence of these two.

which together with the results for the couplings $g_d(a)$ and the fermionic CDW amplitude η_F^a from chapters 9 and 10 allow to construct the phase diagram at zero bosonic hopping. This is shown in figure 12.1, where the chemical potentials are displayed as a function of the interaction V for a fixed fermionic hopping J_F. Note that the chemical potentials $\mu_{\frac{1}{2}}^{\pm}$ for the CDW lobe enclose the chemical potentials μ_0^+ and μ_1^- for the Mott lobes. The shaded region in figure 12.1 depicts exactly this region. This behavior is uncommon, since it indicates a *negative compressibility*

$$\kappa = \frac{\partial \langle \hat{N} \rangle}{\partial \mu_B} < 0. \tag{12.27}$$

Starting with the case of half filling, adding particles will lead to a formation of a spatially connected region of unity filling (for sufficient small hopping). This can be seen as follows: the first additional particle can go to any empty site of the CDW. The next particle will occupy a previously unoccupied site closest to the first additional particle since this requires the lowest energy due to the attractive long-range interaction for even distances. A similar argument can be made for the third particle and so on. Thus, within this region of the (μ_B, J_B)-phase diagram, there is a *phase separation between a Mott insulator and a CDW*. These kind of coexistence phases are not new

(see e.g. [200, 205, 206, 208] for a variety of different coexistence phases), but the coexistence of a Mott insulator and a CDW phase has to our knowledge not been reported before.

The data points are obtained from numerical results, where the Mott insulators are calculated using a finite size extrapolated exact diagonalization and the numerical results for the CDW are resulting from DMRG calculations where the boson distribution is fixed, acting as a potential to the fermions. This procedure is necessary here, since the full DMRG for this system has severe problems in obtaining the proper ground state. The reason for this is on the one hand the sensitivity of the system to the boundary in the open boundary DMRG and on the other hand the problem of seeking the ground state within the energy manifold with many close-lying meta-stable states. This complicates the numerical calculation enormously. A detailed discussion of these issues can be found in the last section of this chapter.

12.2   2nd order strong-coupling theory

After the discussion of the phase diagram for zero hopping $J_B = 0$, showing the existence of phases of coexistence between Mott insulator and CDW, we aim in this section at a perturbation theory in the hopping amplitude J_B to generate the full phase diagram in the $(\mu - J_B)$ plane. Since the methodology of the perturbation theory will also be used in part IV, we restrict ourselves on the presentation of the basic ideas here. The details of the calculation may be found in part IV.

In order to perform a second order perturbation theory we need the energy of the involved ground states as a function of the bosonic hopping J_B. For the states corresponding to the filling of the incompressible phases this is quite easy. In this case, the ground state is non-degenerate and simple perturbation theory is sufficient. When adding or removing a single particle, the ground state is degenerate, since all possible positions of the extra or less particle are allowed[2]. The resulting ground-state manifold consisting of states $|\Psi\rangle_j$[3] requires a non-degenerate perturbation theory, where several equivalent formulations are available as for instance used in [97] for the pure and disordered Bose Hubbard model.

---

[2]The removing is of course only allowed if a particle exists in this site for the ground state.

[3]The index j labels the different states within the manifold. For the Mott insulators, the additional particle is located at the site j, for the CDW phase at site $2j + 1$.

Here we use Kato's expansion [159, 170, 239, 240], which relies on the calculation of an effective Hamiltonian (in arbitrary order) within the degenerate subspace. The last step is to solve this effective Hamiltonian and obtain the ground-state energy as a function of the perturbation parameter. In part I we already made use of this method in the derivation of the effective model for the composite particles according to [121, 158, 160].

Before we discuss the analytic results, we at least outline the used method. Up to second order, Kato's expansion is given by

$$\hat{H}^{\text{eff}} = E_0 + \mathcal{P}\hat{H}_1\mathcal{P} + \mathcal{P}\hat{H}_1\mathcal{Q}\frac{1}{E_0 - \hat{H}_0}\mathcal{Q}\hat{H}_1\mathcal{P}, \qquad (12.28)$$

where $\mathcal{P}$ is the projector onto the degenerate subspace, $\mathcal{Q} = \mathbb{1} - \mathcal{P}$ the orthogonal projector and E_0 is the zero order energy of the manifold. Here, the Hamiltonian is written in the form

$$\hat{H} = \hat{H}_0 + \hat{H}_1, \qquad (12.29)$$

where $\hat{H}_1$ is the perturbation, i.e., the hopping in our case. The calculation of the effective Hamiltonian is now straightforward. The first step is to take any state $|\Psi\rangle_j$ from the degenerate subspace and apply a single hopping operation to this state. Those parts which are still within the subspace (found by the projector $\mathcal{P}$) give a first-order contribution and connect the state $|\Psi\rangle_j$ to the state $|\Psi\rangle_m$; for those outside the manifold (surviving the projector $\mathcal{Q}$) the second order term holds. For this term, the energy resolvent for the intermediate state is evaluated and the final hopping brings the state back to the initial state $|\Psi\rangle_j$, or, if possible, to another state $|\Psi\rangle_k$ within the manifold. Thus the action of the effective Hamiltonian $\hat{H}^{\text{eff}}$ on the state $|\Psi\rangle_j$ has the form

$$\hat{H}^{\text{eff}}|\Psi\rangle_j = E_0(|\Psi\rangle_j) + J_1\left[|\Psi\rangle_{j-1} + |\Psi\rangle_{j+1}\right] + J_2\left[|\Psi\rangle_{j-2} + |\Psi\rangle_{j+2}\right] + W|\Psi\rangle_j. \qquad (12.30)$$

The special form of the perturbation in our case is already taken into account (see part IV for a more general form of the perturbation). This (maximally) tridiagonal matrix representation of the effective Hamiltonian can be solved by a Fourier transform, which gives the energy

$$E = E_0 + 2J_1\cos(2\pi\frac{k}{L}) + 2J_2\cos(4\pi\frac{k}{L}) + W, \qquad (12.31)$$

where the k mode has to be chosen such that the energy is minimal. In this system this is typically the case for $k = 0$ since both $J_1 \sim J_B$ and

$J_2 \sim \frac{J_B^2}{E_0 - \langle \hat{H}_0 \rangle}$ are negative (the energy resolvent for the intermediate state is always negative). This procedure has to be done for all involved ground states with the proper number of particles, i.e., $N = 1, L/2-1, L/2, L/2+1, L-1, L$. The calculation is lengthy and does not provide a deeper insight. Nevertheless we give a graphical representation of the intermediate states as well as the final states in figure 12.2. This gives deeper insight into the possible processes in second order, where inversion symmetric processes are not shown. A crucial point comes from the nature of the effective bosonic Hamiltonian in (12.1). Since the density-density interaction is long ranged, the energy denominator depends on the distance of the particle performing the first hopping process from the reference site where the additional particle (hole) is situated. This needs to be taken into account for the calculation of the chemical potentials.

As a result, we will here only give the chemical potentials for the considered lobes. These are given by

$$\mu_0^+ = \frac{V}{2} + g_0(0) - 2J_B \tag{12.32}$$

$$\mu_{\frac{1}{2}}^- = \frac{V}{2} - \frac{V}{2}\eta_F^a - g_0(a) + 2J_B^2 \left(\frac{1}{V\eta_F^a + 2g_0(a) - 4g_1(a) + 2g_2(a)} \right.$$
$$\left. - \frac{1}{V\eta_F^a + 4g_0(a) - 4g_1(a)} - \sum_{m \text{ even}} \left[\frac{1}{V\eta_F^a + 2g_0(a) - 2g_1(a)} \right. \right. \tag{12.33}$$
$$\left. \left. - \frac{1}{V\eta_F^a + 2g_0(a) - 2g_1(a) + 2g_m(a) - 2g_{m+1}(a)} \right] \right)$$

$$\mu_{\frac{1}{2}}^+ = \frac{V}{2} + \frac{V}{2}\eta_F^a + g_0(a) - 2J_B^2 \left(\frac{4}{U + V\eta_F^a + 4g_0(a) - 4g_1(a)} \right.$$
$$- \frac{1}{V\eta_F^a + 4g_0(a) - 4g_1(a)} + \frac{1}{V\eta_F^a + 2g_0(a) - 4g_1(a) + 2g_2(a)}$$
$$+ \frac{2}{U - V\eta_F^a} - \sum_{m \text{ even}} \left[\frac{1}{V\eta_F^a + 2g_0(a) - 2g_1(a)} \right. \tag{12.34}$$
$$\left. \left. - \frac{1}{V\eta_F^a + 2g_0(a) - 2g_1(a) + 2g_m(a) - 2g_{m-1}(a)} \right] \right)$$

a) $N = 1$

$\circ \circ \circ \circ \,\|\, \bullet \,\|\, \circ \circ \circ \circ \longrightarrow \circ \circ \circ \circ \,\|\, \circ \,\|\, \bullet \circ \circ \circ$

b) $N = L/2 - 1$

c) $N = L/2$

$\bullet \circ \bullet \circ \,\|\, \bullet \,\|\, \circ \bullet \circ \bullet \longrightarrow \bullet \circ \bullet \circ \,\|\, \circ \,\|\, \bullet \bullet \circ \bullet \longrightarrow \bullet \circ \bullet \circ \,\|\, \bullet \,\|\, \circ \bullet \circ \bullet$

d) $N = L/2 + 1$

e) $N = L - 1$

f) $N = L$

$\bullet \bullet \bullet \bullet \,\|\, \bullet \,\|\, \bullet \bullet \bullet \bullet \longrightarrow \bullet \bullet \bullet \bullet \,\|\, \circ \,\|\, \overset{\bullet}{\bullet} \bullet \bullet \bullet \longrightarrow \bullet \bullet \bullet \bullet \,\|\, \bullet \,\|\, \bullet \bullet \bullet \bullet$

Figure 12.2: Visualization of intermediate processes in the derivation of the energy in second order perturbation theory. Double arrows are contributions in first order, the single arrows are the steps in the second order processes.
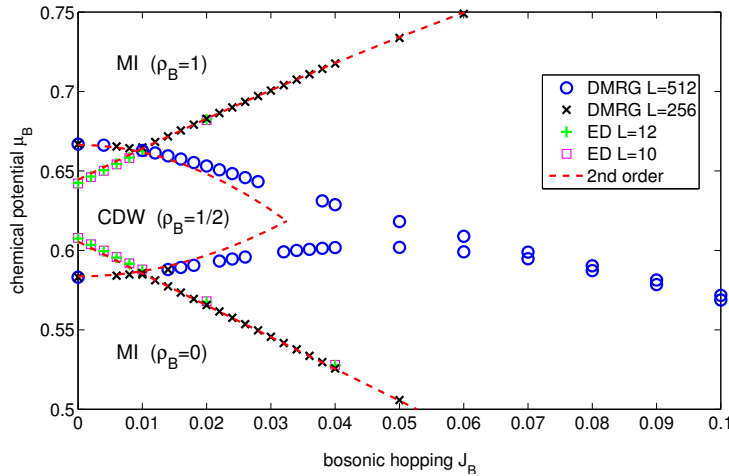
Figure 12.3: Analytic results for the phase diagram together with the numerical results from figure 7.3. The agreement between the analytics and the numerics is quite reasonable with the natural deterioration for larger hopping J_B due to the perturbative treatment. Though the critical point for the vanishing of the CDW lobe is underestimated, the general agreement is quite satisfactory.

$$\mu_1^- = \frac{V}{2} - g_0(0) + 2J_B - 4J_B^2 \left(\frac{1}{U} + \frac{1}{U + 4g_0(0) - 4g_1(0)} \right.$$

$$\left. - \frac{1}{U + 2g_0(0) - 4g_1(0) + 2g_2(0)} + \sum_m \left[\frac{1}{U + 2g_0(0) - 2g_1(0)} \right. \right.$$

$$\left. \left. - \frac{1}{U + 2g_0(0) - 2g_1(0) + 2g_{m+1}(0) - 2g_m(0)} \right] \right) \tag{12.35}$$

A major problem is the aforementioned dependence of the results on all coupling strengths $g_d(a)$, which need to be calculated up to a large distance. For the analytic results used in figure 12.3 it turns out, that $d \approx 100$ is sufficient to gain convergence. A possible series expansion of the summands for the CDW case does not work out because all parts in the denominator are of the same order. Using (12.32)-(12.35) and directly plugging in numbers for the data from figure 7.3 allows for the determination of the behavior of the incompressible lobes. This gives

$$\mu_0^+ = 0.605469 - 2J_B, \tag{12.36}$$

$$\mu_{\frac{1}{2}}^- = 0.583612 + 33.076J_B^2, \tag{12.37}$$

$$\mu_{\frac{1}{2}}^+ = 0.666388 - 45.4392 J_B^2, \tag{12.38}$$

$$\mu_1^- = 0.644531 + 2J_B - 4.12927 J_B^2 \tag{12.39}$$

for the chemical potentials which are shown together with the numerical results in figure 12.3. From the figure it may be seen, that the overall agreement is quite reasonable, whereas the quantitative prediction, especially of the tip of the CDW lobe, is not that satisfying.

12.3 Boundary effects in an effective model with long-range interactions

As already mentioned at several places, boundary effects play an important role in this system. The long-range character of the fermion mediated interactions leads to a substantial modification of the system dynamics even for relatively large systems[4]. This can directly be seen for the case of the CDW phase, where we first discuss the zero hopping case. Assuming the bosons (within the effective Hamiltonian) to be in CDW phase, i.e., half filling, and adding an additional particle to the system, this particle occupies an odd site (i.e., a previously unoccupied site). If the particle would choose the site close to the center of the system, the energy to be paid is $\sum_{d=-L/4}^{L/4} g_{2d+1}$, whereas a particle at the border will only pay the energy $\sum_{d=0}^{L/2} g_{2d+1}$. Remember that all the couplings at odd distances are positive. Because of the decay of the couplings with distance, the first sum is much larger then the latter one, resulting in the particle to pin to the border. Now, with a second additional particle, the same argument holds and the particle also pins to the border. Because of the attractive next-nearest-neighbor interaction, this takes place at a distance of two from the first additional particle as was the case in the infinite system discussed before. This gives a ground state, where a Mott plateau is continuously building up from the boundary, reaching further and further into the CDW phase when adding more particles. As long as the hopping is small compared to the energy difference between the state with a particle pinned close to the border and the state with the additional particle at the center, the reduction of the interaction energy due to the pinning to the boundary dominates the increase of the kinetic energy. When removing a particle from the system, i.e., going below half filling, the same arguments apply.

---

[4]Also the convergence of the DMRG seems to be affected by the boundaries
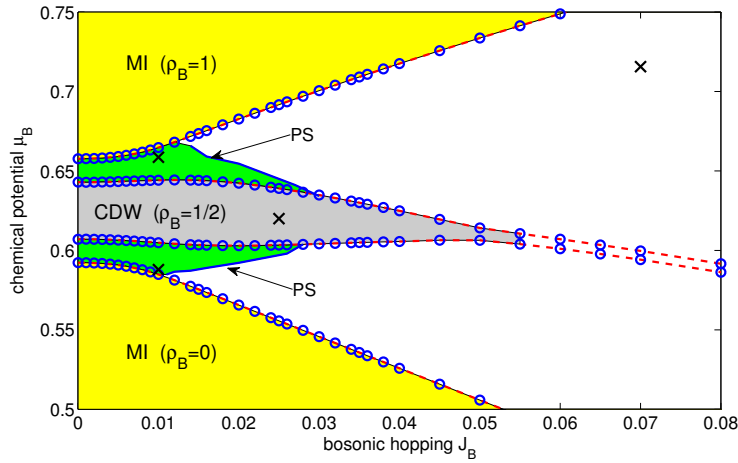
Figure 12.4: Phase diagram of the full Bose-Fermi-Hubbard model with open boundaries. One can see that the lobes bend apart from each other, resulting in an extent region where the CDW and the Mott insulator exist together (filled green region), but with a spatial phase separation (PS). The data are obtained with DMRG and open boundary conditions for a fixed length of $L = 128$ sites. The other parameters are $J_F = 10$ and $V = 1.25$. Black crosses show the points where the density profiles in figure 12.5 are taken from. The dashed lines are to guide the eye.

This means as in the case of an infinite system that there is a region in the (μ_B, J_B)-phase diagram where we have a *phase separation between a Mott insulator and a CDW*. However, the (open) boundary leads to a different dependence of the chemical potential on the particle number. While in the infinite case we found negative compressibility at least in the vicinity of integer or half fillings, this is no longer the case here, where

$$\kappa = \frac{\partial \langle \hat{N} \rangle}{\partial \mu_B} > 0. \tag{12.40}$$

Figure 12.4 shows the DMRG results, where the system is exposed to open boundaries. There it can be seen that all the incompressible lobes bend away different from the analytic results for the infinite case in figure 12.3, not overlapping anymore. For the different phases occurring in this finite size phase diagram, figure 12.5 illustrates the bosonic and fermionic density profile. Figure 12.6 shows a cut along the chemical potential axis for three different, fixed hoppings J_B. From 12.5, the incompressible regions (CDW and Mott insulators) are easily seen while 12.6 clearly shows the
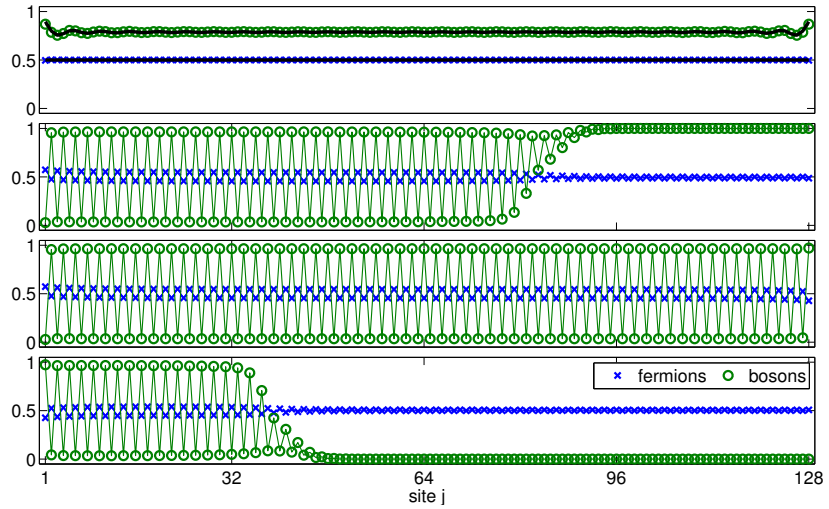
Figure 12.5: Density profile obtained by DMRG for various numbers of particles. From bottom to top: $N_B = 20, 64, 86, 101$ for a system of $L = 128$ sites. The lower three are for $J_B = 0.01$ and the uppermost for $J_B = 0.07$. One can immediately see the pinning of the additional particles to the boundary resulting in a phase separation of Mott insulator and CDW. In the uppermost plot, the fermionic state is roughly given by a homogeneous distribution according to the Friedel oscillations whereas the bosons behave as interacting bosons. This can be seen from the additional solid line which gives the density profile for the same choice of parameters but without interaction, decoupling the bosons and the fermions. The positions of the data set for the density cuts in the phase diagram are depicted by the small marks in figure 12.4.

positive compressibility. Interestingly, in our system the so-called *Devil's staircase* as described in [202, 241, 242] for the case of a dipolar Bose gas with density-density interactions decaying as $g_d \sim \frac{1}{d^3}$ does not exist. Most presumably this is because of the alternating sign in our coupling constants together with the alternating potential, where a detailed discussion of this fact might be an interesting supplement to the present work.

For the infinite size case, the coexistence phase is unstable preferring the CDW state if the chemical potential rather than the particle number is fixed, i.e., for the grand-canonical ensemble. From a canonical point of view, it inherits the phase separation between CDW and Mott insulator, since here the energy is minimal. Thus, in the canonical picture, the phase separation between CDW and Mott insulator is always present with a pinning to the
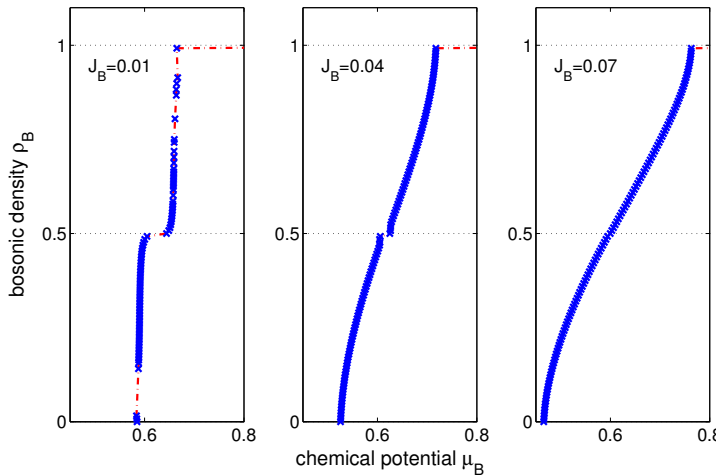
Figure 12.6: Density cut along the chemical potential axis in figure 12.4 for three different bosonic hoppings $J_B = 0.01, 0.04, 0.07$ (from left to right). Shown is the density as a function of the chemical potential. Clearly the CDW and the Mott plateaus are visible, indicated by the extend region of constant filling, where there is no *devil's staircase* as might be expected because of the long-range interactions. For $J_B = 0.01$, some data points are missing due to some convergence problems of the DMRG.

borders for open boundaries. In the treated parameter regime, we did not observe a supersolid phase so far.

For the phase diagram with open boundaries as presented in 12.4, the extend of the phase-separated phase (PS) is sketched without a rigorous numerical analysis for rather small systems. The boundaries are determined from the behavior of the order parameter

$$\mathcal{O} = \sum_j |\langle \hat{m}_j \rangle - \langle \hat{m}_{j+1} \rangle| \,, \tag{12.41}$$

which accounts for the CDW amplitude of the fermionic subsystem. Figure 12.7 shows the behavior of the order parameter as a function of the bosonic hopping for $N_B = 24$ and $L = 64$. The phase boundary is clearly visible from the sharp drop around $J_B = 0.02$. For larger hopping, the system enters a phase where the fermions finally behave as free fermions, i.e., showing a homogeneous density and the bosons have the density profiles according to that of interacting bosons (in the finite system).
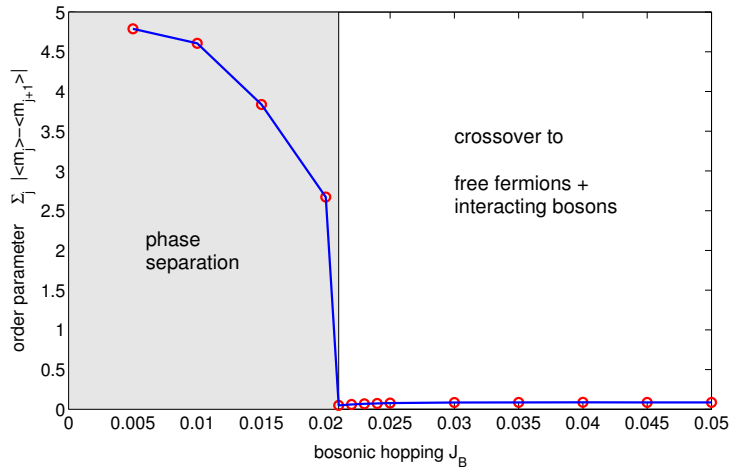
Figure 12.7: Determination of the boundary of the phase separation using the order parameter $\mathcal{O} = \sum_j |\langle \hat{m}_j \rangle - \langle \hat{m}_{j+1} \rangle|$ for open boundary conditions as function of the bosonic hopping. The transition from the phase separation to the crossover regime is seen by the non-analyticity of the order parameter. Data points are obtained for $V = 1.25$, $J_F = 10$ and 24 bosons on 64 sites using DMRG.

Finally, we mention how the DMRG results in figure 7.3 were obtained. As discussed above, the analytic theory relying on the thermodynamic limit forces the additional (less) particle to be added (removed) close to the center. For larger hopping, this state is reproduced by the DMRG, where the overall convergence problem of the method due to the highly degenerate subspace with many close-lying meta-stable states forced us to perform a post-selection of the numerical data. In the figure, only those data points where used, where the numerical results show the additional (less) particle to be situated at the center. This perfectly reproduces the analytic results and is well justified. For small hopping, the DMRG data is replaced by data from exact diagonalization, since here the boundaries become dominant as described above. All described effects were observed numerically even for relatively large system sizes L, indicating the trustworthiness of the analytic results in the thermodynamic limit.

In summary, the derived effective Hamiltonian allows for a full understanding of the physics on the ultrafast-fermion regime.

CHAPTER 13

Conclusion and outlook

The derivation of an effective bosonic Hamiltonian allows for a comprehensive understanding of the bosonic phase diagram in the limit of ultrafast fermions. For double half filling, the physics is dominated by induced long-range density-density interactions alternating in sign, leading to the emergence of a bosonic charge-density wave phase. Divergences arising from the full decoupling of the fermions are overcome by a renormalization scheme which includes the back-action of the bosonic CDW on the fermions. Beyond half filling, the induced interactions lead to thermodynamically unstable regions in the (μ_B, J_B)-phase diagram, displaying coexistence of CDW and Mott insulating phases, i.e., a phase separation between CDW and Mott insulator. Numerical results obtained by DMRG for the full Bose-Fermi-Hubbard model are in a reasonable agreement with our analytic predictions. Application of our effective theory to Bose-Bose of Fermi-Fermi mixtures is straightforward.

Mainly focussing on the study of the incompressible and the phase-separated phases, the nature of the phase transition or crossover for double half filling remains open. Exponentially decaying first-order correlations even beyond the numerically detectable extent of the CDW phase indicate further physical processes in this system for larger bosonic hopping. Here bosonization could give an understanding of the behavior of the correlation functions as well as the nature of the phase transition. Furthermore, the question of supersolidity in the effective model is yet unanswered, where the interplay of the induced potential and the long-range interactions could lead to new effects. Focussing on low densities $\varrho_B < 1$, the nature of the different phases for larger boson densities is not studied so far and should give a variety of further phases.

119

Part III

Nonlinear and multi-band corrections to the single-band Bose-Fermi-Hubbard model

CHAPTER 14

Introduction

Recent experimental results for bosonic atoms in optical lattices [243] revealed that the importance of further contributions in the Hamiltonian beyond the single-band approximation with nearest-neighbor hopping and local two-particle interactions [59]. By means of *quantum phase diffusion*, the value of the two-body interaction U in the Bose-Hubbard model was measured directly. These experiments have also revealed additional three- and four-body interaction constants not occurring in the single-band Bose-Hubbard Hamiltonian. Because of the nature of the continuous Bose-Hubbard Hamiltonian (1.1), these contributions cannot directly when introducing a localized basis. Johnson *et al.* [244] presented a perturbative approach resulting in higher-order interactions. Within this approach, higher Bloch bands are incorporated initially[1] but eliminated. As a consequence, virtual transitions of the bosons lead to new effective many-body interactions.

For the mixture case, the situation is even more involved. After the first experiments on Bose-Fermi mixtures in optical lattices [37, 38] displaying a decrease of the bosonic visibility due to the fermions, the nature of the effect of the fermions to the bosonic superfluid to Mott-insulator transition was discussed controversially. Explanations ranged from localization effects of bosons induced by fermions [38, Mering2008] to heating because of the admixture [37, 247]. Numerical results also predicted an opposite behavior, i.e., the enhancement of bosonic visibility because of fermions [88] with a more detailed discussion in [248]. The situation remained unclear until the systematic study of the dependence of the shift in the bosonic superfluid

---

[1]See for instance [245, 246] for discussions of the physics in the higher bands.

to Mott-insulator transition on the boson-fermion interaction [84] and the subsequent observation of higher-order interactions measured by means of quantum phase diffusion in the mixture. This showed, that higher-band effects need to be taken into account.

The idea of including further contributions to the Hamiltonian coming from higher-band effects can be tackled by two different approaches. In the first approach one assumes that the single-particle Wannier functions are altered due to the fermions and the higher bands [86], which are then calculated from a self-consistent ansatz. The agreement of these results to experiments is very reasonable for repulsive boson-fermion interactions (see [84]), but the method suffers from the fact that it can only be applied to the Mott-insulating state. The second approach, including higher bands in an elimination scheme leading to an effective single-band Hamiltonian [90, 244, 249] is more promising in this sense, but so far did not result in reliable predictions due to the usage of the harmonic oscillator approximation. Further methods including higher-band effects are currently in development such as a multi-band dynamical mean-field theory [250], slave-boson mean-field theory [251] or Gutzwiller approach [252].

Independently to [90, 244, 249] we here develop an adiabatic elimination scheme of the higher Bloch bands, resulting in an effective first-band Hamiltonian. For the renormalized Bose-Hubbard parameters U and J_B, extended by the renormalization due to the fermions, corrections are found in a closed form, including an arbitrary amount of higher bands. All interaction amplitudes are calculated from Wannier functions without approximations such as the harmonic oscillator wavefunctions. Furthermore we found that there are additional corrections resulting from the interaction term in the original continuous Hamiltonian already within the first band. This allows for a direct study of the influence of the interactions on the bosonic superfluid to Mott-insulator transition, both in one and three dimensions.

Derivation of the multi-band Bose-Fermi-Hubbard model

For the derivation of the multi-band Bose-Fermi-Hubbard Hamiltonian we follow the usual route presented in the introduction in chapter 1. In our treatment, the higher bands are incorporated in an adiabatic approximation resulting in a renormalization of the physics in the first band as well as additional nonlinear terms. In this adiabatic elimination, only virtual processes to the empty higher bands are taken into account which corresponds to a second order perturbation theory in the interband coupling. This second order approach is equivalent to the assumption, that higher Bloch bands are uncoupled to each other and it suffices to calculate the effect of an individual band to the renormalization of the first band and finally sum up all higher bands. Thereby, depending on the symmetry, different virtual processes can occur.

Within this approach, the resulting Hamiltonian for the full multi-band Bose-Fermi-Hubbard model takes the form

$$\hat{H} = \hat{H}_1 + \sum_{b=2}^{\infty} \hat{H}_b + \sum_{b=2}^{\infty} \hat{H}_{1b}, \qquad (15.1)$$

where $\hat{H}_1$ is the Hamiltonian of the first band, $\hat{H}_b$ the (free) b-th-band Hamiltonian and $\hat{H}_{1b}$ couples the first band to the b-th band. For a detailed derivation it is convenient to rewrite the continuous Hamiltonian (1.26) for a mix-

ture of bosons and fermions in the form

$$
\hat{\mathcal{H}} = \sum_{X \in \{\mathrm{B,F}\}} \left\{ \int \mathrm{d}z \, \Psi_X^\dagger(z) \left[-\frac{\hbar^2}{2m_X} \Delta + V_{\mathrm{Pot}}^X(z) \right] \Psi_X(z) \right.
$$
$$
\left. + \frac{g_{\mathrm{BX}}}{2} \int \mathrm{d}z \, \Psi_B^\dagger(z) \Psi_X^\dagger(z) \Psi_X(z) \Psi_B(z) \right\}.
$$

(15.2)

The notation with $X \in \{\mathrm{B,F}\}$ denoting the species allows for a simplified treatment of the upcoming algebra. The intra- and interspecies interaction constants are defined as

$$
g_{\mathrm{BB}} = \frac{4\pi\hbar^2}{m_B} \, a_{\mathrm{BB}} \qquad\qquad g_{\mathrm{BF}} = \frac{4\pi\hbar^2}{m_R} \, a_{\mathrm{BF}}
$$

(15.3)

with $m_R = \frac{m_B m_F}{m_B + m_F}$ being the reduced mass and $a_{\mathrm{BB/BF}}$ the intra- and interspecies scattering length, respectively. Whereas in the standard approach the field operators in (15.2) are expanded in terms of Wannier functions for the first band only, we here use an expansion to all orders of higher Bloch bands:

$$
\Psi_X(z) = \sum_{b=1}^{\infty} \sum_j \hat{a}_{b,j}^X \, w_b^X(z - ja).
$$

(15.4)

For the moment we stick with all bands and make a reduction to a single higher band later. a is the lattice spacing of the optical lattice. The operator $\hat{a}_{b,j}^X$ means the annihilation of a particle ($X = B$ a boson and $X = F$ a fermion) in the b-th band on site j and $w_b^X(z - aj)$ is the corresponding Wannier function of the b-th band located at site j.

Using the expansion of the field operator, the full multi-band Bose-Fermi-Hubbard Hamiltonian is given by

$$
\hat{H} = \sum_X \left\{ \sum_{b_1,b_2} \sum_{j_1,j_2} J_{j_1,j_2}^{X;b_1,b_2} \left(\hat{a}_{b_1,j_1}^X \right)^\dagger \hat{a}_{b_2,j_2}^X \right.
$$

(15.5)

$$
\left. + \frac{1}{2} \sum_{b_1,b_2,b_3,b_4} \sum_{j_1,j_2,j_3,j_4} U_{j_1 j_2 j_3 j_4}^{X;b_1 b_2 b_3 b_4} \left(\hat{a}_{b_1,j_1}^B \right)^\dagger \left(\hat{a}_{b_2,j_2}^X \right)^\dagger \hat{a}_{b_3,j_4}^X \hat{a}_{b_4,j_4}^B \right\}.
$$

The generalized hopping amplitude (still containing local contributions)

$$
J_{b_1 b_2}^{X;j_1 j_2} = \int \mathrm{d}z \, \bar{w}_{b_1}^X(z - j_1 a) \left[-\frac{\hbar^2}{2m_X} \Delta + V_{\mathrm{Pot}}^X(z) \right] w_{b_2}^X(z - j_2 a),
$$

(15.6)

and the generalized interaction amplitudes

$$U_{b_1 b_2 b_3 b_4}^{X; j_1 j_2 j_3 j_4} = g_{\mathrm{BX}} \int \mathrm{d}z \, \bar{w}_{b_1}^B (z - j_1 a) \bar{w}_{b_2}^X (z - j_2 a) w_{b_3}^X (z - j_3 a) w_{b_4}^B (z - j_4 a) \quad (15.7)$$

are defined corresponding to the discussion in the introduction in section 1.2. We restrict our model in such a way, that only terms of interest are kept. Furthermore, many of the matrix elements vanish because of the symmetry of the Wannier functions.

15.1 Contributing hopping matrix elements

The generalized hopping amplitude (15.6) incorporates several physical processes. These are the typical intraband hopping processes ($b_1 = b_2$ and $|j_1 - j_2| = 1$) and the energy of the particles within a band ($b_1 = b_2$ and $j_1 - j_2 = 0$). Interband transitions are not present because of the orthogonality of the Bloch functions. This gives, as remaining contributions

a) the band energy

$$\Delta_b^X = \int \mathrm{d}z \, \bar{w}_b^X (z) \left[-\frac{\hbar^2}{2m_X} \Delta + V_{\mathrm{Pot}}^X (z) \right] w_b^X (z), \quad (15.8)$$

b) the intraband nearest-neighbor hopping

$$J_b^X = \int \mathrm{d}z \, \bar{w}_b^X (z - a) \left[-\frac{\hbar^2}{2m_X} \Delta + V_{\mathrm{Pot}}^X (z) \right] w_b^X (z). \quad (15.9)$$

In summary, the part of the multi-band Hamiltonian resulting from the generalized hoppings reads

$$\hat{H} = \sum_{X, j, b} J_b^X \left[\left(\hat{a}_{b,j}^X \right)^\dagger \hat{a}_{b,j+1}^X + \left(\hat{a}_{b,j+1}^X \right)^\dagger \hat{a}_{b,j}^X \right] + \Delta_b^X \left(\hat{a}_{b,j}^X \right)^\dagger \hat{a}_{b,j}^X, \quad (15.10)$$

where hopping between sites with $|j_1 - j_2| = 2$ is omitted since it is small compared to the nearest-neighbor hopping (see figure 1.6). Figure 15.1 shows a graphical representation of the different processes.

15.2 Contributing interaction matrix elements

a) Discussion of the matrix elements

The discussion for the remaining contributions from the interaction term is more involved. This stems on the one hand side from the large number
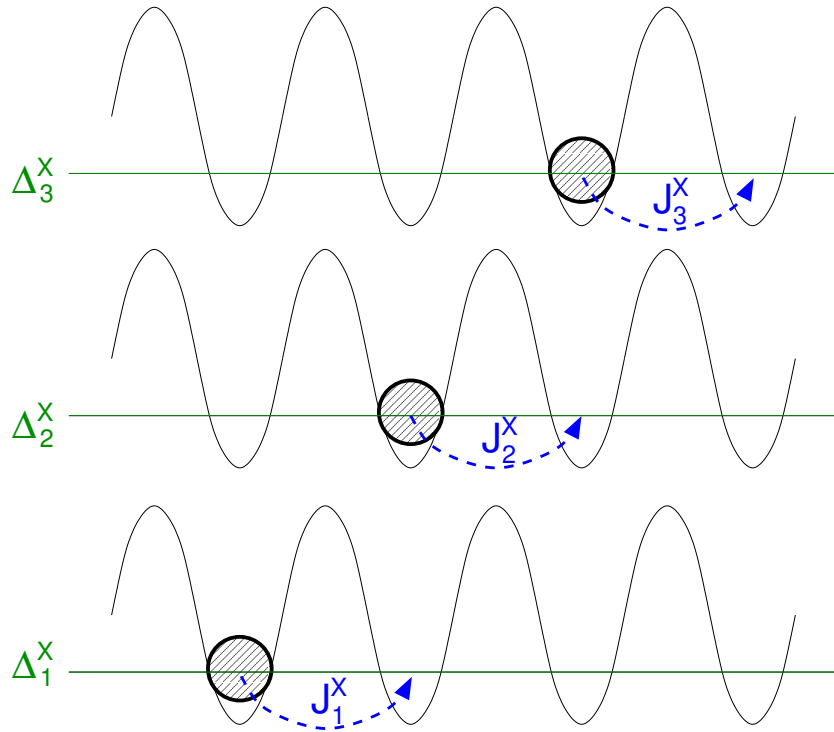
Figure 15.1: Different processes coming from the generalized hopping amplitudes depicted for the first three bands. The shaded circles represent either bosons or fermions with no difference for the Hamiltonian. Δ_b^X is the energy of the b-th band and J_b^X is the intraband nearest-neighbor hopping in the b-th band.

of possible matrix elements and on the other hand from the simplification within our ansatz. The full calculation of the Hamiltonian without these simplifications is of course doable, but due to its complexity the physical processes behind it would become intransparent. To summarize, we calculate the matrix elements in (15.7) with the following assumption:

All *Wannier functions used in* (15.7) *not coming from the first band, have to come from the* **same** *band.*

This assumption assures that the irrelevant (in the sense of the adiabatic elimination) contributions are left out. These are for instance, the density-density interaction between higher bands, transitions between the higher bands and transitions from the first to the b_1-th band together with a transition from the b_2-th to the b_3-th band. All these matrix elements do not contribute in the adiabatic elimination in second order. Additionally,

intraband density-density interactions are neglected for the higher bands.

Performing this analysis, the resulting terms may be grouped as follows, where the pure first-band terms are left out.

One Wannier function from a higher band

For this case, the discussion depends on the band index b. As mentioned earlier, the Wannier function for the first band and all other *odd* bands is axisymmetric and mirror-symmetric for any *even* band. This means, that all matrix elements vanish if the higher band is an even one. For the odd ones, with the shortened definition

$$U^X_{b_1 b_2 b_3 b_4} = g_{\mathrm{BX}} \int \mathrm{d}z \, \bar{w}^B_{b_1}(z) \bar{w}^X_{b_2}(z) w^X_{b_3}(z) w^B_{b_4}(z), \qquad (15.11)$$

the Hamiltonian is given by

$$
\begin{aligned}
\hat{H}^b_{X,1} = \frac{1}{2} \sum_j \Big[& U^X_{b111} \hat{n}^X_1 \left(\hat{a}^B_b\right)^\dagger \hat{a}^B_1 + U^X_{1b11} \hat{n}^B_1 \left(\hat{a}^X_b\right)^\dagger \hat{a}^X_1 \\
& + U^X_{11b1} \left(\hat{a}^X_1\right)^\dagger \hat{a}^X_b \hat{n}^B_1 + U^X_{111b} \left(\hat{a}^B_1\right)^\dagger \hat{a}^B_b \hat{n}^X_1 \Big].
\end{aligned}
\qquad (15.12)
$$

Here we have dropped the site index j from the operators for notational simplicity. All contributions have in common that a single particle makes a transition from the first (the higher) band to the higher (the first) band with another particle being in the lowest band. Note again, that the higher band has to be an odd one.

Two Wannier functions from the higher band

This situation is the most complex since the symmetry of the Wannier functions does not play a role. Altogether, six contributions emerge, for which a detailed discussion can be found in figure 15.2. Using above definition of the interaction constants, the Hamiltonian results in

$$
\begin{aligned}
\hat{H}^b_{X,2} = \frac{1}{2} \sum_j \Big[& U^X_{bb11} \left(\hat{a}^B_b\right)^\dagger \left(\hat{a}^X_b\right)^\dagger \hat{a}^X_1 \hat{a}^B_1 + U^X_{b1b1} \left(\hat{a}^B_b\right)^\dagger \left(\hat{a}^X_1\right)^\dagger \hat{a}^X_b \hat{a}^B_1 \\
& + U^X_{b11b} \hat{n}^X_1 \hat{n}^B_b + U^X_{1bb1} \hat{n}^X_b \hat{n}^B_1 \\
& + U^X_{1b1b} \left(\hat{a}^B_1\right)^\dagger \left(\hat{a}^X_b\right)^\dagger \hat{a}^X_1 \hat{a}^B_b + U^X_{11bb} \left(\hat{a}^B_1\right)^\dagger \left(\hat{a}^X_1\right)^\dagger \hat{a}^X_b \hat{a}^B_b \Big],
\end{aligned}
\qquad (15.13)
$$

where again the site index is dropped. Several of the interaction constants are the same because of symmetry. A detailed discussion of the symmetries will be given later.
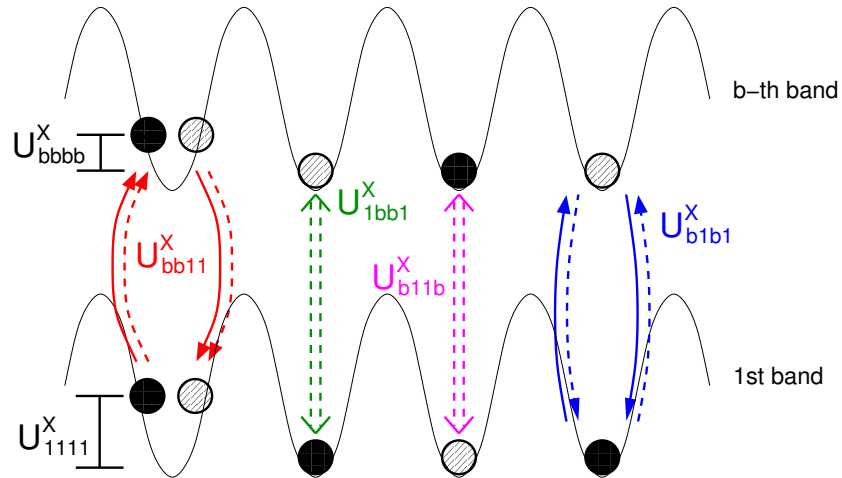
Figure 15.2: Matrix elements for the coupling of any higher Bloch band to the first band via the generalized interaction (15.7) for two Wannier functions from the higher bands. Bosons are shown as filled circles and shaded circles are bosons or fermions depending on X, solid arrows are bosonic processes, dashed arrows are processes corresponding to the species X and double arrows give a density-density interaction. U_{bb11}^X describes the transition of a boson and a X-particle from the first (higher) to the higher (first) band and U_{b1b1}^X gives the transition of a boson from the first (higher) to the higher (first) band together with a transition of a X-particle from the higher (first) band to the first (higher) band. The remaining two U_{b11b}^X and U_{1bb1}^X give density-density interactions between the two bands.

Three Wannier functions from the higher band

Similar to the discussion of a single Wannier function in the higher band, again only odd bands with axis-symmetric Wannier functions contribute. The Hamiltonian is therefore given by

$$\hat{H}_{X,3}^b = \frac{1}{2} \sum_j \left[U_{1bbb}^X \hat{n}_b^X \left(\hat{a}_1^B \right)^\dagger \hat{a}_b^B + U_{b1bb}^X \hat{n}_b^B \left(\hat{a}_1^X \right)^\dagger \hat{a}_b^X \right.$$
$$\left. + U_{bb1b}^X \left(\hat{a}_b^X \right)^\dagger \hat{a}_1^X \hat{n}_b^B + U_{bbb1}^X \left(\hat{a}_b^B \right)^\dagger \hat{a}_1^B \hat{n}_b^X \right]. \tag{15.14}$$

and this completes the derivation of the matrix elements connecting the first band to higher bands. Figure 15.3 shows the corresponding processes for this case together with the results for the case of a single Wannier function in the higher band.
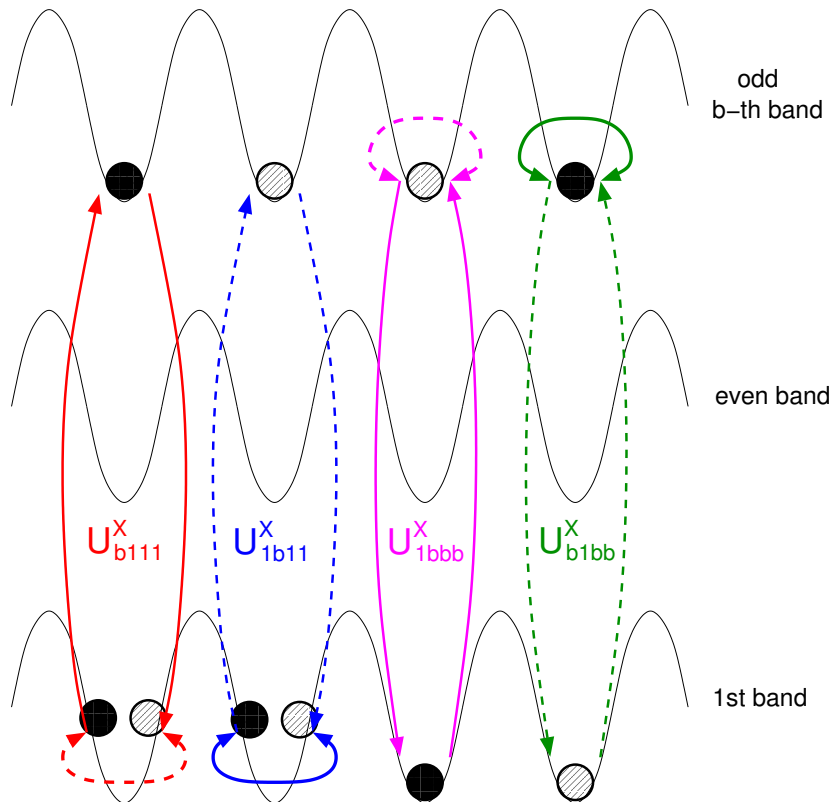
Figure 15.3: Matrix elements for the coupling of the odd higher bands to the first band for one or three Wannier functions from the higher bands via the generalized interaction (15.7). The notation is the same as in figure 15.2. Additionally, the bidirectional arrows are local density contributions as stated in the main text. All processes feature the interband transition of a single particle together with a density interaction, either from the higher or the first band.

b) Complete Hamiltonian for the b-th band from the interaction

Combining all results for the different cases and exploiting the symmetries of the generalized coupling constants, the full Hamiltonian for the coupling of the first to the b-th band is given by

$$
\hat{H}_X^b = \hat{H}_{X,1}^b + \hat{H}_{X,2}^b + \hat{H}_{X,3}^b + \hat{H}_{X,4}^b
$$

$$
= \sum_j \left[\frac{U_{b11b}^X}{2} \hat{n}_{1,j}^X \hat{n}_{b,j}^B + \frac{U_{1bb1}^X}{2} \hat{n}_{b,j}^X \hat{n}_{1,j}^B \right.
$$

$$
+ \frac{U_{bb11}^X}{2} \left(\left(\hat{a}_{b,j}^B\right)^\dagger \left(\hat{a}_{b,j}^X\right)^\dagger \hat{a}_{1,j}^X \hat{a}_{1,j}^B + \left(\hat{a}_{b,j}^B\right)^\dagger \left(\hat{a}_{1,j}^X\right)^\dagger \hat{a}_{b,j}^X \hat{a}_{1,j}^B \right.
$$

$$
\left. \left. + \left(\hat{a}_{1,j}^B\right)^\dagger \left(\hat{a}_{b,j}^X\right)^\dagger \hat{a}_{1,j}^X \hat{a}_{b,j}^B + \left(\hat{a}_{1,j}^B\right)^\dagger \left(\hat{a}_{1,j}^X\right)^\dagger \hat{a}_{b,j}^X \hat{a}_{b,j}^B \right) \right] \Bigg|_{\text{all bands}}
$$

$$
+ \sum_j \left[\frac{U_{b111}^X}{2} \left(\hat{n}_{1,j}^X \left(\hat{a}_{b,j}^B\right)^\dagger \hat{a}_{1,j}^B + \left(\hat{a}_{1,j}^B\right)^\dagger \hat{a}_{b,j}^B \hat{n}_{1,j}^X \right) + \frac{U_{1b11}^X}{2} \left(\hat{n}_{1,j}^B \left(\hat{a}_{b,j}^X\right)^\dagger \hat{a}_{1,j}^X \right. \right.
$$

$$
\left. + \left(\hat{a}_{1,j}^X\right)^\dagger \hat{a}_{b,j}^X \hat{n}_{1,j}^B \right) + \frac{U_{1bbb}^X}{2} \left(\hat{n}_{b,j}^X \left(\hat{a}_{1,j}^B\right)^\dagger \hat{a}_{b,j}^B + \left(\hat{a}_{b,j}^B\right)^\dagger \hat{a}_{1,j}^B \hat{n}_{b,j}^X \right)
$$

$$
\left. \left. + \frac{U_{b1bb}^X}{2} \left(\hat{n}_{b,j}^B \left(\hat{a}_{1,j}^X\right)^\dagger \hat{a}_{b,j}^X + \left(\hat{a}_{b,j}^X\right)^\dagger \hat{a}_{1,j}^X \hat{n}_{b,j}^B \right) \right] \right|_{\text{odd bands}}.
$$

$$\tag{15.15}$$

For the interaction amplitudes, the following symmetry relations hold and have been used:

$$
U_{abcd}^X = U_{dbca}^X = U_{acbd}^X. \tag{15.16}
$$

This results from the structure of the Wannier functions which are real valued.

15.3 Full (relevant) multi-band Bose-Fermi-Hubbard Hamiltonian

With the above results, we are able to pin down the full multi-band Bose-Fermi-Hubbard model. Using $U_{abcd} := U_{abcd}^B$ for the boson-boson interaction and $V_{abcd} = U_{abcd}^F$ for the boson-fermion interaction, the Hamiltonian including the first band as well as all relevant couplings to an arbitrary higher band

is given by

$$\hat{H}_b = \hat{H}_{1\text{st}}^{\text{free}} + \hat{H}_{b\text{th}}^{\text{free}} + \hat{H}_{b\text{th}}^{\text{int, any}} + \hat{H}_{b\text{th}}^{\text{int, odd}} \tag{15.17}$$

with the Hamiltonian of the 1st

$$\begin{aligned}
\hat{H}_{1\text{st}}^{\text{free}} = {}& J_1^B \sum_j \left(\hat{a}_{1,j}^\dagger \hat{a}_{1,j+1} + \hat{a}_{1,j+1}^\dagger \hat{a}_{1,j} \right) + \frac{U_{1111}}{2} \sum_j \hat{n}_{1,j}(\hat{n}_{1,j} - 1) \\
&+ J_1^F \sum_j \left(\hat{c}_{1,j}^\dagger \hat{c}_{1,j+1} + \hat{c}_{1,j+1}^\dagger \hat{c}_{1,j} \right) + \frac{V_{1111}}{2} \sum_j \hat{n}_{1,j} \hat{m}_{1,j} \\
&+ \Delta_1^B \sum_j \hat{n}_{1,j} + \Delta_1^F \sum_j \hat{m}_{1,j}
\end{aligned} \tag{15.18}$$

and the *free* Hamiltonian of the b-th band

$$\begin{aligned}
\hat{H}_{b\text{th}}^{\text{free}} = {}& J_b^B \sum_j \left(\hat{a}_{b,j}^\dagger \hat{a}_{b,j+1} + \hat{a}_{b,j+1}^\dagger \hat{a}_{b,j} \right) + \Delta_b^B \sum_j \hat{n}_{b,j} \\
&+ J_b^F \sum_j \left(\hat{c}_{b,j}^\dagger \hat{c}_{b,j+1} + \hat{c}_{b,j+1}^\dagger \hat{c}_{b,j} \right) + \Delta_b^F \sum_j \hat{m}_{b,j}
\end{aligned} \tag{15.19}$$

whith $b \in 2 \ldots \infty$, the *interaction* Hamiltonian

$$\begin{aligned}
\hat{H}_{b\text{th}}^{\text{int, any}} = {}& \sum_j \frac{U_{bb11}}{2} \left[\left(\hat{a}_{b,j}^\dagger \right)^2 \hat{a}_{1,j}^2 + 4\hat{n}_{b,j}\hat{n}_{1,j} + \left(\hat{a}_{1,j}^\dagger \right)^2 \hat{a}_{b,j}^2 \right] \\
&+ \sum_j \left[\frac{V_{b11b}}{2} \hat{m}_{1,j}\hat{n}_{b,j} + \frac{V_{1bb1}}{2} \hat{m}_{b,j}\hat{n}_{1,j} \right. \\
&\left. \quad + \frac{V_{bb11}}{2} \left(\hat{a}_{b,j}^\dagger \hat{c}_{b,j}^\dagger \hat{c}_{1,j} \hat{a}_{1,j} + \hat{a}_{b,j}^\dagger \hat{c}_{1,j}^\dagger \hat{c}_{b,j} \hat{a}_{1,j} \right.\right. \\
&\left.\left. \qquad + \hat{a}_{1,j}^\dagger \hat{c}_{b,j}^\dagger \hat{c}_{1,j} \hat{a}_{b,j} + \hat{a}_{1,j}^\dagger \hat{c}_{1,j}^\dagger \hat{c}_{b,j} \hat{a}_{b,j} \right) \right]
\end{aligned} \tag{15.20}$$

coupling **any** band and

$$
\begin{aligned}
\hat{H}_{\text{bth}}^{\text{int, odd}} = \sum_j &\left[U_{b111} \left(\hat{n}_{1,j} \hat{a}_{b,j}^\dagger \hat{a}_{1,j} + \hat{a}_{1,j}^\dagger \hat{a}_{b,j} \hat{n}_{1,j} \right) \right. \\
&\left. + U_{1bbb} \left(\hat{n}_{b,j} \hat{a}_{1,j}^\dagger \hat{a}_{b,j} + \hat{a}_{b,j}^\dagger \hat{a}_{1,j} \hat{n}_{b,j} \right) \right] \\
+ \sum_j &\left[\frac{V_{b111}}{2} \hat{m}_{1,j} \left(\hat{a}_{b,j}^\dagger \hat{a}_{1,j} + \hat{a}_{1,j}^\dagger \hat{a}_{b,j} \right) + \frac{V_{1b11}}{2} \hat{n}_{1,j} \left(\hat{c}_{b,j}^\dagger \hat{c}_{1,j} \right. \right. \\
&\left. + \hat{c}_{1,j}^\dagger \hat{c}_{b,j} \right) + \frac{V_{1bbb}}{2} \hat{m}_{b,j} \left(\hat{a}_{1,j}^\dagger \hat{a}_{b,j} + \hat{a}_{b,j}^\dagger \hat{a}_{1,j} \right) \\
&\left. + \frac{V_{b1bb}}{2} \hat{n}_{b,j} \left(\hat{c}_{1,j}^\dagger \hat{c}_{b,j} + \hat{c}_{b,j}^\dagger \hat{c}_{1,j} \right) \right]
\end{aligned}
$$

$$(15.21)$$

coupling only the **odd** bands. For the bosonic interaction amplitudes the additional symmetry relation $U_{abcd} = U_{bacd} = U_{abdc} = U_{adcb} = \dots$ holds. This Hamiltonian now incorporates all relevant terms needed for the derivation of the effective single-band model.

CHAPTER 16

Adiabatic elimination of higher bands and nonlinear corrections

16.1 Adiabatic elimination and effective single-band Hamiltonian

With the full Hamiltonian (15.17), the adiabatic elimination follows the same route as performed in chapter 8 for the case of fast fermions, but, instead of tracing out the fermions, the trace is performed over the higher bands. The Hamiltonian is split up into a free and an interaction part, defined as

$$\hat{H}_b = \hat{H}_{\text{free}} + \hat{H}_{\text{I}} \tag{16.1}$$

with

$$\hat{H}_{\text{free}} = \hat{H}_{\text{1st}}^{\text{free}} + \hat{H}_{b\text{th}}^{\text{free}} \tag{16.2}$$

$$\hat{H}_{\text{I}} = \hat{H}_{b\text{th}}^{\text{int, any}} + \hat{H}_{b\text{th}}^{\text{int, odd}}. \tag{16.3}$$

In the interaction picture, the dynamics of the free part is incorporated by the time dependent interaction Hamiltonian $\hat{H}_{\text{I}}(\tau) = e^{-\frac{i}{\hbar}\hat{H}_{\text{free}}\tau} \; \hat{H}_{\text{I}} \; e^{\frac{i}{\hbar}\hat{H}_{\text{free}}\tau}$ and the scattering matrix of the full system is given by

$$\hat{\mathcal{S}} = \mathcal{T} \exp\left\{ -\frac{i}{\hbar} \int\limits_{-\infty}^{\infty} \mathrm{d}\tau \hat{H}_{\text{I}}(\tau) \right\}. \tag{16.4}$$

Tracing over the higher-band degrees of freedom assuming vacuum in that band and using the cumulant expansion (8.7) up to second order as described

135

in chapter 8, the effective scattering matrix for the lowest band reads

$$
\hat{\mathcal{S}}_{\mathrm{eff}}^{\mathrm{1st}} = \mathcal{T} \exp\left\{ -\frac{i}{\hbar} \int\limits_{-\infty}^{\infty} \mathrm{d}\tau \ \left(-\frac{i}{2\hbar}\right) \int\limits_{-\infty}^{\infty} \mathrm{d}T \ \langle\langle \mathcal{T} \ \hat{H}_{\mathrm{I}}(\tau + T)\hat{H}_{\mathrm{I}}(\tau) \rangle\rangle_{b\mathrm{th}} \right\}.
$$
(16.5)

From the first order in the cumulant expansion no contributions occur since either the number of creation and annihilation operators in the higher band applied on the vacuum state is unequal or the higher band operators are normal ordered.

The calculation of the second order cumulant is rather lengthy and can be found in appendix B.1. Together with a subsequent Markov approximation already used in chapter 8[1], the effective Hamiltonian for the first-band Bose-Fermi-Hubbard model is given by

$$
\begin{aligned}
\hat{H}_{\mathrm{1st}}^{\mathrm{eff}} = \hat{H}_{\mathrm{1st}}^{\mathrm{free}} + \sum_{jd} &\left\{ \frac{U_{bb11}^2 \mathcal{I}_{BB,b}^d}{2} \left(\hat{a}_{j+d}^\dagger\right)^2 \hat{a}_j^2 + \frac{V_{bb11}^2 \mathcal{I}_{BF,b}^d}{4} \ \hat{a}_{j+d}^\dagger \hat{c}_{j+d}^\dagger \hat{c}_j \hat{a}_j \right. \\[2mm]
&+ U_{b111}^2 \mathcal{I}_{B,b}^d \ \hat{a}_{j+d}^\dagger \hat{n}_{j+d} \hat{n}_j \hat{a}_j + \frac{U_{b111} V_{b111} \mathcal{I}_{B,b}^d}{2} \ \hat{m}_{j+d} \hat{a}_{j+d}^\dagger \hat{n}_j \hat{a}_j \\[2mm]
&+ \frac{V_{b111} U_{b111} \mathcal{I}_{B,b}^d}{2} \ \hat{a}_{j+d}^\dagger \hat{n}_{j+d} \hat{m}_j \hat{a}_j + \frac{V_{b111}^2 \mathcal{I}_{B,b}^d}{4} \ \hat{m}_{j+d} \hat{a}_{j+d}^\dagger \hat{m}_j \hat{a}_j \\[2mm]
&\left. + \frac{V_{1b11}^2 \mathcal{I}_{F,b}^d}{4} \ \hat{n}_{j+d} \hat{c}_{j+d}^\dagger \hat{n}_j \hat{c}_j \right\}.
\end{aligned}
$$
(16.6)

Here, explicit distinction between even and odd bands is omitted for notational simplicity. The first two terms account for any band whereas all other terms come into play only for odd bands[2]. In the Hamiltonian, the time integrals over the bosonic and fermionic correlators are defined as

$$
\mathcal{I}_{B,b}^d = -\frac{i}{\hbar} \int\limits_0^\infty \mathrm{d}T \ \mathcal{C}_{B,b}^T(d), \qquad \mathcal{I}_{BB,b}^d = -\frac{i}{\hbar} \int\limits_0^\infty \mathrm{d}T \ \left(\mathcal{C}_{B,b}^T(d)\right)^2, \qquad (16.7)
$$

$$
\mathcal{I}_{F,b}^d = -\frac{i}{\hbar} \int\limits_0^\infty \mathrm{d}T \ \mathcal{C}_{F,b}^T(d), \qquad \mathcal{I}_{BF,b}^d = -\frac{i}{\hbar} \int\limits_0^\infty \mathrm{d}T \ \mathcal{C}_{F,b}^T(d)\mathcal{C}_{B,b}^T(d), \quad (16.8)
$$

---

[1] The Markov approximation here is justified because the absolute value of the hopping amplitudes in the higher bands are larger than in the first band. See [110, 253] and section 1.2 for details.

[2] As a rule of thumb, terms with an odd number of "b"'s in the interaction amplitudes U and V only stem from odd bands.

with

$$\mathcal{C}^T_{B,b}(d) = \langle \hat{a}_{b,j+d}(\tau+T)\hat{a}^\dagger_{b,j}(\tau)\rangle_{b\mathrm{th}}, \qquad \mathcal{C}^T_{F,b}(d) = \langle \hat{c}_{b,j+d}(\tau+T)\hat{c}^\dagger_{b,j}(\tau)\rangle_{b\mathrm{th}}. \tag{16.9}$$

As shown in B.2, these evaluate to

$$\langle \hat{a}_{b,j+d}(\tau+T)\hat{a}^\dagger_{b,j}(\tau)\rangle_{b\mathrm{th}} = \frac{1}{L}\sum_k e^{-2\pi i d\frac{k}{L}} e^{\frac{i}{\hbar}T\varepsilon^{B,b}_k} \tag{16.10}$$

$$\langle \hat{c}_{b,j+d}(\tau+T)\hat{c}^\dagger_{b,j}(\tau)\rangle_{b\mathrm{th}} = \frac{1}{L}\sum_k e^{-2\pi i d\frac{k}{L}} e^{\frac{i}{\hbar}T\varepsilon^{F,b}_k} \tag{16.11}$$

which, together with the time integration, give

$$\mathcal{I}^d_{X,b} = \frac{1}{\pi}\int\limits_0^\pi \mathrm{d}\xi \frac{\cos(d\xi)}{\varepsilon^{X,b}(\xi)} \tag{16.12}$$

$$\mathcal{I}^d_{BX,b} = \frac{1}{\pi^2}\int\limits_0^\pi \mathrm{d}\xi \int\limits_0^\pi \mathrm{d}\xi' \frac{\cos(d\xi)\cos(d\xi')}{\varepsilon^{B,b}(\xi) + \varepsilon^{X,b}(\xi)} \tag{16.13}$$

in the thermodynamic limit[3]. $\varepsilon^{X,b}(\xi) = 2J^X_b\cos(\xi) + \Delta^X_b$ is the energy of a free particle (either bosonic or fermionic) in the higher band and the further details can be found in appendix B.3.

16.2 Nonlinear corrections for the first band

From equation (16.6), the structure of the effective first-band Hamiltonian can be seen. As one can see, for a proper derivation of the effective first-band Hamiltonian, the approximations commonly used for the first-band interaction amplitudes are too stringent and need to be expanded. Since nonlocal density-density interactions and density-mediated hopping processes are a direct consequence of the couplings to higher bands, these should also be included in the pure first-band treatment. Doing so, the generalized interaction (15.7) needs to be extended by terms featuring either a two-particle (equal distance) hopping

$$U^{2d}_{1111}\left(\hat{a}^\dagger_{j+d}\right)^2\hat{a}^2_j, \tag{16.14}$$

$$V^{2d}_{1111}\,\hat{a}^\dagger_{j+d}\hat{c}^\dagger_{j+d}\hat{c}_j\hat{a}_j, \tag{16.15}$$

---

[3]As in part II, the thermodynamic limit is reached for $L \to \infty$ by setting $\xi = \frac{k}{L}$ and changing $\frac{1}{L}\sum_k$ to $\int \mathrm{d}\xi$.

or density mediated hoppings

$$
\begin{aligned}
&U_{1111}^{3d,B} \; \hat{a}_{j+d}^{\dagger} \left(\hat{n}_{j+d} + \hat{n}_j \right) \hat{a}_j, \\
&V_{1111}^{3d,B} \; \hat{a}_{j+d}^{\dagger} \left(\hat{m}_{j+d} + \hat{m}_j \right) \hat{a}_j, \\
&V_{1111}^{3d,F} \; \hat{c}_{j+d}^{\dagger} \left(\hat{n}_{j+d} + \hat{n}_j \right) \hat{c}_j,
\end{aligned}
\tag{16.16}
$$

both for bosons and fermions. The interaction amplitudes are defined via the generalized interaction amplitudes as

$$
\begin{aligned}
U_{1111}^{2d} &= U_{1111}^{B;j+d,j+d,j,j}, \\
V_{1111}^{2d} &= U_{1111}^{F;j+d,j+d,j,j}, \\
U_{1111}^{3d,B} &= U_{1111}^{B;j+d,j+d,j+d,j}, \\
V_{1111}^{3d,B} &= U_{1111}^{F;j+d,j+d,j+d,j}, \\
V_{1111}^{3d,F} &= U_{1111}^{F;j+d,j+d,j,j+d},
\end{aligned}
\tag{16.17}
$$

where the upper index $2d$ ($3d$) denotes two (three) Wannier functions shifted by one lattice site according to (15.7). For the amplitudes, it does not matter whether the two (three) Wannier functions stem from the site $j + d$ or j.

The upcoming contributions to the Hamiltonian are also reported in [254, 255] and in the following will be referred to as nonlinear hopping corrections. They renormalize the single- and two-particle hopping processes and will give a major influence on the location of the phase transition as will be discussed in the following sections.

It should be noted that these terms have been missed out in earlier, non-systematic discussions of higher-band effects [90, 249].

16.3 Full effective single-band Bose-Fermi-Hubbard Hamiltonian

In summary, the full effective Hamiltonian for the first band reduced to hopping contributions and local interactions is given by

$$
\begin{aligned}
\hat{H}^{\mathrm{eff}} = \sum_j & \Big[\frac{U_3}{6} \, \hat{n}_j \left(\hat{n}_j - 1 \right) \left(\hat{n}_j - 2 \right) + \frac{V_3}{2} \, \hat{m}_j \hat{n}_j \left(\hat{n}_j - 1 \right) \\
& + \frac{U_2}{2} \hat{n}_j \left(\hat{n}_j - 1 \right) + V \hat{n}_j \hat{m}_j \Big] \\
& + \sum_j \Delta_1^B \hat{n}_j + \sum_j \sum_{\substack{d=-\infty \\ d \neq 0}}^{\infty} \hat{a}_{j+d}^{\dagger} \, J_B[d; \hat{n}_j, \hat{n}_{j+d}, \hat{m}_j, \hat{m}_{j+d}] \, \hat{a}_j \\
& + \sum_j \Delta_1^F \hat{m}_j + \sum_j \sum_{\substack{d=-\infty \\ d \neq 0}}^{\infty} \hat{c}_{j+d}^{\dagger} \, J_F[d; \hat{n}_j, \hat{n}_{j+d}] \, \hat{c}_j \\
& + \sum_j \sum_{\substack{d=-\infty \\ d \neq 0}}^{\infty} \left[J_B^{(2)}(d) \left(\hat{a}_{j+d}^{\dagger} \right)^2 \hat{a}_j^2 + J_F^{(2)}(d) \, \hat{a}_{j+d}^{\dagger} \hat{c}_{j+d}^{\dagger} \hat{c}_j \hat{a}_j \right] .
\end{aligned}
$$

(16.18)

For a definition of the constants refer to appendix B.4. In comparison to the usual single-band picture, the emergence of some new terms can be seen. The inclusion of the higher bands leads on the one hand to a renormalization of the local interaction amplitudes and on the other hand to (long-range), density mediated hopping processes as well as correlated two-particle tunneling. Most prominent is the appearance of the three-body interaction U_3 which has been measured experimentally recently by means of quantum phase diffusion [243]. Using the method for the calculation of the Wannier functions presented in the next chapter, the value of U_3 turns out to be of the same sign as seen in the experiments (and analytic theory in [244] using the harmonic oscillator approximation), whereas the ratio U_3/U_2 is only correct up to an order of magnitude. This is not surprising, since there are further contributions of higher order in the interband coupling not included in our second-order approach. Nevertheless, the accordance of this simple quantity already shows that our used method allow for a proper description of the influence of the higher bands.

In order to discuss the phase transition of the bosonic subsystem, we furthermore reduce the Hamiltonian to the relevant parts. These are, compared to the pure single-band nonlinear Bose-Hubbard model the on-site

interaction as well as the nearest-neighbor hopping. We start our discussion coming from the Mott insulator, thus the local number of particles is approximately given by the integer filling of the system, i.e., $\langle \hat{n}_j \rangle \approx n$. This is used to replace the number operators in the hopping terms by the filling n, giving a reasonable approximation for the calculation of the renormalized hoppings. For the fermionic species, we also replace the number operator by the fermionic filling $\hat{m}_j \rightarrow m = 1$, assuming a homogeneous filling of the fermions in the lattice. Having an experimental realization with cold atoms in mind, this specific case is a valid assumption in the center of the harmonic trap at least for attractive inter-species interactions. It should be valid however also for sufficiently small inter-species repulsion. This assumption is also supported by the results from [84], where the fermionic density did not influence the transition from a Mott-insulator to a superfluid (for medium and large filling). It also agrees with the result in [86] which is based on this assumption, showing a good agreement to the experimental results. All further contributions in the Hamiltonian as the three-particle interaction and two-particle hoppings are neglected in the following.

With these approximations, the renormalized Bose-Hubbard Hamiltonian is given by

$$\hat{H}^{\text{eff}} = -J[n,m] \sum_j \left(\hat{a}_j^\dagger \hat{a}_{j+1} + \hat{a}_{j+1}^\dagger \hat{a}_j \right) + \frac{U[n,m]}{2} \sum_j \hat{n}_j \left(\hat{n}_j - 1 \right) \quad (16.19)$$

with

$$J[n,m] = J_1^B + 2n \frac{U_{1111}^{3d,B}}{2} + 2m \frac{V_{1111}^{3d,B}}{2} \quad (16.20)$$
$$+ \sum_{\substack{b>1 \\ b \text{ odd}}} \mathcal{I}_{B,b}^1 \left[U_{b111}^2 \, n^2 + 2 \frac{U_{b111} V_{b111}}{2} \, nm + \frac{V_{b111}^2}{4} m^2 \right]$$

$$U[n,m] = U_{1111} + \sum_{b>1} U_{bb11}^2 \mathcal{I}_{BB,b}^0 + \sum_{\substack{b>1 \\ b \text{ odd}}} 2 \, U_{b111}^2 \mathcal{I}_{B,b}^0 \quad (16.21)$$

$$+ m \sum_{\substack{b>1 \\ b \text{ odd}}} \left[2 \, U_{b111} V_{b111} \mathcal{I}_{B,b}^0 + \frac{V_{1b11}^2 \mathcal{I}_{F,b}^0}{2} \right]$$

For the correlator integrals $\mathcal{I}_{X,b}^0$ and $\mathcal{I}_{X,b}^1$, equation (16.12), simple expressions

can be found:

$$\begin{aligned}
\mathcal{I}_{X,b}^0 &= \frac{1}{\sqrt{(\Delta_b^X)^2 - (2J_b^X)^2}} \\
\mathcal{I}_{X,b}^1 &= \frac{1}{2J_b^X \left(1 - \Delta_b^X \mathcal{I}_{X,b}^0\right)}.
\end{aligned} \tag{16.22}$$

This Hamiltonian serves as the starting point for the discussion of the influence of the boson-fermion interaction on the Mott-insulator to superfluid transition as studied in the experiments in [37, 38, 84]. This will be done after a short summary of the relevant experimental parameters and their implications on the discussions so far.

Real (experimental) parameters

17.1 Optical lattice effects

With the knowledge of the full form of the effective first-band Hamiltonian, the next step is to calculate the Wannier functions and the interaction amplitudes. In the introduction 1.2 we showed, how the Wannier functions are calculated for the optical lattice. For the mixture case, another important effect needs to be taken into account. Since the optical lattice is generated by an off-resonant standing laser field, the potential itself results from the ac-Stark shift. As shown in [13, 91] the potential induced by the Stark shift is given by

$$V_{\text{pot}}(\mathbf{r}) = \frac{3\pi c^2}{2\omega_0^3} \frac{\Gamma}{\Delta} \, I(\mathbf{r}) \qquad (17.1)$$

for a single line. If the laser field couples to more lines but is sufficiently detuned from each one, the potential may be calculated by the independent sum of the contributions from each of these lines. For typical alkali atoms Li, Rb and K, the most dominant contribution comes from the coupling to the D-line doublet. Thus, the potential is given by [91]

$$V_{\text{pot}}(\mathbf{r}) = \frac{3\pi c^2}{2} \left(\frac{\Gamma_{D_1}}{\omega_{0,D_1}^3 \Delta_{D_1}} + \frac{2\Gamma_{D_2}}{\omega_{0,D_2}^3 \Delta_{D_2}} \right) \, I(\mathbf{r}) \qquad (17.2)$$

and depends on the properties of the D_1 and D_2 lines. These are the decay rates $\Gamma_{D_{1,2}}$ of the excited states, $\Delta_{D_{1,2}} = \omega_{\text{laser}} - \omega_{0,D_{1,2}}$ the detunings of the laser frequency ω_{laser} from the atomic transition frequencies $\omega_{0,D_{1,2}}$ and $I(\mathbf{r}) = I_0 \, \sin^2(\mathbf{kr})$ the laser intensity. Since for different

atomic species (in general even for different isotopes but here the effect is marginal), the atomic transition frequencies differ, i.e., all species in the optical setup experience different amplitudes of the optical lattices[1]. This influences the Wannier functions which we take into account in the following.

Conveniently, all energies in the system are normalized to the so-called recoil energy, which is defined as the change in kinetic energy of an atom upon absorption of a photon from the optical lattice laser. In our case, we normalize to the recoil energy of the bosonic species, given by

$$E^B_{\text{rec}} = \frac{\hbar^2 k^2}{2 m_B},$$ (17.3)

with the wavenumber k of the optical lattice. It is useful to rewrite the optical lattice potential for the fermionic atoms with respect to the bosonic optical lattice. Following the notation in [110], the optical lattice potential for the second (fermionic) species is written in the form

$$V^F_{\text{pot}}(\mathbf{r}) = \eta_F \, \sin^2(\mathbf{kr})$$ (17.4)

where $\eta_F = \frac{3\pi c^2}{2} \left(\frac{\Gamma^F_{D_1}}{\left(\omega^F_{0,D_1}\right)^3 \Delta^F_{D_1}} + \frac{2\Gamma^F_{D_2}}{\left(\omega^F_{0,D_2}\right)^3 \Delta^F_{D_2}} \right) I_0$. The definition of the amplitude η_F allows for an easy connection of the fermionic potential to the bosonic one as

$$\eta_F = \frac{\dfrac{\Gamma^F_{D_1}}{\left(\omega^F_{0,D_1}\right)^3 \Delta^F_{D_1}} + \dfrac{2\Gamma^F_{D_2}}{\left(\omega^F_{0,D_2}\right)^3 \Delta^F_{D_2}}}{\dfrac{\Gamma^B_{D_1}}{\left(\omega^B_{0,D_1}\right)^3 \Delta^B_{D_1}} + \dfrac{2\Gamma^B_{D_2}}{\left(\omega^B_{0,D_2}\right)^3 \Delta^B_{D_2}}} \, \eta_B = \widetilde{f} \, \eta_B.$$ (17.5)

The prefactor $\widetilde{f}$ connects the bosonic and fermionic potential depth. For the calculation of the prefactor, the values for the different atomic species can be found for typical isotopes in [256, 257, 258] or at the NIST[2] homepage [259].

For the calculation of the Wannier functions for the fermions using the Schrödinger equation

$$\left[-\frac{\hbar^2}{2 m_F} \Delta + \eta_F \, \sin^2(\mathbf{kr}) \right] \, \Phi(\mathbf{r}) = E \, \Phi(\mathbf{r}),$$ (17.6)

---

[1]If the one species is red, the other species blue detuned, the two species do not just experience different amplitudes but also different positions of the minima of the potential.

[2]National Institute of Standards and Technology

the normalization to the bosonic recoil energy leads to additional factors which originate from the mass difference. This gives the fermionic Schrödinger equation

$$\left[-\frac{\hbar^2}{2m_B}\Delta + \frac{m_F}{m_B}\widetilde{f}\ \eta_B\ \sin^2(\mathbf{kr})\right]\ \Phi(\mathbf{r}) = \frac{m_F}{m_B}E\ \Phi(\mathbf{r}). \qquad (17.7)$$

Note, that the depth of the optical lattice potential for the fermions is altered by a prefactor $\frac{m_F}{m_B}\widetilde{f}$ compared to the bosonic one and the energy of the fermionic system is altered by $\frac{m_F}{m_B}$. This factor in the energy demands a careful treatment of the intraband hopping J_b^F and the band energy Δ_b^F. For a fixed amplitude η of an optical lattice (in units of the recoil energy[3]), they are given by the Fourier transform of the energy dispersion respectively the mean value as shown in section 1.2. This gives

$$J_b = \frac{1}{2}\int_{-1}^{1} \mathrm{d}p\ E_b(p)\ e^{-i\pi p} \qquad\qquad \Delta_b = \frac{1}{2}\int_{-1}^{1} \mathrm{d}p\ E_b(p), \qquad (17.8)$$

where $E_b(p)$ is the dispersion of the b-th band. For the calculation of the energy dispersion, the free Hamiltonian (17.6) was normalized to the recoil energy, giving, for the fermionic species, the hopping and the band energy with respect to the fermionic recoil energy. In bosonic units, the factor

$$\frac{E_{rec}^F}{E_{rec}^B} = \frac{m_B}{m_F} \qquad\qquad (17.9)$$

needs to be included, giving the dependence of the hopping and the band energy as a function of η_B (by using the prefactor $\widetilde{f}\frac{m_F}{m_B}$) in units of the bosonic recoil energy.

At this point, we specify the experimental system. In the following, we analyze the experiment reported in [84] and use the parameters given there. The experiment treats the visibility of the bosonic cloud in the optical lattice as a function of the boson-fermion scattering length a_{BF} tuned by a Feshbach resonance [13, 260, 261]. A mixture of bosonic ^{87}Rb and fermionic ^{40}K is cooled and put into an optical lattice with $\lambda_L = 755$ nm. For Rubidium [258] and Potassium [259, 262], the transition wavelengths and decay rates

---

[3]Here we discuss the general case and therefore remove any index B or F.

are given by

$$
\begin{array}{ll}
\lambda_{D_1}^{K} = 766.5 \text{ nm} & \lambda_{D_1}^{Rb} = 795.0 \text{ nm} \\[4pt]
\Gamma_{D_1}^{K} = 38.7 \times 10^6 \text{ Hz} & \Gamma_{D_1}^{Rb} = 36.1 \times 10^6 \text{ Hz} \\[4pt]
\lambda_{D_2}^{K} = 769.9 \text{ nm} & \lambda_{D_2}^{Rb} = 780.2 \text{ nm} \\[4pt]
\Gamma_{D_2}^{K} = 38.2 \times 10^6 \text{ Hz} & \Gamma_{D_2}^{Rb} = 38.1 \times 10^6 \text{ Hz}.
\end{array}
\tag{17.10}
$$

Using these values the prefactor $\widetilde{f}$ in equation (17.5) evaluates to

$$
\widetilde{f} = 2.04043,
\tag{17.11}
$$

which means, that the fermionic lattice potential, in terms of the bosonic recoil energy is twice as deep as the bosonic one. Nevertheless it should be noted that the fermionic lattice potential normalized to the fermionic recoil energy is roughly the same as the bosonic potential normalized to the bosonic recoil energy as stated in [84], since

$$
\frac{E_{rec}^{F}}{E_{rec}^{B}} = \frac{m_B}{m_F} = 2.175
\tag{17.12}
$$

which almost compensates $\widetilde{f}$ in (17.7). Nevertheless, the mass factor persists in the hopping and the band energy when normalizing the fermionic quantities to the bosonic recoil energy. In [84] it is stated, that the wavelength of the optical lattice is chosen such that the overlap between the bosonic and fermionic Wannier functions is maximal. To a good approximation, this is reached as $\frac{m_F}{m_B}\widetilde{f} = 0.93$. In the following we assume a perfect matching of the Wannier functions which only leaves a difference between the bosons and the fermions in the hopping and the band energies as stated above. This, in particular, has the consequence, that the bosonic and fermionic interaction integrals are equal apart from the prefactor g_{BX}. Along with the results for perfect matching, we shortly discuss the influence of a small deviation of the potential depth for the different species.

17.2   Dimensional effects

The derivation of the effective first-band Hamiltonian in chapter 16 relies on one important restriction: a one-dimensional lattice setup. In one dimension, the atomic interaction is different from the three-dimensional case and demands an effective description, relating the *real* three-dimensional (which we will always refer to) scattering amplitude g_{BX} to their one-dimensional

counterpart. Under the assumption of a three-dimensional gas in a strong cigar-shaped trap, Olshanii derived the effective one-dimensional scattering amplitude [263] for a point like interaction between two atoms. With a strong confinement of the atomic cloud in the transversal direction given by $\omega_\perp \gg \omega_\parallel$, the effective one-dimensional scattering amplitude g_{1D} for a two-particle interaction[4] results in

$$g_{1D} = \frac{g_{3D}}{\pi l_\perp^2} \frac{1}{1 + \zeta(\frac{1}{2}) \frac{a_{3D}}{l_\perp}}.$$ (17.13)

$g_{3D} = \frac{2\pi\hbar^2}{m_R} a_{3D}$ is the scattering amplitude, m_R is the reduced mass of the scattering partners, a_{3D} is the scattering length for the treated scattering process in three dimensions and $\zeta(x)$ is the Riemann-Zeta function. Because of the strong harmonic confinement in the transversal direction, the value of the oscillator length $l_\perp = \sqrt{\frac{\hbar}{\mu \omega_\perp}}$ is of major importance. The transversal trap frequency is typically in the range of some kHz [63, 264, 265] depending on the actual realization of the trap. In the following we use the value of $\omega_\perp \approx 80$kHz given in [264].

For the calculation of the one-dimensional scattering amplitude, the last missing ingredient is the three-dimensional scattering length. For the Rb-Rb interaction, the experimental (background) scattering length is measured to be $a_{87\text{Rb}} = a_{BB} = 108\, a_0$, with the Bohr radius $a_0 = 0.053$nm [266]. The boson-fermion scattering length a_{BF} from now on serves as a free, tunable parameter, used to study the influence of the fermions to the bosonic superfluid to Mott-insulator transition. The background value and reference point for the mixture of ^{87}Rb and ^{40}K is $a_{BF} = -205\, a_0$, i.e., is attractive [37, 38].

In the derivation of the effective one-dimensional scattering amplitude g_{1D} it is assumed, that the two particles which scatter experience the same transversal confinement. For a homonuclear scattering process, this is true. For the heterogeneous scattering between bosons and fermions, this does not necessarily hold. But usually, the cigar-shaped optical potential is created by a strong far off-resonant dipole trap. The large detuning to both, bosons and fermions then leads roughly to the same transversal confinement for both species. This is seen in our situation by comparing the intensities of the optical dipole trap, calculated using equation (17.5) for a typical laser setup with $\lambda_{\text{dipole}} = 1030\ nm$. The prefactor $\widetilde{f} \approx 0.9$ turns out to be close to

---

[4]Here we omit the index X since the discussion does not depend on it.

	$n = 1$	$n = 2$	$n = 3$	$n = 4$
$1D$	4.65	7.86	11.04	14.23
$3D$	29.34	49.83	70.11	90.32

Table 17.1: Critical ratio U/J in the Bose-Hubbard model for the Mott-insulator to superfluid transition in one and three dimensions. $1D$: results from strong-coupling theory [97]. $3D$: For the first lobe, the exact quantum monte-carlo result from [267] is used. For the higher lobes, analytic field theory results from [173] are used. For details see the main text.

unity and therefore, both species are attributed to the same dipole trapping geometry and the assumptions in the derivation of the scattering strength are valid even in the mixture case.

17.3   Bose-Hubbard phase transition

Before we discus the net effect of the fermions, the higher bands and nonlinear hopping corrections on the phase diagram of the Bose-Hubbard model, we shortly summarize the results for the Mott-insulator to superfluid transition in the pure bosonic system. This serves as an example which shows how to calculate the transition point of the phase transition and gives the starting point for the analysis of the shift of the transition as a function of the boson-fermion scattering length a_{BF}.

The key feature for the determination of the Mott-insulator to superfluid transition is the ratio of interaction to kinetic energy, U/J. Several analytic [14, 97, 170, 173, 181, 240] and numerical [183, 211, 267] results for this transition exist, with slight deviations coming from the different methods but all are in good agreement with each other. For the experiments, the transition is found by calculating the interaction amplitude U and the hopping amplitude J as a function of the optical lattice depth η and seek for the value of η, at which the ratio U/J equals the analytic or numeric results for the transition point for a fixed filling n. Here we make use of the strong-coupling results from [97] in one dimension as well as a combination
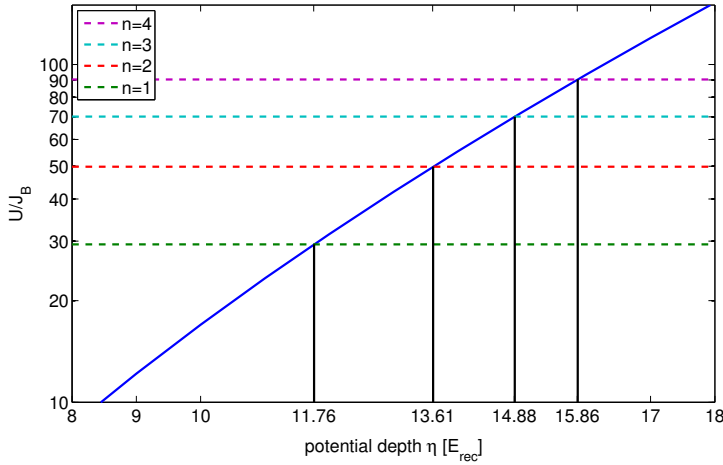
Figure 17.1: Ratio U/J as a function of the optical lattice depth for a three-dimensional setup. The critical point, where the Mott-insulator to superfluid transition occurs is found at the place, where U/J reaches the critical value determined by numerical or analytic methods. Also shown are the transition points for the first four Mott lobes.

of the analytic results from [173] and the numerical ones from [267] in three dimension. Table 17.1 shows a list of the transition points in one and three dimensions. For three dimensions, the critical ratio for $n = 1$ lobe is taken from the high precision quantum monte-carlo result in [267]. The other lobes are calculated with the analytic result in [173], where the overestimation from the approximative field theory of about 3% for the first lobe is also substracted from the analytic results for the higher lobes. These values are in good agreement with the numerical results from [170] and are preferable to be used because they are given in a closed analytic form.

Figure 17.1 shows how the transition point is determined as a function of the lattice depth η as described in [15]. Plotting the ratio U/J as a function of η, the crossing point of this ratio with the calculated transition points from table 17.1 gives the position of the Mott-insulator to superfluid transition for the different Mott lobes. For the pure Bose-Hubbard model plotted in figure 17.1, this prediction is in reasonable agreement with the experimental result of $\eta_{\text{crit}} \approx 12.5 \ E_{rec}$ [15]. Using this method, the influence of the different corrections to the pure Bose-Hubbard model is studied in the next chapter.

CHAPTER 18

Evaluation of the extensions to the Bose-Hubbard model

The derivation of the corrections to both the bosonic interaction U and the hopping J presented in chapter 16 together with the discussion of the real experimental parameters in chapter 17 brings us to the point, where their influence on the bosonic Mott-insulator to superfluid transition can be studied in depth. According to the experimental results presented in [84], we consider the shift of the bosonic transition as a function of the boson-fermion interaction determined by the scattering length a_{BF}. The results from [84] are shown in figure 18.1, together with theoretical predictions from [86] calculated numerically from a self-consistent approach. Although the predictions from Lühmann *et al.* are in good agreement with the experimental results, the applied method uses a completely different approach which might have some drawbacks. Their point of view, as well as used by other authors [268, 269, 270, 271] is, that the description of the system in terms of single-particle Wannier functions is not suitable. This basically leads to the alteration of the Wannier function itself. With these renormalized Wannier functions, the system is reconsidered, giving a new estimate for the transition point. An essential drawback of the self-consistent approach is that it can be applied only to integer filling, while our treatment is in principal general. Furthermore, the self-consistent approach does not provide a satisfactory explanation of the physics for repulsive boson-fermion interaction.

As described earlier, our approach relies on the assumption that the effects of the higher bands do not alter the Wannier functions but renormalize
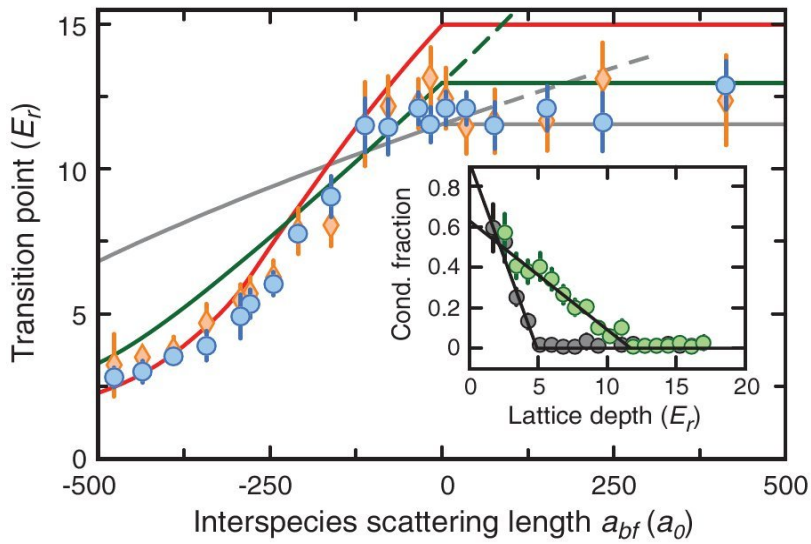
Figure 18.1: Experimental results for the shift of the bosonic Mott-insulator to superfluid transition taken from [84]. Data points (blue and yellow) are from the same experiment with different fermion numbers, the lines are various theoretical predictions. For details see [84] and [86].

the parameters in the Hamiltonian itself and provide new nonlinear terms. This approach is similar to the one chosen in Ref. [90, 244, 249]. The main difference between our approach and the mentioned works is, that all three rely on the harmonic oscillator assumption. Furthermore, they restrict themselves to a rather small number of higher bands. Though these assumptions easily allow to apply the higher-band corrections to dimensions larger than one, they are inaccurate when comparing to the experimental results as the correct form of the Wannier functions is important as demonstrated in this chapter. For instance, the ground state of a harmonic oscillator is a strictly positive function, while the Wannier function in the lowest band has small negative parts with a sizeable effect on overlap integrals involving Wannier functions of different sites. Finally, nonlinear hopping corrections have been neglected in [90, 244, 249] which play an important role however.

After these initial comments, we first discuss our results for one dimension and afterward give some preliminary results for three dimensions.

18.1 One-dimensional lattice

Hamiltonian (16.19) describes both the nonlinear corrections and the effects from the higher bands. Using the dependence of the hopping amplitudes and the interaction amplitudes on the boson-fermion scattering length, the influence on the phase transition is studied. Figure 18.2 shows, how the ratio U/J changes upon inclusion of the different corrections. Shown is the ratio as a function of the lattice depth η for four different situations:

- pure bosonic
  From the definition of the plain Bose-Hubbard Hamiltonian, the interaction and hopping amplitudes are calculated using the real Wannier functions[1]

- nonlinear bosonic
  Beside the plain amplitudes, the nonlinear corrections are taken into account. For repulsive bosons, the net effect is an increase of the hopping amplitude and therefore a shift of the transition to higher lattice depths.

- nonlinear bosonic with bands
  An additional inclusion of the band effects leads dominantly to an increase of the interaction amplitude together with a slight decrease of the hopping resulting in a reduction of the transition point compared to the nonlinear case. This defines the transition point in the pure bosonic system for the study of the influence of the fermions.

- nonlinear bosonic and fermionic with bands
  The addition of the (attractively interacting) fermions with unity filling leads to a slight reduction of the interaction amplitude and a (relatively) large reduction of the hopping. The overall effect gives a shift of the transition to smaller lattice depths.

This example shows, that the addition of the different levels of corrections to the pure Bose-Hubbard model results in a shift of the bosonic Mott-insulator to superfluid transition. Figure 18.3 shows the shift of this transition for the first four lobes as a function of the boson-fermion scattering length a_{BF}^{3D} [2]. The solid lines include all corrections described earlier. For the results,

---

[1]The Wannier functions are calculated numerically without any approximations as presented in section 1.2.

[2]The superscript $3D$ is used in this section to emphasize that the scattering length is the one for the three-dimensional scattering process
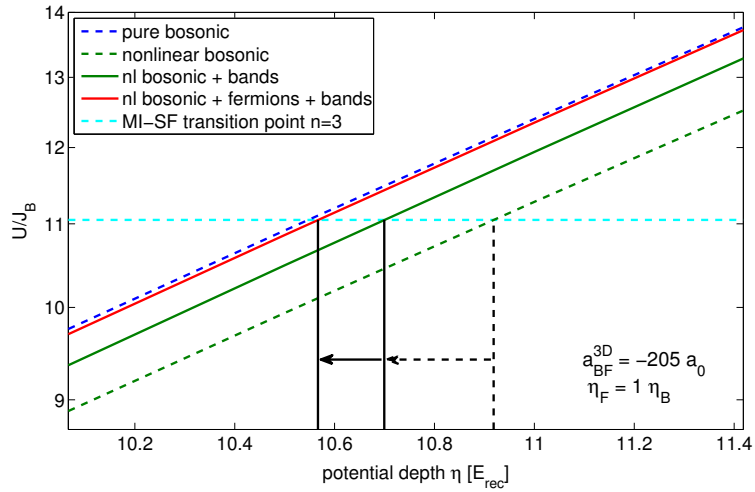
Figure 18.2: Determination of the transition point for a one-dimensional system. Shown are the different levels of corrections as described in the main text. Upon inclusion of the fermionic corrections, the location of the phase transition shifts to smaller lattice depths. Treated is the third lobe $n = 3$ with a perfect match of the fermionic and bosonic wave functions for attractive boson-fermion interaction with a scattering length $a_{BF}^{3D} = -205\, a_0$.

the first 50 bands are summed up which gives a satisfying convergence of the resulting amplitudes U and J. Additionally, the results for a sole inclusion of the nonlinear corrections are shown as a dashed line. As an important further information, the gray-filled region shows the deviation of the transition point if the Wannier functions of bosons and fermions do not perfectly match; here the results are shown for a mismatch of the bosonic and fermionic lattice depth of $\pm 30\%$, which shows to have a strong impact on the precise position of the transition. This should be kept in mind when experimental results are analyzed.

For the discussion of the experimental results in figure 18.1 together with the application of our method in the next section, two more features should be observed. Figure 18.3 shows, that the corrections due to the higher bands always shift the transition point to smaller lattice depths. Secondly, the combination of the nonlinear corrections with the higher-band corrections for positive scattering lengths, i.e., repulsive boson-fermion interaction sum up in such a way, that the net effect is an overall reduction of the transition point, at least for the higher fillings. All these features resembles precisely
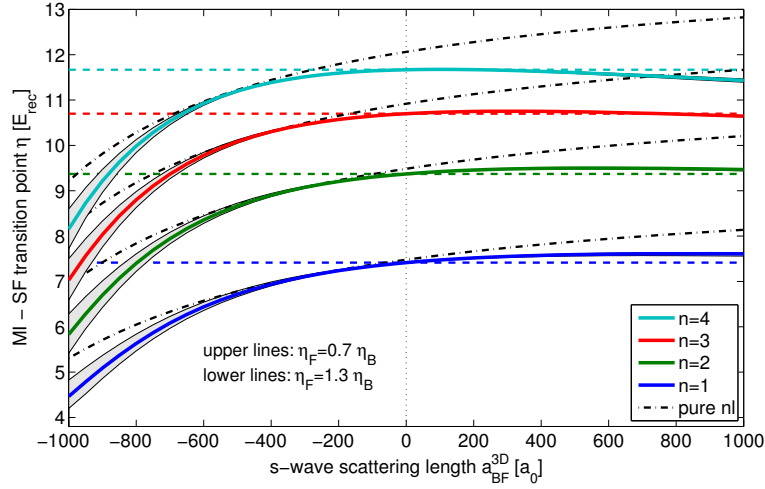
Figure 18.3: Shift of the bosonic Mott-insulator to superfluid transition as a function of the boson-fermion scattering length a_{BF}^{3D} for different lobes (solid lines) in one dimension. The gray-shaded region depicts the influence of a mismatch of the bosonic and fermionic lattice depth. The dashed lines give the shifts of the transition solely from the nonlinear corrections.

the behavior of the experimental results in figure 18.1 for the transition point and the visibility in the same experiment [84, figure 2 therein].

Finally, figure 18.4 shows the effect of the different levels of corrections to the first lobe in the phase diagram of the Bose-Hubbard model. The transition points for a fixed chemical potential μ are calculated using the 3rd-order strong-coupling in [97] and the ratio U/J is translated in the lattice depth η_B for the pure Bose-Hubbard parameters (dashed blue line in figure 18.2). For this lattice depth, the different corrected parameters are calculated and displayed in the phase diagram to visualize the influence of those on the phase diagram. Again, the gray-filled region gives the results for a mismatch of the potential depths. In general, the effect of the fermionic atoms depends on the sign of the boson-fermion interaction. For negative a_{BF}^{3D}, the fermion and higher-band corrections increase the superfluid region. Generally, the analysis of the transition shift in one dimension already resembles all features seen in the experiment.
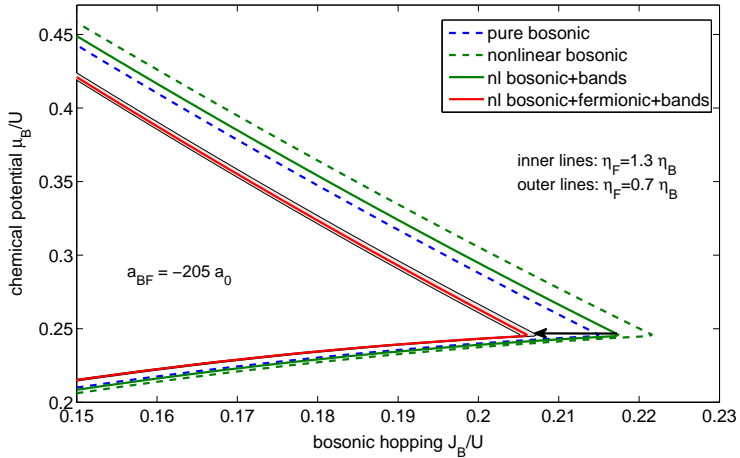
Figure 18.4: Shift of the boundary of the first Mott insulating lobe for different levels of corrections in a one-dimensional setup. For negative scattering length, i.e., attractive interaction, the superfluid region is enlarged.

18.2   Three-dimensional lattice

While the situation in one dimension is rather easy, the three-dimensional case adds some subtle points. The first, and most important one is the degeneracy of higher bands. In contrast to the one-dimensional case, where all higher bands are non-degenerate, in three dimensions most higher bands consist of different orbitals. Writing down the Hamiltonian for the (non-degenerate) first-band together with a single higher-band manifold blows up the calculation enormously. The reason is, that beside interband transitions to a single orbital (which is the equivalent to the processes studied earlier), also mixed orbital transitions occur. Furthermore, the dynamics in the higher-band manifold becomes coupled between the different orbitals, not allowing for a simple solution. An additional peculiarity comes into play from the order of the bands. While in the harmonic oscillator approximation all band manifolds with the same total energy are degenerate, in the real system the ordering of the bands will change as a function of the lattice depth. This finally demands a full summation over all possible higher-band manifolds, with an inclusion of all intra- and interband and orbit-mixing contributions.

This is not done here. For the moment we restrict ourself to the nonlinear hopping corrections introduced in the one-dimensional case. Rewriting the

one-dimensional Bose-Hubbard Hamiltonian to the three-dimensional case is straightforward and gives

$$\hat{H}^{\text{eff}} = -J[n,m] \sum_{\langle \mathbf{ij} \rangle} \left(\hat{a}_{\mathbf{i}}^{\dagger} \hat{a}_{\mathbf{j}} + \hat{a}_{\mathbf{j}}^{\dagger} \hat{a}_{\mathbf{i}} \right) + \frac{U}{2} \sum_{\mathbf{j}} \hat{n}_{\mathbf{j}} \left(\hat{n}_{\mathbf{j}} - 1 \right). \tag{18.1}$$

$\langle \mathbf{ij} \rangle$ is the sum over nearest neighbors. Since in the lowest-band approximation only corrections to the hopping occur, the bosonic interaction amplitude is given by

$$U = g_{BB} \left[\int \mathrm{d}z \; \left| w_1^B(z) \right|^4 \right]^3. \tag{18.2}$$

This results from the fact that the three-dimensional Wannier function at site $\mathbf{r}$ is the product of the one-dimensional ones:

$$w_1^B(\mathbf{r}) = w_1^B(x) w_1^B(y) w_1^B(z). \tag{18.3}$$

Employing the same arguments as before, the leading correction to the hopping amplitude is given by the nonlinear hopping. Again replacing the number operators by the fillings, the hopping reads

$$J[n,m] = J_1^B + 2n \frac{U_{nl}}{2} + 2m \frac{V_{nl}}{2}. \tag{18.4}$$

Note, that this is the same as in the one-dimensional case without the higher-band corrections. In three dimensions, the hopping amplitude

$$
\begin{aligned}
J_1^B &= \int \mathrm{d}^3 r \; \bar{w}_1^B(\mathbf{r} - a\hat{\mathbf{e}}_x) \left[-\frac{\hbar^2}{2m_B} \Delta + V_{\text{Pot}}^B(\mathbf{r}) \right] w_1^B(\mathbf{r}) \\
&= \int \mathrm{d}z \; \bar{w}_1^B(x - a) \left[-\frac{\hbar^2}{2m_B} \frac{\partial^2}{\partial x^2} + V_{\text{Pot}}^B(x) \right] w_1^B(x)
\end{aligned}
\tag{18.5}
$$

equals the one for the one-dimensional case since all other terms are zero due to the properties of the Wannier functions [113]. The nonlinear hopping corrections in the three-dimensional setup are defined via the one-dimensional ones according to

$$U_{nl} = \frac{1}{g_{BB}^2} \; U_{1111}^{3d,B} \left(U_{1111} \right)^2 \qquad\qquad V_{nl} = \frac{1}{g_{BF}^2} \; V_{1111}^{3d,B} \left(V_{1111} \right)^2. \tag{18.6}$$

With these definitions, we are in the position to discuss the influence of the nonlinear hopping corrections to the shift of the transition.
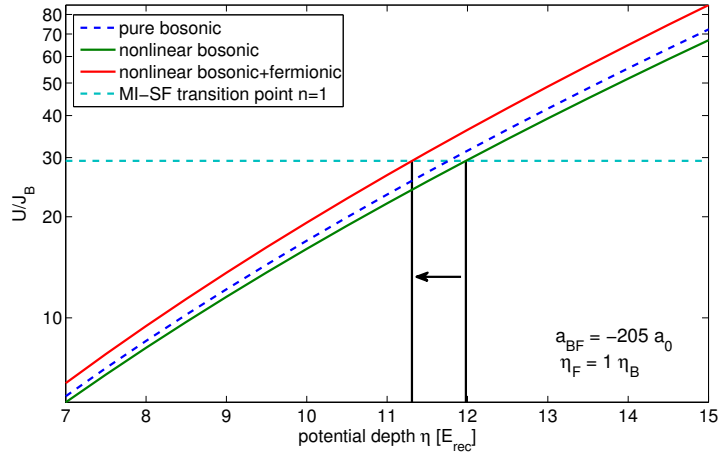
Figure 18.5: Determination of the Mott-insulator to superfluid transition for a three-dimensional setup. Shown are the pure Bose-Hubbard, the Bose-Hubbard with nonlinear correction and furthermore the corrections due to the fermionic nonlinear process. The shift is seen by the crossing of the ratio U/J with the transition point $U/J = 29.34$ for $n = 1$.

The method to determine the transition point is shown in figure 18.5. From the crossing point of the ratio U/J with the transition point, the location of the transition in terms of the potential depth is found. For the transition points, the results from [173, 267] are used as discussed in section 17.3.

Figure 18.6 shows the shift of the transition as a function of the boson-fermion scattering length. Compared to the one-dimensional case, two main differences can be seen. The first is, that the relative shift in three dimensions is much larger than in one dimension. Secondly, the influence of a mismatch in the lattice potentials for fermions and bosons is much more pronounced. This is an important feature in the analysis of the experimental data. A direct comparison of the experimental data to the results for the nonlinear corrections shows, that the inclusion of the effects of higher bands, which compared to the one-dimensional case should further reduce the transition point, promises a good understanding of the experimental results. This also holds for the case $a_{BF} > 0$. Finally, figure 18.7 shows the influence of the transition shift on the phase diagram of the Bose-Hubbard model.
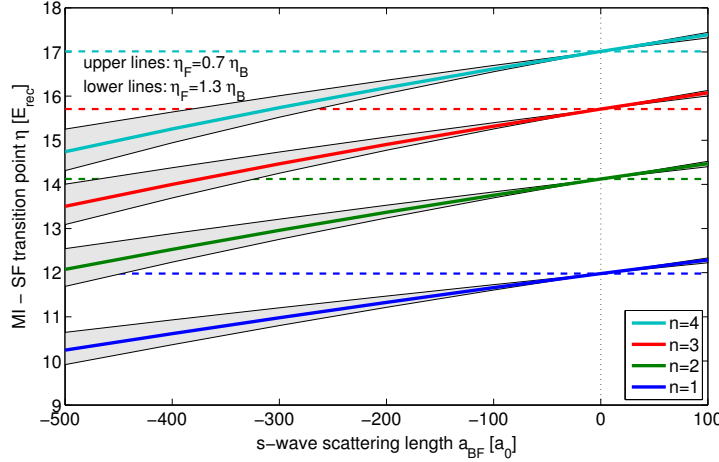
Figure 18.6: Shift of the bosonic Mott-insulator to superfluid transition as a function of the boson-fermion scattering length a_{BF} for different lobes (solid lines) in three dimension. Included is only the nonlinear hopping correction. The gray-shaded region depicts the influence of a mismatch of the bosonic and fermionic lattice depth.
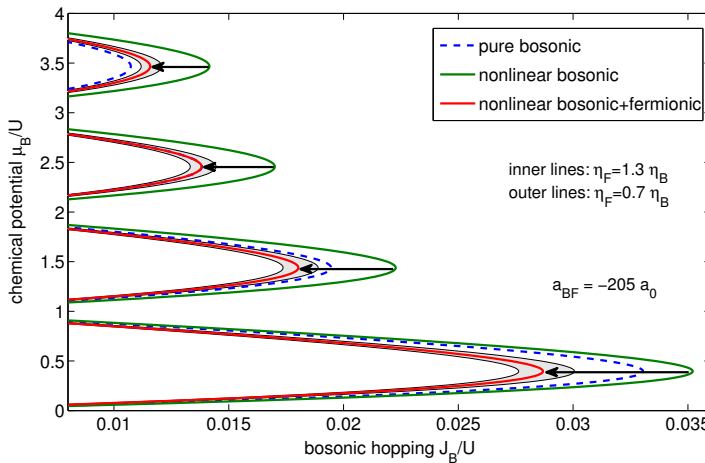

Figure 18.7: Effect of the nonlinear correction to the hopping in the phase diagram of the Bose-Hubbard model. Note the increase of the superfluid region for the lower lobes for an attractive interaction.

CHAPTER 19

Conclusion and outlook

Inclusion of higher-band effects to the single-band Bose-Fermi-Hubbard model allows for a precise study of the effect of admixed fermionic atoms to the bosonic superfluid to Mott-insulator transition. Here we derived an analytic theory, renormalizing the Bose-Hubbard parameters U and J_B by means of virtual transitions from the first to the higher bands. Furthermore we showed that it is important to include non-local contributions when treating the originally continuous interaction Hamiltonian which leads to a nonlinear hopping correction. Using real Wannier functions rather than harmonic oscillator states, the shift of the transition point is studied as a function of the boson-fermion interaction. For one dimension, all features of the experimental results are recovered even for repulsive interactions between bosons and fermions. For three dimensions, the inclusion of the nonlinear hopping corrections already gives a reasonable qualitative agreement.

Extending our results to three dimensions demands a full treatment of the three-dimensional band structure which has not been done here. Although the band structure displays a high degree of complexity, a full numerical analysis of the couplings to the different bands can be performed. For the solution of the free dynamics in the higher bands with intra-orbital mixing, further simplifications allow for the treatment of any level of degeneracy of the higher band. In higher-order perturbation theory effective many-body interactions will arise similar to the one-dimensional case, which will be important for the interpretation of the experimental results.

Part IV

Jaynes-Cummings-Hubbard model

CHAPTER 20

Introduction

Cavity-based setups [272] or ion chains [273] are promising realizations of certain quantum many-body systems. Representing Bose-Hubbard-like model Hamiltonians, implementations of this kind open new perspectives to the study and control of quantum systems. Of particular interest in this context is the Jaynes-Cummings-Hubbard model, describing the coupling of two-level atoms to a bosonic field [274, 275]. The most interesting feature of the Jaynes-Cummings-Hubbard model is the existence of Mott-insulating lobes, not of the bosonic species but of combined excitations of the bosonic and atomic degrees of freedom.

For these Mott lobes, mean-field results [275, 276, 277] give a first insight into the physics. Those results are supported by further numerical [278] and analytic calculations [276, 279, 280, 281, Mering2009]. Apart from the phase diagram, other quantities such as the spectral function [279, 280, 281, 282], the sound velocity [282, 283], spectral gap [283], band structure [276], and the dynamic structure factor [282] have been studied. Further investigations look for the dynamics of different aspects in this system [272, 274, 284, 285, 286, 287].

Analytic treatments of the Jaynes-Cummings-Hubbard model are based so far on strong-coupling theory [279, 280, 281], the polariton mapping [277, 283, 284] or single-excitation approaches [276, 287, Mering2009], each allowing for the calculation of different quantities. Though being applicable to the Jaynes-Cummings-Hubbard model with nearest-neighbor hopping, an easy extension of most methods to arbitrary long-ranged

hoppings is out of reach. Ivanov *et al.* recently showed [Ivanov2009] that transversal excitations of cold ions in a linear chain implement this kind of Jaynes-Cummings-Hubbard model, thus pointing out the need for a simplified treatment of long-ranged hopping.

Here we develop a simple approximative solution [Mering2009] for the calculation of the phase diagram of the Jaynes-Cummings-Hubbard model, which, most importantly, is also applicable to arbitrary long-ranged hopping. Comparing this solution to numerical and perturbative results for nearest-neighbor hopping first, we discuss the accuracy of our method in the determination of the phase diagram. The closed analytic form of the boundaries of the Mott insulators allows to study the behavior of the Mott lobes as a function of the different parameters in the system. Finally, the critical hopping where the Mott insulators vanish are calculated and compared to perturbative results for the long-ranged hopping case.

Lattice bosons coupled to spins

21.1 Jaynes-Cummings and Jaynes-Cummings-Hubbard model

The interaction of a single spin-$\frac{1}{2}$ system with a single bosonic mode is well described by the Jaynes-Cummings-Hubbard model [288, 289, 290], a well known, exactly solvable model of quantum optics. It also describes the physics of a two-level atom in a cavity and within rotating wave approximation [291], the Hamiltonian is given by

$$\hat{H} = \omega \hat{a}^\dagger \hat{a} + \Delta \hat{\sigma}^+ \hat{\sigma}^- + g \left(\hat{\sigma}^+ \hat{a} + \hat{a}^\dagger \hat{\sigma}^- \right). \tag{21.1}$$

The bosonic creation and annihilation operators $\hat{a}, \hat{a}^\dagger$ belong for instance to the cavity mode with resonance frequency ω and the spin operators $\hat{\sigma}^+, \hat{\sigma}^-$ describe the two-level atom with energy Δ in the excited state. Since the total number of excitations

$$\hat{N} = \hat{a}^\dagger \hat{a} + \hat{\sigma}^+ \hat{\sigma}^- \tag{21.2}$$

commutes with (21.1), the Hamiltonian becomes block-diagonal in the excitation-number subspaces. For zero excitations, we find the ground state

$$|0\rangle = |\downarrow, 0\rangle, \tag{21.3}$$

which is given by the vacuum for the cavity mode and the ground state of the two-level atom. For arbitrary number $n > 0$ of excitations, the eigenstates
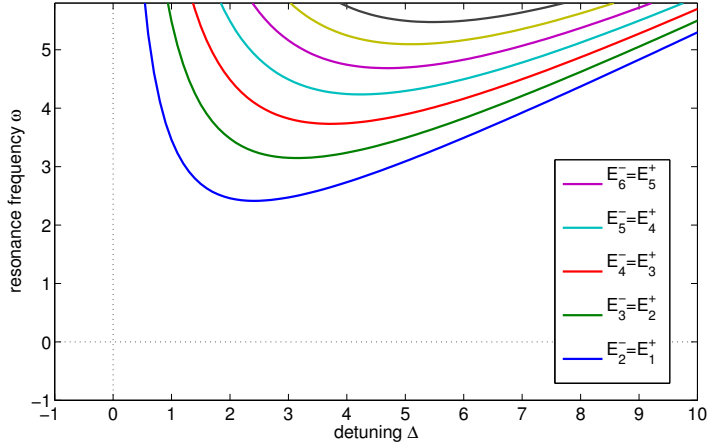
Figure 21.1: Degeneracy points of the energies E_{n+1}^- and E_n^+ for the states $|-, n+1\rangle$ and $|+, n\rangle$ for $g = 1$. Above the corresponding lines, the state $|+, n\rangle$ is energetically more favorable, below $|-, n+1\rangle$.

within the subspace of given excitation number are denoted as [292]

$$|\pm, n\rangle = \frac{[\chi_n \mp (\omega - \Delta)]\,|\uparrow, n-1\rangle \pm 2g\sqrt{n}\,|\downarrow, n\rangle}{\sqrt{2}\sqrt{\chi_n^2 \mp (\omega - \Delta)\chi_n}} \tag{21.4}$$

$$:= \alpha_n^\pm\,|\uparrow, n-1\rangle \pm \beta_n^\pm\,|\downarrow, n\rangle \tag{21.5}$$

with $\chi_n = \sqrt{(\Delta - \omega)^2 + 4ng^2}$ and the eigenenergies are given by

$$E_n^\pm = n\omega + \frac{\Delta - \omega}{2} \pm \frac{1}{2}\chi_n. \tag{21.6}$$

The eigenenergies show the important feature, that the higher level for n excitations always lies above the lower level for $n + 1$ excitations in the interesting parameter regime. This allows to restrict ourselves in the following to the states $|-, n\rangle$ when discussing the ground state of coupled Jaynes-Cummings systems. Figure 21.1 shows the points in the (ω, Δ)-plane where $E_{n+1}^- = E_n^+$. Below each line, only the states $|-, n\rangle$ are important.

Well known extension of the Jaynes-Cummings model are the so-called Dicke [293] or Tavis-Cummings [294] model, which describes the coupling of N two-level atoms to a single bosonic mode or the multimode Jaynes-Cummings model. The model considered in this part of the thesis is the so-called Jaynes-Cummings-Hubbard model [274, 275], which describes an ensemble

of coupled Jaynes-Cummings systems. It is defined by the Hamiltonian

$$\hat{H} = \omega \sum_{j=1}^{L} \hat{a}_j^\dagger \hat{a}_j + \Delta \sum_{j=1}^{L} \hat{\sigma}_j^\dagger \hat{\sigma}_j^- + g \sum_{j=1}^{L} \left(\hat{\sigma}_j^\dagger \hat{a}_j + \hat{a}_j^\dagger \hat{\sigma}_j^- \right)$$
$$+ \sum_d t_d \sum_{j=1}^{L} \left(\hat{a}_j^\dagger \hat{a}_{j+d} + \hat{a}_{j+d}^\dagger \hat{a}_j \right) \tag{21.7}$$

and inherits besides a collection of L single-mode Jaynes-Cummings systems at sites j the exchange of bosons between the different sites, governed by the hopping Hamiltonian in the second line of (21.7). Here we consider a general long ranged hopping with amplitudes t_d. Throughout this part, the atom-photon coupling g is set as the energy scale, i.e., $g = 1$.

There are several physical systems which are described by the Jaynes-Cummings-Hubbard model. The most prominent ones are realizations using arrays of high-Q cavities or other cavity based systems [272] (and references therein). Recently, Ivanov *et al.* [Ivanov2009] suggested the realization of the Jaynes-Cummings-Hubbard model using cold ions in a linear Paul trap. In this system, the model describes the transversal phonon excitations of a linear chain of ions coupled to an external laser field tuned to the red motional sideband with Coulomb mediated short-range hopping. In the following we focus on the ion chain realization in the thermodynamic limit and present a novel approach to the solution of the Jaynes-Cummings-Hubbard Hamiltonian. We compare the result of our method to the usual strong-coupling results, a mean-field theoretical approach and numerical data obtained by DMRG.

Before deriving the solution of the Jaynes-Cummings-Hubbard model, we discuss the phase diagram in the zero hopping limit. For $t_d = 0$, Hamiltonian (21.7) decouples in the site index j and the ground state is given by a product state of the local Jaynes-Cummings ground states. For an arbitrary filling $\varrho = N/L$ with N being the total number of excitations in a system of L sites, Mott insulating states can be found for integer filling. The operator for the total number of excitations

$$\hat{N} = \sum_j \left(\hat{a}_j^\dagger \hat{a}_j + \hat{\sigma}_j^+ \hat{\sigma}_j^- \right) \tag{21.8}$$

commutes with Hamiltonian (21.7) and thus its eigenvalues serve as good quantum numbers. For integer filling n, the ground state results in a Mott
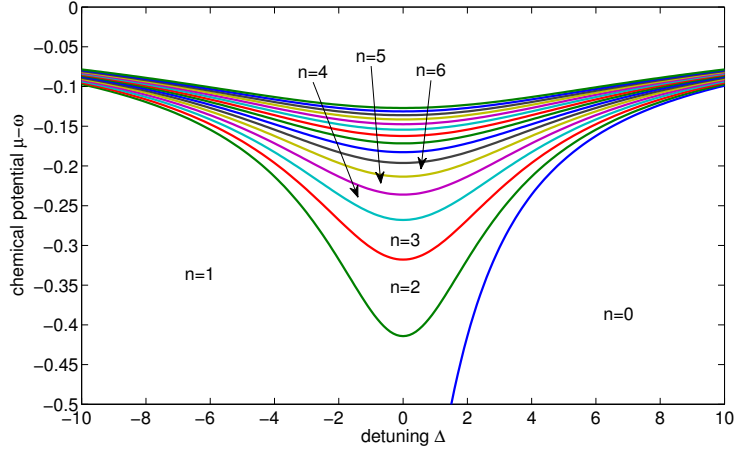
Figure 21.2: Mott insulating lobes in the Jaynes-Cummings-Hubbard model for zero hopping $t_d = 0$ and $g = 1$ for $\omega = 1$.

insulator, where the chemical potentials for the upper and lower boundary are easily calculated to be

$$\mu_n^+ = E_{n+1}^- - E_n^- = \omega - \frac{\chi_{n+1}}{2} + (1 - \delta_{n0})\frac{\chi_n}{2} + \delta_{n,0}\frac{\Delta - \omega}{2}, \qquad (21.9)$$

for any n and

$$\mu_n^- = E_n^- - E_{n-1}^- = \omega - \frac{\chi_n}{2} + (1 - \delta_{n1})\frac{\chi_{n-1}}{2} + \delta_{n,1}\frac{\Delta - \omega}{2}, \qquad (21.10)$$

for $n > 0$. As found in [275], the Mott insulators extend over a wide region for the energy in the excited state Δ as can be seen in figure 21.2. Our goal here is to derive closed expressions for the phase diagram for non-vanishing hoppings t_d..

21.2 Thermodynamic limit of the Jaynes-Cummings-Hubbard model for ion chains

As discussed in [Ivanov2009], a linear ion chain coupled to an external field in the red motional sideband and in the Lamb-Dicke regime [295, 296] is

described by the Jaynes-Cummings-Hubbard model, where the hopping corresponds to phonon transfer through Coulomb interaction. Due to the equilibrium positions of the ion in the harmonic axial potential [297], the bosonic frequencies and the hopping amplitudes become site-dependent. The full Hamiltonian

$$
\hat{H} = \sum_{j=0}^{L-1} \omega_j \hat{a}_j^\dagger \hat{a}_j + \Delta \sum_j \hat{\sigma}_j^\dagger \hat{\sigma}_j^- + g \sum_j \left(\hat{\sigma}_j^\dagger \hat{a}_j + \hat{a}_j^\dagger \hat{\sigma}_j^- \right)
$$
$$
+ \sum_{j=0}^{L-2} \sum_{d=1}^{L-j-1} t_{j,j+d} \left(\hat{a}_{j+d}^\dagger \hat{a}_j + \hat{a}_j^\dagger \hat{a}_{j+d} \right)
\tag{21.11}
$$

depends on the number of ions L through the equilibrium positions u_j of the ions which can be determined as shown in [297]. $\hat{a}_j^\dagger$ and $\hat{a}_j$ describe the creation and annihilation of a local transversal phonon at the jth site (ion), $\hat{\sigma}_j^\pm$ are the spin flip operators between the internal states of the ion, Δ is the detuning of the external laser field from the red motional sideband. g describes the phonon-ion coupling in the Lamb-Dicke limit and defines the energy scale through $g = 1$; for precise definitions of the quantities see [Ivanov2009]. The local oscillation frequencies ω_j and the hopping amplitudes $t_{j,j+d}$ are determined by the longitudinal and transversal trap frequencies ω_z and ω_x via

$$
\omega_j = -\frac{\omega_z^2}{2\omega_x} \sum_{\substack{l=0 \\ l \neq j}}^{L-1} \frac{1}{|u_j - u_l|^3} \qquad t_{j,j+d} = \frac{\omega_z^2}{2\omega_x} \frac{1}{|u_j - u_{j+d}|^3}.
\tag{21.12}
$$

For sufficiently large L, the equilibrium positions u_j of the ions at the center are approximately equidistant, giving $u_j = j\,\widetilde{u}$, with $\widetilde{u}$ being the distance of two adjacent ions. With this, the oscillation frequencies and the hopping amplitudes (21.12) can be rewritten for $L \to \infty$, yielding position independent phonon energies $\omega_j \equiv -\omega$ and hopping amplitudes $t_{j,j+d} \equiv t_d$ satisfying

$$
t_d = \frac{\omega_z^2}{2\omega_x \widetilde{u}^3} \frac{1}{d^3} \quad = t\,\frac{1}{d^3},
\tag{21.13}
$$
$$
\omega = 2\frac{\omega_z^2}{2\omega_x \widetilde{u}^3}\zeta(3) = 2t\,\zeta(3),
\tag{21.14}
$$

where in the following $t = \frac{\omega_z^2}{2\omega_x \widetilde{u}^3}$ acts as a small parameter and $\omega > 0$. $\zeta(x)$ is the Riemann ζ-function. In the expressions (21.13) and (21.14) one notices a negative oscillator energy $-\omega$ and a negative effective mass, which is a
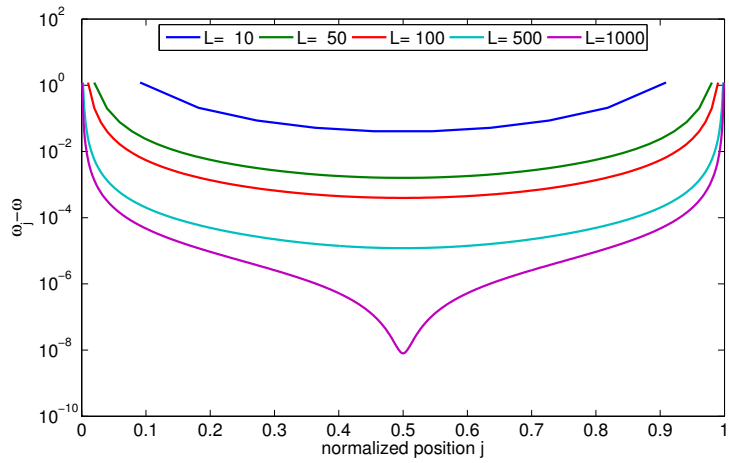
Figure 21.3: Deviation of the finite system phonon energies (21.12) for different lengths L from the infinite size result (21.14). Beside the larger deviation at the boundaries, the infinite sum gives a good estimate for the finite system even for rather small system sizes.

result of the positive hopping strength t which will be of importance later on.

Figure 21.3 shows the accuracy of the assumption of homogeneous phonon energies for different numbers of ions L. Shown is the difference of the exact summation over the ion positions for a finite chain of length L as found in the original expression (21.12) for equidistant ions compared to the infinite size results from (21.14). Beside the larger deviations close to the ends of the ion chain, the approximative results are quite satisfying, supporting the validity of the homogeneous system assumption in the thermodynamic limit.

CHAPTER 22

Approximative calculation of the phase diagram

This chapter presents two different approximations for the determination of the phase diagram. First, a new approach referred to as *fermion approximation* is introduced. The second approximation is similar to the strong-coupling expansion common for Hubbard-like Hamiltonians [97] and already applied to the calculation of the phase diagram of the Jaynes-Cummings-Hubbard model in lower order [276, 277, 280, 284, 283]. We here present the full derivation of the second order strong-coupling expansion using the formulation of [97]. Though in [280] a second order treatment is used, the authors do not discuss the phase diagram but focus on the excitation spectrum. Recent work presented in [298] applies a field theoretic approach for finite temperature T to the simple cubic Jaynes-Cummings-Hubbard model.

22.1 Fermion approximation

From (21.7) we note that all terms of the Jaynes-Cummings-Hubbard Hamiltonian are quadratic. These kinds of models are in general suited for an exact solution by means of a Fourier transform (9.2). The problem at this point is however, that the commutation relations of spin operator $\hat{\sigma}_j^{\pm}$ are not as simple as that of bosons or fermions. Naively defining the Fourier transform of the spin operators as

$$\hat{\sigma}_k^- = \frac{1}{\sqrt{L}} \sum_j e^{-2\pi i \frac{kj}{L}} \hat{\sigma}_j^- \tag{22.1}$$

destroys the commutator relation for the spins in momentum space:

$$[\sigma_k^+, \sigma_{k'}^-] = \frac{2}{\sqrt{L}} \, \sigma_{k-k'}^z \neq 2 \, \sigma_k^z \, \delta_{kk'}. \tag{22.2}$$

Thus, a Fourier transformation of the spins is not useful. The often used usual trick of a prior Jordan-Wigner transformation [299], transforming the spin operators to fermionic operators, is not applicable in this case, since the interaction part is linear in the spin operators, so the Jordan-Wigner factors do not cancel out. Thus both transformations cannot be carried out exactly without increasing the descriptional complexity of the problem. Nevertheless the Hamiltonian can be diagonalized by a Fourier-transform in an approximate way introducing fermionic operators.

As noted above, all modes decouple for $t_d = 0$. For this reason, the spin-operators are in this limit equivalent to fermionic operators. Assuming the replacement $\hat{\sigma}_j^+ \mapsto \hat{c}_j^\dagger$ to hold also for small values of t_d, the Jaynes-Cummings-Hubbard model (21.7) can be rewritten in a fermionic approximation

$$\begin{aligned}
\hat{H} = \omega \sum_j \hat{a}_j^\dagger \hat{a}_j + \Delta \sum_j \hat{c}_j^\dagger \hat{c}_j + g \sum_j \left(\hat{c}_j^\dagger \hat{a}_j + \hat{a}_j^\dagger \hat{c}_j \right) \\
+ \sum_d t_d \sum_j \left(\hat{a}_j^\dagger \hat{a}_{j+d} + \hat{a}_{j+d}^\dagger \hat{a}_j \right).
\end{aligned} \tag{22.3}$$

Within this approximation, a Fourier transform of both, the bosonic and fermionic degrees of freedom can be easily accomplished as defined in (9.2). Doing so, and transforming the momentum-space fermionic operators back to spins, the Jaynes-Cummings-Hubbard Hamiltonian transforms to that of uncoupled Jaynes-Cummings systems in *k-space*

$$\hat{H} = \sum_k \omega_k \hat{a}_k^\dagger \hat{a}_k + \Delta \sum_k \hat{\sigma}_k^+ \hat{\sigma}_k^- + g \sum_k \left(\hat{\sigma}_k^+ \hat{a}_k + \hat{a}_k^\dagger \hat{\sigma}_k^- \right) \tag{22.4}$$

with mode dependent phonon energies

$$\omega_k = \omega + 2 \sum_d t_d \cos(2\pi \frac{kd}{L}). \tag{22.5}$$

The ground state in any mode is given by the Jaynes-Cummings ground state (21.4) with frequency ω_k and the energy of mode k with n excitations is

$$E_k^n = (1 - \delta_{n0}) \left[n \, \omega_k + \frac{\Delta - \omega_k}{2} - \frac{1}{2} \sqrt{(\Delta - \omega_k)^2 + 4ng^2} \right]. \tag{22.6}$$

Since still the total number of excitations $\hat{N}$ (in momentum space) in the system commutes with the Hamiltonian (22.4), a common basis can be chosen. Thus the full solution of (22.4) for a fixed total number of excitations N is given by the distribution $\mathbf{n} = \{n_{k_1}, n_{k_2}, \dots\}$ of N excitations on L momentum modes with minimal energy $E_N[\mathbf{n}] = \sum_k E_k^{n_k}$, together with the constraint $\sum_k n_k \equiv N$. Note that the number of momentum modes L is equal to the number of ions (sites).

To construct the phase diagram as usual, the energy for $N = nL - 1$, $N = nL$ and $N = nL + 1$ excitations needs to be calculated. In the limit of vanishing hopping ($t_d \equiv 0$) and for commensurate filling, i.e., $N = nL$, the distribution of occupation numbers which has the lowest energy is $\mathbf{n} = \{n, n, \dots, n\}$. This corresponds to a Mott-insulating state with an integer number of excitations on every lattice site. The phase is gapped with a particle-hole gap as described in chapter 21. When t_d is increased, the gap slowly closes and eventually a quantum phase transition occurs from the Mott insulator to the superfluid phase at some critical value of t. The only remaining task in order to calculate the chemical potentials is to find the momentum mode where the addition (removal) of an excitation gives the maximum (minimum) reduction (increase) in the total energy. This yields

$$\mu_n^+ = E_{k'}^{n+1} - E_{k'}^n \qquad\qquad \mu_n^- = E_k^n - E_k^{n-1}, \qquad (22.7)$$

where k' $[k]$ is chosen such that $\mu_n^+(k')$ $[\mu_n^-(k)]$ is minimal [maximal]. The actual values of k and k' depend mainly on the sign of the hopping amplitudes t_d.

Interpretation of the approximation

The transformation used above is not a transformation in the strict sense; it has to be seen as a valid replacement for $t_d \equiv 0$. To understand its validity in terms of a proper transformation, we apply a Jordan-Wigner transformation

$$\hat{\sigma}_j^+ = e^{i\pi \sum_{l<j} \hat{c}_l^\dagger \hat{c}_l}\ \hat{c}_j = \prod_{l<j} \left(1 - 2\hat{c}_l^\dagger \hat{c}_l\right)\ \hat{c}_j \qquad (22.8)$$

which connects spin degrees of freedom and fermions. The spins and fermions are equivalent, if one neglects the phase factor $e^{i\pi \sum_{l<j} \hat{c}_l^\dagger \hat{c}_l}$ which takes care of the proper commutation relation within the transformation. This is done in our case as approximative scheme, which ignores effects arising from the commutator between different sites.

22.2 Strong-coupling

The second, more systematic approximative scheme is a strong-coupling expansion in the hopping t_d. This method is well known and determines the energy of the ground state in a second order perturbative treatment. Having the energy as a function of the hopping, the calculation of the chemical potentials is straightforward.

a) Initial considerations

For the following discussion it will be useful to consider the action of a single bosonic creation or annihilation operator on a given (single-site) Jaynes-Cummings eigenstate $|\pm, n\rangle$. This establishes the main influence of the hopping operator, since no atomic degrees come up in the perturbation theory. Defining[1]

$$A_n^\pm = \begin{cases} \sqrt{n}\ \alpha_n^\pm \beta_{n+1}^- \pm \sqrt{n+1}\ \beta_n^\pm \alpha_{n+1}^- & n > 0 \\ \alpha_1^- & n = 0 \end{cases}, \qquad (22.9)$$

$$B_n^\pm = \begin{cases} \sqrt{n}\ \alpha_n^\pm \beta_{n+1}^+ \mp \sqrt{n+1}\ \beta_n^\pm \alpha_{n+1}^+ & n > 0 \\ -\alpha_1^+ & n = 0 \end{cases}, \qquad (22.10)$$

$$C_n^\pm = \begin{cases} \sqrt{n-1}\ \alpha_n^\pm \beta_{n-1}^- \pm \sqrt{n}\ \beta_n^\pm \alpha_{n-1}^- & n > 1 \\ 0 & n \le 1 \end{cases}, \qquad (22.11)$$

$$D_n^\pm = \begin{cases} \sqrt{n-1}\ \alpha_n^\pm \beta_{n-1}^+ \mp \sqrt{n}\ \beta_n^\pm \alpha_{n-1}^+ & n > 1 \\ \pm \beta_1^\pm \delta_{n,1} & n \le 1 \end{cases}, \qquad (22.12)$$

the action of $\hat{a}^\dagger$ and $\hat{a}$ on the state Jaynes-Cummings eigenstate $|\pm, n\rangle$ can be seen to be

$$\hat{a}^\dagger |\pm, n\rangle = A_n^\pm |+, n+1\rangle + B_n^\pm |-, n+1\rangle \qquad (22.13)$$

$$\hat{a} |\pm, n\rangle = C_n^\pm |+, n-1\rangle + D_n^\pm |-, n-1\rangle, \qquad (22.14)$$

i.e., $\hat{a}^\dagger$ and $\hat{a}$ connect the manifold of states $|\pm, n\rangle$ to the manifolds $|\pm, n+1\rangle$ and $|\pm, n-1\rangle$ respectively as expected. As already discussed in chapter 21 and figure 21.1, all contributions from the excited Jaynes-Cummings states $|+, n\rangle$ can be neglected. This means, that the annihilation (creation) operator on the Jaynes-Cummings ground state acts precisely as the annihilation

---

[1]The definition of $\alpha_n^\pm$ and $\beta_n^\pm$ can be found in (21.4).

(creation) operator on a number state, i.e., connecting the state $|-, n\rangle$ to the state $|-, n \pm 1\rangle$, together with a prefactor[2]. This similarity basically allows the application of the perturbation theory to the pure Bose-Hubbard model with only slight modifications[3].

b) Corrections to the energy in second order

In order to calculate the phase boundaries of the Mott insulating lobes for the Jaynes-Cummings-Hubbard model, we follow the scheme already used in chapter 12. In the following we present a detailed derivation of this scheme. The task is to calculate the energy of the ground state with N excitations as function of the hoppings t_d. Here we explicitly discuss the situation of one additional excitation, i.e., $N = nL + 1$, which is the most complex one.

We make again use of Kato's expansion as presented in [159]. This allows to derive an effective Hamiltonian within the degenerate ground states $\{|\Psi\rangle_j\}$ for the $N = nL + 1$ manifold, which is L-fold degenerate. Degenerate perturbation theory is straightforward because the hopping processes couple the different states within the manifold already in first order. The detailed calculation can be found in appendix C.1. Here we shortly summarize the main steps and results.

The ground-state manifold for $N = nL + 1$ excitations is L-fold degenerate, leading to a coupling of all degenerate states via the hopping operator

$$\hat{V} = \sum_d t_d \sum_j \left(\hat{a}_j^\dagger \hat{a}_{j+d} + \hat{a}_{j+d}^\dagger \hat{a}_j \right). \tag{22.15}$$

This coupling is taken into account by the derivation of an effective Hamiltonian within the degenerate manifold [159], where the matrix elements of the effective Hamiltonian up to second order are defined by

$$_q\langle\Psi| \hat{H}_{eff} |\Psi\rangle_p =_q \langle\Psi| \hat{H}_0 + \mathcal{P}\hat{V}\mathcal{P} + \mathcal{P}\hat{V}\mathcal{Q}\frac{1}{E_0 - \hat{H}_0}\mathcal{Q}\hat{V}\mathcal{P} |\Psi\rangle_p. \tag{22.16}$$

$\mathcal{P}$ projects onto the degenerate manifold, $\mathcal{Q} = \mathbb{1} - \mathcal{P}$ and E_0 is the ground-state energy of the manifold.

---

[2]Here, the prefactors are given by B_n^- and D_n^-, whereas the action on a simple number state would be given by $\sqrt{n}$ and $\sqrt{n+1}$, respectively.

[3]Replacing the expressions for the energy and the prefactors

The matrix elements of the effective Hamiltonian given in (C.19) show, that the additional excitation behaves as a free particle within the manifold. Introducing fermionic operators $\hat{c}_j^\dagger, \hat{c}_j$, which describe the two-dimensional Hilbert space consisting of the states $|1\rangle \hat{=} |-, n+1\rangle$ and $|0\rangle \hat{=} |-, n\rangle$, the effective model is given by the Hamiltonian

$$\hat{H} = \sum_d \widetilde{T}_d \sum_j \left(\hat{c}_j^\dagger \hat{c}_{j+d} + \hat{c}_{j+d}^\dagger \hat{c}_j \right) + \Delta \sum_j \hat{c}_j^\dagger \hat{c}_j. \tag{22.17}$$

The local energy Δ reads

$$\Delta = E_{n+1}^- + 2 \left(\frac{B_{n+1}^- D_n^- D_{n+2}^- B_{n-1}^-}{E_{n+1}^- + E_n^- - E_{n+2}^- - E_{n-1}^-} \right.$$
$$\left. + (L-2) \, \frac{B_n^- D_n^- B_{n-1}^- D_{n+1}^-}{2E_n^- - E_{n-1}^- - E_{n+1}^-} \right) \sum_d t_d^2 \tag{22.18}$$

and the modified hopping constants $\widetilde{T}_d$ are

$$\widetilde{T}_d = B_n^- D_{n+1}^- t_d + \frac{B_n^- D_n^- B_{n-1}^- D_{n+1}^-}{2E_n^- - E_{n-1}^- - E_{n+1}^-} T_d \tag{22.19}$$

with T_d (which is of order t_d^2) given in (C.18).

The solution of the effective fermion Hamiltonian in (22.17) is straightforward. Applying a Fourier transformation (9.2) to the Hamiltonian gives

$$\hat{H} = \sum_k \left[\Delta + 2 \sum_d \widetilde{T}_d \cos\left(2\pi \frac{kd}{L} \right) \right] \hat{c}_k^\dagger \hat{c}_k = \sum_k \Omega_k \, \hat{c}_k^\dagger \hat{c}_k. \tag{22.20}$$

The ground state for the single additional excitation case is equivalent to the determination of the minimum in the dispersion relation Ω_k. Thus, the energy in second order of the hopping amplitudes for the additional excitation state is given by $E(N = nL + 1) = \Omega_q$, where q has to be determined from the dispersion. If all t_d are of the same sign, the minimum is easy to find, where for $t_d < 0$ the mode $q = 0$ gives the minimum and for $t_d > 0$ the minimum is found for $q = L/2$. In all intermediate situations, i.e., if the t_d have different signs, the situation has to be analyzed more carefully. This result generalizes the findings from [277, 280] to arbitrary hoppings t_d.

A similar treatment finally allows to calculate the energy of the Mott insulator as well as for the system with one excitation less. The slightly deviating expressions for Δ and $\widetilde{T}_d$ are not given explicitly here, however. From these energies, the chemical potentials are defined as usually, giving the boundary of the Mott insulator through $\mu_n^\pm = \pm E(nL \pm 1) \mp E(nL)$.

22.3 Mean-field theory

The simplest numerical method to obtain a qualitative phase diagram is the so-called mean-field theory. As described for instance in [181, 272, 275, 292, 300], a mean-field theory can be implemented by introducing an order parameter Ψ, which in our case is chosen to be homogeneous and real valued. Decoupling the hopping term by using

$$\hat{a}_j^\dagger \hat{a}_l \mapsto \Psi\left(\hat{a}_j^\dagger + \hat{a}_l\right) - |\Psi|^2, \tag{22.21}$$

the Jaynes-Cummings-Hubbard Hamiltonian (21.7) in the grand-canonical ensemble uncouples in real space to a local Hamiltonian

$$\hat{H}^{\mathrm{MF}} = (\omega - \mu)\,\hat{a}^\dagger \hat{a} + (\Delta - \mu)\,\hat{\sigma}^+ \hat{\sigma}^- + g\left(\hat{a}^\dagger \hat{\sigma}^- + \hat{a}\hat{\sigma}^+\right)$$
$$- 2\widetilde{J}\Psi\left(\hat{a}^\dagger + \hat{a}\right) + 2\widetilde{J}|\Psi|^2. \tag{22.22}$$

At this point, we omitted the spatial index because the problem is purely local. The modified hopping amplitude $\widetilde{J} = -\sum_d t_d$ gives the effective coupling within the mean-field scheme. The phase diagram is now found by diagonalizing the mean-field Hamiltonian (22.22) either exactly by means of perturbation theory [181] or numerically, setting an upper bound for the maximal number of bosonic excitations in the system. The ground-state energy is then given by $\min_\Psi E[\Psi]$ and the Mott insulator is distinguished from the superfluid by the value of Ψ for the minimal energy. For $\Psi \equiv 0$, the system is in a Mott insulating state, for $\Psi > 0$, the ground state is superfluid. This sets the point of the Mott-insulator to superfluid transition. It should be mentioned at this point, that this method gives inadequate results in one dimension $(D = 1)$ but is exact for $D \to \infty$. Additionally, the effective hopping $\widetilde{J}$ must be larger than zero to yield any result.

Benchmarking against the Jaynes-Cummings-Hubbard model with nearest-neighbor hopping

In this chapter, we benchmark the newly introduced *fermion approximation* on the simple cubic Jaynes-Cummings-Hubbard model with nearest-neighbor hopping $t_d = -t\delta_{d1}$. This is the natural choice, since for this variant of the model, well established numerical results from DMRG calculations [278] as well as earlier (perturbative) analytic results exist. Furthermore, the results of the introduced mean-field theory are well understood in this case.

The simple cubic Jaynes-Cummings-Hubbard model with nearest-neighbor hopping is given by

$$
\begin{aligned}
\hat{H} = \omega \sum_j \hat{a}_j^\dagger \hat{a}_j + \Delta \sum_j \hat{\sigma}_j^\dagger \hat{\sigma}_j^- + g \sum_j \left(\hat{\sigma}_j^\dagger \hat{a}_j + \hat{a}_j^\dagger \hat{\sigma}_j^- \right) \\
- t \sum_j \left(\hat{a}_j^\dagger \hat{a}_{j+1} + \hat{a}_{j+1}^\dagger \hat{a}_j \right),
\end{aligned}
\tag{23.1}
$$

where we focus on the resonant case, i.e., $\omega = \Delta$.

23.1 Strong-coupling results

To calculate the chemical potentials using the strong-coupling approximation, we first have to determine the momentum mode q and q' which minimizes the energy (22.20). Since $t_d < 0$ for any distance d, this is found for $q = 0$.

Furthermore, the coefficients in (21.4) are $\alpha_n^\pm = \frac{1}{\sqrt{2}} = \beta_n^\pm$ and therefore

$$B_n^- = \begin{cases} \frac{\sqrt{n}+\sqrt{n+1}}{2} & n > 0 \\ -\frac{1}{\sqrt{2}} & n = 0 \end{cases} = D_{n+1}^-. \tag{23.2}$$

This allows for a conclusive calculation of the chemical potentials which are not shown here. Nevertheless, we give the approximative results for the tip of the lobe in the first order perturbation theory. The chemical potentials are found to be

$$\mu_n^+ = \omega - \frac{1}{2}\chi_{n+1} + \frac{1-\delta_{n0}}{2}\chi_n - t\frac{\left(\sqrt{n}+\sqrt{n+1}\right)^2}{2-\delta_{n0}}, \tag{23.3}$$

for any n and

$$\mu_n^- = \omega - \frac{1}{2}\chi_n + \frac{1-\delta_{n1}}{2}\chi_{n-1} + t\frac{\left(\sqrt{n}+\sqrt{n-1}\right)^2}{2-\delta_{n1}}, \tag{23.4}$$

for $n > 0$, which gives the tip of the Mott lobe, defined by $\mu_n^+ = \mu_n^-$ to be

$$t_{\text{crit}}/g = 2\frac{2\sqrt{n}-\sqrt{n+1}-\sqrt{n-1}}{(\sqrt{n}+\sqrt{n+1})^2 + (\sqrt{n+\delta_{n1}}+\sqrt{n-1})^2}. \tag{23.5}$$

A comparison of these results to the numerical results from DMRG is given in figure 23.1

23.2   Fermion approximation

Secondly we apply the fermion approximation to this model. With the given system parameters, the momentum dependent phonon energies (22.5) are $\omega_k = \omega - 2t\cos(2\pi\frac{k}{L})$ and the energy (22.6) in the kth momentum mode for a given filling n reads

$$E_k^n = (1-\delta_{n0})\left[n\omega - 2nt\cos(2\pi\frac{k}{L}) + t\cos(2\pi\frac{k}{L}) - \sqrt{t^2\cos^2(2\pi\frac{k}{L}) + ng^2}\right]. \tag{23.6}$$

Finally, following (22.7), the momentum modes k' (k) which minimize (maximize) the chemical potentials need to be found. In the present case ($t_1 < 0$), these are $k' = 0$ and $k = \frac{L}{2}$. Thus the resulting chemical potentials are

$$\mu_n^+ - \omega = -2t + t\delta_{n0} - \sqrt{t^2 + (n+1)g^2} + (1-\delta_{n0})\sqrt{t^2 + ng^2}, \tag{23.7}$$
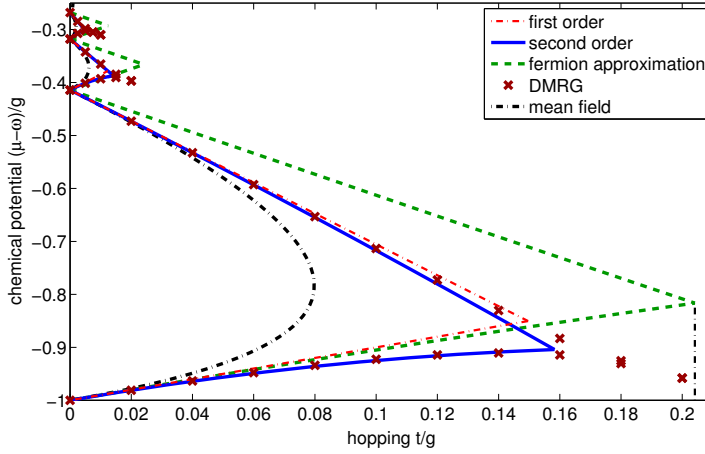
Figure 23.1: Comparison of the ground-state phase diagram of the one-dimensional simple cubic Jaynes-Cummings-Hubbard model with nearest-neighbor hopping (23.1) obtained by DMRG (red crosses, from Rossini and Fazio [278]) as well as mean-field results (black dash-dotted line) with the prediction from our approaches (red dash-dotted, solid line: strong-coupling theory; dashed line: fermion approximation) for $\Delta = \omega = 1$ and $g = 1$. Taking into account the simplicity of both approaches, the agreement with the DMRG data is rather good while the mean-field predictions are rather poor as expected for 1D systems. The critical hopping amplitudes estimated from the DMRG data agree surprisingly well with those predicted within the fermion approximation, although the shape of the Mott lobe is different.

for any n and

$$\mu_n^- - \omega = 2t - t\delta_{n1} - \sqrt{t^2 + ng^2} + (1 - \delta_{n1})\sqrt{t^2 + (n-1)g^2}, \qquad (23.8)$$

for $n > 0$. A closed form for the critical hopping can be derived, but is rather lengthy and is therefore be skipped.

We now compare the analytic results to both the DMRG [278][1] and mean-field results [275], shown in figure 23.1. For the mean-field results (see equation 22.22), the modified hopping amplitude evaluates as $\widetilde{J} = t$. From the figure, it can be seen that the strong-coupling result gives a much better agreement to numerical DMRG data in first order as well as in second order; especially the slopes of the lobes agree perfectly for small

---

[1]Thanks to D. Rossini for the permission to use their DMRG results.

hopping. The fermion approximation overestimates the size of the Mott lobe. In particular, while the lower boundaries are rather well reproduced, the upper boundaries have the wrong slope. For this behavior we do not have an explanation yet, which could point out a possible improvement of the approach for instance by including an additional prefactor to the hopping. Surprisingly, the critical hopping amplitudes from the fermion approximation seem to agree much better with the DMRG data than the results obtained from the strong-coupling theory as depicted by the dashed vertical line.

Although the fermion approximation is quantitatively worse than the strong-coupling theory, it provides a simple approximative solution to the Jaynes-Cummings-Hubbard model beyond the mean-field level which has the advantage of giving a closed form of the ground state. A detailed analysis of the implications of the approximation demands some deeper work.

CHAPTER 24

Application to the ion-chain setup

The first thing to notice in the Hamiltonian for the ion-chain setup in the thermodynamic limit is the negative oscillator energy $\omega_j = -\omega < 0$ (21.14) as well as the negative effective mass $t_d = t\frac{1}{d^3} > 0$ (21.13). This negative mass is the reason why the application of the mean-field theory is not that straightforward. Simply calculating the modified hopping amplitude $\widetilde{J} = -t \sum_d \frac{1}{d^3} = -t\zeta(3)$ as defined in section 22.3, the hopping becomes negative and therefore mean-field theory is inapplicable. This problem can be overcome by first applying a canonical transformation to all used operators. The transformation

$$\hat{a}_j \mapsto (-1)^j \hat{a}_j \tag{24.1}$$

for the annihilation operator and accordingly to all the other operators $\hat{a}_j^\dagger, \hat{\sigma}_j^\pm$, maps the Jaynes-Cummings-Hubbard model (21.7) onto itself, but with $t_d \mapsto (-1)^d t_d$. After this transformation, the modified hopping evaluates to $\widetilde{J} = -t \sum_d \frac{(-1)^d}{d^3} = 3t\zeta(3)/4$, being positive. Now the application of the mean-field theory is straightforward, following the usual route.

Starting with the effective strong-coupling theory described in detail in section C.1, the chemical potentials for the upper and lower boundary of the lobes can be calculated. The proper momentum modes q, q', which minimize (maximize) the chemical potentials are both found to be $q = q' = L/2$, which results from the negative mass. Due to the complexity of the problem, especially the analytic form of B_n^- and D_n^-, analytic expressions of the chemical potentials are omitted. Up to second order, the results for the phase diagram are shown in figure 24.3, together with a comparison to the mean-field results and the fermion approximation.

185
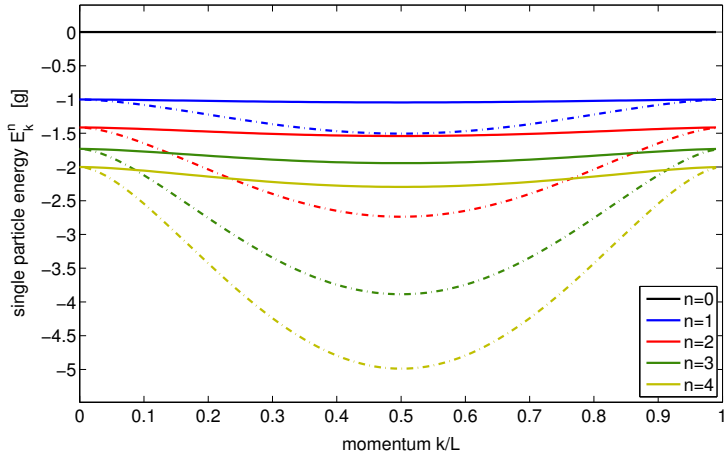
Figure 24.1: Energies of the Jaynes-Cummings-Hubbard Hamiltonian in momentum space after application of the fermion approximation for fixed filling n. Shown are the energies (22.6) for the five lowest fillings $0 \ldots 4$ (from top to bottom) for $\Delta = 0$ and $g = 1$. Solid lines: $t/g = 0.02$; Dash-dotted lines: $t/g = 0.2$. One clearly recognizes the minimum at $k = L/2$ and the flat dispersion for $t/g \to 0$.

Following the approximative method from section 22.1, the Hamiltonian for the uncoupled Jaynes-Cummings models is given by (22.4), with the phonon energies

$$\omega_k = -\omega + 2t \sum_d \frac{\cos(2\pi \frac{kd}{L})}{d^3}, \tag{24.2}$$

according to (22.5). Note that since $\omega = 2t\,\zeta(3)$, all ω_k's are negative. Using the polylogarithm $\mathrm{Li}_n(x) = \sum_{d=1}^{\infty} \frac{x^d}{d^n}$ they can be written explicitly as

$$\omega_k = t \left[\mathrm{Li}_3 \left(e^{2\pi i \frac{k}{L}} \right) + \mathrm{Li}_3 \left(e^{-2\pi i \frac{k}{L}} \right) - 2\zeta(3) \right]. \tag{24.3}$$

The minimum value of $\omega_k = -7t\zeta(3)/2$ is attained for $k = \frac{L}{2}$ as expected from the positive sign of the hopping term. The energies for each momentum mode are given by the solution (22.6) of the Jaynes-Cummings model and the corresponding spectrum is shown in figure 24.1. Note the minimum at $k = \frac{L}{2}$.

From the dispersion relation for different fillings, it is now easy to construct the phase diagram. As discussed in section 22.1, the flat dispersion for $t = 0$
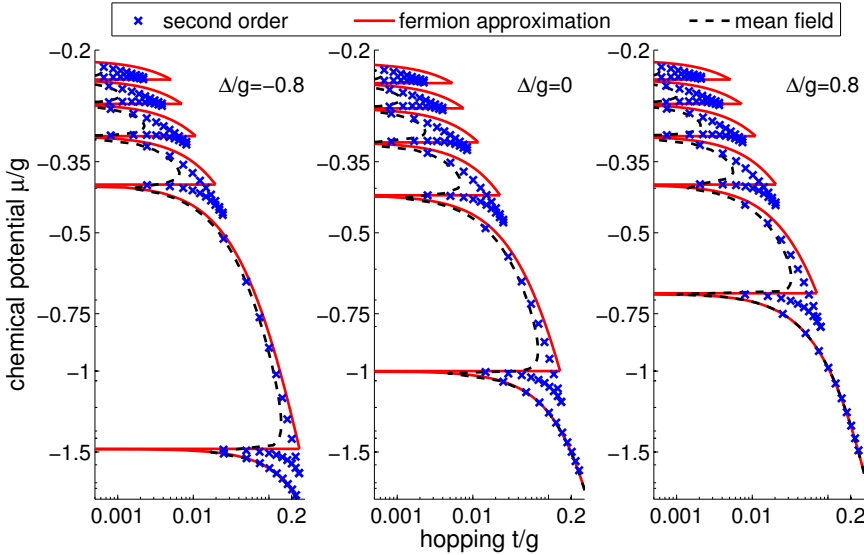
Figure 24.2: Phase diagram of the Jaynes-Cummings-Hubbard model for a linear ion chain for three depicted values $\Delta/g = -0.8, 0, 0.8$. Shown are the upper boundary of the zero filling lobe (always lowest line) and the boundaries of the lobes with filling from 1 to 5 on a double logarithmic scale. Beside the used approximations (solid line: fermion approximation, crosses: second order perturbation theory) the results from the mean-field theory (dashed line) are shown. It can be seen, that the fermionic approximation again overestimates the phase boundary (compared to the more reliable effective strong-coupling theory) but gives a better agreement compared to the mean-field theory (mind the logarithmic scale).

leads to the ground state having an equal number of excitations in every momentum mode k. The chemical potentials for $t > 0$ are then determined by the k' and k values which minimize or maximize equation (22.7), respectively. From the dispersion in figure 24.1, one recognizes that this is given for $k' = L/2$ and $k = 0$ and thus the chemical potentials read

$$\mu_n^+ = E_{\frac{L}{2}}^{n+1} - E_{\frac{L}{2}}^n \qquad\qquad \mu_n^- = E_0^n - E_0^{n-1}, \qquad (24.4)$$

which together with the analytic form (22.6) yields

$$\mu_n^- = \frac{1-\delta_{n1}}{2}\sqrt{4(n-1)g^2 + \Delta^2} - \frac{1}{2}\sqrt{4ng^2 + \Delta^2} + \frac{\delta_{n1}}{2}\Delta, \qquad (24.5)$$
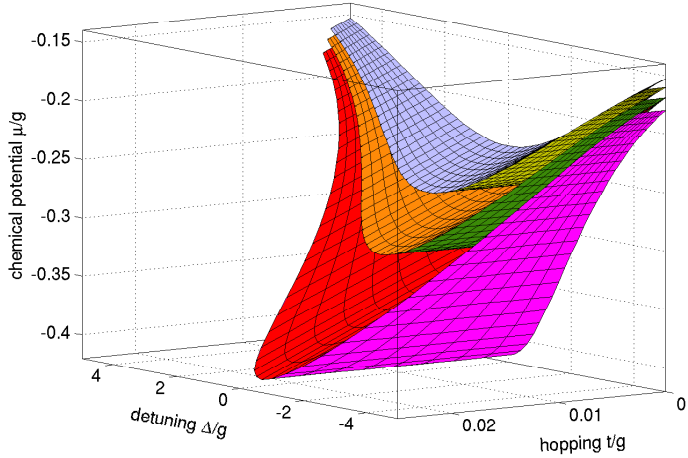
Figure 24.3: Phase diagram of the Jaynes-Cummings-Hubbard model for a linear ion chain from the fermion approximation. Boundaries of the Mott lobes (from bottom to top) for $n = 2, 3, 4$. The lobes $n = 0$ and $n = 1$ are not displayed since they are unbounded for $\Delta \to -\infty$.

and

$$\mu_n^+ = \frac{1}{2}\left[-\sqrt{4(n+1)g^2 + \left(\frac{7}{2}\zeta(3)t + \Delta\right)^2} - \frac{7}{1+\delta_{n0}}\zeta(3)t + \delta_{n0}\Delta \right.$$
$$\left. + (1 - \delta_{n0})\sqrt{4ng^2 + (\frac{7}{2}\zeta(3)t + \Delta)^2} \right]. \quad (24.6)$$

This allows to determine the resulting phase diagram shown in figure 24.2 for three values of Δ comparing the different approaches. One recognizes the typical lobe structure of the Mott insulator phases with a closing of the lobes at some value $t_n^{\mathrm{crit}}(\Delta)$. While the mean-field results underestimate the extent of the Mott insulating regions greatly (note the logarithmic scale), the fermionic approach overestimates them but with a better agreement to the strong-coupling theory than the mean-field solution. The main advantage of the fermionic approximation is the closed form for the chemical potentials for the ground state. Figure 24.3 shows the full phase diagram of the model as a function of the detuning Δ obtained from the fermionic approximation only.

The critical hopping amplitude $t_n^{\mathrm{crit}}(\Delta)$ can be calculated from the analytic expressions for the chemical potential given above. Figure 24.4 shows the dependence of the critical hopping amplitude on the detuning Δ for
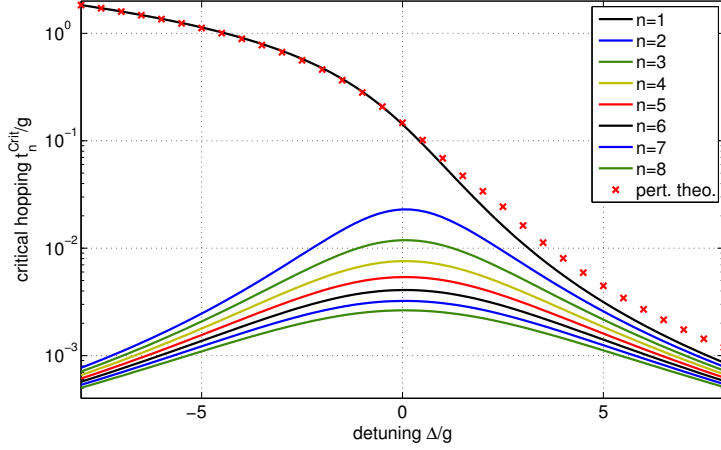
Figure 24.4: Critical hopping amplitude $t_n^{\mathrm{crit}}(\Delta)$ which gives the point where the Mott-insulator to superfluid transition takes place. From top to bottom: $n = 1 \ldots 8$, all for g=0.05. The crosses present the results for the strong-coupling theory whereas the solid lines are the results from the fermionic approximation.

the different Mott lobes. Note the unboundedness of the first lobe, i.e., $t_n^{\mathrm{crit}}(\Delta) \to \infty$ as $\Delta \to -\infty$. Additionally, the figure shows the critical hopping calculated from the strong-coupling theory for the first lobe giving a reasonable agreement of both methods.

CHAPTER 25

Conclusion and outlook

Approximating the spin-degrees of freedom in the Jaynes-Cummings-Hubbard model as fermions results in an easy analytic solution of the Hamiltonian, yielding closed expressions for the phase diagram. Although the used approximation is not fully understood yet, the predictions based on it give quite reasonable results compared to DMRG or strong-coupling theory. Being applicable to arbitrary long-ranged hopping, we constructed the phase diagram for a system describing ions in a linear ion chain. This solution of allows for an easy estimate of the position of the phase transition, not available from other methods, yet.

Though providing reasonable results, the used fermionic approximation lacks some important features. The missing understanding limits its trustworthiness where further extensions of the approximation should improve the results compared to perturbation theory, especially for the upper boundaries of the Mott insulators. Nevertheless, applications to the dynamics in the Jaynes-Cummings-Hubbard model or extensions thereof such as the spin-boson model will provide a deeper understanding of the model as well as further benchmarks of the approximation.

Appendix

Ultrafast Fermions

A.1 Fourier transform of the coupling constants

As discussed in section 9.3 in part II, the Fourier transform of the couplings (9.12) is governed by the Fourier transform of the numerator. At this place we will prove the result given in the main text using the Poisson sum formula [301]

$$\sum_{d=-\infty}^{\infty} f(d) = \sum_{l=-\infty}^{\infty} \int_{-\infty}^{\infty} f(x) e^{-2\pi i l x} \mathrm{d}x. \tag{A.1}$$

Using the definition of the Fourier transform (9.18) together with a rewriting of the cosine parts, the Fourier transformation can be written as

$$\sum_{d=-\infty}^{\infty} \cos d\xi \cos d\xi' e^{ikd} = \frac{1}{4} \sum_{C_1,C_2=-1,1} \sum_{d=-\infty}^{\infty} e^{id(C_1\xi + C_2\xi' + k)} \tag{A.2}$$

$$:= \frac{1}{4} \sum_{C_1,C_2=-1,1} \sum_{d=-\infty}^{\infty} e^{id\alpha}. \tag{A.3}$$

For the last term, we now apply the Poisson sum formula:

$$\sum_{d=-\infty}^{\infty} e^{i\alpha d} = \sum_{l=-\infty}^{\infty} \int_{-\infty}^{\infty} e^{ix\alpha} e^{-2\pi i l x} \mathrm{d}x \tag{A.4}$$

$$= \sum_{l=-\infty}^{\infty} \int_{-\infty}^{\infty} e^{i(\alpha - 2\pi l)x} \mathrm{d}x \qquad (A.5)$$

$$= 2\pi \sum_{l=-\infty}^{\infty} \delta(\alpha - 2\pi l). \qquad (A.6)$$

Together with the definition of α we end up in the stated relation

$$\sum_{d=-\infty}^{\infty} \cos d\xi \cos d\xi' e^{ikd} = \frac{\pi}{2} \sum_{l=-\infty}^{\infty} \sum_{C_1, C_2 = -1, 1} \delta(2\pi l - C_1 \xi - C_2 \xi' - k). \quad (A.7)$$

A.2 Fourier transform of the Green's functions

In section 10.2, the solution of the Dyson equation for the Green's function is presented. At this point we summarize the important points in the Fourier transform of the Green's functions, going back from the frequency domain to time domain. From equations (10.15) and (10.16) and with the definition of the Fourier transform

$$\mathcal{G}_{kk'}^{(\pm)}(t+T, t) = \frac{1}{\sqrt{2\pi}} \int_{-\infty}^{\infty} \mathrm{d}\omega \, \mathcal{G}_{kk'}^{(\pm)}(\omega) e^{i\omega T}, \qquad (A.8)$$

the calculation of $\mathcal{G}_{kk'}^{(\pm)}(t+T, t)$ is straight forward.

a) Equal momentum

For $\mathcal{G}_{kk}^{(\pm)}(t+T, t)$, the Fourier transformation together with (10.15) gives

$$\mathcal{G}_{kk}^{(\pm)}(t+T, t) = \pm \frac{i}{2\pi} \int_{-\infty}^{\infty} \mathrm{d}\omega \, \frac{\varepsilon_k \pm \omega \oplus i\delta}{\varepsilon_k^2 \oplus 2i\delta\varepsilon_k - \delta^2 - \omega^2 + \frac{V^2 \eta_B^2 \varrho_B^2}{\hbar^2}} e^{i\omega T}. \qquad (A.9)$$

Since the convergence factor δ is chosen in the limit $\delta \to 0$, the δ^2 in the denominator may be neglected. Looking at the dispersion of the free fermions (10.9) and taking into account the definition of $\oplus$, the combination $\oplus\varepsilon_k$ is always of negative sign, since for $k \in \mathcal{K}_F$, $\oplus$ means $+$ but $\varepsilon_k < 0$. In the

other case the signs are just the other way around. Neglecting the factor of 2 before the δ and defining the renormalized dispersion

$$\bar{\varepsilon}_k = \sqrt{\varepsilon_k^2 + \frac{V^2 \eta_B^2 \eta_B^2}{\hbar^2}}, \tag{A.10}$$

the Green's function calculates as

$$\mathcal{G}_{kk}^{(\pm)}(t+T,t) = \pm \frac{i}{2\pi} \int\limits_{-\infty}^{\infty} \mathrm{d}\omega \, \frac{\varepsilon_k \pm \omega \oplus i\delta}{\bar{\varepsilon}_k^2 - \omega^2 - i\delta} \, e^{i\omega T}. \tag{A.11}$$

This integration is done by means of residue integration [302], where the contour is closed in the upper half plain, enclosing the pole at $\omega_0 = -\sqrt{\bar{\varepsilon}_k^2 - i\delta}$. Finally, after performing the limit $\delta \to 0$, the Green's function is given by

$$\mathcal{G}_{kk}^{(\pm)}(t+T,t) = \frac{1}{2} e^{-i\bar{\varepsilon}_k T} \left(1 \mp \frac{\varepsilon_k}{\bar{\varepsilon}_k} \right). \tag{A.12}$$

b)   Unequal momentum

The calculation for $\mathcal{G}_{kk+\frac{L}{2}}^{(\pm)}(t+T,t)$ follows the same route as described above. Using the result for the Green's function in the frequency domain (10.16) and the same argument for the combination $\oplus \varepsilon_k$ as above, the Fourier transform is calculated from

$$\mathcal{G}_{k\pm\frac{L}{2}k}^{(\pm)}(t+T,t) = i \frac{V \eta_B \varrho_B}{2\pi\hbar} \int\limits_{-\infty}^{\infty} \mathrm{d}\omega \, \frac{1}{\bar{\varepsilon}_k^2 - \omega^2 - i\delta} e^{i\omega T}. \tag{A.13}$$

Again closing the contour in the upper half plain with the same pole as above, the residue integration gives

$$\mathcal{G}_{k\pm\frac{L}{2}k}^{(\pm)}(t+T,t) = -\frac{V \eta_B \varrho_B}{2\hbar} \frac{1}{\bar{\varepsilon}_k} e^{-i\bar{\varepsilon}_k T} \tag{A.14}$$

as stated in the main text.

A.3   Zero-hopping energies for the phase diagram

Chapter 12 shows, how to calculate the phase diagram of the effective bosonic Hamiltonian analytically. Here we present exemplary the calculation of the energies for the three different incompressible phases.

a)   CDW phase $\varrho_B = \frac{1}{2}$

As discussed in the main text, the ground state for precisely half filling is given by the distribution

$$\bullet \circ \bullet \circ \| \bullet \| \circ \bullet \circ \bullet \qquad \triangleq \qquad n_j = \widetilde{n}_j = \frac{1}{2}\left[1 + (-1)^j\right]. \qquad (\text{A.15})$$

Adding a single particle results in the two possible situation, where the additional particle goes to a double occupation at an even site or to an odd site having only single occupations.

i)   Double occupation

In the case for the double occupation, the boson distribution is written as

$$\bullet \circ \bullet \circ \| \overset{\bullet}{\bullet} \| \circ \bullet \circ \bullet \qquad \Rightarrow \qquad n_j = \widetilde{n}_j + \delta_{j,0}. \qquad (\text{A.16})$$

Plugging this into the effective Hamiltonian (12.1), the energy may be calculated straightforwardly.

$$
\begin{aligned}
E[\bullet \circ \bullet \circ \| \overset{\bullet}{\bullet} \| \circ \bullet \circ \bullet] \\
&= \frac{U}{2}\sum_j (\widetilde{n}_j + \delta_{j,0})(\widetilde{n}_j + \delta_{j,0} - 1) - \bar{\mu}\sum_j (\widetilde{n}_j + \delta_{j,0}) \qquad &(\text{A.17}) \\
&\quad - \Delta\sum_j (\widetilde{n}_j + \delta_{j,0})(-1)^j + \sum_j \sum_d g_d(a)(\widetilde{n}_j + \delta_{j,0})(\widetilde{n}_{j+d} + \delta_{j+d,0}) \\
&= \frac{U}{2}\sum_j \left[2\widetilde{n}_j\delta_{j,0} + \delta_{j,0}^2 - \delta_{j,0}\right] - \bar{\mu} - \Delta \\
&\quad + \sum_j \sum_d g_d(a)\left[\widetilde{n}_j\delta_{j+d,0} + \widetilde{n}_{j+d}\delta_{j,0} + \delta_{j,0}\delta_{j+d,0}\right] \qquad &(\text{A.18}) \\
&\quad - \bar{\mu}\sum_j \widetilde{n}_j - \Delta\sum_j \widetilde{n}_j(-1)^j + \sum_j \sum_d g_d(a)\widetilde{n}_j\widetilde{n}_{j+d} \\
&= E[\bullet \circ \bullet \circ \| \bullet \| \circ \bullet \circ \bullet] \qquad &(\text{A.19}) \\
&\quad + U - \bar{\mu} - \Delta + \frac{1}{2}\sum_d g_d(a)\left(1 + (-1)^d\right) + g_0(a) \\
&= E[\bullet \circ \bullet \circ \| \bullet \| \circ \bullet \circ \bullet] \qquad &(\text{A.20}) \\
&\quad + U - \bar{\mu} - \Delta + \widetilde{g}_a(0) + \widetilde{g}_a(\pi) + g_0(a).
\end{aligned}
$$

ii) Single occupation

For the single occupation, the calculation of the energy follows exactly the same route. The boson occupation may be written as

$$\bullet \circ \bullet \circ \| \bullet \| \bullet \bullet \circ \bullet \qquad \Rightarrow \qquad n_j = \widetilde{n}_j + \delta_{j,1} \tag{A.21}$$

and the energy gives:

$$
\begin{aligned}
E[\bullet \circ \bullet \circ \| \bullet \| \bullet \bullet \circ \bullet] & \\
&= \frac{U}{2} \sum_j (\widetilde{n}_j + \delta_{j,1})(\widetilde{n}_j + \delta_{j,1} - 1) - \bar{\mu} \sum_j (\widetilde{n}_j + \delta_{j,1}) \tag{A.22} \\
&\quad - \Delta \sum_j (\widetilde{n}_j + \delta_{j,1})(-1)^j + \sum_j \sum_d g_d(a)(\widetilde{n}_j + \delta_{j,1})(\widetilde{n}_{j+d} + \delta_{j+d,1}) \\
&= \frac{U}{2} \sum_j \left[2\widetilde{n}_j \delta_{j,1} + \delta_{j,1}^2 - \delta_{j,1} \right] - \bar{\mu} + \Delta \\
&\quad + \sum_j \sum_d g_d(a) \left[\widetilde{n}_j \delta_{j+d,1} + \widetilde{n}_{j+d} \delta_{j,1} + \delta_{j,1} \delta_{j+d,1} \right] \tag{A.23} \\
&\quad - \bar{\mu} \sum_j \widetilde{n}_j - \Delta \sum_j \widetilde{n}_j (-1)^j + \sum_j \sum_d g_d(a) \widetilde{n}_j \widetilde{n}_{j+d} \\
&= E[\bullet \circ \bullet \circ \| \bullet \| \circ \bullet \circ \bullet] \tag{A.24} \\
&\quad - \bar{\mu} + \Delta + \frac{1}{2} \sum_d g_d(a) \left(1 - (-1)^d \right) + g_0(a) \\
&= E[\bullet \circ \bullet \circ \| \bullet \| \circ \bullet \circ \bullet] - \bar{\mu} + \Delta + \widetilde{g}_a(0) - \widetilde{g}_a(\pi) + g_0(a). \tag{A.25}
\end{aligned}
$$

b) Mott insulator $\varrho_B = 1$

Now, for $\eta_B \equiv 0$, the calculation of the energy for the addition or removal of a single particle is straightforward. The states themselves are given by

$$\bullet \bullet \bullet \bullet \| {\overset{\bullet}{\bullet}} \| \bullet \bullet \bullet \bullet \qquad \Rightarrow \qquad n_j = 1 + \delta_{j,0} \tag{A.26}$$

and

$$\bullet \bullet \bullet \bullet \| \circ \| \bullet \bullet \bullet \bullet \qquad \Rightarrow \qquad n_j = 1 - \delta_{j,0}. \tag{A.27}$$

Using the effective Hamiltonian (10.39) for $\eta_B \equiv 0$ we can calculate the energy for both configurations at once. This gives

$$E(L \pm 1) = \pm \frac{U}{2} \sum_j (1 \pm \delta_{j,0}) \delta_{j,0} - \bar{\mu} \sum_j (1 \pm \delta_{j,0}) \tag{A.28}$$

$$- \Delta \sum_j (-1)^j (1 \pm \delta_{j,0}) + \sum_j \sum_d g_d(0)(1 \pm \delta_{j,0})(1 \pm \delta_{j+D,0})$$

$$= \pm \frac{U}{2}(1 \pm 1) - L\bar{\mu} \mp \bar{\mu} \mp \Delta \tag{A.29}$$

$$+ \sum_j \sum_d g_d(0) \left[1 \pm \delta_{j+D,0} \pm \delta_{j,0} + \delta_{j,0}\delta_{j+D,0}\right]$$

$$= E(L) + \frac{U}{2}(1 \pm 1) \mp \bar{\mu} \mp \Delta \pm 2\widetilde{g}_0(0) + g_0(0). \tag{A.30}$$

A.4 Green's function approach to spinless fermions in an alternating potential

Chapter 10 provides a renormalization procedure for the case of double half filling of the fermions and bosons. In this chapter we generalize these results to arbitrary fillings of the form $\varrho_F = \frac{1}{m}$, where $m \in \mathbb{N}$ and $\varrho_B = \varrho_F$. As already discussed in chapter 9, the fermions trigger a bosonic CDW at the same density, where the term CDW for $m > 2$ is not that accurate. For instance for $m = 4$, i.e., $\varrho_F = \varrho_B = \frac{1}{4}$, the bosonic distribution according to the induced couplings is given by the case where a boson is found in every fourth site. So as a starting point for the renormalization of the fermionic system, the potential influencing the fermions is that of a potential with a singular peak in every fourth site. For general m, the fermionic problem is thus given by the bosonic mean-field amplitude

$$\widetilde{n}_j = \varrho_B(1 - \eta_B) + m\varrho_B\eta_B \; \delta(\sin(\pi \frac{j}{m})), \tag{A.31}$$

as introduced in chapter 10 and together with this, the fermionic Hamiltonian from (8.3) looks like

$$\hat{H}_{\mathrm{F}} = -J_F \sum_j \left(\hat{c}_j^\dagger \hat{c}_{j+1} + \hat{c}_{j+1}^\dagger \hat{c}_j \right) + Vm \sum_j \delta(\sin(\pi \frac{j}{m}))\hat{c}_j^\dagger \hat{c}_j. \tag{A.32}$$

Here we replaced the factor $V\eta_B\varrho_B$ by V since our result is more general than only renormalizing the coupling constants as a function of η_B. Again,
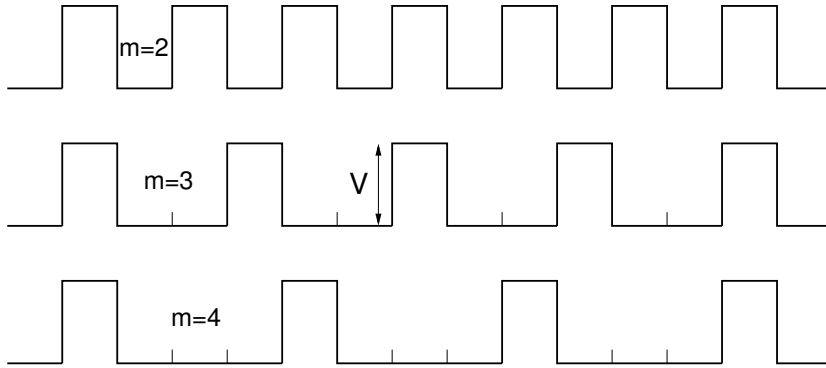
Figure A.1: Visualization of the Dirac comb potential for different periods m.

the constant energy $\varrho_F \varrho_B (1 - \eta_B)$ is neglected and in the following we will refer to this model as to free fermions in a Dirac comb potential. Figure A.1 visualizes the underlying potential in this problem for different values of m.

In the direct solution for the case $m = 2$ we switched into momentum space since this turned out to be much simpler. This still holds for the generalized Hamiltonian (A.32) which in momentum space, after application of the Fourier transform (9.2) is given by

$$\hat{H}_{\mathrm{F}} = \sum_{k=-L/2}^{L/2-1} \varepsilon_k \, \hat{f}_k^\dagger \hat{f}_k + V \sum_{\substack{\alpha=-(m-1) \\ \alpha \neq 0}}^{m-1} \sum_{k=-L/2}^{L/2-1} \hat{f}_{k+\frac{L}{m}\alpha}^\dagger \hat{f}_k, \,. \tag{A.33}$$

The summation over α is restricted because of the limitation in the possible momentum modes $k \in [-\frac{L}{2}, \frac{L}{2} - 1]$ and the $\alpha = 0$ term is neglected because it would only give a constant energy. The single particle energies are given by $\varepsilon_k = -2J_F \cos(2\pi \frac{k}{L})$. This Hamiltonian is the starting point for the calculation of the Green's function as already done in chapter 10. But before using the perturbative treatment, we discuss the possibility of a direct solution of the real space version (A.32) of the model.

a)   Exact solution via canonical transformation

The considered Hamiltonian (A.32) is quadratic in the creation and annihilation operators and can be solved analytically by means of a canonical transformation. This can be easily seen after rewriting the Hamiltonian such

that the quadratic structure becomes obvious:

$$
\hat{\mathcal{H}} = \sum_l \hat{\mathbf{c}}_l^{\dagger}
\begin{bmatrix}
0 & -J_F & & & \\
-J_F & V & -J_F & & \\
& -J_F & 0 & -J_F & \\
& & \ddots & \ddots & \ddots \\
& & & -J_F & 0
\end{bmatrix}
\hat{\mathbf{c}}_l.
\tag{A.34}
$$

Here $\hat{\mathbf{c}}_l = (\hat{c}_{lm-1}, \hat{c}_{lm}, \hat{c}_{lm+1}, \ldots, \hat{c}_{lm+\underline{m}-1})^{\mathrm{T}}$. The transformation can now be found by diagonalizing the matrix $\bar{M} = [\cdots] = U^{\dagger} D U$ from above Hamiltonian and defining new fermionic operators $\hat{\mathbf{e}}_l = U \hat{\mathbf{c}}_l$ (a similar approach is presented in [178, 234]). The diagonalized Hamiltonian is then given by

$$
\hat{\mathcal{H}} = \sum_l \sum_{n=-1}^{m-1} \epsilon_{n+2} \, \hat{e}_{lm+n}^{\dagger} \hat{e}_{lm+n} = \sum_j \widetilde{\epsilon}_j \hat{e}_j^{\dagger} \hat{e}_j,
\tag{A.35}
$$

where ϵ_p is the $p-$th eigenvalues of $\bar{\bar{M}}$ and the on-site energies $\widetilde{\epsilon}_j$ are defined as

$$
\widetilde{\epsilon}_j =
\begin{cases}
\epsilon_1 + \epsilon_{m+1} & \mathrm{rem}(j, m) = m - 1 \\
\epsilon_{\mathrm{rem}(j,m)+2} & \mathrm{else}
\end{cases}.
\tag{A.36}
$$

$\mathrm{rem}(j, m)$ is the remainder after division of j by m.

Since for any m the system is periodic, the single particle energies $\widetilde{\epsilon}_j$ have period m, too and are typically non-degenerate. The solution of this Hamiltonian for a fixed fermionic density

$$
\varrho_F = \sum_j \hat{c}_j^{\dagger} \hat{c}_j = \sum_j \hat{e}_j^{\dagger} \hat{e}_j
\tag{A.37}
$$

is straightforward. Defining the set $\mathcal{J}$ of minimal single particle energies

$$
\mathcal{J} = \{ j \in \mathbb{Z} \big| \widetilde{\epsilon}_j = \min_{p=0\ldots m-1} \widetilde{\epsilon}_p \},
\tag{A.38}
$$

the ground state of Hamiltonian (A.35) manifold is given by any possible combination of particles located at sites, where only sites from $\mathcal{J}$ are occupied. For the typical case of a unique minimal value $\widetilde{\epsilon}_j$ and a finite lattice of length L, the cardinality of the set $\mathcal{J}$ is equal to $\varrho_F L$ and the ground state is given by

$$
|\Psi\rangle = \prod_{j \in \mathcal{J}} \hat{e}_j^{\dagger} |0\rangle.
\tag{A.39}
$$

Although this solution of Hamiltonian (A.32) using the canonical transformation is straightforward, the resulting ground state is nontrivial and therefore the transformation back to the original system will not be done. Instead we will apply a Green's functions approach for the calculation of different expectation values of the ground state of Hamiltonian (A.33).

b) Green's functions approach

So far, the derivation of the Dyson equation for the Green's function does not strongly differ from the results already presented in section 10.1. The only difference is given by the different range of the sum over α (compare the Hamiltonian (A.32) to the $m = 2$ Hamiltonian from (10.5)). This leads, restricting our discussion to the case of the advanced Green's function $\mathcal{G}_{k,k'}^{(+)}(\omega)$, to the Dyson equation

$$\mathcal{G}_{k,k'}^{(+)}(\omega) = \mathcal{G}_{k,k'}^{(0+)}(\omega) + \frac{i}{\hbar}\sqrt{2\pi}V\mathcal{G}_{k,k}^{(0+)}(\omega)\sum_{\substack{\alpha=-m+1 \\ \alpha\neq 0}}^{m-1}\mathcal{G}_{k+\frac{L}{m}\alpha,k'}^{(+)}(\omega) \qquad (A.40)$$

in both momentum and frequency space. This Dyson equation allows for a straightforward solution in the case $m = 2$ as presented in chapter 10 with more difficulties for other m. Nevertheless, a full algebraic solution may be found. Recognizing that above Dyson equation may be rewritten in the form

$$\mathcal{G}_{kk'}^{(0+)}(\omega) = \sum_{\alpha=-(m-1)}^{m-1}\Gamma_{k,\alpha}\,\mathcal{G}_{k+\frac{L}{m}\alpha,k'}^{(+)}(\omega) \qquad (A.41)$$

and that according to the properties of the unperturbed Green's function $\mathcal{G}_{k,k'}^{(0+)} \sim \delta_{k,k'}$ only the contributions of the form $\mathcal{G}_{k+p\frac{L}{m},k'}^{(+)}$ are non-zero, all Dyson equations for the non-zero elements may be put into matrix form:

$$\begin{pmatrix} \mathcal{G}_{k+\frac{m-1}{m}L,k'}^{(0+)}(\omega) \\ \mathcal{G}_{k+\frac{m-2}{m}L,k'}^{(0+)}(\omega) \\ \vdots \\ \mathcal{G}_{k,k'}^{(0+)}(\omega) \\ \vdots \\ \mathcal{G}_{k-\frac{m-2}{m}L,k'}^{(0+)}(\omega) \\ \mathcal{G}_{k-\frac{m-1}{m}L,k'}^{(0+)}(\omega) \end{pmatrix} = \bar{\bar{\Gamma}} \begin{pmatrix} \mathcal{G}_{k+\frac{m-1}{m}L,k'}^{(+)}(\omega) \\ \mathcal{G}_{k+\frac{m-2}{m}L,k'}^{(+)}(\omega) \\ \vdots \\ \mathcal{G}_{k,k'}^{(+)}(\omega) \\ \vdots \\ \mathcal{G}_{k-\frac{m-2}{m}L,k'}^{(+)}(\omega) \\ \mathcal{G}_{k-\frac{m-1}{m}L,k'}^{(+)}(\omega) \end{pmatrix} \qquad (A.42)$$

with

$$
\bar{\bar{\Gamma}} = \begin{bmatrix}
1 & \widetilde{\Gamma}_{\frac{m-1}{m}} & \widetilde{\Gamma}_{\frac{m-1}{m}} & \dots & 0 & 0 & 0 \\
\widetilde{\Gamma}_{\frac{m-2}{m}} & 1 & \widetilde{\Gamma}_{\frac{m-2}{m}} & \dots & \widetilde{\Gamma}_{\frac{m-2}{m}} & 0 & 0 \\
\vdots & & \ddots & & & \vdots & \\
\widetilde{\Gamma}_0 & \widetilde{\Gamma}_0 & \dots & 1 & \dots & \widetilde{\Gamma}_0 & \widetilde{\Gamma}_0 \\
\vdots & & & \ddots & & \vdots & \vdots \\
0 & 0 & \widetilde{\Gamma}_{-\frac{m-2}{m}} & \dots & \widetilde{\Gamma}_{-\frac{m-2}{m}} & 1 & \widetilde{\Gamma}_{-\frac{m-2}{m}} \\
0 & 0 & 0 & \dots & \widetilde{\Gamma}_{-\frac{m-1}{m}} & \widetilde{\Gamma}_{-\frac{m-1}{m}} & 1
\end{bmatrix} . \tag{A.43}
$$

Here $\widetilde{\Gamma}_\beta = \Gamma_{k+\beta L,1}$ and $\Gamma_{k,\alpha} = \delta_{\alpha 0} - (1-\delta_{\alpha 0})\frac{i}{\hbar}\sqrt{2\pi}V\mathcal{G}_{k,k}^{(0+)}$ simplify the writing.

This matrix equation can be solved for $\mathcal{G}_{k,k'}^{(+)}$ by inverting the matrix $\bar{\bar{\Gamma}}$ and considering the proper entries. All further results rely on this procedure, where the remaining task in the solution is not the inversion of the matrix $\bar{\bar{\Gamma}}$ which is (only) of size $(2m-1) \times (2m-1)$, but the following Fourier transformation of the Green's function into time domain. For $m = 2$ this may be done easily whereas for larger m numerical residue integration turns out to be more suitable. Together with the numerical evaluation of the Fourier transform, this now allows for the calculation of the real space Green's functions and the expectation values of the system from these.

c)   Expectation values

Above algebraic equation allows for the calculation of the Green's function $\mathcal{G}_{k,k'}^{(+)}(\omega)$ which is directly connected to all needed expectation values. The real space Green's function connects to the momentum space Green's functions as

$$
\mathcal{G}_{j,j+d}^{(+)}(\omega) = \frac{1}{L} \sum_{k_1,k_2=-L/2}^{L/2-1} e^{-2\pi i \frac{(k_1-k_2)}{L} j} e^{-2\pi i \frac{k_1}{L} d} \mathcal{G}_{k_2,k_1}^{(+)}(\omega). \tag{A.44}
$$

Again, the summation over the second index is limited because of the properties of the Green's function, in general incorporated by including the term

$$
\sum_{n=-(m-1)}^{m-1} \delta_{k_1+\frac{n}{m}L,k_2} \tag{A.45}
$$

to the summation. This results in

$$
\mathcal{G}_{j,j+d}^{(+)}(\omega) = \frac{1}{L} \sum_{k} \sum_{n=-m+1}^{m-1} e^{-2\pi i \frac{k}{L} d} e^{-2\pi i \frac{n}{m} j} \mathcal{G}_{k_1+\frac{n}{m}L,k_1}^{(+)}(\omega) \tag{A.46}
$$

which together with

$$\mathcal{G}^{(\pm)}_{j,j+d}(t+T,t) = \frac{1}{\sqrt{2\pi}} \int\limits_{-\infty}^{\infty} d\omega\, \mathcal{G}^{(\pm)}_{j,j+d}(\omega) e^{i\omega T} \qquad (A.47)$$

at the end gives the final expression for the calculation of the expectation values.

Multi-band physics

B.1 Calculation of the second order cumulant

We present the derivation of the effective first-band Hamiltonian from the scattering matrix in (16.5) together with the full interaction Hamiltonian. In the reduced scattering matrix of the multi-band Bose-Fermi-Hubbard model, the second order cumulant

$$\langle\langle \mathcal{T}\ \hat{H}_{\mathrm{I}}(\tau + T)\hat{H}_{\mathrm{I}}(\tau)\rangle\rangle_{b\mathrm{th}} \tag{B.1}$$

in the interaction picture needs to be calculated with respect to the vacuum in the b-th band. Because of the average over the vacuum, the evaluation of the cumulant simplifies considerably. For instance, from the last interaction Hamiltonian at time τ, only those terms with no annihilation operators in the b-th band contribute. This strongly reduces the computational effort. For a detailed analysis, we first rewrite the interaction Hamiltonian $\hat{H}_{\mathrm{I}}(\sigma)$ in such a way, that the occurring contributions become apparent. Omitting the explicit time dependence σ, the Hamiltonian in the interaction picture is given by

$$\hat{H}_{b\mathrm{th}}^{\mathrm{int}} = \sum_{j}\left\{ \underbrace{\frac{U_{bb11}}{2}\left(\hat{a}_{b,j}^{\dagger}\right)^{2}\hat{a}_{1,j}^{2}}_{\textcircled{1}} \ + \underbrace{\frac{U_{bb11}}{2}\left(\hat{a}_{1,j}^{\dagger}\right)^{2}\hat{a}_{b,j}^{2}}_{\textcircled{1}} \ + 4\frac{U_{bb11}}{2}\hat{n}_{b,j}\hat{n}_{1,j} \right.$$
$$\left. + \underbrace{\frac{V_{bb11}}{2}\hat{a}_{b,j}^{\dagger}\hat{c}_{b,j}^{\dagger}\hat{c}_{1,j}\hat{a}_{1,j}}_{\textcircled{2}} \ + \underbrace{\frac{V_{bb11}}{2}\hat{a}_{1,j}^{\dagger}\hat{c}_{1,j}^{\dagger}\hat{c}_{b,j}\hat{a}_{b,j}}_{\textcircled{2}} \ + \frac{V_{b11b}}{2}\hat{m}_{1,j}\hat{n}_{b,j} \right. \tag{B.2}$$

$$
\begin{aligned}
&+ \frac{V_{bb11}}{2}\hat{a}^{\dagger}_{b,j}\hat{c}^{\dagger}_{1,j}\hat{c}_{b,j}\hat{a}_{1,j} + \frac{V_{bb11}}{2}\hat{a}^{\dagger}_{1,j}\hat{c}^{\dagger}_{b,j}\hat{c}_{1,j}\hat{a}_{b,j} + \frac{V_{1bb1}}{2}\hat{m}_{b,j}\hat{n}_{1,j} \\
&+ \underset{\textcircled{3}}{\underwave{U_{b111}\hat{n}_{1,j}\hat{a}^{\dagger}_{b,j}\hat{a}_{1,j}}} \quad + \underset{\textcircled{3},\textcircled{4}}{\underline{\underline{U_{b111}\hat{a}^{\dagger}_{1,j}\hat{a}_{b,j}\hat{n}_{1,j}}}} \quad + U_{1bbb}\hat{n}_{b,j}\hat{a}^{\dagger}_{1,j}\hat{a}_{b,j} \\
&+ \underset{\textcircled{4}}{\underwave{\frac{V_{b111}}{2}\hat{m}_{1,j}\hat{a}^{\dagger}_{b,j}\hat{a}_{1,j}}} \; + \underset{\textcircled{3},\textcircled{4}}{\underline{\underline{\frac{V_{b111}}{2}\hat{m}_{1,j}\hat{a}^{\dagger}_{1,j}\hat{a}_{b,j}}}} \quad + U_{1bbb}\hat{a}^{\dagger}_{b,j}\hat{a}_{1,j}\hat{n}_{b,j} \qquad\qquad \text{(B.3)} \\
&+ \underset{\textcircled{5}}{\underwave{\frac{V_{1b11}}{2}\hat{n}_{1,j}\hat{c}^{\dagger}_{b,j}\hat{c}_{1,j}}} \; + \underset{\textcircled{5}}{\underline{\underline{\frac{V_{1b11}}{2}\hat{n}_{1,j}\hat{c}^{\dagger}_{1,j}\hat{c}_{b,j}}}} \; + \frac{V_{1bbb}}{2}\hat{m}_{b,j}\hat{a}^{\dagger}_{1,j}\hat{a}_{b,j} \\
&+ \frac{V_{1bbb}}{2}\hat{m}_{b,j}\hat{a}^{\dagger}_{1,j}\hat{a}_{1,j} + \frac{V_{b1bb}}{2}\hat{n}_{b,j}\hat{c}^{\dagger}_{1,j}\hat{c}_{b,j} + \frac{V_{b1bb}}{2}\hat{n}_{b,j}\hat{c}^{\dagger}_{b,j}\hat{c}_{1,j}\Bigg\}.
\end{aligned}
$$

Interaction amplitudes U or V with an even number of higher-band indices b contribute for any bands, those with an odd number only for odd bands. A wavy underline corresponds to the terms with non-vanishing action onto the vacuum, i.e., those terms relevant for the application of $\hat{H}_{\mathrm{I}}(\tau)$. Double underlines accordingly highlight the terms relevant in the subsequent application of $\hat{H}_{\mathrm{I}}(\tau + T)$. The circled numbers denote the combination of operators which after all give a non-zero matrix element. This means, that the calculation of $\langle\langle \underset{\textcircled{1}}{\underwave{A}} \;\; \underset{\textcircled{1}}{\underline{\underline{B}}} \rangle\rangle$ gives a non-zero contribution; other combinations give a zero. The remaining terms not underlined give no contribution in second order of the cumulant expansion.

The calculation of the second order cumulant is straightforward and for $T > 0$ evaluates to

$$
\begin{aligned}
\langle\langle \underline{\hat{H}_{\mathrm{I}}(\tau + T)}\hat{H}_{\mathrm{I}}(\tau)\rangle\rangle_{b\mathrm{th}} = \sum_{jl}\Bigg\{ &\frac{U^2_{bb11}}{4}\left(\underline{\hat{a}^{\dagger}_{1,j+d}}\right)^2\hat{a}^2_{1,j}\langle\langle \underline{\hat{a}^2_{b,j+d}}\left(\hat{a}^{\dagger}_{b,j}\right)^2\rangle\rangle_{b\mathrm{th}} \\
&+ \frac{V^2_{bb11}}{4}\underline{\hat{a}^{\dagger}_{1,j+d}\hat{c}^{\dagger}_{1,j+d}}\hat{c}_{1,j}\hat{a}_{1,j}\langle\langle \underline{\hat{c}_{b,j+d}\hat{a}_{b,j+d}}\hat{a}^{\dagger}_{b,j}\hat{c}^{\dagger}_{b,j}\rangle\rangle_{b\mathrm{th}} \\
&+ U^2_{b111}\mathcal{C}^T_{B,b}(d)\underline{\hat{a}^{\dagger}_{1,j+d}\hat{n}_{1,j+d}}\hat{n}_{1,j}\hat{a}_{1,j} + \frac{U_{b111}V_{b111}}{2}\mathcal{C}^T_{B,b}(d)\underline{\hat{m}_{1,j+d}\hat{a}^{\dagger}_{1,j+d}}\hat{n}_{1,j}\hat{a}_{1,j} \\
&+ \frac{V_{b111}U_{b111}}{2}\mathcal{C}^T_{B,b}(d)\underline{\hat{a}^{\dagger}_{1,j+d}\hat{n}_{1,j+d}}\hat{m}_{1,j}\hat{a}_{1,j} + \frac{V^2_{b111}}{4}\mathcal{C}^T_{B,b}(d)\underline{\hat{m}_{1,j+d}\hat{a}^{\dagger}_{1,j+d}}\hat{m}_{1,j}\hat{a}_{1,j} \\
&+ \frac{V^2_{1b11}}{4}\mathcal{C}^T_{F,b}(d)\underline{\hat{n}_{1,j+d}\hat{c}^{\dagger}_{1,j+d}}\hat{n}_{1,j}\hat{c}_{1,j}\Bigg\}.
\end{aligned}
$$

$$\text{(B.4)}$$

Here, the time dependence of each operator is encoded in the underlines. The time-argument of the underlined operators is $\tau + T$, whereas the argument

for the others is τ. The higher-band cumulants are defined as

$$\mathcal{C}_{B,b}^T(d) = \langle \hat{a}_{b,j+d}(\tau + T)\hat{a}_{b,j}^\dagger(\tau)\rangle_{b\text{th}} \quad \mathcal{C}_{F,b}^T(d) = \langle \hat{c}_{b,j+d}(\tau + T)\hat{c}_{b,j}^\dagger(\tau)\rangle_{b\text{th}} \quad (\text{B.5})$$

and, as will turn out in the next section, only depend on the distance d between j and l. The higher cumulants simplify according to [226] and [227] to

$$\langle\langle \hat{a}_{b,j+d}^2(\tau + T)\left(\hat{a}_{b,j}^\dagger(\tau)\right)^2\rangle\rangle_{b\text{th}} = 2\left(\mathcal{C}_{B,b}^T(d)\right)^2 \qquad (\text{B.6})$$

$$\langle\langle \hat{c}_{b,j+d}(\tau + T)\hat{a}_{b,j+d}(\tau + T)\hat{a}_{b,j}^\dagger(\tau)\hat{c}_{b,j}^\dagger(\tau)\rangle\rangle_{b\text{th}} = \mathcal{C}_{B,b}^T(d)\mathcal{C}_{F,b}^T(d). \qquad (\text{B.7})$$

For $T < 0$, the time ordering operator interchanges the times, which has the net effect that T in the higher-band cumulants has to be replaced by $-T$.

B.2 Bosonic and fermionic correlators

Using the free Hamiltonian

$$\begin{aligned}
\hat{H}_{b\text{th}}^{\text{free}} = J_b^B \sum_j \left(\hat{a}_{b,j}^\dagger\hat{a}_{b,j+1} + \hat{a}_{b,j+1}^\dagger\hat{a}_{b,j}\right) + \Delta_b^B \sum_j \hat{n}_{b,j} \\
+ J_b^F \sum_j \left(\hat{c}_{b,j}^\dagger\hat{c}_{b,j+1} + \hat{c}_{b,j+1}^\dagger\hat{c}_{b,j}\right) + \Delta_b^F \sum_j \hat{m}_{b,j},
\end{aligned} \qquad (\text{B.8})$$

within the b-th band, we calculate the bosonic and fermionic correlators used in B.4. In both cases, this is done in momentum space. For the simple two-point correlators the interaction terms are always irrelevant and are thus left out. Since the structure of both, the bosonic and fermionic components, are equal the calculation of the correlators is roughly the same. Focussing on the fermionic component with the free Hamiltonian

$$\hat{H}_{b\text{th}}^{\text{free}} = J_b^F \sum_j \left(\hat{c}_{b,j}^\dagger\hat{c}_{b,j+1} + \hat{c}_{b,j+1}^\dagger\hat{c}_{b,j}\right) + \Delta_b^F \sum_j \hat{m}_{b,j} \qquad (\text{B.9})$$

the calculation of the fermionic correlator $\langle \hat{c}_{b,j+d}(\tau+T)\hat{c}_{b,j}^\dagger(\tau)\rangle_{b\text{th}}$ with respect to the vacuum state is straightforward. Using the Fourier transform of the bosonic or fermionic operators presented in (9.2), the fermionic correlator

evaluates as

$$
\begin{aligned}
\langle \hat{c}_{b,j+d}(\tau + T)\hat{c}_{b,j}^\dagger(\tau)\rangle_{\mathrm{bth}} &= \frac{1}{L}\sum_{k_1 k_2} e^{-2\pi i j \frac{k_1 - k_2}{L}} e^{-2\pi i d \frac{k_1}{L}} \langle \hat{c}_{b,k_1}(\tau + T)\hat{c}_{b,k_2}^\dagger(\tau)\rangle_{\mathrm{bth}} \\
&= \frac{1}{L}\sum_{k_1 k_2} e^{-2\pi i j \frac{k_1 - k_2}{L}} e^{-2\pi i d \frac{k_1}{L}} \langle \hat{c}_{b,k_1} e^{\frac{i}{\hbar}T\hat{H}_{\mathrm{bth}}^{\mathrm{free}}}\hat{c}_{b,k_2}^\dagger\rangle_{\mathrm{bth}} \\
&= \frac{1}{L}\sum_{k_1 k_2} e^{-2\pi i j \frac{k_1 - k_2}{L}} e^{-2\pi i d \frac{k_1}{L}} e^{\frac{i}{\hbar}T\varepsilon_{k_2}^{F,b}} \langle \hat{c}_{b,k_1}\hat{c}_{b,k_2}^\dagger\rangle_{\mathrm{bth}} \\
&= \frac{1}{L}\sum_k e^{-2\pi i d \frac{k}{L}} e^{\frac{i}{\hbar}T\varepsilon_k^{F,b}}.
\end{aligned}
\tag{B.10}
$$

From the second to the third line it is used that in momentum space only the k_2 mode with energy $\varepsilon_k^{F,b} = 2J_b^F \cos(2\pi k) + \Delta_b^F$ is occupied and from the third to fourth line that $\langle \hat{c}_{b,k_1}\hat{c}_{b,k_2}^\dagger\rangle_{\mathrm{bth}} = \delta_{k_1 k_2}$. Accordingly, the bosonic correlator evaluates as

$$
\langle \hat{a}_{b,j+d}(\tau + T)\hat{a}_{b,j}^\dagger(\tau)\rangle_{\mathrm{bth}} = \frac{1}{L}\sum_k e^{-2\pi i d \frac{k}{L}} e^{\frac{i}{\hbar}T\varepsilon_k^{B,b}},
\tag{B.11}
$$

with $\varepsilon_k^{B,b} = 2J_b^B \cos(2\pi k) + \Delta_b^B$. Note that the correlators only depend on the difference T in time and the distance d between the operator sites.

B.3   Time integration of the correlators

The final step to perform is to integrate the correlators as shown in equation (16.8). With

$$
\mathcal{C}_{X,b}^T(d) = \frac{1}{L}\sum_k e^{-2\pi i d \frac{d}{L}} e^{\frac{i}{\hbar}T\varepsilon_k^{X,b}}
\tag{B.12}
$$

describing both bosonic and fermionic correlators, the two different kinds of time integrals are given by

$$
\mathcal{I}_{X,b}^d = -\frac{i}{\hbar}\int\limits_0^\infty \mathrm{d}T\, \mathcal{C}_{X,b}^T(d) \qquad\qquad \mathcal{I}_{BX,b}^d = -\frac{i}{\hbar}\int\limits_0^\infty \mathrm{d}T\, \mathcal{C}_{X,b}^T(d)\mathcal{C}_{B,b}^T(d).
\tag{B.13}
$$

For the single correlator, straightforward calculation yields

$$\mathcal{I}^d_{X,b} = -\frac{i}{\hbar}\frac{1}{L}\sum_k e^{-2\pi i d \frac{k}{L}} \int\limits_0^\infty \mathrm{d}T \, e^{\frac{i}{\hbar}T\varepsilon_k^{X,b}} \tag{B.14}$$

$$= \frac{1}{L}\sum_k \frac{e^{-2\pi i d \frac{k}{L}}}{\varepsilon_k^{X,b}}. \tag{B.15}$$

In the last step, the Riemann-Lebesgue lemma (9.10) applies. Going to the thermodynamic limit $L \to \infty$ by introducing $\xi = \frac{k}{L}$ and substituting $\frac{1}{L}\sum_k \mapsto \int \mathrm{d}\xi$, the result in its final form is found to be

$$\mathcal{I}^d_{X,b} = \int\limits_{-\frac{1}{2}}^{\frac{1}{2}} \mathrm{d}\xi \frac{e^{-2\pi i d\xi}}{\varepsilon^{X,b}(\xi)}. \tag{B.16}$$

For the double correlators, the product of the two correlators turns into a double integration, which, in the thermodynamic limit is given by

$$\mathcal{I}^d_{BX,b} = \int\limits_{-\frac{1}{2}}^{\frac{1}{2}} \mathrm{d}\xi \int\limits_{-\frac{1}{2}}^{\frac{1}{2}} \mathrm{d}\xi' \frac{e^{-2\pi i d\xi}e^{-2\pi i d\xi'}}{\varepsilon^{B,b}(\xi) + \varepsilon^{X,b}(\xi)}. \tag{B.17}$$

B.4 Definition of the constants

In the effective single-band Hamiltonian (16.18), several interaction and hopping amplitudes were introduced. These are defined as

$$U_3 = 6\sum_{\substack{b>1 \\ b \text{ odd}}} U^2_{b111}\mathcal{I}^0_{B,b}, \tag{B.18}$$

$$U_2 = U_{1111} + \sum_{b>1} U^2_{bb11}\mathcal{I}^0_{BB,b} + \sum_{\substack{b>1 \\ b \text{ odd}}} 2\, U^2_{b111}\mathcal{I}^0_{B,b}, \tag{B.19}$$

$$V_3 = \sum_{\substack{b>1 \\ b \text{ odd}}} \left[2\, U_{b111}V_{b111}\mathcal{I}^0_{B,b} + \frac{V^2_{1b11}\mathcal{I}^0_{F,b}}{2} \right], \tag{B.20}$$

$$V = \frac{V_{1111}}{2} + \sum_{b>1} \frac{V^2_{bb11}\mathcal{I}^0_{BF,b}}{4} + \sum_{\substack{b>1 \\ b \text{ odd}}} \left[\frac{V^2_{b111}\mathcal{I}^0_{B,b}}{4} + \frac{V^2_{1b11}\mathcal{I}^0_{F,b}}{4} \right], \tag{B.21}$$

$$J_B[d; \hat{n}_j, \hat{n}_{j+d}, \hat{m}_j, \hat{m}_{j+d}] = J_1^B \delta_{|d|,1}$$
$$+ \frac{U_{1111}^{3d,B}}{2} (\hat{n}_{j+d} + \hat{n}_j) + \frac{V_{1111}^{3d,B}}{2} (\hat{m}_{j+d} + \hat{m}_j)$$
$$+ \sum_{\substack{b>1 \\ b \text{ odd}}} \left[U_{b111}^2 \mathcal{I}_{B,b}^d \, \hat{n}_{j+d}\hat{n}_j + \frac{U_{b111}V_{b111}\mathcal{I}_{B,b}^d}{2} \, \hat{m}_{j+d}\hat{n}_j \right. \tag{B.22}$$
$$\left. + \frac{V_{b111}U_{b111}\mathcal{I}_{B,b}^d}{2} \, \hat{n}_{j+d}\hat{m}_j + \frac{V_{b111}^2\mathcal{I}_{B,b}^d}{4} \, \hat{m}_{j+d}\hat{m}_j \right],$$

$$J_F[d; \hat{n}_j, \hat{n}_{j+d}] = J_1^F \delta_{|d|,1} + \frac{V_{1111}^{3d,F}}{2} \, (\hat{n}_{j+d} + \hat{n}_j)$$
$$+ \sum_{\substack{b>1 \\ b \text{ odd}}} \frac{V_{1b11}^2 \mathcal{I}_{F,b}^d}{4} \, \hat{n}_{j+d}n_j, \tag{B.23}$$

$$J_B^{(2)}(d) = \frac{U_{1111}^{2d}}{2} + \sum_{b>1} \frac{U_{bb11}^2 \mathcal{I}_{BB,b}^d}{2}, \tag{B.24}$$

$$J_F^{(2)}(d) = \frac{V_{1111}^{2d}}{2} + \sum_{b>1} \frac{V_{bb11}^2 \mathcal{I}_{BF,b}^d}{4}. \tag{B.25}$$

Jaynes-Cummings-Hubbard model

C.1 Degenerate perturbation theory

Here we present the application of degenerate perturbation theory as described in [159] to calculate the energy corrections in second order. Though the system treated here is quite different, all arguments also apply to the calculation of the phase diagram for the effective bosonic model derived in part I and II and to Hubbard-like models in general.

Focussing on the situation with one additional excitation $N = nL + 1$, the states within the degenerate manifold are defined by

$$|\Psi\rangle_p^{+1} := |-, n+1\rangle_p \prod_{l \neq p} |-, n\rangle_l. \qquad \text{(C.1)}$$

The different matrix elements of the effective Hamiltonian are given by

$$_q^{+1}\langle\Psi| \hat{H}_{eff} |\Psi\rangle_p^{+1} = {}_q^{+1}\langle\Psi| \hat{H}_0 + \mathcal{P}\hat{V}\mathcal{P} + \mathcal{P}\hat{V}\mathcal{Q}\frac{1}{E_0 - \hat{H}_0}\mathcal{Q}\hat{V}\mathcal{P} |\Psi\rangle_p^{+1}. \qquad \text{(C.2)}$$

In the following we use

$$\hat{V} = \sum_d t_d \sum_j \left(\hat{a}_{j-d}^\dagger + \hat{a}_{j+d}^\dagger\right) \hat{a}_j = \sum_d t_d \sum_j \hat{a}_j^\dagger \left(\hat{a}_{j+d} + \hat{a}_{j-d}\right). \qquad \text{(C.3)}$$

a) Zeroth order

The zeroth order $\hat{H}_0$ is nothing but the energy of the manifold, given by

$$_q^{+1}\langle\Psi| \hat{H}_{eff} |\Psi\rangle_p^{+1} = E_{n+1}^- \delta_{q,p}. \qquad \text{(C.4)}$$

b) First order

The first order in the hopping operator $\hat{V}$ gives a direct coupling of the different states within the manifold. Because of the treatment of the long-range hopping t_d for any $d > 0$, the matrix elements of (C.2) result in

$$
{}^{+1}_{q}\langle\Psi|\,\hat{H}_{eff}\,|\Psi\rangle^{+1}_{p} = {}^{+1}_{q}\langle\Psi|\sum_{d,j} t_d \left(\hat{a}^{\dagger}_{j-d} + \hat{a}^{\dagger}_{j+d}\right)\hat{a}_j\,|\Psi\rangle^{+1}_{p}, \tag{C.5}
$$

which together with the action of the annihilation and creation operator on the Jaynes-Cummings states (22.14) gives

$$
= B^{-}_{n}D^{-}_{n+1}\sum_{d} t_d \left(\delta_{q,p+d} + \delta_{q,p-d}\right) \tag{C.6}
$$

c) Second order

The calculation of the second order matrix elements are more involved. This stems from the large number of intermediate steps, whose energies are accounted by the resolvent $\frac{1}{E_0 - \hat{H}_0}$. Furthermore we have to distinguish, whether the first application of the hopping operator annihilates an excitation at site p or $j \neq p$

$$
\hat{V}\,|\Psi\rangle^{+1}_{p} = \sum_{d} t_d \left(\hat{a}^{\dagger}_{p-d} + \hat{a}^{\dagger}_{p+d}\right)\hat{a}_p\,|\Psi\rangle^{+1}_{p} \tag{C.7}
$$

$$
+ \sum_{d}t_d\sum_{j\neq p}\left(\hat{a}^{\dagger}_{j-d} + \hat{a}^{\dagger}_{j+d}\right)\hat{a}_j\,|\Psi\rangle^{+1}_{p}, \tag{C.8}
$$

since the first term acting on site p just gives the first order expression and hence has to be neglected. Defining the intermediate states as

$$
|\Psi\rangle^{abc}_{pqr} := |-, n+a\rangle_p\,|-, n+b\rangle_q\,|-, n+c\rangle_r\prod_{l\neq pqr}|-, n\rangle_l, \tag{C.9}
$$

accounting for the deviation of the intermediate state from the Mott insulator $|\Psi\rangle = \prod_l|-, n\rangle_l$, the action of the first annihilation operator as described above is found to be

$$
\mathcal{Q}\hat{V}\,|\Psi\rangle^{+1}_{p} = \mathcal{Q}D^{-}_{n}\sum_{d}t_d\sum_{j\neq p}\left(\hat{a}^{\dagger}_{j-d} + \hat{a}^{\dagger}_{j+d}\right)|\Psi\rangle^{+1,-1}_{p,j}.
$$

Here, a distinction whether the creation operators create on site p or any other site is necessary, because the subsequent energy denominator gives different factors in both cases. This gives

$$
\begin{aligned}
\mathcal{Q}\hat{V}\left|\Psi\right\rangle_p^{+1} = {} & \mathcal{Q}D_n^- \sum_d t_d \left(\sum_{\substack{j\neq p \\ j-d\neq p}} \hat{a}_{j-d}^\dagger \left|\Psi\right\rangle_{p,j}^{+1,-1} + \sum_{\substack{j\neq p \\ j+d\neq p}} \hat{a}_{j+d}^\dagger \left|\Psi\right\rangle_{p,j}^{+1,-1} \right) \\
& + \mathcal{Q}D_n^- \sum_d t_d \left(\hat{a}_p^\dagger \left|\Psi\right\rangle_{p,p+d}^{+1,-1} + \hat{a}_p^\dagger \left|\Psi\right\rangle_{p,p-d}^{+1,-1} \right) \\
= {} & B_n^- D_n^- \sum_d t_d \left(\sum_{\substack{j\neq p \\ j\neq p+d}} \left|\Psi\right\rangle_{p,j,j-d}^{+1,-1,+1} + \sum_{\substack{j\neq p \\ j\neq p-d}} \left|\Psi\right\rangle_{p,j,j+d}^{+1,-1,+1} \right) \quad \text{(C.10)} \\
& + B_{n+1}^- D_n^- \sum_d t_d \left(\left|\Psi\right\rangle_{p,p+d}^{+2,-1} + \left|\Psi\right\rangle_{p,p-d}^{+2,-1} \right).
\end{aligned}
$$

The projector $\mathcal{Q}$ is dropped because the intermediate states are not from the treated manifold. For these states, the energy denominators are

$$
\frac{1}{E_0 - \hat{H}_0} \left|\Psi\right\rangle_{p,j,j\pm d}^{+1,-1,+1} = \frac{1}{2E_n^- - E_{n-1}^- - E_{n+1}^-} \qquad := \frac{1}{\Delta_1}, \qquad \text{(C.11)}
$$

$$
\frac{1}{E_0 - \hat{H}_0} \left|\Psi\right\rangle_{p,p\pm d}^{+2,-1} = \frac{1}{E_{n+1}^- + E_n^- - E_{n+2}^- - E_{n-1}^-} \qquad := \frac{1}{\Delta_2^+}. \qquad \text{(C.12)}
$$

Applying the remaining second hopping operator to the second term in (C.10) and restricting to only those output states within the manifold[1] gives

$$
\begin{aligned}
\mathcal{P}\hat{V}\,[2nd] = {} & \frac{B_{n+1}^- D_n^-}{\Delta_2^+} \sum_{d,d'} t_d t_{d'} \left(\hat{a}_{p-d'}^\dagger \hat{a}_p + \hat{a}_{p+d'}^\dagger \hat{a}_p \right) \left(\left|\Psi\right\rangle_{p,p+d}^{+2,-1} + \left|\Psi\right\rangle_{p,p-d}^{+2,-1} \right) \\
= {} & \frac{B_{n+1}^- D_n^- D_{n+2}^-}{\Delta_2^+} \sum_{d,d'} t_d t_{d'} \left(\hat{a}_{p-d'}^\dagger + \hat{a}_{p+d'}^\dagger \right) \left(\left|\Psi\right\rangle_{p,p+d}^{+1,-1} + \left|\Psi\right\rangle_{p,p-d}^{+1,-1} \right) \\
= {} & 2\frac{B_{n+1}^- D_n^- D_{n+2}^- B_{n-1}^-}{\Delta_2^+} \sum_d t_d^2 \left|\Psi\right\rangle_p^{+1}. \qquad \text{(C.13)}
\end{aligned}
$$

In the last line, half of the terms drop out since $d, d' > 0$ and because of the final $\mathcal{P}$, the final state has to be within the degenerate manifold.

---

[1]Thus passing the final projector $\mathcal{P}$.

For the first term in (C.10), a simplification arises from the observation that due to the final $\mathcal{P}$, the creation operator has to be situated at site j, which gives

$$
\mathcal{P}\hat{V}[\text{1st}] = \frac{B_n^- D_n^- B_{n-1}^-}{\Delta_1} \sum_{d'} t_{d'} \sum_d t_d \left(\hat{a}_{j+d'} + \hat{a}_{j-d'}\right) \sum_{\substack{j \neq p \\ j-d \neq p}} |\Psi\rangle_{p,j-d}^{+1,+1} \quad (\text{C.14})
$$

$$
+ \frac{B_n^- D_n^- B_{n-1}^-}{\Delta_1} \sum_{d'} t_{d'} \sum_d t_d \left(\hat{a}_{j+d'} + \hat{a}_{j-d'}\right) \sum_{\substack{j \neq p \\ j+d \neq p}} |\Psi\rangle_{p,j+d}^{+1,+1} \, .
$$

The annihilation operator in each case has two possibilities, either being applied to the site p or the site $j \pm d$. All other possibilities are ruled out because of the final projection $\mathcal{P}$, which together with $d > 0$ gives:

$$
\mathcal{P}\hat{V}[\text{1st}] = 2(L-3)\, \frac{B_n^- D_n^- B_{n-1}^- D_{n+1}^-}{\Delta_1} \sum_d t_d^2\, |\Psi\rangle_p^{+1} \quad\quad\quad (\text{C.15})
$$

$$
+ \frac{B_n^- D_n^- B_{n-1}^- D_{n+1}^-}{\Delta_1}
$$

$$
\sum_{dd'} t_{d'} t_d \left[|\Psi\rangle_{p-d'-d}^{+1} + |\Psi\rangle_{p+d'-d}^{+1} + |\Psi\rangle_{p-d'+d}^{+1} + |\Psi\rangle_{p+d'+d}^{+1} \right]
$$

Altogether, the matrix elements of the effective Hamiltonian in second order are given by

$$
{}_q^{+1}\langle\Psi| \hat{H}_{eff} |\Psi\rangle_p^{+1} = \delta_{q,p}\, E_{n+1}^- + B_n^- D_{n+1}^- \sum_d t_d\, (\delta_{q,p+d} + \delta_{q,p-d}) \quad\quad (\text{C.16})
$$

$$
+ 2 \left(\frac{B_{n+1}^- D_n^- D_{n+2}^- B_{n-1}^-}{\Delta_2^+} + (L-3)\, \frac{B_n^- D_n^- B_{n-1}^- D_{n+1}^-}{\Delta_1} \right) \sum_d t_d^2\, \delta_{q,p}
$$

$$
+ \frac{B_n^- D_n^- B_{n-1}^- D_{n+1}^-}{\Delta_1} \sum_{dd'} t_{d'} t_d\, (\delta_{p-d'-d} + \delta_{p+d'-d} + \delta_{p-d'+d} + \delta_{p+d'+d}) \, .
$$

For the sum in the last line, a resummation turns out to be more convenient. After some algebra, it can be rewritten as

$$
\sum_{dd'} t_{d'} t_d\, (\delta_{p-d'-d} + \delta_{p+d'-d} + \delta_{p-d'+d} + \delta_{p+d'+d}) \quad\quad\quad (\text{C.17})
$$

$$
= 2 \sum_d t_d^2\, \delta_{q,p} + \sum_{d=1}^{\infty} T_d\, (\delta_{q,p-d} + \delta_{q,p+d}) \, ,
$$

where the modified hoppings T_d are defined as

$$T_D = \sum_{d=1}^{D-1} t_d t_{D-d} + \sum_{d=D+1}^{\infty} t_d t_{d-D} + \sum_{d=1}^{\infty} t_d t_{D+d}. \qquad \text{(C.18)}$$

This finally gives the second order effective Hamiltonian for the state with an additional excitation which in this form is given by

$$_q^{+1}\langle\Psi|\,\hat{H}_{eff}\,|\Psi\rangle_p^{+1} = \delta_{q,p}\,E_{n+1}^- + B_n^- D_{n+1}^- \sum_d t_d\,(\delta_{q,p+d} + \delta_{q,p-d}) \qquad \text{(C.19)}$$

$$+ 2\left(\frac{B_{n+1}^- D_n^- D_{n+2}^- B_{n-1}^-}{\Delta_2^+} + (L-2)\,\frac{B_n^- D_n^- B_{n-1}^- D_{n+1}^-}{\Delta_1}\right)\sum_d t_d^2\,\delta_{q,p}$$

$$+ \frac{B_n^- D_n^- B_{n-1}^- D_{n+1}^-}{\Delta_1}\sum_d T_d\,(\delta_{p-d} + \delta_{p+d})\,.$$

Applying the same method to the situation with one excitation less as well as the (non-degenerate) Mott insulator[2], the matrix elements of the effective Hamiltonian for these cases are given by

$$_q^{-1}\langle\Psi|\,\hat{H}_{eff}\,|\Psi\rangle_p^{-1} = \delta_{q,p}\,E_{n-1}^- + B_{n-1}^- D_n^- \sum_d t_d\,(\delta_{q,p+d} + \delta_{q,p-d}) \qquad \text{(C.20)}$$

$$+ 2\left(\frac{B_n^- D_{n-1}^- D_{n+1}^- B_{n-2}^-}{\Delta_2^-} + (L-2)\,\frac{B_n^- D_n^- B_{n-1}^- D_{n+1}^-}{\Delta_1}\right)\sum_d t_d^2\,\delta_{q,p}$$

$$+ \frac{B_n^- D_n^- B_{n-1}^- D_{n+1}^-}{\Delta_1}\sum_d T_d\,(\delta_{p-d} + \delta_{p+d})\,.$$

and

$$\langle\Psi|\,\hat{H}_{eff}\,|\Psi\rangle = \delta_{q,p}\,E_n^- + 2L\,\frac{B_n^- D_n^- B_{n-1}^- D_{n+1}^-}{\Delta_1}\sum_d t_d^2\,\delta_{q,p} \qquad \text{(C.21)}$$

with $\Delta_2^{\pm} = E_{n\pm1}^- + E_n^- - E_{n\pm2}^- - E_{n\mp1}^-$.

---

[2]Which is naturally not necessary since simple perturbation theory suffices.

List of figures

Bibliography

[1] S. Chu, *Nobel Lecture: The manipulation of neutral particles*, Rev. Mod. Phys. **70**, 685, (1998).

[2] C. N. Cohen-Tannoudji, *Nobel Lecture: Manipulating atoms with photons*, Rev. Mod. Phys. **70**, 707, (1998).

[3] W. D. Phillips, *Nobel Lecture: Laser cooling and trapping of neutral atoms*, Rev. Mod. Phys. **70**, 721, (1998).

[4] S. Bose, *Planck's law and light quantum hypothesis*, Z. Phys. **26**, 178, (1924).

[5] A. Einstein, *Quantum theory of the ideal gas*, Sitzungsber. Preuss. Akad. Wiss. 18, (1925).

[6] K. B. Davis, M. O. Mewes, M. R. Andrews, N. J. van Druten, D. S. Durfee, D. M. Kurn, and W. Ketterle, *Bose-Einstein condensation in a gas of sodium atoms*, Phys. Rev. Lett. **75**, 3969, (1995).

[7] W. Ketterle, *Nobel lecture: When atoms behave as waves: Bose-Einstein condensation and the atom laser*, Rev. Mod. Phys. **74**, 1131, (2002).

[8] M. H. Anderson, J. R. Ensher, M. R. Matthews, C. E. Wieman, and E. A. Cornell, *Observation of Bose-Einstein condensation in a dilute atomic vapor*, Science **269**, 198, (1995).

[9] E. A. Cornell and C. E. Wieman, *Nobel Lecture: Bose-Einstein condensation in a dilute gas, the first 70 years and some recent experiments*, Rev. Mod. Phys. **74**, 875, (2002).

[10] C. C. Bradley, C. A. Sackett, J. J. Tollett, and R. G. Hulet, *Evidence of Bose-Einstein condensation in an atomic gas with attractive interactions*, Phys. Rev. Lett. **75**, 1687, (1995).

[11] B. DeMarco and D. Jin, *Onset of Fermi degeneracy in a trapped atomic gas*, Science **285**, 1703, (1999).

[12] S. Giorgini, L. P. Pitaevskii, and S. Stringari, *Theory of ultracold atomic Fermi gases*, Rev. Mod. Phys. **80**, 1215, (2008).

[13] I. Bloch, J. Dalibard, and W. Zwerger, *Many-body physics with ultracold gases*, Rev. Mod. Phys. **80**, 885, (2008).

[14] M. P. A. Fisher, P. B. Weichman, G. Grinstein, and D. S. Fisher, *Boson localization and the superfluid-insulator transition*, Phys. Rev. B **40**, 546, (1989).

[15] M. Greiner, O. Mandel, T. Esslinger, T. W. Hänsch, and I. Bloch, *Quantum phase transition from a superfluid to a Mott insulator in a gas of ultracold atoms*, Nature **415**, 39, (2002).

[16] R. Jördens, N. Strohmaier, K. Günter, H. Moritz, and T. Esslinger, *A Mott insulator of fermionic atoms in an optical lattice*, Nature **455**, 204, (2008).

[17] U. Schneider, L. Hackermüller, S. Will, T. Best, I. Bloch, T. A. Costi, R. W. Helmes, D. Rasch, and A. Rosch, *Metallic and insulating phases of repulsively interacting fermions in a three-dimensional optical lattice*, Science **322**, 1520, (2008).

[18] S. O. Demokritov, V. E. Demidov, O. Dzyapko, G. A. Melkov, A. A. Serga, B. Hillebrands, and A. N. Slavin, *Bose-Einstein condensation of quasi-equilibrium magnons at room temperature under pumping*, Nature **443**, 430, (2006).

[19] J. Kasprzak, M. Richard, S. Kundermann, A. Baas, P. Jeambrun, J. M. J. Keeling, F. M. Marchetti, M. H. Szymanska, R. Andre, J. L. Staehli, V. Savona, P. B. Littlewood, B. Deveaud, and L. S. Dang, *Bose-Einstein condensation of exciton polaritons*, Nature **443**, 409, (2006).

[20] F. London, *The λ-phenomenon of liquid helium and the Bose-Einstein degeneracy*, Nature **141**, 643, (1938).

[21] F. London, *On the Bose-Einstein condensation*, Phys. Rev. **54**, 947, (1938).

[22] L. N. Cooper, *Bound electron pairs in a degenerate Fermi gas*, Phys. Rev. **104**, 1189, (1956).

[23] J. Bardeen, L. N. Cooper, and J. R. Schrieffer, *Microscopic theory of superconductivity*, Phys. Rev. **106**, 162, (1957).

[24] J. Bardeen, L. N. Cooper, and J. R. Schrieffer, *Theory of superconductivity*, Phys. Rev. **108**, 1175, (1957).

[25] A. J. Leggett, *Bose-Einstein condensation in the alkali gases: Some fundamental concepts*, Rev. Mod. Phys. **73**, 307, (2001).

[26] S. Kraft, F. Vogt, O. Appel, F. Riehle, and U. Sterr, *Bose-Einstein condensation of alkaline earth atoms:* ^{40}Ca, Phys. Rev. Lett. **103**, 130401, (2009).

[27] S. Stellmer, M. K. Tey, B. Huang, R. Grimm, and F. Schreck, *Bose-Einstein condensation of Strontium*, Phys. Rev. Lett. **103**, 200401, (2009).

[28] Y. Takasu, K. Maki, K. Komori, T. Takano, K. Honda, M. Kumakura, T. Yabuzaki, and Y. Takahashi, *Spin-singlet Bose-Einstein condensation of two-electron atoms*, Phys. Rev. Lett. **91**, 040404, (2003).

[29] F. Pereira Dos Santos, J. Léonard, J. Wang, C. J. Barrelet, F. Perales, E. Rasel, C. S. Unnikrishnan, M. Leduc, and C. Cohen-Tannoudji, *Bose-Einstein condensation of metastable Helium*, Phys. Rev. Lett. **86**, 3459, (2001).

[30] A. Robert, O. Sirjean, A. Browaeys, J. Poupard, S. Nowak, D. Boiron, C. I. Westbrook, and A. Aspect, *A Bose-Einstein condensate of metastable atoms*, Science **292**, 461, (2001).

[31] D. G. Fried, T. C. Killian, L. Willmann, D. Landhuis, S. C. Moss, D. Kleppner, and T. J. Greytak, *Bose-Einstein condensation of atomic Hydrogen*, Phys. Rev. Lett. **81**, 3811, (1998).

[32] A. Griesmaier, J. Werner, S. Hensler, J. Stuhler, and T. Pfau, *Bose-Einstein condensation of Chromium*, Phys. Rev. Lett. **94**, 160401, (2005).

[33] A. G. Truscott, K. E. Strecker, W. I. McAlexander, G. B. Partridge, and R. G. Hulet, *Observation of Fermi pressure in a gas of trapped atoms*, Science **291**, 2570, (2001).

[34] F. Schreck, L. Khaykovich, K. L. Corwin, G. Ferrari, T. Bourdel, J. Cubizolles, and C. Salomon, *Quasipure Bose-Einstein condensate immersed in a Fermi sea*, Phys. Rev. Lett. **87**, 080403, (2001).

[35] Z. Hadzibabic, C. A. Stan, K. Dieckmann, S. Gupta, M. W. Zwierlein, A. Görlitz, and W. Ketterle, *Two-species mixture of quantum degenerate Bose and Fermi gases*, Phys. Rev. Lett. **88**, 160401, (2002).

[36] G. Roati, F. Riboli, G. Modugno, and M. Inguscio, *Fermi-Bose quantum degenerate ^{40}K-^{87}Rb mixture with attractive interaction*, Phys. Rev. Lett. **89**, 150403, (2002).

[37] K. Günter, T. Stoferle, H. Moritz, M. Kohl, and T. Esslinger, *Bose-Fermi mixtures in a three-dimensional optical lattice*, Phys. Rev. Lett. **96**, 180402, (2006).

[38] S. Ospelkaus, C. Ospelkaus, O. Wille, M. Succo, P. Ernst, K. Sengstock, and K. Bongs, *Localization of bosonic atoms by fermionic impurities in a three-dimensional optical lattice*, Phys. Rev. Lett. **96**, 180403, (2006).

[39] A. Albus, F. Illuminati, and J. Eisert, *Mixtures of bosonic and fermionic atoms in optical lattices*, Phys. Rev. A **68**, 023606, (2003).

[40] N. Gemelke, X. Zhang, C.-L. Hung, and C. Chin, *In situ observation of incompressible Mott-insulating domains in ultracold atomic gases*, Nature **460**, 995, (2009).

[41] W. S. Bakr, J. I. Gillen, A. Peng, S. Folling, and M. Greiner, *A quantum gas microscope for detecting single atoms in a Hubbard-regime optical lattice*, Nature **462**, 74, (2009).

[42] T. Gericke, P. Wurtz, D. Reitz, T. Langen, and H. Ott, *High-resolution scanning electron microscopy of an ultracold quantum gas*, Nat. Phys. **4**, 949, (2008).

[43] S. Fölling, F. Gerbier, A. Widera, O. Mandel, T. Gericke, and I. Bloch, *Spatial quantum noise interferometry in expanding ultracold atom clouds*, Nature **434**, 481, (2005).

[44] G. K. Campbell, J. Mun, M. Boyd, P. Medley, A. E. Leanhardt, L. G. Marcassa, D. E. Pritchard, and W. Ketterle, *Imaging the Mott insulator shells by using atomic clock shifts*, Science **313**, 649, (2006).

[45] F. Dalfovo, S. Giorgini, L. P. Pitaevskii, and S. Stringari, *Theory of Bose-Einstein condensation in trapped gases*, Rev. Mod. Phys. **71**, 463, (1999).

[46] T. Stöferle, H. Moritz, C. Schori, M. Köhl, and T. Esslinger, *Transition from a strongly interacting one-dimensional superfluid to a Mott insulator*, Phys. Rev. Lett. **92**, 130403, (2004).

[47] C. Chin, M. Bartenstein, A. Altmeyer, S. Riedl, S. Jochim, J. H. Denschlag, and R. Grimm, *Observation of the pairing gap in a strongly interacting Fermi gas*, Science **305**, 1128, (2004).

[48] J. Stenger, S. Inouye, A. P. Chikkatur, D. M. Stamper-Kurn, D. E. Pritchard, and W. Ketterle, *Bragg spectroscopy of a Bose-Einstein condensate*, Phys. Rev. Lett. **82**, 4569, (1999).

[49] D. Clement, N. Fabbri, L. Fallani, C. Fort, and M. Inguscio, *Multiband spectroscopy of inhomogeneous Mott-insulator states of ultracold bosons*, New J. Phys. **11**, 103030, (2009).

[50] P. T. Ernst, S. Götze, J. S. Krauser, K. Pyka, D.-S. Lühmann, D. Pfannkuche, and K. Sengstock, *Probing superfluids in optical lattices by momentum-resolved Bragg spectroscopy*, Nat. Phys. **6**, 56, (2010).

[51] H. Moritz, *Quantum gases: Atomic superfluids see the light*, Nat. Phys. **6**, 10, (2010).

[52] R. Folman, P. Krueger, J. Schmiedmayer, J. Denschlag, and C. Henkel, *Microscopic atom optics: from wires to an atom chip*, in *Advances in Atomic, Molecular and Optical Physics* (B. Bederson and H. Walther, eds.), vol. 48, 263, Academic Press, (2002).

[53] S. Knoop, F. Ferlaino, M. Berninger, M. Mark, H.-C. Nägerl, R. Grimm, J. P. D'Incao, and B. D. Esry, *Magnetically controlled exchange process in an ultracold atom-dimer mixture*, Phys. Rev. Lett. **104**, 053201, (2010).

[54] R. V. Krems, *Ultracold controlled chemistry*, Physics **3**, 10, (2010).

[55] S. Ospelkaus, K.-K. Ni, D. Wang, M. H. G. de Miranda, B. Neyenhuis, G. Quemener, P. S. Julienne, J. L. Bohn, D. S. Jin, and J. Ye, *Quantum-state controlled chemical reactions of ultracold Potassium-Rubidium molecules*, Science **327**, 853, (2010).

[56] V. N. Efimov, *Weakly-bound states of three resonantly-interacting particles*, Sov. Nucl. Phys. **12**, 589, (1971).

[57] T. Kraemer, M. Mark, P. Waldburger, J. G. Danzl, C. Chin, B. Engeser, A. D. Lange, K. Pilch, A. Jaakkola, H.-C. Nägerl, and R. Grimm, *Evidence for Efimov quantum states in an ultracold gas of Caesium atoms*, Nature **440**, 315, (2006).

[58] C. H. Greene, *Universal insights from few-body land*, Physics Today **3**, 40, (2010).

[59] D. Jaksch, C. Bruder, J. I. Cirac, C. W. Gardiner, and P. Zoller, *Cold bosonic atoms in optical lattices*, Phys. Rev. Lett. **81**, 3108, (1998).

[60] L.-M. Duan, E. Demler, and M. D. Lukin, *Controlling spin exchange interactions of ultracold atoms in optical lattices*, Phys. Rev. Lett. **91**, 090402, (2003).

[61] A. Kuklov and B. Svistunov, *Counterflow superfluidity of two-species ultracold atoms in a commensurate optical lattice*, Phys. Rev. Lett. **90**, 100401, (2003).

[62] T. Barthel, C. Kasztelan, I. P. McCulloch, and U. Schollwöck, *Magnetism, coherent many-particle dynamics, and relaxation with ultracold bosons in optical superlattices*, Phys. Rev. A **79**, 053627, (2009).

[63] T. Kinoshita, T. Wenger, and D. S. Weiss, *Observation of a one-dimensional Tonks-Girardeau gas*, Science **305**, 1125, (2004).

[64] B. Paredes, A. Widera, V. Murg, O. Mandel, S. Folling, I. Cirac, G. V. Shlyapnikov, T. W. Hansch, and I. Bloch, *Tonks-Girardeau gas of ultracold atoms in an optical lattice*, Nature **429**, 277, (2004).

[65] P. Jessen and I. H. Deutsch, *Optical lattices*, in *Advances in Atomic, Molecular and Optical Physics* (B. Bederson and H. Walther, eds.), vol. 37, 95, Academic Press, (1996).

[66] G. Grynberg and C. Robilliard, *Cold atoms in dissipative optical lattices*, Phys. Rep. **355**, 335, (2001).

[67] F. Schmitt, M. Hild, and R. Roth, *Phase diagram of bosons in two-color superlattices from experimental parameters*, Phys. Rev. A **80**, 023621, (2009).

[68] B. Damski, J. Zakrzewski, L. Santos, P. Zoller, and M. Lewenstein, *Atomic Bose and Anderson glasses in optical lattices*, Phys. Rev. Lett. **91**, 080403, (2003).

[69] J. E. Lye, L. Fallani, M. Modugno, D. S. Wiersma, C. Fort, and M. Inguscio, *Bose-Einstein condensate in a random potential*, Phys. Rev. Lett. **95**, 070401, (2005).

[70] D. Clément, A. F. Varón, M. Hugbart, J. A. Retter, P. Bouyer, L. Sanchez-Palencia, D. M. Gangardt, G. V. Shlyapnikov, and A. Aspect, *Suppression of transport of an interacting elongated Bose-Einstein condensate in a random potential*, Phys. Rev. Lett. **95**, 170409, (2005).

[71] L. Fallani, J. E. Lye, V. Guarrera, C. Fort, and M. Inguscio, *Ultracold atoms in a disordered crystal of light: Towards a Bose glass*, Phys. Rev. Lett. **98**, 130404, (2007).

[72] R. P. Feynman, *Simulating physics with computer*, Int. J. Theor. Phys. **21**, 467, (1982).

[73] G. K. Brennen, C. M. Caves, P. S. Jessen, and I. H. Deutsch, *Quantum logic gates in optical lattices*, Phys. Rev. Lett. **82**, 1060, (1999).

[74] P. Treutlein, T. Steinmetz, Y. Colombe, B. Lev, P. Hommelhoff, J. Reichel, M. Greiner, O. Mandel, A. Widera, T. Rom, I. Bloch, and T. W. Hänsch, *Quantum information processing in optical lattices and magnetic microtraps*, Fortschr. Phys. **54**, 702, (2006).

[75] D. N. Basov and T. Timusk, *Electrodynamics of high-T_C superconductors*, Rev. Mod. Phys. **77**, 721, (2005).

[76] P. A. Lee, N. Nagaosa, and X.-G. Wen, *Doping a Mott insulator: Physics of high-temperature superconductivity*, Rev. Mod. Phys. **78**, 17, (2006).

[77] A. J. Leggett, *What DO we know about high T_C?*, Nat. Phys. **2**, 134, (2006).

[78] M. W. Zwierlein, A. Schirotzek, C. H. Schunck, and W. Ketterle, *Fermionic superfluidity with imbalanced spin populations*, Science **311**, 492, (2006).

[79] G. B. Partridge, W. Li, R. I. Kamar, Y.-a. Liao, and R. G. Hulet, *Pairing and phase separation in a polarized Fermi gas*, Science **311**, 503, (2006).

[80] M. Takamoto, F.-L. Hong, R. Higashi, and H. Katori, *An optical lattice clock*, Nature **435**, 321, (2005).

[81] E. Pazy and A. Vardi, *Holstein model and Peierls instability in one-dimensional boson-fermion lattice gases*, Phys. Rev. A **72**, 033609, (2005).

[82] L. Mathey, D.-W. Wang, W. Hofstetter, M. D. Lukin, and E. Demler, *Luttinger liquid of polarons in one-dimensional boson-fermion mixtures*, Phys. Rev. Lett. **93**, 120404, (2004).

[83] M. Lewenstein, L. Santos, M. A. Baranov, and H. Fehrmann, *Atomic Bose-Fermi mixtures in an optical lattice*, Phys. Rev. Lett. **92**, 050401, (2004).

[84] T. Best, S. Will, U. Schneider, L. Hackermüller, D. van Oosten, I. Bloch, and D.-S. Lühmann, *Role of interactions in ^{87}Rb-^{40}K Bose-Fermi mixtures in a three-dimensional optical lattice*, Phys. Rev. Lett. **102**, 030408, (2009).

[85] J. Catani, L. De Sarlo, G. Barontini, F. Minardi, and M. Inguscio, *Degenerate Bose-Bose mixture in a three-dimensional optical lattice*, Phys. Rev. A **77**, 011603, (2008).

[86] D. S. Lühmann, K. Bongs, K. Sengstock, and D. Pfannkuche, *Self-trapping of bosons and fermions in optical lattices*, Phys. Rev. Lett. **101**, 050402, (2008).

[87] R. M. Lutchyn, S. Tewari, and S. Das Sarma, *Boson Hubbard model with weakly coupled fermions*, Phys. Rev. B **78**, 220504(R), (2008).

[88] L. Pollet, C. Kollath, U. Schollwöck, and M. Troyer, *Mixture of bosonic and spin-polarized fermionic atoms in an optical lattice*, Phys. Rev. A **77**, 023608, (2008).

[89] L. Pollet, M. Troyer, K. Van Houcke, and S. M. A. Rombouts, *Phase diagram of Bose-Fermi mixtures in one-dimensional optical lattices*, Phys. Rev. Lett. **96**, 190402, (2006).

[90] S. Tewari, R. M. Lutchyn, and S. D. Sarma, *Effects of fermions on the superfluid-insulator phase diagram of the Bose-Hubbard model*, Phys. Rev. B **80**, 054511, (2009).

[91] R. Grimm, M. Weidemuller, and Y. B. Ovchinnikov, *Optical dipole traps for neutral atoms*, in *Advances in Atomic, Molecular and Optical Physics* (B. Bederson and H. Walther, eds.), vol. 42, 95, Academic Press, (2000).

[92] J. Reppy, ^{4}*He as a dilute bose gas*, Physica B+C **126**, 335, (1984).

[93] S. Doniach, *Quantum fluctuations in two-dimensional superconductors*, Phys. Rev. B **24**, 5063, (1981).

[94] M. P. A. Fisher and G. Grinstein, *Quantum critical phenomena in charged superconductors*, Phys. Rev. Lett. **60**, 208, (1988).

[95] V. L. Berezinsky, *Destruction of long range order in one-dimensional and two-dimensional systems having a continuous symmetry group. 1. Classical systems*, Sov. Phys. JETP **32**, 493, (1971).

[96] J. M. Kosterlitz and D. J. Thouless, *Ordering, metastability and phase transitions in two-dimensional systems*, J. Phys. C **6**, 1181, (1973).

[97] J. K. Freericks and H. Monien, *Strong-coupling expansions for the pure and disordered Bose-Hubbard model*, Phys. Rev. B **53**, 2691, (1996).

[98] H. Bethe, *Zur Theorie der Metalle*, Z. Phys. A **71**, 205, (1931).

[99] T. Giamarchi, *Quantum physics in one dimension*, vol. 121, of *International Series of Monographs on Physics*, Oxford: Clarendon Press, (2004).

[100] F. D. M. Haldane, *Effective harmonic-fluid approach to low-energy properties of one-dimensional quantum fluids*, Phys. Rev. Lett. **47**, 1840, (1981).

[101] E. Miranda, *Introduction to bosonization*, Braz. J. Phys. **33**, 3, (2003).

[102] M. A. Cazalilla, *Bosonizing one-dimensional cold atomic gases*, J. Phys. B **37**, S1, (2004).

[103] S. Eggert, *One-dimensional quantum wires: A pedestrian approach to bosonization*, in *Theoretical Survey of One Dimensional Wire Systems* (Y. K. *et al.*, ed.), ch. 2, Seoul: Sowha Publishing, (2007).

[104] M. E. Fisher, M. N. Barber, and D. Jasnow, *Helicity modulus, superfluidity, and scaling in isotropic systems*, Phys. Rev. A **8**, 1111, (1973).

[105] S. Rapsch, U. Schollwöck, and W. Zwerger, *Density matrix-renormalization group for disordered bosons in one dimension*, Europhys. Lett. **46**, 559, (1999).

[106] M. White, M. Pasienski, D. McKay, S. Q. Zhou, D. Ceperley, and B. DeMarco, *Strongly interacting bosons in a disordered optical lattice*, Phys. Rev. Lett. **102**, 055301, (2009).

[107] T. D. Kühner, S. R. White, and H. Monien, *One-dimensional Bose-Hubbard model with nearest-neighbor interaction*, Phys. Rev. B **61**, 12474, (2000).

[108] A. van Otterlo, K.-H. Wagenblast, R. Baltin, C. Bruder, R. Fazio, and G. Schön, *Quantum phase transitions of interacting bosons and the supersolid phase*, Phys. Rev. B **52**, 16176, (1995).

[109] T. Giamarchi and H. J. Schulz, *Anderson localization and interactions in one-dimensional metals*, Phys. Rev. B **37**, 325, (1988).

[110] B. Schmidt, *Exact numerical simulations of strongly interacting atoms in one-dimensional trap potentials and optical latticesl*, PhD thesis, Technische Universität Kaiserslautern, (2009).

[111] F. Bloch, *Über die Quantenmechanik der Elektronen in Kristallgittern*, Z. Phys. A **52**, 555, (1929).

[112] G. H. Wannier, *The structure of electronic excitation levels in insulating crystals*, Phys. Rev. **52**, 191, (1937).

[113] W. Kohn, *Analytic properties of Bloch waves and Wannier functions*, Phys. Rev. **115**, 809, (1959).

[114] L. X. He and D. Vanderbilt, *Exponential decay properties of Wannier functions and related quantities*, Phys. Rev. Lett. **86**, 5341, (2001).

[115] H. P. Büchler, *Microscopic derivation of Hubbard parameters for cold atomic gases*, Phys. Rev. Lett. **104**, 090402, (2010).

[116] S. Q. Zhou and D. M. Ceperley, *Construction of localized wave functions for a disordered optical lattice and analysis of the resulting Hubbard model parameters*, Phys. Rev. A **81**, 013402, (2010).

[117] H. P. Büchler and G. Blatter, *Supersolid versus phase separation in atomic Bose-Fermi mixtures*, Phys. Rev. Lett. **91**, 130404, (2003).

[118] L. Mathey and D.-W. Wang, *Phase diagrams of one-dimensional Bose-Fermi mixtures of ultracold atoms*, Phys. Rev. A **75**, 013612, (2007).

[119] F. Hébert, F. Haudin, L. Pollet, and G. G. Batrouni, *Mott insulators and correlated superfluids in ultracold Bose-Fermi mixtures*, Phys. Rev. A **76**, 043619, (2007).

[120] F. Hébert, G. G. Batrouni, X. Roy, and V. G. Rousseau, *Supersolids in one-dimensional Bose-Fermi mixtures*, Phys. Rev. B **78**, 184505, (2008).

[121] V. Ahufinger, L. Sanchez-Palencia, A. Kantian, A. Sanpera, and M. Lewenstein, *Disordered ultracold atomic gases in optical lattices: A case study of Fermi-Bose mixtures*, Phys. Rev. A **72**, 063616, (2005).

[122] L. Sanchez-Palencia, V. Ahufinger, A. Kantian, J. Zakrzewski, A. Sanpera, and M. Lewenstein, *Strongly correlated Fermi-Bose mixtures in disordered optical lattices*, J. Phys. B **39**, S121, (2006).

[123] F. Schmitt, M. Hild, and R. Roth, *Bose-Fermi mixtures in one-dimensional optical superlattices using full and truncated single-band bases*, J. Phys. B **40**, 371, (2007).

[124] L. Sanchez-Palencia and M. Lewenstein, *Disordered quantum gases under control*, Nat. Phys. **6**, 87, (2010).

[125] W. Long, Q.-f. Sun, and J. Wang, *Disorder-induced enhancement of transport through graphene $p - n$ junctions*, Phys. Rev. Lett. **101**, 166806, (2008).

[126] J. Hubbard, *Electron correlations in narrow energy bands*, Proc. Phys. Soc. London **276**, 238, (1963).

[127] K. Byczuk, M. Ulmke, and D. Vollhardt, *Ferromagnetism and metal-insulator transition in the disordered Hubbard model*, Phys. Rev. Lett. **90**, 196403, (2003).

[128] K. Byczuk and M. Ulmke, *Curie temperature in the Hubbard model with alloy disorder*, Eur. Phys. J. B **45**, 449, (2005).

[129] Y. Braiman, W. L. Ditto, K. Wiesenfeld, and M. L. Spano, *Disorder-enhanced synchronization*, Phys. Let. A **206**, 54, (1995).

[130] P. Sengupta, A. Raghavan, and S. Haas, *Disorder-enhanced phase coherence in trapped bosons on optical lattices*, New J. Phys. **9**, 103, (2007).

[131] P. W. Anderson, *Absence of diffusion in certain random lattices*, Phys. Rev. **109**, 1492, (1958).

[132] A. Lagendijk, B. van Tiggelen, and D. Wiersma, *50 Years of Anderson Localization Symposium*, www.andersonlocalization.com

[133] J. Billy, V. Josse, Z. Zuo, A. Bernard, B. Hambrecht, P. Lugan, D. Clement, L. Sanchez-Palencia, P. Bouyer, and A. Aspect, *Direct observation of Anderson localization of matter waves in a controlled disorder*, Nature **453**, 891, (2008).

[134] G. Roati, C. D'Errico, L. Fallani, M. Fattori, C. Fort, M. Zaccanti, G. Modugno, M. Modugno, and M. Inguscio, *Anderson localization of a non-interacting Bose-Einstein condensate*, Nature **453**, 895, (2008).

[135] T. Paul, P. Schlagheck, P. Leboeuf, and N. Pavloff, *Superfluidity versus Anderson localization in a dilute Bose gas*, Phys. Rev. Lett. **98**, 210602, (2007).

[136] A. S. Pikovsky and D. L. Shepelyansky, *Destruction of Anderson localization by a weak nonlinearity*, Phys. Rev. Lett. **100**, 094101, (2008).

[137] B. Deissler, M. Zaccanti, G. Roati, C. D/'Errico, M. Fattori, M. Modugno, G. Modugno, and M. Inguscio, *Delocalization of a disordered bosonic system by repulsive interactions*, Nat Phys **6**, 354–358, (2010).

[138] M. Pasienski, D. McKay, M. White, and B. DeMarco, *Disordered insulator in an optical lattice*, cond-mat/0908.1182, (2009).

[139] H. Gimperlein, S. Wessel, J. Schmiedmayer, and L. Santos, *Ultracold atoms in optical lattices with random on-site interactions*, Phys. Rev. Lett. **95**, 170401, (2005).

[140] E. Altman, Y. Kafri, A. Polkovnikov, and G. Refael, *Insulating phases and superfluid-insulator transition of disordered boson chains*, Phys. Rev. Lett. **100**, 170402, (2008).

[141] P. Buonsante, F. Massel, V. Penna, and A. Vezzani, *Mean-field phase diagram for Bose-Hubbard Hamiltonians with random hopping*, Laser Phys. **17**, 538, (2007).

[142] P. Sengupta and S. Haas, *Quantum glass phases in the disordered Bose-Hubbard model*, Phys. Rev. Lett. **99**, 050403, (2007).

[143] R. Roth and K. Burnett, *Phase diagram of bosonic atoms in two-color superlattices*, Phys. Rev. A **68**, 023604, (2003).

[144] X. L. Deng, R. Citro, A. Minguzzi, and E. Orignac, *Phase diagram and momentum distribution of an interacting Bose gas in a bichromatic lattice*, Phys. Rev. A **78**, 013625, (2008).

[145] G. Roux, T. Barthel, I. P. McCulloch, C. Kollath, U. Schollwöck, and T. Giamarchi, *Quasiperiodic Bose-Hubbard model and localization in one-dimensional cold atomic gases*, Phys. Rev. A **78**, 023628, (2008).

[146] T. Roscilde, *Bosons in one-dimensional incommensurate superlattices*, Phys. Rev. A **77**, 063605, (2008).

[147] U. Gavish and Y. Castin, *Matter-wave localization in disordered cold atom lattices*, Phys. Rev. Lett. **95**, 020401, (2005).

[148] B. Horstmann, J. I. Cirac, and T. Roscilde, *Dynamics of localization phenomena for hard-core bosons in optical lattices*, Phys. Rev. A **76**, 043625, (2007).

[149] K. V. Krutitsky, M. Thorwart, R. Egger, and R. Graham, *Ultracold bosons in lattices with binary disorder*, Phys. Rev. A **77**, 053609, (2008).

[150] M. Iskin and J. K. Freericks, *Dynamical mean-field theory for light-fermion–heavy-boson mixtures on optical lattices*, Phys. Rev. A **80**, 053623, (2009).

[151] L. M. Falicov and J. C. Kimball, *Simple model for semiconductor-metal transitions: SmB_6 and transition-metal oxides*, Phys. Rev. Lett. **22**, 997, (1969).

[152] D. Semmler, K. Byczuk, and W. Hofstetter, *Mott-Hubbard and Anderson metal-insulator transitions in correlated lattice fermions with binary disorder*, Phys. Rev. B **81**, 115111, (2010).

[153] P. Buonsante, F. Massel, V. Penna, and A. Vezzani, *Mean-field description of ultracold bosons on disordered two-dimensional optical lattices*, J. Phys. B **40**, F265, (2007).

[154] P. Buonsante, V. Penna, A. Vezzani, and P. B. Blakie, *Mean-field phase diagram of cold lattice bosons in disordered potentials*, Phys. Rev. A **76**, 011602, (2007).

[155] U. Bissbort and W. Hofstetter, *Stochastic mean-field theory for the disordered Bose-Hubbard model*, Europhys. Lett. **86**, 50007, (2009).

[156] A. Zujev, A. Baldwin, R. T. Scalettar, V. G. Rousseau, P. J. H. Denteneer, and M. Rigol, *Superfluid and Mott-insulator phases of one-dimensional Bose-Fermi mixtures*, Phys. Rev. A **78**, 033619, (2008).

[157] P. Buonsante, V. Penna, and A. Vezzani, *Fractional-filling loophole insulator domains for ultracold bosons in optical superlattices*, Phys. Rev. A **70**, 061603, (2004).

[158] H. Fehrmann, M. Baranov, M. Lewenstein, and L. Santos, *Quantum phases of Bose-Fermi mixtures in optical lattices*, Opt. Express **12**, 55, (2004).

[159] D. J. Klein, *Degenerate perturbation theory*, J. Chem. Phys. **61**, 786, (1974).

[160] A. Sanpera, A. Kantian, L. Sanchez-Palencia, J. Zakrzewski, and M. Lewenstein, *Atomic Fermi-Bose mixtures in inhomogeneous and random lattices: From Fermi glass to quantum spin glass and quantum percolation*, Phys. Rev. Lett. **93**, 040401, (2004).

[161] A. Mering, *Bose-Fermi-Gemische in eindimensionalen Gittern*, Diplomarbeit, Technische Universität Kaiserslautern, (2005).

[162] R. Roth and K. Burnett, *Quantum phases of atomic boson-fermion mixtures in optical lattices*, Phys. Rev. A **69**, 021601, (2004).

[163] U. Schollwöck, *The density-matrix renormalization group*, Rev. Mod. Phys. **77**, 259, (2005).

[164] *The ALPS project (Algorithms and Libraries for Physics Simulations)*, http://alps.comp-phys.org/mediawiki/index.php/Main_Page

[165] A. Albuquerque, F. Alet, P. Corboz, P. Dayal, A. Feiguin, S. Fuchs, L. Gamper, E. Gull, S. Gürtler, A. Honecker, R. Igarashi, M. Körner, A. Kozhevnikov, A. Läuchli, S. Manmana, M. Matsumoto, I. McCulloch, F. Michel, R. Noack, G. Pawlowski, L. Pollet, T. Pruschke, U. Schollwöck, S. Todo, S. Trebst, M. Troyer, P. Werner, and S. Wessel, *The ALPS project release 1.3: Open-source software for strongly correlated systems*, J. Magn. Magn. Mater. **310**, 1187, (2007).

[166] R. Fazio, S. Montangero, G. D. Chiara, D. Rossini, and M. Rizzi, *Parallel open well-adapting DMRG enhanced research with power*, http://www.qti.sns.it/dmrg/phome.html

[167] I. P. McCulloch, *From density-matrix renormalization group to matrix product states*, J. Stat. Mech: Theory Exp. **2007**, P10014, (2007).

[168] G. Vidal, *Efficient Classical Simulation of Slightly Entangled Quantum Computations*, Phys. Rev. Lett. **91**, 147902, (2003).

[169] G. Vidal, *Classical simulation of infinite-size quantum lattice systems in one spatial dimension*, Phys. Rev. Lett. **98**, 070201, (2007).

[170] N. Teichmann, D. Hinrichs, M. Holthaus, and A. Eckardt, *Bose-Hubbard phase diagram with arbitrary integer filling*, Phys. Rev. B **79**, 100503(2009), (2009).

[171] M. Ohliger and A. Pelster, *Green's function approach to the Bose-Hubbard model*, (2008).

[172] B. Bradlyn, F. E. A. dos Santos, and A. Pelster, *Effective action approach for quantum phase transitions in bosonic lattices*, Phys. Rev. A **79**, 013615, (2009).

[173] F. E. A. dos Santos and A. Pelster, *Quantum phase diagram of bosons in optical lattices*, Phys. Rev. A **79**, 013614, (2009).

[174] P. Buonsante, V. Penna, and A. Vezzani, *Fractional-filling Mott domains in two-dimensional optical superlattices*, Phys. Rev. A **72**, 031602, (2005).

[175] P. Buonsante, V. Penna, and A. Vezzani, *Strong-coupling expansions for the topologically inhomogeneous Bose-Hubbard model*, Phys. Rev. B **70**, 184520, (2004).

[176] P. Buonsante and A. Vezzani, *Cell strong-coupling perturbative approach to the phase diagram of ultracold bosons in optical superlattices*, Phys. Rev. A **72**, 013614, (2005).

[177] P. Buonsante and A. Vezzani, *Phase diagram for ultracold bosons in optical lattices and superlattices*, Phys. Rev. A **70**, 033608, (2004).

[178] V. G. Rousseau, D. P. Arovas, M. Rigol, F. Hébert, G. G. Batrouni, and R. T. Scalettar, *Exact study of the one-dimensional boson Hubbard model with a superlattice potential*, Phys. Rev. B **73**, 174516, (2006).

[179] H. Fehrmann, M. A. Baranov, B. Damski, M. Lewenstein, and L. Santos, *Mean-field theory of Bose-Fermi mixtures in optical lattices*, Opt. Commun. **243**, 23, (2004).

[180] M. Cramer, J. Eisert, and F. Illuminati, *Inhomogeneous atomic Bose-Fermi mixtures in cubic lattices*, Phys. Rev. Lett. **93**, 190405, (2004).

[181] D. van Oosten, P. van der Straten, and H. T. C. Stoof, *Quantum phases in an optical lattice*, Phys. Rev. A **63**, 053601, (2001).

[182] A. W. Sandvik, *Quantum monte carlo simulations of bosonic and fermionic impurities in a two-dimensional hard-core boson system*, Phys. Rev. Lett. **101**, 120405, (2008).

[183] T. D. Kühner and H. Monien, *Phases of the one-dimensional Bose-Hubbard model*, Phys. Rev. B **58**, 14741(R), (1998).

[184] J. M. Luttinger, *An exactly soluble model of a many-fermion system*, J. Math. Phys. **4**, 1154, (1963).

[185] S. Tomonaga, *Remarks on Bloch's method of sound waves applied to many-fermion problems*, Progr. Theoret. Phys. **5**, 544, (1950).

[186] J. Voit, *One-dimensional Fermi liquids*, Rep. Prog. Phys. **58**, 977, (1995).

[187] F. Schwabl, *Statistische Mechanik*, Springer, (2000).

[188] P. N. Suding and R. M. Ziff, *Site percolation thresholds for Archimedean lattices*, Phys. Rev. E **60**, 275, (1999).

[189] P. Buonsante, F. Massel, V. Penna, and A. Vezzani, *Gutzwiller approach to the Bose-Hubbard model with random local impurities*, Phys. Rev. A **79**, 013623, (2009).

[190] R. V. Pai, R. Pandit, H. R. Krishnamurthy, and S. Ramasesha, *One-dimensional disordered bosonic Hubbard model: A density-matrix renormalization group study*, Phys. Rev. Lett. **76**, 2937, (1996).

[191] L. Pollet, N. V. Prokof'ev, B. V. Svistunov, and M. Troyer, *Absence of a direct superfluid to Mott insulator transition in disordered Bose systems*, Phys. Rev. Lett. **103**, 140402, (2009).

[192] V. Gurarie, L. Pollet, N. V. Prokof'ev, B. V. Svistunov, and M. Troyer, *Phase diagram of the disordered Bose-Hubbard model*, Phys. Rev. B **80**, 214519, (2009).

[193] S. F. Edwards and P. W. Anderson, *Theory of spin glasses*, J. Phys. F **5**, 965, (1975).

[194] S. Morrison, *Characterization of quantum phase transitions in dissipative cavity QED systems and cold atoms with disorder*, PhD thesis, Leopold-Franzens-Universität Innsbruck, (2008).

[195] E. Kim and M. H. W. Chan, *Probable observation of a supersolid Helium phase*, Nature **427**, 225, (2004).

[196] D. J. Thouless, *The flow of a dense superfluid*, Ann. Phys. **52**, 403, (1969).

[197] A. F. Andreev and I. M. Lifshitz, *Quantum theory of defects in crystals*, Sov. Phys. JETP **29**, 1107, (1969).

[198] A. J. Leggett, *Can a Solid Be "Superfluid"?*, Phys. Rev. Lett. **25**, 1543, (1970).

[199] S. Balibar, *The enigma of supersolidity*, Nature **464**, 176, (2010).

[200] G. G. Batrouni and R. T. Scalettar, *Phase separation in supersolids*, Phys. Rev. Lett. **84**, 1599, (2000).

[201] P. Sengupta, L. P. Pryadko, F. Alet, M. Troyer, and G. Schmid, *Supersolids versus phase separation in two-dimensional lattice bosons*, Phys. Rev. Lett. **94**, 207202, (2005).

[202] B. Capogrosso-Sansone, C. Trefzger, M. Lewenstein, P. Zoller, and G. Pupillo, *Quantum phases of cold polar molecules in two-dimensional optical lattices*, Phys. Rev. Lett. **104**, 125301, (2010).

[203] T. Mishra, R. V. Pai, S. Ramanan, M. S. Luthra, and B. P. Das, *Supersolid and solitonic phases in the one-dimensional extended Bose-Hubbard model*, Phys. Rev. A **80**, 043614, (2009).

[204] P. P. Orth, D. L. Bergman, and K. Le Hur, *Supersolidity of cold-atom Bose-Fermi mixtures in optical lattices*, Phys. Rev. A **80**, 023624, (2009).

[205] I. Titvinidze, M. Snoek, and W. Hofstetter, *Supersolid Bose-Fermi mixtures in optical lattices*, Phys. Rev. Lett. **100**, 100401, (2008).

[206] A. Hubener, M. Snoek, and W. Hofstetter, *Magnetic phases of two-component ultracold bosons in an optical lattice*, Phys. Rev. B **80**, 245109, (2009).

[207] T. Keilmann, J. I. Cirac, and T. Roscilde, *Dynamical creation of a supersolid in asymmetric mixtures of bosons*, Phys. Rev. Lett. **102**, 255304, (2009).

[208] S. G. Söyler, B. Capogrosso-Sansone, N. V. Prokof'ev, and B. V. Svistunov, *Sign-alternating interaction mediated by strongly correlated lattice bosons*, New J. Phys. **11**, 073036, (2009).

[209] L. Mathey, I. Danshita, and C. W. Clark, *Creating a supersolid in one-dimensional Bose mixtures*, Phys. Rev. A **79**, 011602, (2009).

[210] I. Titvinidze, M. Snoek, and W. Hofstetter, *Generalized dynamical mean-field theory for Bose-Fermi mixtures in optical lattices*, Phys. Rev. B **79**, 144506, (2009).

[211] L. Pollet, S. Rombouts, K. Heyde, and J. Dukelsky, *Bosons confined in optical lattices: The numerical renormalization group revisited*, Phys. Rev. A **69**, 043601, (2004).

[212] E. Altman, W. Hofstetter, E. Demler, and M. D. Lukin, *Phase diagram of two-component bosons on an optical lattice*, New J. Phys. **5**, 113, (2003).

[213] H. P. Büchler and G. Blatter, *Phase separation of atomic Bose-Fermi mixtures in an optical lattice*, Phys. Rev. A **69**, 063603, (2004).

[214] G. Mazzarella, *How the effective boson-boson interaction works in Bose-Fermi mixtures in periodic geometries*, Eur. Phys. J. D **50**, 61, (2008).

[215] K. Yang, *Superfluid-insulator transition and fermion pairing in Bose-Fermi mixtures*, Phys. Rev. B **77**, 085115, (2008).

[216] D. H. Santamore and E. Timmermans, *Fermion-mediated interactions in a dilute Bose-Einstein condensate*, Phys. Rev. A **78**, 013619, (2008).

[217] G. Refael and E. Demler, *Superfluid-insulator transition in Fermi-Bose mixtures and the orthogonality catastrophe*, Phys. Rev. B **77**, 144511, (2008).

[218] J. Friedel, *The distribution of electrons round impurities in monovalent metals*, Philos. Mag. **43**, 153, (1952).

[219] G. Bedürftig, B. Brendel, H. Frahm, and R. M. Noack, *Friedel oscillations in the open Hubbard chain*, Phys. Rev. B **58**, 10225, (1998).

[220] G. D. Mahan, *Many-particle physics*, Plenum Press, New York, third ed., (2000).

[221] S. A. Söffing, M. Bortz, I. Schneider, A. Struck, M. Fleischhauer, and S. Eggert, *Wigner crystal versus Friedel oscillations in the one-dimensional Hubbard model*, Phys. Rev. B **79**, 195114, (2009).

[222] J. Stepisnik, *Validity limits of Gaussian approximation in cumulant expansion for diffusion attenuation of spin echo*, Physica B **270**, 110, (1999).

[223] C. W. Gardiner, *Handbook of Stochastic Methods*, Berlin: Springer, (1985).

[224] M. Fleischhauer and S. F. Yelin, *Radiative atom-atom interactions in optically dense media: Quantum corrections to the Lorentz-Lorenz formula*, Phys. Rev. A **59**, 2427, (1999).

[225] R. Kubo, *Generalized cumulant expansion method*, J. Phys. Soc. Jpn. **17**, 1100, (1962).

[226] R. Kubo, *Stochastic Liouville equations*, J. Math. Phys. **4**, 174, (1963).

[227] W. H. Louisell, *Quantum statistical properties of radiation*, Wiley New York, (1973).

[228] H. Carmichael, *An Open Systems Approach to Quantum Optics*, Springer-Verlag, (1993).

[229] S. Bochner and K. Chandrasekharan, *Fourier Transforms*, Princeton University Press, (1949).

[230] M. A. Ruderman and C. Kittel, *Indirect exchange coupling of nuclear magnetic moments by conduction electrons*, Phys. Rev. **96**, 99, (1954).

[231] T. Kasuya, *A theory of metallic ferromagnetism and antiferromagnetism on Zeners model*, Progr. Theoret. Phys. **16**, 45, (1956).

[232] K. Yosida, *Magnetic properties of Cu-Mn alloys*, Phys. Rev. **106**, 893, (1957).

[233] L. van Hove, *The occurrence of singularities in the elastic frequency distribution of a crystal*, Phys. Rev. **89**, 1189, (1953).

[234] E. Lieb, T. Schultz, and D. Mattis, *Two soluble models of an antiferromagnetic chain*, Ann. Phys. **16**, 407, (1961).

[235] G. C. Wick, *The evaluation of the collision matrix*, Phys. Rev. **80**, 268, (1950).

[236] F. Schwabl, *Quantenmechanik für Fortgeschrittene*, Berlin: Springer-Verlag, second ed., (2000).

[237] M. Abramowitz and I. A. Stegun, *Handbook of mathematical functions*, New York: Dover, (1964).

[238] R. J. Glauber, *Coherent and incoherent states of the radiation field*, Phys. Rev. **131**, 2766, (1963).

[239] N. Teichmann, D. Hinrichs, M. Holthaus, and A. Eckardt, *Process chain approach to the Bose-Hubbard model: Ground-state properties and phase diagram*, Phys. Rev. B **79**, 224515, (2009).

[240] A. Eckardt, *Process-chain approach to high-order perturbation calculus for quantum lattice models*, Phys. Rev. B **79**, 195131, (2009).

[241] P. Bak and R. Bruinsma, *One-dimensional Ising model and the complete devil's staircase*, Phys. Rev. Lett. **49**, 249, (1982).

[242] F. J. Burnell, M. M. Parish, N. R. Cooper, and S. L. Sondhi, *Devil's staircases and supersolids in a one-dimensional dipolar Bose gas*, Phys. Rev. B **80**, 174519, (2009).

[243] S. Will, T. Best, U. Schneider, L. Hackermuller, D.-S. Luhmann, and I. Bloch, *Time-resolved observation of coherent multi-body interactions in quantum phase revivals*, Nature **465**, 197, (2010).

[244] P. R. Johnson, E. Tiesinga, J. V. Porto, and C. J. Williams, *Effective three-body interactions of neutral bosons in optical lattices*, New J. Phys. **11**, 093022, (2009).

[245] J. Larson, A. Collin, and J.-P. Martikainen, *Multiband bosons in optical lattices*, Phys. Rev. A **79**, 033603, (2009).

[246] A. Collin, J. Larson, and J.-P. Martikainen, *Quantum states of p-band bosons in optical lattices*, Phys. Rev. A **81**, 023605, (2010).

[247] M. Cramer, S. Ospelkaus, C. Ospelkaus, K. Bongs, K. Sengstock, and J. Eisert, *Do mixtures of bosonic and fermionic atoms adiabatically heat up in optical lattices?*, Phys. Rev. Lett. **100**, 140409, (2008).

[248] C. N. Varney, V. G. Rousseau, and R. T. Scalettar, *Quantum monte carlo study of the visibility of one-dimensional Bose-Fermi mixtures*, Phys. Rev. A **77**, 041608, (2008).

[249] R. M. Lutchyn, S. Tewari, and S. Das Sarma, *Loss of superfluidity by fermions in the boson Hubbard model on an optical lattice*, Phys. Rev. A **79**, 011606(R), (2009).

[250] I. Titvinidze, M. Snoek, and W. Hofstetter, *Resonant superfluidity in an optical lattice*, cond-mat/0912.1589, (2009).

[251] J. Bünemann, *A slave-boson mean-field theory for general multi-band Hubbard models*, cond-mat/1002.3228, (2010).

[252] M. Ohliger, M. Cramer, and J. Eisert, *Multi-band Gutzwiller ansatz for interacting bosons and fermions for finite temperature*, Private communication.

[253] A. Isacsson and S. M. Girvin, *Multiflavor bosonic Hubbard models in the first excited Bloch band of an optical lattice*, Phys. Rev. A **72**, 053604, (2005).

[254] G. Mazzarella, S. M. Giampaolo, and F. Illuminati, *Extended Bose Hubbard model of interacting bosonic atoms in optical lattices: From superfluidity to density waves*, Phys. Rev. A **73**, 013625, (2006).

[255] L. Amico, G. Mazzarella, S. Pasini, and F. S. Cataliotti, *Hidden order in bosonic gases confined in one-dimensional optical lattices*, New J. Phys. **12**, 013002, (2010).

[256] M. E. Gehm, *Properties of ^6Li*,
http://www.phy.duke.edu/research/photon/qoptics/techdocs

[257] D. A. Steck, *^{85}Rb D-Line Data*,
http://steck.us/alkalidata

[258] D. A. Steck, *^{87}Rb D-Line Data*,
http://steck.us/alkalidata

[259] *NIST Atomic Spectra Database*,
http://www.nist.gov/physlab/data/asd.cfm

[260] H. Feshbach, *Unified theory of nuclear reactions*, Ann. Phys. **5**, 357, (1958).

[261] U. Fano, *Effects of configuration interaction on intensities and phase shifts*, Phys. Rev. **124**, 1866, (1961).

[262] P. Risberg, *A revision of the term systems for Na and K based on hollow-cathode observations*, Arkiv For Fysik **10**, 583, (1956).

[263] M. Olshanii, *Atomic scattering in the presence of an external confinement and a gas of impenetrable bosons*, Phys. Rev. Lett. **81**, 938, (1998).

[264] I. Bouchoule, M. Morinaga, C. Salomon, and D. S. Petrov, *Caesium gas strongly confined in one dimension: Sideband cooling and collisional properties*, Phys. Rev. A **65**, 033402, (2002).

[265] A. van Amerongen, *One dimensional Bose gas on an atom chip*, PhD thesis, University of Amsterdam, (2008).

[266] T. Volz, S. Dürr, S. Ernst, A. Marte, and G. Rempe, *Characterization of elastic scattering near a Feshbach resonance in ^{87}Rb*, Phys. Rev. A **68**, 010702, (2003).

[267] B. Capogrosso-Sansone, N. V. Prokof'ev, and B. V. Svistunov, *Phase diagram and thermodynamics of the three-dimensional Bose-Hubbard model*, Phys. Rev. B **75**, 134302, (2007).

[268] J. Li, Y. Yu, A. M. Dudarev, and Q. Niu, *Interaction broadening of Wannier functions and Mott transitions in atomic BEC*, New J. Phys. **8**, 154, (2006).

[269] P.-I. Schneider, S. Grishkevich, and A. Saenz, *Ab initio determination of Bose-Hubbard parameters for two ultracold atoms in an optical lattice using a three-well potential*, Phys. Rev. A **80**, 013404, (2009).

[270] Z. X. Liang, B. B. Hu, and B. Wu, *Interaction effects on Wannier functions of a Bose-Einstein condensate in an optical lattice and implications for Bose-Hubbard model*, cond-mat/0903.4058, (2009).

[271] B. Wu and J. Shi, *Self-consistent single-band approximation for interacting boson systems*, cond-mat/0907.2046, (2009).

[272] M. J. Hartmann, F. G. S. L. Brandao, and M. B. Plenio, *Quantum many-body phenomena in coupled cavity arrays*, Laser Photonics Rev. **2**, 527, (2008).

[273] M. Johanning, A. F. Varon, and C. Wunderlich, *Quantum simulations with cold trapped ions*, J. Phys. B **42**, 154009, (2009).

[274] M. J. Hartmann, F. G. S. L. Brandao, and M. B. Plenio, *Strongly interacting polaritons in coupled arrays of cavities*, Nat. Phys. **2**, 849, (2006).

[275] A. D. Greentree, C. Tahan, J. H. Cole, and L. C. L. Hollenberg, *Quantum phase transitions of light*, Nat. Phys. **2**, 856, (2006).

[276] J. Quach, M. I. Makin, C.-H. Su, A. D. Greentree, and L. C. L. Hollenberg, *Band structure, phase transitions, and semiconductor analogs in one-dimensional solid light systems*, Phys. Rev. A **80**, 063838, (2009).

[277] J. Koch and K. Le Hur, *Superfluid–Mott-insulator transition of light in the Jaynes-Cummings lattice*, Phys. Rev. A **80**, 023811, (2009).

[278] D. Rossini and R. Fazio, *Mott-insulating and glassy phases of polaritons in one-dimensional arrays of coupled cavities*, Phys. Rev. Lett. **99**, 186401, (2007).

[279] M. Aichhorn, M. Hohenadler, C. Tahan, and P. B. Littlewood, *Quantum fluctuations, temperature, and detuning effects in solid-light systems*, Phys. Rev. Lett. **100**, 216401, (2008).

[280] S. Schmidt and G. Blatter, *Strong coupling theory for the Jaynes-Cummings-Hubbard model*, Phys. Rev. Lett. **103**, 086403, (2009).

[281] M. Knap, E. Arrigoni, and W. von der Linden, *Spectral properties of coupled cavity arrays in one dimension*, Phys. Rev. B **81**, 104303, (2010).

[282] P. Pippan, H. G. Evertz, and M. Hohenadler, *Excitation spectra of strongly correlated lattice bosons and polaritons*, Phys. Rev. A **80**, 033612, (2009).

[283] S. Schmidt and G. Blatter, *Excitations of Strongly Correlated Lattice Polaritons*, Phys. Rev. Lett. **104**, 216402, (2010).

[284] D. G. Angelakis, M. F. Santos, and S. Bose, *Photon-blockade-induced Mott transitions and XY spin models in coupled cavity arrays*, Phys. Rev. A **76**, 031805(R), (2007).

[285] M. J. Hartmann, F. G. S. L. Brandao, and M. B. Plenio, *A polaritonic two-component Bose-Hubbard model*, New J. Phys. **10**, 033011, (2008).

[286] C. D. Ogden, E. K. Irish, and M. S. Kim, *Dynamics in a coupled-cavity array*, Phys. Rev. A **78**, 063805, (2008).

[287] M. I. Makin, J. H. Cole, C. D. Hill, A. D. Greentree, and L. C. L. Hollenberg, *Time evolution of the one-dimensional Jaynes-Cummings-Hubbard Hamiltonian*, Phys. Rev. A **80**, 043842, (2009).

[288] E. T. Jaynes and F. W. Cummings, *Comparison of quantum and semi-classical radiation theories with application to the beam maser*, Proc. IEEE **51**, 89, (1963).

[289] F. W. Cummings, *Stimulated emission of radiation in a single mode*, Phys. Rev. **140**, A1051, (1965).

[290] B. W. Shore and P. L. Knight, *The Jaynes-Cummings model*, J. Mod. Opt. **40**, 1195, (1993).

[291] C. Cohen-Tannoudji, J. Dupont-Roc, and G. Grynberg, *Atom-photon interactions: Basic processes and applications*, Wiley-Interscience, (1992).

[292] M. I. Makin, J. H. Cole, C. Tahan, L. C. L. Hollenberg, and A. D. Greentree, *Quantum phase transitions in photonic cavities with two-level systems*, Phys. Rev. A **77**, 053819, (2008).

[293] R. H. Dicke, *Coherence in spontaneous radiation processes*, Phys. Rev. **93**, 99, (1954).

[294] M. Tavis and F. W. Cummings, *Exact solution for an N-molecule—radiation-field Hamiltonian*, Phys. Rev. **170**, 379, (1968).

[295] W. Neuhauser, M. Hohenstatt, P. Toschek, and H. Dehmelt, *Optical-sideband cooling of visible atom cloud confined in parabolic well*, Phys. Rev. Lett. **41**, 233, (1978).

[296] J. Eschner, G. Morigi, F. Schmidt-Kaler, and R. Blatt, *Laser cooling of trapped ions*, J. Opt. Soc. Am. B **20**, 1003, (2003).

[297] D. F. V. James, *Quantum dynamics of cold trapped ions with application to quantum computation*, Appl. Phys. B **66**, 181, (1998).

[298] C. Nietner and A. Pelster, *Effective action approach for the Jaynes-Cummings-Hubbard model*, Private communication.

[299] P. Jordan and E. Wigner, *Über das Paulische Äquivalenzverbot*, Z. Phys. A **47**, 631, (1928).

[300] S.-C. Lei and R.-K. Lee, *Quantum phase transitions of light in the Dicke-Bose-Hubbard model*, Phys. Rev. A **77**, 033827, (2008).

[301] E. W. Weisstein, *Poisson Sum Formula*, http://mathworld.wolfram.com/PoissonSumFormula.html

[302] K. Jänich, *Funktionen-Theorie*, Berlin: Springer-Lehrbuch, (1993).

Publikationen

Publikationen in referierten Zeitschriften:

[Mering2008] A. Mering and M. Fleischhauer
One-dimensional Bose-Fermi-Hubbard model in the heavy-fermion limit
Physical Review A **77**, 023601 (2008).

[Muth2008] D. Muth, A. Mering, and M. Fleischhauer
Ultracold bosons in disordered superlattices: Mott insulators induced by tunneling
Physical Review A **77**, 043618 (2008).

[Mering2009] A. Mering, M. Fleischhauer, P. A. Ivanov, and K. Singer
Analytic approximations to the phase diagram of the Jaynes-Cummings-Hubbard model
Physical Review A **80**, 053821 (2009).

[Ivanov2009] P. A. Ivanov, S. S. Ivanov, N. V. Vitanov, A. Mering, M. Fleischhauer, and K. Singer
Simulation of a quantum phase transition of polaritons with trapped ions
Physical Review A **80**, 060301(R) (2009).

[Mering2010] A. Mering and M. Fleischhauer
Fermion-mediated long-range interactions of bosons in the one-dimensional Bose-Fermi-Hubbard model
Physical Review A **81**, 011603(R) (2010).

Lebenslauf Alexander Mering

Persönliche Daten

Geboren am 10. 05. 1979 in Idar-Oberstein

Familienstand: verheiratet

Staatsangehörigkeit: deutsch

Schulbildung

08/1985–07/1989	Grundschule in Herrstein
08/1989–06/1998	Gymnasium an der Heinzenwies, Idar-Oberstein
06/1998	Abitur

Wehrdienst

07/1998–09/1999	Fallschirmjägerbataillon 263 / Zweibrücken 6-wöchiger Übungsaufenthalt in Fort Bragg, NC, USA

Studium

10/1999–07/2002	Grundstudium Physik an der Universität Kaiserslautern (Nebenfach Informatik)
08/2002–02/2004	Hauptstudium Physik an der Universität Kaiserslautern (Nebenfach Mathematik)

02/2004–02/2005	Diplomarbeit an der TU Kaiserslautern *Bose-Fermi-Gemische in eindimensionalen Gittern* Betreuer: Prof. Dr. Michael Fleischhauer
seit 04/2005	Promotion an der TU Kaiserslautern Betreuer: Prof. Dr. Michael Fleischhauer
11/2005-08/2007	Stipendiat im Graduiertenkolleg 792: Nichtlineare Optik und Ultrakurzzeitphysik, Betreuer: Prof. Dr. Michael Fleischhauer

Fremdsprachen

Englisch, fließend

Französisch, Schulkenntnisse

EDV

Betriebssysteme	Linux (Administratortätigkeit), Windows
Sprachen	Shell-Skripte, HTML, Pascal, Fortran, C
Anwendungen	Matlab, Mathematica, LaTeX, Word, Excel

Danksagung

Der größte Dank gebührt meinem Betreuer Prof. Dr. Michael Fleischhauer, der mir das Abfassen dieser Arbeit ermöglicht hat und bei vielen Gelegenheiten durch fachliche Diskussionen den Inhalt maßgeblich beeinflusst hat. Er hatte zu jeder Zeit ein offenes Ohr für Fragen und Probleme. Auch danke ich ihm für die weitreichenden Möglichkeiten, die er mir eröffnet hat.

Was soll ich an dieser Stelle zu *meinem* Jürgen sagen? Abgesehen davon, dass er mein Hauptkorrektor war, der die Thematik der kalten Atome nun wohl besser kennt, als ihm lieb ist, hat er mich die ganzen Jahre unterhalten, angespornt und mit seinem Interesse an physikalischen Fragestellungen auch immer wieder ein Stück weiter gebracht. Darüber hinaus hat er noch viele weitere, unverzichtbare Aufgaben erfüllt. Danke Jürgen.

Ebenso danke ich der gesamten AG Fleischhauer für die unzähligen fachlichen Diskussionen, insbesondere mit Dominik, Johannes und Razmik. Hier sind auch die erfrischenden Ausritte in den Dschungel der deutschen und armenischen Sprache von unschätzbarem Wert gewesen. Gesonderte Erwähnung verdienen die kreativen Illustrationen des David D.

Nicht zu vergessen sind die Personen, die immer wieder durch Diskussionen zum Thema beigetragen haben, sei dies auf Konferenzen, Seminaren oder auf unserem Flur gewesen.

Auch danke ich meiner Frau Marena, die mich stets unterstützt und meine kleinen und großen Macken geduldig ertragen hat und erträgt. Vor allem danke ich Ihr für Anna Theresa, die mir des Nachts so manche Zeit zum Nachdenken ermöglicht hat.